Mechanisms of centrosome separation in *C. elegans*

THÈSE N^{O} 6916 (2016)

PRÉSENTÉE LE 18 MARS 2016
À LA FACULTÉ DES SCIENCES DE LA VIE
UNITÉ DU PROF. GÖNCZY
PROGRAMME DOCTORAL EN APPROCHES MOLÉCULAIRES DU VIVANT

ÉCOLE POLYTECHNIQUE FÉDÉRALE DE LAUSANNE

POUR L'OBTENTION DU GRADE DE DOCTEUR ÈS SCIENCES

PAR

Alessandro DE SIMONE

acceptée sur proposition du jury:

Prof. F. G. van der Goot Grunberg, présidente du jury
Prof. P. Gönczy, Prof. F. Naef, directeurs de thèse
Prof. S. Grill, rapporteur
Dr F. Nédélec, rapporteur
Prof. V. Simanis, rapporteur

ÉCOLE POLYTECHNIQUE
FÉDÉRALE DE LAUSANNE

Suisse
2016

Ai nonni - Antonia, Carlo, Eugenia e Rocco -
e alle loro storie nelle sere d'estate

When I was a boy I felt that the role of rhyme in poetry was to compel one to find the unobvious because of the necessity of finding a word which rhymes. This forces novel associations and almost guarantees deviations from routine chains or trains of thought. It becomes paradoxically a sort of automatic mechanism of originality.

— Stanislaw Ulam, 1976

Abstract

Centrosomes are the major microtubule organizing centers of animal cells. The two centrosomes present at the onset of mitosis must separate in a timely fashion along the nuclear envelope to ensure proper bipolar spindle assembly and thus genome stability. Microtubule-associated motors of the kinesin-5 family are required for centrosome separation in several systems, but are partially redundant or entirely dispensable in others, where the minus-end directed motor dynein plays an important role. The mechanisms by which dynein powers centrosome separation are incompletely understood. Furthermore, the nature of the symmetry-breaking mechanisms that imbalance the forces acting on centrosomes to favor their movement away from each other are not known.

We addressed these questions using a combination of 3D time-lapse microscopy, image processing and computational modeling to dissect centrosome separation in the polarized one-cell *C. elegans* embryo that entirely relies on dynein for this process. First, we have characterized the quantitative features of centrosome separation in the wild-type. Next, we compared centrosome separation between wild-type and mutant/RNAi conditions. Our analysis revealed that centrosome separation is powered by the combined action of dynein at the nuclear envelope and at the cell cortex. Moreover, we demonstrated that cortical dynein requires actomyosin contractility to separate centrosomes. These observations suggest that cortical dynein acts by harnessing anterior-directed actomyosin cortical flows initiated earlier in the cell cycle by the centrosomes themselves. To confirm this model, we successfully tested experimentally two of its key predictions, namely that dynein complexes flow toward the anterior together with the cortex and that the velocity of centrosome separation correlates with that of the flow of the nearby cortex. Taken together, these results demonstrate that centrosome separation is driven by nuclear and cortical dynein, where the latter acts by transmitting forces produced by the cortical actomyosin flow.

To test whether this model is sufficient to explain centrosome separation, we developed a 3D computational model of centrosome dynamics. Indeed, predicted centrosome separation agrees quantitatively with the experimental observations in wild-type and mutant/RNAi conditions. Moreover, the qualitative predictions of the model are robust for parameter changes. Furthermore, computational simulations demonstrate that forces are intrinsically organized to move centrosomes away from each other without the need of any extrinsic symmetry-breaking mechanism. Indeed, in the case of nuclear dynein-driven separation, the position of centrosomes between the nuclear envelope and the cortex results in an asymmetric microtubule aster that leads to centrosome outward movement. In the case of cortical dynein, cortical flows are triggered by centrosomes and always move away from them, such that their forces are always directed to separate centrosomes. Therefore, this separation mechanism functions irrespective of the initial position of centrosomes along the cortex. In conclusion, in this thesis we uncover a novel organizing principle in which dynein, coupled with cell geometry and flow pattern, serves to robustly separate centrosomes and thus ensure genome stability.

Key words: *C. elegans*, one cell-stage embryo, centrosome separation, symmetry-breaking mechanisms, cytoskeleton, dynein, actomyosin network, cell polarization, actomyosin flow, cell geometry, mathematical and computational modeling

Riassunto

I centrosomi sono il principale centro organizzatore dei microtubuli. All'inizio della mitosi, i due centrosomi devono separarsi muovendosi lungo la superficie del nucleo al fine di assicurare la corretta formazione del fuso mitotico e quindi la stabilità del genoma. I motori della famiglia delle chinesine-5, necessari per la separazione dei centrosomi in molti sistemi, sono tuttavia parzialmente o completamente superflui in altri, nei quali assume un ruolo importante il motore dineina, diretto verso l'estremità negativa del microtubulo. Il meccanismo con cui la dineina sostiene la separazione dei centrosomi non è completamente compreso, così come non è nota la natura del meccanismo di rottura di simmetria che sbilancia le forze che, agendo sui centrosomi, ne favoriscono il movimento in direzione diametralmente opposta.

Al fine di rispondere a queste domande, abbiamo studiato la separazione dei centrosomi nell'embrione di *C. elegans* allo stadio di singola cellula, utilizzando una combinazione di microscopia time-lapse in 3D, analisi automatica della immagini e modellizzazione computazionale. Inizialmente, abbiamo comparato la separazione dei centrosomi nel wild-type e in mutanti o condizioni RNAi. La nostra analisi ha rivelato che la dineina al pronucleo e alla corteccia separano insieme i centrosomi. Abbiamo inoltre dimostrato che, per questa separazione, la dineina corticale necessita della contrattilità della corteccia di actomiosina. Queste osservazioni suggeriscono che la dineina corticale agisca sfruttando il flusso della corteccia, il quale è diretto verso il polo anteriore dell'embrione ed è stato innescato precedentemente dai centrosomi stessi. Al fine di confermare questo modello, ne abbiamo verificato sperimentalmente due predizioni: che la dineina fluisca insieme alla corteccia e che la velocità di separazione dei centrosomi correli con quella del flusso corticale. Complessivamente, questi risultati dimostrano che la forza che separa i centrosomi è esercitata dalla dineina nucleare e corticale, dove quest'ultima agisce trasmettendo le forze prodotte dal flusso della corteccia.

Per verificare che questo modello sia sufficiente per spiegare la separazione dei centrosomi, abbiamo sviluppato un modello computazionale 3D della dinamica del citoscheletro. Le predizioni del modello concordano quantitativamente con le osservazioni sperimentali sia nel wild-type che nelle condizioni mutanti/RNAi e sono qualitativamente robuste al variare dei parametri. Inoltre, il modello dimostra che le forze sono intrinsecamente dirette per allontanare i centrosomi tra loro senza la necessità di un meccanismo estrinseco di rottura di simmetria. Infatti, nel caso della dineina nucleare, la posizione dei centrosomi tra il pronucleo e la corteccia genera una asimmetria della stella di microtubuli, la quale porta al movimento dei centrosomi l'uno in direzione opposta all'altro. Invece, nel caso della dineina corticale, il flusso della corteccia è innescato dai centrosomi stessi e si muove sempre in direzione opposta a loro, per cui le forze esercitate sono sempre dirette per separarli. Questo meccanismo di separazione funziona indipendentemente dalla specifica posizione dei centrosomi lungo la corteccia. In conclusione, nel lavoro di tesi abbiamo scoperto un nuovo meccanismo in cui la dineina, insieme alla geometria della cellula e alla profilo di velocità del flusso corticale, separa i centrosomi, assicurando la stabilità del genoma.

Parole chiave: *C. elegans*, embrione, singola cellula, separazione dei centrosomi, rottura di simmetria, citoscheletro, dineina, corteccia di actomiosina, polarizzazione cellulare, flusso di actomiosina, geometria cellulare, modellizzazione matematica e computazionale

Contents

Abstract **i**

Sommario **iii**

List of figures **ix**

List of tables **xi**

1 Introduction **1**

1.1 Components of the cytoskeleton . . . 2
  1.1.1 Microtubules . . . 3
  1.1.2 Centrosomes . . . 5
  1.1.3 Microtubule-associated molecular motors . . . 6
  1.1.4 The actomyosin cortex . . . 8
1.2 The mitotic spindle . . . 9
  1.2.1 Spindle assembly and function . . . 9
  1.2.2 On the importance of timely centrosome separation . . . 12
  1.2.3 Building a spindle without centrosomes . . . 13
1.3 Forces acting on the microtubule aster . . . 14
  1.3.1 Microtubule polymerization forces . . . 14
  1.3.2 Microtubule depolymerization forces . . . 15
  1.3.3 Length-dependent forces . . . 15
  1.3.4 Cortical forces . . . 18
  1.3.5 Motors on overlapping microtubules . . . 20
1.4 Mechanisms of centrosome separation . . . 20
  1.4.1 Kinesin-5 . . . 21
  1.4.2 Microtubule polymerization forces . . . 21
  1.4.3 Dynein . . . 23
  1.4.4 Actomyosin cortex . . . 25
  1.4.5 Symmetry breaking mechanisms . . . 25
1.5 The one-cell stage *C. elegans* embryo . . . 27
  1.5.1 Cell polarization and mitosis . . . 29
  1.5.2 The *C. elegans* centrosome . . . 31
  1.5.3 The roles of dynein . . . 31

1.6 Aim of this work 34

2 Materials and Methods **37**

2.1 Worm strains 37

2.2 RNAi bacterial feeding 37

2.3 Indirect immunofluorescence 38

2.4 Imaging 38

2.5 Centrosome and pronuclear tracking 39

2.6 Centrosome separation curves synchronization 40

2.7 Centration and pronuclear migration curves synchronization 41

2.8 Cortical flow measurements 42

2.9 Calculation of angle between centrosomes 42

2.10 Statistical comparison of centrosome separation in different conditions 43

2.11 Centrosomes overshoot 43

2.12 Computer simulation 43

2.12.1 Microtubules and centrosomes 44

2.12.2 Pronuclei 44

2.12.3 Dynein motors 45

2.12.4 Initial condition 45

2.12.5 Parameters fit 46

3 Centrosome separation in one-cell stage *C. elegans* embryos **47**

3.1 Measurement of centrosome separation 47

3.2 Opposing forces keep centrosomes at an equilibrium angle after separation . . 51

4 Mechanisms of centrosome separations **55**

4.1 Kinesin-5 does not contribute to centrosome separation in *C. elegans* 55

4.2 Nuclear and cortical dynein cooperate to ensure timely centrosome separation 56

4.3 Actomyosin contractions power cortical dynein-mediated centrosome separation 60

4.4 Dynein couples actomyosin cortical flow with centrosome separation 65

4.4.1 Cortical dynein complexes flow together with the actomyosin network . 65

4.4.2 Centrosome separation movements correlate locally with actomyosin cortical flows 65

4.4.3 Centrosome separation upon perturbation of cortical flow velocity . . . 69

4.5 Working model 70

4.6 Considerations on dynein motility 71

5 Computational model of centrosome separation **73**

5.1 Description of the computational model 73

5.2 Predictions of the computational model 74

5.3 The role of dynein motility in centrosome separation 78

5.4 Impact of cortical flow velocity on centrosome separation 79

5.5 Partial dynein depletion 81

6 Symmetry breaking mechanisms 85
- 6.1 Nuclear dynein . . . 85
- 6.2 Cortical dynein . . . 89
- 6.3 Centrosomes and the control of cortical flow pattern . . . 91
- 6.4 KLP-7: a potential external symmetry breaking mechanism . . . 93

7 Discussion 95
- 7.1 Overview of results . . . 95
- 7.2 Cortical dynein as a novel coupling device . . . 97
- 7.3 On the role of nuclear dynein . . . 98
- 7.4 Dynein in the cytoplasm: possible root of opposing forces . . . 99
- 7.5 Microtubule polymerization forces . . . 100
- 7.6 Kinesin-5: a silent spectator? . . . 101
- 7.7 Limitations, improvements and further developments . . . 101
  - 7.7.1 Centrosome separation: further experiments . . . 101
  - 7.7.2 Limitations and improvements of the computational model . . . 103
  - 7.7.3 Centrosome separation beyond dynein . . . 105
  - 7.7.4 Beyond centrosome separation . . . 106
- 7.8 Concluding remarks . . . 106

A Mechanisms of centration 109
- A.1 Centrosome centration . . . 109
- A.2 Migration of the female pronucleus . . . 115
- A.3 Estimation of the microtubule asters drag coefficient . . . 117

B Modeling the effect of clathrin heavy chain on force generation 121
- B.1 Computational model details . . . 127
  - B.1.1 Rotational dynamics . . . 127
  - B.1.2 Microtubule aster . . . 129
  - B.1.3 Microtubule dynamics . . . 129
  - B.1.4 Cortical force generators . . . 129
  - B.1.5 Asymmetric distribution of force generators . . . 130

C Centrosome separation parameters fit 133

D Computational model parameters 137

E Movies legends 141

Acknowledgements 143

Bibliography 145

List of Figures

1.1 Schematics of centrosome separation 2
1.2 Microtubule structure and dynamics 4
1.3 Microtubule-associated motors 6
1.4 Actin and myosin 8
1.5 Spindle assembly and function 11
1.6 Forces acting on the microtubule aster 17
1.7 Mechanisms of centrosome separation 23
1.8 Examples of symmetry breaking mechanisms 26
1.9 *C. elegans* embryo first cell cycle 29

2.1 Example of synchronization procedure for *goa-1/gpa-16(RNAi)* embryos 41

3.1 Centrosome separation in one-cell *C. elegans* embryo 48
3.2 Quantification of centrosome separation 49
3.3 Quantification of male pronucleus size during centrosome separation 49
3.4 Quantification of angle between centrosomes during centrosome separation . 50
3.5 Centrosome angles at equilibrium and comparison with mathematical models 53

4.1 Centrosome separation in kinesin-5 BMK-1 deletion mutant embryos 56
4.2 Centrosome separation upon dynein heavy-chain DHC-1 depletion 57
4.3 Cortical and nuclear dynein cooperate to separate centrosomes 58
4.4 Quantification of centrosome separation in embryos depleted of cortical and/or nuclear dynein 59
4.5 Centrosome separation in embryos depleted of other components of the ternary complex 59
4.6 NMY-2 depletion does not impair cortical dynein localization 61
4.7 Actomyosin contractions power centrosome separation through cortical dynein 62
4.8 Quantification of centrosome separation in actomyosin contractility depleted embryos 63
4.9 Centrosome separation in embryos with perturbed actomyosin contractility . . 63
4.10 Centrosome separation in embryos enhanced of actomyosin contractility . . . 64
4.11 Correlated flows of cortical actomyosin network and cortical dynein anchors . 66
4.12 Actomyosin cortex flows correlate with separation movements of the closest centrosome 67

4.13 Separation movements of the closest centrosome correlate with flow of the closest region of the actomyosin cortex 68
4.14 Separation movements of the closest centrosome upon perturbation of cortical flows 70
4.15 Working model of centrosome separation in the *C. elegans* one-cell stage embryo 71

5.1 Computer simulation and fitting of centrosome separation. 75
5.2 Computer simulation and validation of centrosome separation. 76
5.3 Computer simulations parameter sensitivity analysis 77
5.4 Centrosome separation upon reduction of microtubule aster size 78
5.5 Computer simulations of centrosome dynamics upon impairment of nuclear and cortical dynein motility. 79
5.6 Centrosome separation upon variation of cortical flow speed 80
5.7 Centrosome separation upon partial dynein depletion 82

6.1 Computational analysis of symmetry breaking mechanisms: nuclear dynein . . 87
6.2 Schematics of symmetry breaking mechanism for nuclear dynein-based centrosome separation 88
6.3 Computational analysis of symmetry breaking mechanisms: cortical dynein . . 90
6.4 Computer simulation of the dynamics of a single centrosomes 92
6.5 Centrosome separation upon depletion of the depolymerizing kinesin KLP-7 . 94

A.1 Pronuclear migration and centrosome/pronuclear centration 110
A.2 Quantification of centrosomes centration 112
A.3 Female pronucleus migration 116
A.4 Estimation of the drag coefficient of the male pronucleus-microtubule aster complex 119

B.1 Clathrin negatively regulates net pulling forces acting on centrosomes during centration/rotation 122
B.2 Clathrin contributes to cortical tension in *C. elegans* embryos. 125
B.3 Model of cortical force generation 126
B.4 2D computational model of stochastic centrosome movements driven by cortical force generators. 128

List of Tables

B.1 Parameters of 2D simulation of cortical tension-dependent centrosome rotation 131

C.1 Fitted parameters of centrosome separation 133
C.2 Comparison of centrosome separation rates between mutant/RNAi and reference conditions. 134
C.3 Comparison of centrosome separation starting time t_0 between mutant/RNAi and reference conditions. 135

D.1 Parameters of 3D simulation of centrosome separation 138

1 Introduction

A fundamental feature of life is the ability to propagate information (reviewed in Szathmáry and Smith, 1995). Information is transmitted as a message, the genome, and as an interpreter, the cellular material. Genome stability is an absolute requirement for the survival of the species. During development of multicellular organisms, correct transmission of the genome across cell cycles is required to form a healthy and fertile adult. During development and in the adult, defects in genome transmission can result, among other problems, in cell death or in the formation of abnormally proliferating cells, thus potentially leading to cancer (reviewed in Weinberg, 2013). Therefore, cells evolved to reliably transmit their genetic information from parents to progeny. Despite the variety of life forms, the fundamental mechanisms of segregating the genetic material to the two daughter cells during cell division are conserved across species (reviewed in Alberts et al., 2014). Every cell performs cell division using cytoskeletal elements, together with their associated motor proteins, to correctly position and segregate chromosomes. Thus, studying the mechanics of cell division in one system sheds light on more general mechanisms that are common to several species.

In eukaryotes, faithful chromosome segregation is performed by the mitotic spindle (reviewed in Walczak et al., 2010). The spindle has a bipolar diamond-shape structure in which chromosomes are located between two microtubule organizing centers on each side. Microtubule organizing centers nucleate microtubules with which they bind and pull apart sister chromatids. The assembly, maintenance and function of the mitotic spindle must be tightly regulated to ensure correct chromosome segregation. In particular, the correct positioning of the microtubule organizing centers is fundamental for these processes.

The centrosome is the major microtubule organizing center of animal cells (reviewed in Bornens, 2012). Centrosomes are membrane-less organelles composed of a pair of centrioles surrounded by a matrix of amorphous pericentriolar material. This pericentriolar material includes proteins that nucleate microtubules and regulate their function and that are thus responsible for centrosome function as microtubule organizing center.

A prerequisite for proper bipolar spindle assembly is the timely separation of the two cen-

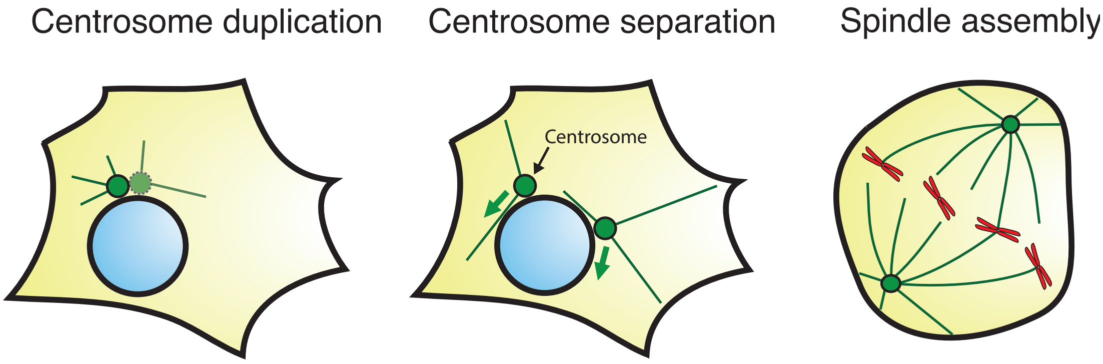

Figure 1.1 – **Schematics of centrosome separation.** In S phase the centrosome duplicates and, shortly before mitosis, the two centrosomes separate along the surface of the nucleus. Then, the nuclear envelope breaks down and the mitotic spindle is assembled.

trosomes present at the onset of mitosis (Fig. 1.1) (reviewed in Tanenbaum and Medema, 2010). At the beginning of each cell cycle, a single centrosome is present in the cell. The centrosome duplicates during S-phase; thereafter, during prophase, at the onset of mitosis, the two centrosomes separate while moving along the surface of the nucleus. Afterwards, the nuclear envelope breaks down and the mitotic spindle forms. Backup mechanisms exist to move centrosomes apart even after nuclear envelope breakdown, but at the cost of risking higher chromosome segregation defects (Silkworth et al., 2012 and reviewed in Rosenblatt, 2005). Therefore, timely prophase centrosome separation is fundamental for correct spindle assembly, chromosome segregation and thus genome integrity.

In this work, we investigate the mechanisms of centrosome separation using the *C. elegans* early embryo as a model system. In this chapter, we will introduce the mechanical components of the cell and describe their function and regulation. In particular, we will describe how cytoskeletal components are assembled in the mitotic spindle in order to segregate chromosomes. Then, we will describe the most important forces that act on the cytoskeleton. The role of these forces will be discussed in the context of centrosome separation. Finally, we will introduce the key features of one-cell stage *C. elegans* embryos, focusing especially on cell mechanics.

1.1 Components of the cytoskeleton

Cells in all domains of life have a cytoskeleton. The cytoskeleton is a dynamic ensemble that cells use to exert forces (reviewed in Howard, 2001; Phillips et al., 2012). In eukaryotic cells, the components of the cytoskeleton comprise three types of filaments: microtubules, intermediate filaments and actin. These three components have a different molecular nature, structure and physical properties, but are similarly formed by the polymerization of globular subunits. Since centrosomes, the subject of this study, are microtubule organizing centers, we will focus on the role of microtubules. Moreover, we will describe molecular motors, the fundamental force generating component of the cytoskeleton, by focusing on their role in exerting forces within the cytoplasm. Finally, we will also briefly introduce the actin network, since we will demonstrate its important role in centrosome separation.

1.1.1 Microtubules

Microtubules are long fiber-like polymers that can span the whole cell volume and that function to exert and transmit forces within the cell (reviewed in Desai and Mitchison, 1997; Dogterom et al., 2005; Howard and Hyman, 2009). In addition, microtubules serve as tracks for molecular motors that can move along them while transporting cargos (reviewed in Howard, 2001).

Structurally, microtubules are hollow cylinders composed of tubulin subunits (Fig. 1.2) (reviewed in Desai and Mitchison, 1997). Each subunit is a dimer of two globular proteins, α-tubulin and β-tubulin. Tubulin dimers are polarized and can bind one to another head-to-tail (Fig. 1.2A). In addition, tubulin dimers can form lateral contacts between monomers of the same type, $\alpha - \alpha$ and $\beta - \beta$. Tubulin subunits typically assemble as 13 linear strings, called protofilaments, which associate laterally to form a hollow cylinder, called microtubule (Fig. 1.2B). This structure guarantees microtubule rigidity and stability to lateral forces, since microtubule breakage internally requires breaking a high number of bonds. In the microtubule, each tubulin monomer is aligned in a certain direction, so that the microtubule itself has a defined polarity, with α-tubulin on the surface of one end, the minus-end, and β-tubulin at the other end, the plus-end. A fast dynamics of monomer association-dissociation occurs at both microtubule ends, but the rates of these processes differ drastically: the minus-end is more stable, while the plus-end is highly dynamic.

The rate of microtubule polymerization and depolymerization depends on the concentration of free tubulin in the cytoplasm, but also on the GTP state of the tubulin dimers (Fig. 1.2C) (reviewed in Desai and Mitchison, 1997; Howard and Hyman, 2009). Indeed, in each tubulin subunit, both α and β monomers have a binding site for a GTP molecule. The GTP molecule of α-tubulin is stably bound to the monomer and never hydrolyzed or exchanged. By contrast, the nucleotide associated with β-tubulin can be either GTP or GDP and is exchangeable when the tubulin subunits are free in the cytoplasm. Since in the cytoplasm GTP nucleotides are more abundant than GDP ones, free tubulin tend to bind to GTP. Moreover, since the hydrolysis of GTP occurs at a very slow rate when the tubulin dimer is free, free tubulin mostly remains in the GTP form. On the other hand, hydrolysis becomes faster when tubulin is part of a microtubule. As a result, tubulin subunits are added to microtubules mostly in the GTP form and then are progressively hydrolyzed to the GDP form. When β-tubulin is in the GDP form, an elastic strain is applied to the bond with the next subunit, so that the rate of subunit dissociation increases with respect to that in the GTP form. Therefore, for an intermediate range of free tubulin concentrations, there is a situation in which a subunit at the microtubule end is stably associated if in the GTP form, but rapidly dissociates if in the GDP form.

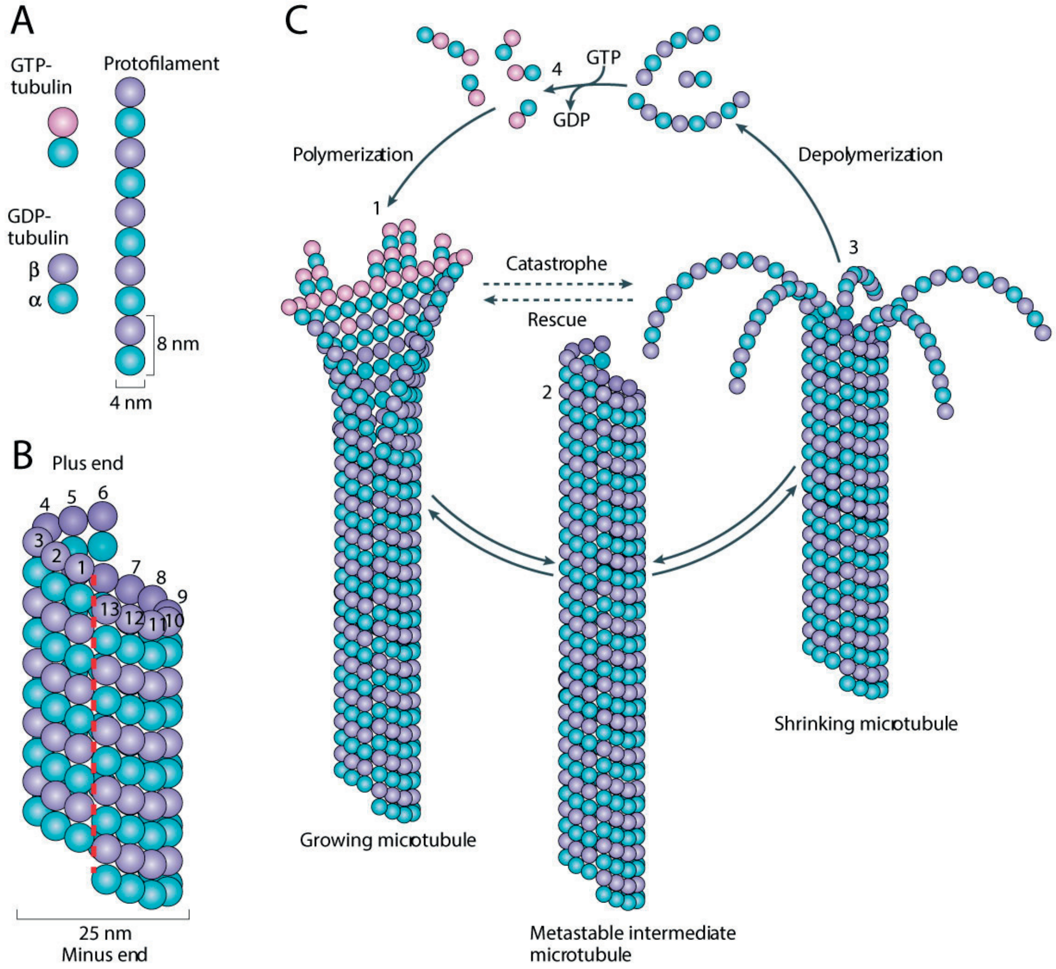
A
GTP-tubulin
Protofilament
GDP-tubulin
β
α
8 nm
4 nm
B
Plus end
4
5
6
3
2
1
7
8
9
13
12
11
10
25 nm
Minus end
C
4
GTP
GDP
Polymerization
Depolymerization
1
Catastrophe
Rescue
3
2
Shrinking microtubule
Growing microtubule
Metastable intermediate microtubule

Figure 1.2 – **Microtubule structure and dynamics. A** $\alpha-\beta$ tubulin dimers assemble in linear protofilaments in a head-to-tail fashion. **B** 13 tubulin protofilaments assemble in a hollow cilinder by $\alpha-\alpha$ and $\beta-\beta$ lateral contacts. **C** Microtubules undergo dynamic instability at the plus-end. Thus, microtubules switch from a growing state to a shrinking state (catastrophe) and viceversa (rescue), depending on the presence of a GTP -tubulin cap at the plus-end. Adapted by permission from Macmillan Publishers Ltd (Akhmanova and Steinmetz, 2008).

Therefore, association-dissociation rates depend on the GTP state of tubulin dimers at the microtubule ends. Since those rates are higher at the microtubule plus-end, GTP subunits will be added to this end and then will be progressively hydrolyzed. Meanwhile, the microtubule continues to grow, so that these older subunits are buried in the middle of the microtubule and the plus-end is continuously supplied with GTP subunits, thus forming a GTP cap. Given the stochastic nature of hydrolysis and polymerization, sometimes the GTP cap is hydrolyzed until the microtubule end. As a result, the rate of subunits dissociation overcomes that of association and the microtubule starts to quickly depolymerize. This switch from the growing to the shrinking state is called catastrophe. Similarly, while the microtubule depolymerizes, if a GTP cap forms stochastically, then microtubule depolymerization stops and polymerization restarts. This process is called rescue. Thus, every microtubule undergoes periods of growth and shrinkage, separated by catastrophes and rescue events, a process referred to as dynamic instability.

A popular and useful model describes microtubule instability as a stochastic process of switching between a growing and a shrinking state with constant catastrophe and rescue rates, while the actual nucleotide hydrolyzation state of each tubulin dimer is not considered (Dogterom and Leibler, 1993). In this model, microtubules grow and shrink at constant velocities, but these rates, as well as the catastrophe and rescue rates, can depend on free tubulin concentration. The model predicts that the length of freely growing microtubules is exponentially distributed, with a typical length depending on microtubule growth, shrinkage, catastrophe and rescue rates (Dogterom and Leibler, 1993; Dogterom and Yurke, 1998). However, *in vivo*, microtubules are not growing freely, but often encounter barriers such as the cell membrane. In this case, microtubule polymerization generates a pushing force against the barrier and, as result, microtubule polymerization itself is inhibited (Dogterom, 1997). This inhibition can be modeled as a reduction of microtubule growth rate and a corresponding increase of catastrophe rate (Dogterom, 1997; Janson et al., 2003). Thus, microtubules exerting pushing forces soon undergo catastrophe and start to shrink.

Microtubule polymerization and depolymerization rates can also be modified by microtubule-associated proteins (MAPs) (reviewed in Howard and Hyman, 2007; van der Vaart et al., 2009). In fact, *in vitro*, microtubule growth rate in the presence of a physiological concentration of free tubulin is several order of magnitudes slower than that observed *in vivo*. This discrepancy is likely due to the presence of proteins that enhance microtubule polymerization and stabilize microtubule ends *in vivo*. For instance, proteins of the XMAP215 family, e.g. ZYG-9 in *C. elegans*, promote microtubule growth and polymer stability by delivering free tubulin subunits to the microtubule plus-ends (reviewed in Howard and Hyman, 2007). Conversely, other MAPs can favor microtubule catastrophe. For instance, proteins of the kinesin-13/MCAK family, e.g. KLP-7 in *C. elegans*, bind to the microtubule plus-end and destabilize it by exerting bending stress on tubulin protofilaments (reviewed in Kinoshita et al., 2006).

1.1.2 Centrosomes

The nucleation of microtubules requires the association of typically 13 tubulin dimers to form a ring of protofilaments (reviewed in Alberts et al., 2014). Since so many dimers are involved, the spontaneous nucleation of microtubules is a statistically unlikely event. Thus, additional proteins are needed to act as a scaffold for the nucleation of a new microtubule. In particular, another tubulin subunit, called γ-tubulin, is important for microtubule nucleation (reviewed in Oakley et al., 2015). γ-tubulin forms a spiral ring complex that serves as seed for the binding of $\alpha - \beta$ tubulin dimers and thus for microtubule nucleation.

During mitosis, microtubules are typically nucleated from microtubule-organizing centers in

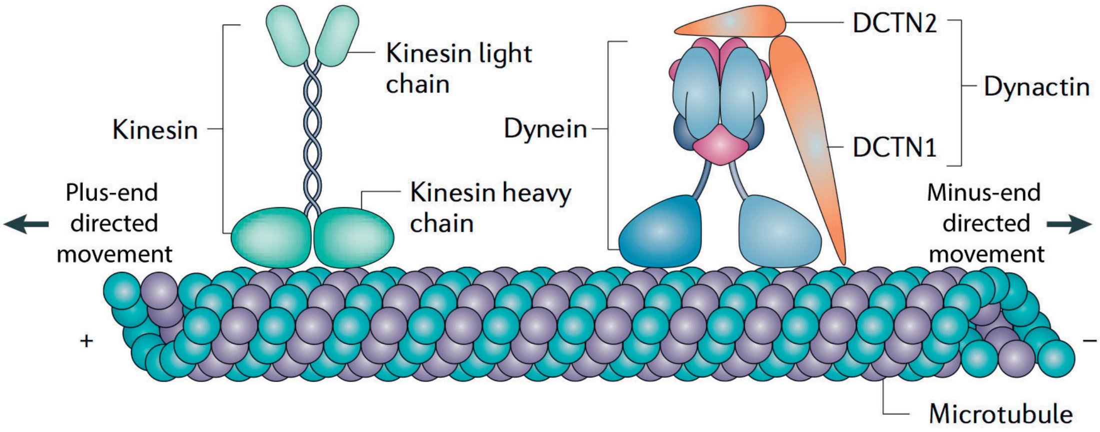

Figure 1.3 – **Microtubule-associated motors.** Schematics representing microtubule-associated motors of the kinesins and dyneins super-families. The preferred walking direction of motors is shown. Dynein is represented together with the dynactin complex, one of its most important regulators. Reprinted by permission from Macmillan Publishers Ltd (Millecamps and Julien, 2013).

which γ-tubulin is enriched. Thus, microtubules have their stable minus-end at the microtubule organizing center and their dynamic plus-end growing away from it. In most animal cells, the centrosome is the microtubule organizing center. The centrosome is composed of a pair of centrioles and of their surrounding amorphous pericentriolar material. Centrioles are barrel-shaped MT-based structures that duplicate at each cell cycle and, among other functions, serve as seeds for the accumulation of pericentriolar material at centrosomes. The pericentriolar material accumulates hundreds of different proteins, among which γ-tubulin rings that hence nucleate a microtubule aster radially out from the centrosome.

1.1.3 Microtubule-associated molecular motors

Microtubule-associated molecular motors can exert force on microtubules and walk along them to transport cargos (Fig. 1.3) (reviewed in Hirokawa et al., 2009; Phillips et al., 2012). In general, molecular motors are protein complexes that undergo cycles of conformational changes upon binding, hydrolysis and unbinding of ATP. In many cases of microtubule-associated motors, these conformational changes, together with the polarized structure of microtubules, lead to the movement of the motor along the microtubule. Each motor has a direction toward which it preferentially moves along the microtubule, so that they can be classified as plus-end or minus-end directed motors. Moreover, when a force is applied to the motor, for example the viscous drag of its cargo or a tethering force to a stable substrate, the motor transmits this force to the associated microtubule.

Microtubule-associated molecular motors are divided in two super-families, kinesins and dyneins. In turn, kinesins are divided into 14 large families having different structures and functions. Some kinesins, for example kinesin-1, transport cargos to specific subcellular locations by moving along microtubules. Other kinesins, for example members of the kinesin-5 family can bind overlapping microtubules and slide them apart (reviewed in Ferenz et al., 2010). This is possible because dimers of kinesin-5, each with plus-end motility, are bound to one another, thus forming a bipolar tetrameric assembly that can bind and walk along a microtubule with each of the two motor domains (see also Fig. 1.6F). In other cases, kinesin force generation is used to catalyze chemical or structural transformations of microtubule. For example, this is the case discussed earlier of the kinesin-13 family that acts at the microtubule plus-end to promote depolymerization (reviewed in Kinoshita et al., 2006).

Dyneins are minus-end directed motors that do not have homology with the kinesin family and that are divided in two branches, axonemal dynein and cytoplasmic dynein (reviewed in Roberts et al., 2013). Axonemal dynein was the first to be discovered and slides microtubules in cilia and flagella, thus allowing movement of those structures. In contrast, cytoplamic dynein acts inside the cell to transport cargos toward the microtubule minus-end and exert force on the microtubule aster. Cytoplasmic dynein is composed of two heavy chains, each containing a ring of AAA ATPase motor domains, and a variable number of intermediate and light chains that favor dynein binding to cargos.

Each kinesin and dynein motor is characterized by the step distance that it walks during one cycle of ATP binding, hydrolysis and unbinding (reviewed in Howard, 2001; Phillips et al., 2012). The rate at which these cycles occur determines the number of steps that a motor can perform per unit of time. The product of the step-size and the number of steps per unit of time is the velocity at which a motor moves. *In vitro* studies of microtubule-associated molecular motors and mathematical modeling have demonstrated that the rate of motor movement decreases when a force is applied to it. As a result, motor velocity decreases with the applied load until a given load, called the stall force, when the motor is not able to move, but only to exert force on the associated microtubule. Therefore, each motor can move at a maximum velocity, the free velocity, and can exert a maximum force, the stall force. The majority of molecular motors can perform multiple cycles of movement before detaching from the associated microtubule. The average microtubule length that a motor can travel before detatching is called processivity. In addition, the rate of detachment increases exponentially with the applied load, as for every chemical bond (Howard, 2001).

Molecular motors form complexes with proteins that regulate their functions (reviewed in Kardon and Vale, 2009; Verhey and Hammond, 2009; Vallee et al., 2012). These associated proteins can work as adapters for cargo binding or regulate motor activity. An important example is the large dynactin complex that mediates dynein binding to membranes and that is necessary for dynein-based organelle transport. Another important contributor to dynein function is the binding cofactor Lis-1 that is necessary for dynein association to nuclei and whose impairment results in nuclear migration defects. A striking example of the importance of Lis-1 comes from the study of neuronal cells migration during brain development, as impairment of Lis-1-mediated nuclear transport results in severe malformations of the brain cortex.

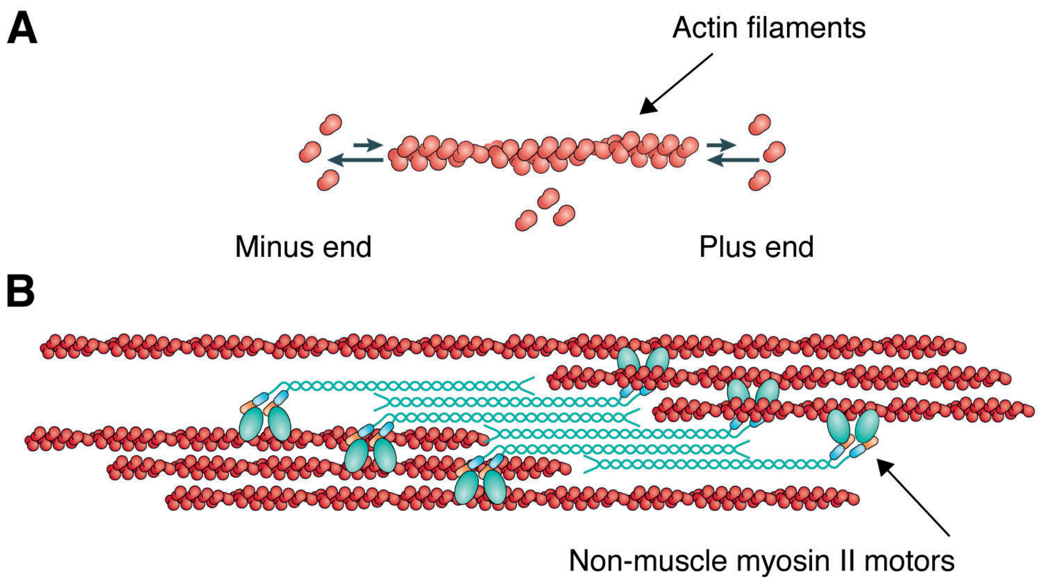

Figure 1.4 – **Actin and myosin.** **A** Filamentous actin is a single filament of actin monomers that undergo dynamic instability at both ends (top). **B** Non-muscle myosin II motors bundle and slide actin filaments, thus forming a contractile network. Adapted by permission from Macmillan Publishers Ltd (Vicente-Manzanares et al., 2009; Lowery and Van Vactor, 2009).

The way in which Lis-1 regulates dynein function is still debated, but it has been implicated in dynein-microtubule binding and function of the dynein AAA1 ATPase subdomain.

1.1.4 The actomyosin cortex

Another fundamental component of the cytoskeleton is the actomyosin cortex, a highly dynamic contractile network present under the plasma membrane (Fig. 1.4) (reviewed in Dominguez and Holmes, 2011; Salbreux et al., 2012; Alberts et al., 2014). The actomyosin network has a pivotal role in determining cell shape and in offering a strong scaffold for the anchoring of certain proteins. As we will discuss in the case of cell polarization, this network can undergo long range contractions that can remodel cell shape or generate cell-wide flows. For example, one of the key roles of the cell cortex during cell division is the formation of a ring that drives cytokinesis by contracting and thus invaginating the cell membrane in the cleavage furrow.

The principal structural elements of the actomyosin network are actin filaments (Fig. 1.4A). Like microtubules, they are composed of asymmetric subunits bound in a head-to-tail fashion, so that actin filaments are polarized and have different association-dissociation dynamics at the two ends. On the other hand, in contrast to microtubules, actin filaments are formed of only two coiled chains of actin subunits, so that actin rigidity is several orders of magnitude lower than that of microtubules. Actin monomers are also bound to a nucleotide, ATP in this case, that can be hydrolyzed to ADP, thus changing actin subunits association and dissociation rates and leading to dynamic instability.

Molecular motors of the myosin super-family bind, walk and exert forces on actin filaments (Fig. 1.4B). In particular, the non-processive motors of the myosin II family can bundle two actin filaments and slide them toward each other. As a result, they form a complex contractile network of interconnected short actin filaments, the actomyosin cortex.

Several proteins can modulate the activity of the actomyosin network by regulating actin filament nucleation, dynamic instability, as well as myosin activity. A key example is the small GTPase RhoA, e.g. RHO-1 in *C. elegans*, that promotes actomyosin contractility by activating myosin-II function and enhancing nucleation and polymerization of actin filaments (reviewed in Sit and Manser, 2011).

1.2 The mitotic spindle

In eukaryotic cells, chromosome segregation is performed by the mitotic spindle (Walczak and Heald, 2008; Walczak et al., 2010; Rago and Cheeseman, 2013). The mitotic spindle is a bipolar structure in which chromosomes are located between two microtubule organizing centers. Even if, as stated before, animal cells mostly rely on centrosomes to organize their mitotic spindle, important exceptions exist in which microtubules self-organize in an acentrosomal spindle pole (reviewed in Bornens and Gönczy, 2014; Dumont and Desai, 2012; Meunier and Vernos, 2015).

Microtubules are the structural element of mitotic spindle architecture (Walczak and Heald, 2008). During mitosis there are three principal subgroups of microtubules depending on where their plus-end is located: kinetochore microtubules, interpolar microtubules and astral microtubules. Kinetochore microtubules (k-fibers) have their plus-end attached to the chromosome kinetochores and exert forces on them. Interpolar microtubules are overlapping microtubules that emanate from opposite spindle poles and that are bound by motor crosslinkers, such as the tetrameric kinesin-5. Therefore, these microtubules join the two spindle poles and, as a result, shape the mitotic spindle. Finally, microtubules directed toward the cell cortex are called astral microtubules and are of critical importance for spindle elongation and positioning.

1.2.1 Spindle assembly and function

At the beginning of the cell cycle, a single centrosome, attached to the nucleus, is present in the cell (Fig. 1.5 - interphase) (reviewed in Walczak et al., 2010). During S phase, the two centrioles duplicate within the centrosome. As a result, two centrosomes, each harboring two centrioles, are formed. Later, at the beginning of mitosis, the two closely apposed centrosomes start to separate while moving along the nuclear surface until they reach roughly opposite poles (Fig. 1.5 - prophase). Then, most eukaryotic cells perform an open mitosis. In this

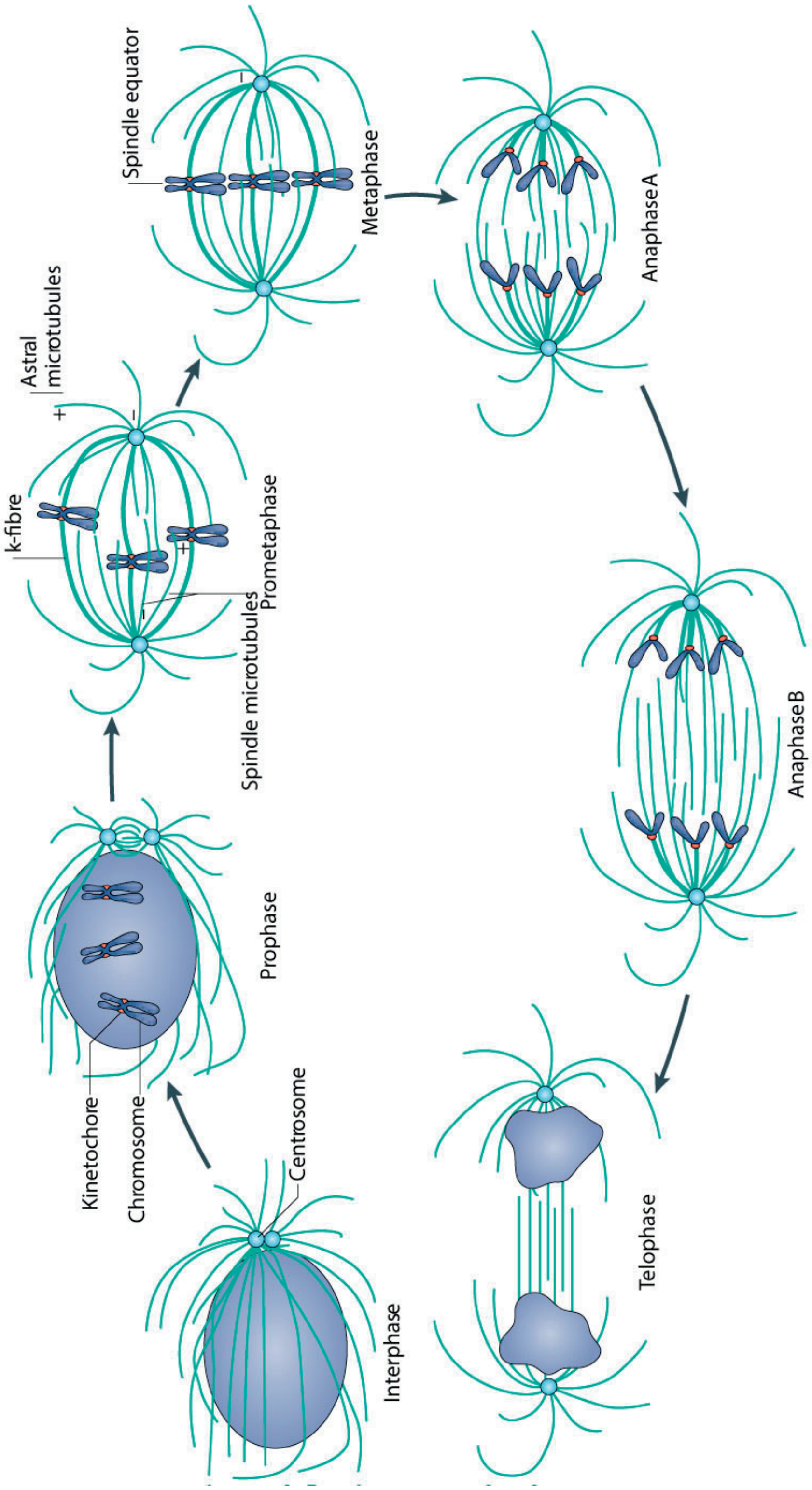
Interphase
Centrosome
Kinetochore
Chromosome
Prophase
Spindle microtubules
Prometaphase
k-fibre
+
−
Astral microtubules
Spindle equator
Metaphase
Anaphase A
Anaphase B
Telophase

process, the nuclear envelope is dismantled during prometaphase and the mitotic spindle is organized (Fig. 1.5 - prometaphase). In the case of some fungi and protists, a closed mitosis is performed, with interpolar and kinetochore microtubules growing inside the nucleus and astral microtubules growing outside (reviewed in Boettcher and Barral, 2013). We will now focus on the case of open mitosis, but analogous mechanisms are found in the case of closed mitosis.

When the nuclear envelope breaks down, microtubules from the two spindle poles start to catch the opposing kinetochores on the paired sister chromatids and position them in a plane perpendicular to the centrosome-centrosome axis, the metaphase plate (Fig. 1.5 - metaphase) (reviewed in Walczak et al., 2010; Rago and Cheeseman, 2013). At this stage, sister chromatids are physically linked by a complex called cohesin. Pulling forces are exerted between microtubule plus-ends and kinetochores and, as a result, tension is exerted between sister chromatids if they are correctly bound, each to a spindle pole (reviewed in Rago and Cheeseman, 2013). This tension controls the transition from metaphase to anaphase through the spindle assembly checkpoint (SAC). The spindle assembly checkpoint is based on a signal produced by any kinetochore that is not under tension, which blocks the activation of the anaphase-promoting complex (APC/C). When all kinetochores are under tension, the block is removed, the APC/C is activated and thus transition to anaphase starts. This is achieved through the activation of the APC/C, which leads to the activation of separase, an enzyme that cleaves the cohesin complex joining sister chromatids, thus allowing them to separate.

The separation of sister chromatids occurs in two phases (reviewed in Walczak et al., 2010). In a first phase, anaphase A, sister chromatids are separated by pulling forces acting between microtubules and kinetochores (Fig. 1.5 - anaphase A). In a second phase, called anaphase B or spindle elongation, sister chromatids are further separated by the outward movement of spindle poles (Fig. 1.5 - anaphase B). Here, the two centrosomes move away from one another and thus further pull apart the sister chromatids. Spindle elongation is often driven by forces exerted by molecular motors on interpolar microtubules that push them away from each other. In addition, pulling forces exerted from the cortex on astral microtubules contribute to spindle elongation in many systems. After anaphase, chromosomes start to decondense, the

Figure 1.5 *(preceding page)* – **Spindle assembly and function.** During G1, a single centrosome is attached to the nucleus and, during S phase, it is duplicated. After, during prophase, the two centrosomes separate along the nuclear surface, while DNA is compacted. Thereafter, the nuclear envelope breaks down and the spindle starts assemble. First, connections between microtubules and chromosomes (k-fibers) are formed (prometaphase). Chromosomes are positioned in a plate at the center of the spindle (metaphase) and, afterwards, sister chromatids are separated by forces acting at the interface between microtubules and kinetochores (anaphase A). Further separation of the sister chromatids is driven by the outward movement of the two spindle poles (anaphase B). Finally, the DNA start to decondense and the mitotic spindle is disassembled (telophase). Reprinted by permission from Macmillan Publishers Ltd (Walczak et al., 2010) nuclear envelope reforms around them and cytokinesis occurs (Fig. 1.5 - telophase). During that phase, the mitotic spindle is dismantled.

1.2.2 On the importance of timely centrosome separation

The correct positioning of centrosomes at the two sides of the nucleus is fundamental for the formation of a correct spindle. If the two centrosomes do not separate, a monopolar spindle may form and cell division may fail or proceed with massive chromosome segregation defects (reviewed in Tillement et al., 2009). In some cells, if centrosomes are not completely separated at the time of nuclear envelope breakdown, a backup mechanism acts during prometaphase to push centrosomes further apart (reviewed in Rosenblatt, 2005). In several cell lines, incomplete prophase centrosome separation occurs in around 50% of the cases, so that this backup mechanism is important to complete the separation of the two centrosomes in those cases (reviewed in Rosenblatt, 2005). However, prometaphase centrosome separation exposes the cell to error-prone microtubule-kinetochore attachments (Silkworth et al., 2012). In particular, merotelic kinetochore attachments, in which one kinetochore is attached to both poles, can be formed. Merotelic kinetochore attachments are not recognized by the spindle assembly checkpoint, since tension is present between the sister chromatids, and thus the cell cycle can proceed into anaphase even if these attachments are not corrected. Therefore, merotelic attachments can lead to chromosome segregation defects, such as lagging chromosomes. Indeed, merotelic attachments are one of the main causes of chromosome missegregation in dividing cells and, in particular, the main source of genome instability in cancer cells (reviewed in Gregan et al., 2011).

The cause of these error-prone attachments in cells that do not separate centrosome completely during prophase is likely the asymmetric position of centrosomes with respect to DNA at the beginning of prometaphase (Silkworth et al., 2012). When centrosomes are completely separated at nuclear envelope breakdown, the two spindle poles are symmetrically positioned at opposite side of the DNA. By contrast, if centrosomes are not completely separated at that time, the microtubule aster is positioned asymmetrically with respect to chromosomes. This asymmetric positioning can lead to the formation of aberrant microtubule-kinetochore attachments and therefore chromosome missegregation. A computational model shows that inappropriate kinetochore attachments result in this case from the fact that, when the two centrosomes are not completely separated, their microtubules do not explore the cellular space efficiently to find kinetochores (Silkworth et al., 2012).

This important result demonstrates that timely prophase centrosome separation is fundamental for correct chromosome segregation and genome stability. Indeed, in many early embryonic systems, centrosomes separate completely during prophase (reviewed in Rosenblatt, 2005). It is likely that in these embryonic systems centrosome are carefully separated in prophase to ensure faithful chromosome segregation during those early stages that are fundamental for the development of the organism (Silkworth et al., 2012). Consistent with this hypothesis, in untransformed retinal pigment epithelial (RPE-1) cells, centrosomes separate before nuclear envelope breakdown in 100% of the cases (Silkworth et al., 2012; Magidson et al., 2011). Conversely, cancer cell lines often show incomplete prophase centrosome separation (Silkworth et al., 2012). Therefore, it is possible that in normal physiological conditions, for example in primary cells or *in vivo*, prophase centrosome separation is utilized primarily, so that the occurrence of incomplete centrosome separation at the time of nuclear envelope breakdown is reduced to avoid chromosome segregation defects (Silkworth et al., 2012).

1.2.3 Building a spindle without centrosomes

Centrosomes are absolutely necessary for spindle formation in many systems, especially in developing embryos (reviewed in Nigg and Raff, 2009; Bornens, 2012). However, several lines of evidence show that a mitotic spindle can be formed also in the absence of centrosomes. A fundamental example is the meiotic spindle of animal species that, in most cases, lacks centrosomes, since centrioles have been precedently eliminated during oogenesis. Similarly, centrosomes are not present in higher plants. Acentrosomal spindles can form also in some cases in which centrosomes are artificially removed or in which centrosome formation is inhibited by genetically depleting components that are needed for centriole assembly.

During acentrosomal spindle assembly, microtubules originate in the cytoplasm and are subsequently organized in two acentrosomal spindle poles (reviewed in Alberts et al., 2014; Kalab and Heald, 2008). In general, microtubules originate in the vicinity of chromatin, where a RanGTP gradient favors microtubule nucleation and growth. This array of microtubules is subsequently organized in an anti-parallel fashion by kinesin-5 motors, and their minus-end are pushed away from chromosomes by motors of the kinesin-4 and kinesin-10 families. Then, the minus-ends of microtubules are focused at the poles by kinesin-14 and dynein motors.

The acentrosomal pathway can assemble a functional spindle that is able to segregate chromosomes. A seminal experiment showed that in *Xenopus* egg extract lacking centrosomes and kinetochores, DNA coated beads could form a bipolar spindle around them (Heald et al., 1996). The case of *Drosophila* mutant embryos lacking the centriole duplication protein Sas-4 is striking (Basto et al., 2006). If the embryo is supplied with a sufficient amount of maternal Sas-4 to build centrioles during the first cell cycles, the subsequent divisions proceed normally until adulthood, despite the absence of centrioles and thus centrosomes. Furthermore, vertebrate cells in which centrosomes have been removed by laser-ablation or microsurgery are able to form a functional bipolar spindle (Hinchcliffe et al., 2001; Khodjakov et al., 2000).

These findings notwithstanding, animals cells lacking centrosomes show clear defects. Thus, adult *Drosophilae* lacking the centriolar protein Sas-4 die quickly, probably because of the lack of cilia, which is in turn due to the absence of centrioles (Basto et al., 2006). In addition, both in flies and in vertebrate cells, spindles lacking centrosomes are often misplaced in the cell (Basto et al., 2006; Hinchcliffe et al., 2001; Khodjakov and Rieder, 2001). The position of the spindle is particularly important for the spatial control of cell division since it determines the site of cytokinesis (reviewed in Gönczy, 2008). For example, in the case of the division of the *Drosophila* neuroblasts which is asymmetric in the wild-type, an acentrosomal situation results in an aberrant symmetric division in 15% of the cases (Basto et al., 2006). Strikingly, in vertebrate cells in which centrosomes have been artificially removed, the acentrosomal spindle is often misoriented, leading to cytokinesis failure (Hinchcliffe et al., 2001; Khodjakov and Rieder, 2001).

Together, these findings demonstrate that centrosomes are not always essential for the assembly of the mitotic spindle, but that they are fundamental for the organization of the forces acting on it (reviewed in Nigg and Raff, 2009). This role is of critical importance for spindle positioning and asymmetric cell division, a key feature of developmental and stem cell systems.

1.3 Forces acting on the microtubule aster

We will now review the most important forces that act on a microtubule aster (Fig. 1.6). We will focus on the mechanisms that contribute to aster positioning and thus also to centrosome separation, which is the focus of this study.

1.3.1 Microtubule polymerization forces

Microtubule plus-ends in contact with a boundary can push against it while polymerizing (Fig. 1.6A) (reviewed in Inoue and Salmon, 1995; Dogterom et al., 2005). These forces are important for aster positioning in some systems (reviewed in Reinsch and Gönczy, 1998). In these cases, the microtubule aster pushes against the cell boundary, and is therefore pushed in reaction toward the cell center, where forces are balanced. Such a central position is stable, since movements away from the center in a certain direction result in more microtubules hitting the cell boundary in that same direction, leading to forces oriented to restore the aster central position (Dogterom and Yurke, 1998). On the other hand, the force that this mechanism can generate is limited by microtubule buckling (Dogterom and Yurke, 1997). When the reaction force applied on the microtubule tip overcomes a threshold, called buckling force, the microtubule bends and, as a result, the force applied abruptly decreases. Microtubule buckling force decreases with the square of microtubule length, so that the number of microtubules needed to exert a certain amount of force increases quadratically with cell size. For example, if a microtubule is $10\,\mu$m long, roughly the same as the diameter of an epithelial cell, and has a flexural rigidity of $20\,\text{pN}\,\mu\text{m}^2$ (reviewed in Dogterom and Yurke, 1997), its buckling force is around 2 pN. If the same microtubule is 5 times longer, as in the *C. elegans* embryo, its buckling force is 25 times smaller, thus of the order of 0.1 pN.

In vitro experiments, together with mathematical modeling, have shown that this mechanism is able to center microtubule asters in microfabricated chambers having solid or flexible boundaries (Fygenson et al., 1997; Holy et al., 1997; Dogterom and Yurke, 1998). At least in the case of the small fission yeast, *in vivo* experiments have demonstrate that a few microtubule bundles emanating from the two spindle poles are able to push the associated nucleus toward the cell center (Drummond and Cross, 2000; Tran et al., 2001). On the other hand, the importance of such a mechanism must decrease quickly with cell size, since the buckling force of a long microtubule, and thus the maximum force that it can generate, is small (reviewed in Dogterom et al., 2005; Reinsch and Gönczy, 1998).

Despite these restrictions, pushing forces could be important to generate forces on objects that are close to the cell aster. For example, this could be the case for the initial movements of the sperm aster away from the cell boundary in some systems. In addition, microtubule bundling or embedding in the crowded cytoplasm could increase the maximum force that a microtubule can sustain before buckling (Wühr et al., 2009; Brangwynne, 2006).

1.3.2 Microtubule depolymerization forces

Microtubule depolymerization can exert a substational amount of force when the microtubule plus-end region, hereafter referred to as the microtubule tip, is anchored to a substrate, such as the kinetochore or the cortex (Fig. 1.6B) (Grishchuk et al., 2005; Molodtsov et al., 2005 and reviewed in Joglekar et al., 2010). In this mechanism, when the microtubule depolymerizes, the anchor maintains the attachment between the microtubule and the substrate by tracking the microtubule tip, thus generating a pulling force. Remarkably, this force does not require energy from the surrounding environment; for example it can occur in the absence of ATP, utilizing the energy stored in the microtubule polymer (Koshland et al., 1988; Coue et al., 1991; Molodtsov et al., 2005).

An example of this mechanism is the force exerted by kinetochore microtubules in fungi (Asbury et al., 2006; Westermann et al., 2006; Powers et al., 2009). In that system, the microtubule tip is associated to the kinetochore through the adapter ring complex Dam1. When the microtubule shrinks, Dam1 tracks the depolymerizing plus-end region, while remaining bound to the kinetochore, so that a pulling force is exerted on the chromatid. A similar mechanism could exert forces on astral microtubules when they are anchored to the cell cortex, for example by the motor protein dynein (Kozlowski et al., 2007). In line with this view, in *C. elegans*, shrinking microtubules are able to invaginate the cell membrane in a dynein-dependent manner (Redemann et al., 2011).

1.3.3 Length-dependent forces

As discussed before, in large cells, polymerization forces are unlikely to drive aster positioning since they decrease quickly with microtubule length (Fig. 1.6C) (Dogterom and Yurke, 1997). In such contexts, molecular motors are needed to exert significant forces on the aster. Molecular motors can bind microtubules and walk along them while being bound to a semi-stable substrate that resists motor movement, such as the endoplasmatic-reticulum, or a cargo, such

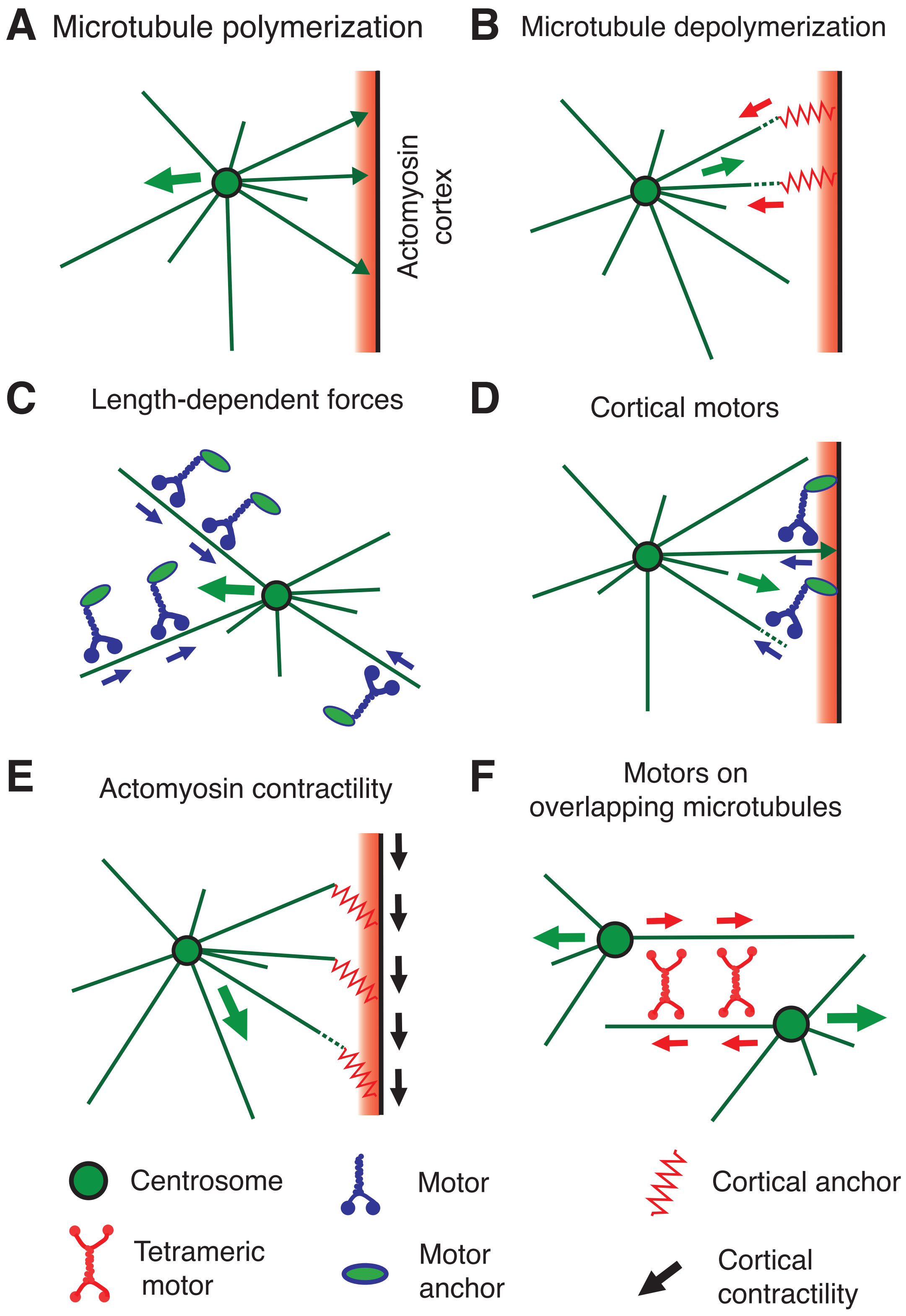
A
Microtubule polymerization
Actomyosin cortex
B
Microtubule depolymerization
C
Length-dependent forces
D
Cortical motors
E
Actomyosin contractility
F
Motors on overlapping microtubules
Centrosome
Motor
Cortical anchor
Tetrameric motor
Motor anchor
Cortical contractility

as a vesicle (reviewed in Reinsch and Gönczy, 1998; Kimura and Kimura, 2011a). This force resists motor motion and results in a reaction force exerted on the microtubule and therefore on the centrosome.

When motors can bind along the whole microtubule, the total number of bound motors, and thus the applied force, increases with microtubule length (reviewed in Reinsch and Gönczy, 1998; Kimura and Kimura, 2011a). Therefore, if a microtubule aster is asymmetric, these length-dependent forces will push away from, or pull toward, depending on the motor in question, the direction in which the microtubule aster is the largest. For example, in the case of minus-end directed motors, pulling forces are exerted in the direction in which microtubules are the longest. When an aster is away from the cell center, microtubules directed toward the cortex are short and, as a result, the aster moves away from it. Therefore, microtubules continue to explore the cellular space, "sensing" asymmetries, until they reach the geometric center of the cell, where the forces in every direction balance each other. Mathematical modeling has greatly contributed to support this view by showing that these minus-end directed forces can indeed center the microtubule aster, compatible with the dynamics observed in several systems (Holy et al., 1997; Kimura and Onami, 2005; Minc et al., 2011; Kimura and Kimura, 2011b).

On the experimental side, a seminal study has shown that length-dependent forces act to center the aster in sand dollar eggs (Hamaguchi and Hiramoto, 1986). In these experiments, microtubules were first depolymerized using the drug colcemid, which can be inactivated by UV exposure. The authors inactivated the drug with UV light in a certain region, thus allowing microtubules to regrow selectively there. Fascinatingly, when the aster was included in the illuminated region, it moved toward the geometric center of that region, even when it was far from the cell boundary. In addition, if the irradiated region was displaced, the aster consequently moved to follow the center of the new region. This elegant experiment demonstrated the existence of length-dependent forces acting independently of the cell boundary.

Length-dependent forces can also act to orient the mitotic spindle and therefore dictate the

Figure 1.6 *(preceding page)* – **Forces acting on the microtubule aster. A** Polymerizing microtubules can push on a boundary, such as the cell cortex. **B** Microtubules anchored to a substrate, such as the cell cortex or kinetochores, can pull on it while depolymerizing **C,D** Motors can act from the cytoplasm (C) or from the cortex (D). **E** Actomyosin contractility can exert forces on microtubules anchored at the cell cortex. **F** Tetrameric motors can bind overlapping microtubules and slide them apart. Here and thereafter unless differently stated, the net force acting on centrosomes is represented by green arrow. Here and thereafter, when relevant, the direction of motor movement and microtubule shrinkage are represented by either blue or red arrows. When relevant, microtubule polymerization is represented by arrowheads, depolymerization by dashed plus-ends. Cortical anchors can be motors, non-motor anchors or direct interaction with the actomyosin network.

position of the division plane. This has been studied quantitatively in micro-patterned sea urchin eggs where the position of the mitotic spindle, its orientation and the consequent position of the cell division plane have been measured and compared with the prediction of a minimal mathematical model (Minc et al., 2011). Strikingly, this mathematical model could predict correctly the position of the division plane and its variability. To demonstrate that the same process could work in a multicellular adult context, the authors were able to use cell shape to correctly predict spindle orientation in a century-old illustration of a tissue of pigeon testis (Guyer; Micheal F., 1900).

Length-dependent forces can also be exerted by the pull of motors attached to the nuclear surface (reviewed in Tanenbaum and Medema, 2010). The resulting force does not depend on the total microtubule length, but on the length of the microtubule region in contact with the nucleus. Importantly, motors can contribute to bend microtubules toward the nuclear surface, thus enlarging the region on which force can be exerted. Several lines of evidence show that the motor dynein is indeed present at the nuclear envelope and that it can exert a relevant force (Beaudouin et al., 2002; Salina et al., 2002; Reinsch and Karsenti, 1997; Gönczy et al., 1999; Splinter et al., 2010; Robinson et al., 1999). For example, this dynein pool likely holds centrosomes attached to the nucleus in *C. elegans* and mammalian cells (Malone et al., 2003; Splinter et al., 2010). In *C. elegans*, nuclear dynein is anchored by the Hook protein ZYG-12, which is directly connected to the nuclear membrane by a trans-membrane domain (Malone et al., 2003), whereas, in mammalian cells, Bicaudal D holds dynein at nuclear pore complexes (Splinter et al., 2010). In these two systems, depletion of the respective anchoring protein, either ZYG-12 or Bicaudal D, leads to loss of dynein at the nuclear envelope and centrosome detachment from the nucleus. In fertilized eggs, motors on the surface of the female pronucleus pull on the male-derived aster, which is in turn attached to the sperm nucleus, to drive pronuclear meeting (reviewed in Reinsch and Gönczy, 1998). Thus, in *C. elegans*, ZYG-12 or dynein depletion prevents pronuclear meeting (Gönczy et al., 1999; Malone et al., 2003). The same nuclear dynein-based mechanism can exert force in a cell-free reconstituted system where DNA-coupled magnetic beads were put in a *Xenopus* extract (Reinsch and Karsenti, 1997). The beads, resembling a female pronucleus, were moving toward the male-derived aster, tracking along microtubules in a dynein-dependent manner and showing dynamics similar to that of female migration.

1.3.4 Cortical forces

Molecular motors at the cell cortex play an important role in spindle positioning (Fig. 1.6D) (reviewed in Dujardin and Vallee, 2002; Kotak and Gönczy, 2013). These motors can work in two ways (reviewed in Moore and Cooper, 2010). First, cortical molecular motors can exert forces on microtubule tips abutting the cortex through their motor activity. Second, molecular motors can anchor depolymerizing microtubules tips and thus harness depolymerization energy to generate force. Importantly, depolymerization forces at the cortex can in principle also be generated by association with non-motor anchor proteins or the actomyosin network.

One of the initial suggestions that a force from the cortex could move the microtubule aster came from an experiment in *Chaetopterus* oocytes (Lutz et al., 1988). In this experiment, the meiotic spindle was moved away from its cortical localization using a micro-needle and, after being released, was seen coming back to the cortex. In addition, laser microtubule-severing experiments in fungi, Ptk cells or *C. elegans* suggested that, in those systems, astral microtubules were responsible for connecting the spindle poles to the cortex and transmitting cortical forces (Aist and Berns, 1981; Aist et al., 1991, 1993; Hyman and White, 1987; Hyman, 1989; Grill et al., 2001, 2003).

Work in many systems has demonstrated that cortical forces are exerted by dynein attached to the cell cortex to position the spindle by pulling on astral microtubules (reviewed in Kotak and Gönczy, 2013). For example, in the *C. elegans* one-cell stage embryo, an asymmetric distribution of cortical dynein, which is more enriched in the posterior side of the embryo, displaces the spindle toward that side, a requisite for asymmetric cell division (Nguyen-Ngoc et al., 2007; Couwenbergs et al., 2007). In mammalian cells, depletion of the cortical pool of dynein leads to spindle misorientation (Kiyomitsu and Cheeseman, 2012; Kotak et al., 2012). Finally, during *S. pombe* meiosis, dynein localizes at the cortex and drives persistent nuclear oscillations by pulling along microtubule length (Yamamoto et al., 1999; Vogel et al., 2009).

Functional genomic studies in *C. elegans* have shown that dynein is enriched at the cell cortex by a ternary complex composed by one of the two G_α subunits, GOA-1 or GPA-16, one of two essentially identical TPR/GoLoco-domain proteins, GPR-1 or GPR-2 (jointly referred to as GPR-1/2), and, finally, the coiled-coil protein LIN-5 which associates with dynein (Lorson et al., 2000; Gotta et al., 2001; Colombo et al., 2003; Gotta et al., 2003; Srinivasan et al., 2003). G_α is directly bound to the lipid membrane and to GPR-1/2, which in turn is bound to LIN-5. Therefore, the resulting G_α/GPR-1/2/LIN-5 complex holds dynein at the cortex and depletion of any of its components prevents posterior displacement of the spindle in the one-cell stage embryo, thus leading to symmetric cell division (Lorson et al., 2000; Gotta et al., 2001; Colombo et al., 2003). A similar complex, composed of the homologues G_α/LGN/NuMA holds dynein at the cortex and orients the mitotic spindle in mammalian cells (Woodard et al., 2010; Kiyomitsu and Cheeseman, 2012; Kotak et al., 2012). In *Drosophila*, the parallel pathway Pins/Dlg/Khc73 is also important for spindle positioning (Siegrist and Doe, 2005; Johnston et al., 2009). In general, cortical dynein function can be regulated by modulating the amount and activity of the components of the ternary complex. For example, proteins of the G_β and G_γ families form heterotrimers with G_α and negatively regulate its function and thus inhibit cortical forces in *C. elegans* (Gotta et al., 2001; Tsou et al., 2002; Afshar et al., 2004, 2005), presumably through competition for GPR-1/2 binding by the $G_{\beta\gamma}$ dimer (Tsou et al., 2002; Thyagarajan et al., 2011).

Finally, actomyosin contractility can also exert forces on bound microtubules (Fig. 1.6E) (reviewed in Tanenbaum and Medema, 2010). In this case, forces can be exerted by holding the microtubule plus-end while the actomyosin network contracts. Indeed, in vertebrate cells, it was shown qualitatively that, during prometaphase, centrosomes moved roughly in the same direction as cortical flows, measured by tracking cortically-bound fluorescent latex beads (Rosenblatt et al., 2004). Importantly, inhibition of myosin using drugs prevented both cortical flows and coordinated centrosome movements. Furthermore, inhibition of actomyosin contractility prevented separation of centrosomes during prometaphase in the subset of cells in which separation was not completed in prophase (see section 1.4.4 for further details).

1.3.5 Motors on overlapping microtubules

Some molecular motors can bind overlapping microtubules and exert opposing forces on them (Fig. 1.6F). Motors of the kinesin-5 family are an important example (reviewed in Ferenz et al., 2010). Kinesin-5 is a plus-end-directed tetrameric motor that binds overlapping microtubules and, when they are in an antiparallel orientation, slides them apart by trying to move toward their plus-ends. In all eukaryotic systems except *C. elegans*, kinesin-5 depletion leads to monopolar spindle formation, due either to failure of spindle assembly or collapse of the bipolar spindle during spindle maintenance, depending on the system (Bishop et al., 2005 and reviewed in Scholey, 2009; Ferenz et al., 2010; Tanenbaum and Medema, 2010). In these cases, the push that kinesin-5 exerts is essential either to move spindle poles apart or to counteract forces that would lead spindle poles to collapse onto each other.

Kinesin-12 motors sustain spindle maintenance in a similar way (reviewed in Tanenbaum and Medema, 2010). Kinesin-12 is a dimeric motor that can bind overlapping microtubules: one with the motor domain and another with the cargo domain. Kinesin-12 walks on the microtubule attached to the motor domain and thus exerts opposite forces on the two bound microtubules and pushes them apart. For example, the *C. elegans* kinesin-12 KLP-18 is needed for meiotic spindle assembly, even if it is not needed for the subsequent mitotic divisions (Segbert et al., 2003; Wignall and Villeneuve, 2009). In mammalian cells, Kinesin-12 is dispensable for bipolar spindle assembly (Zhu et al., 2005; Tanenbaum et al., 2009; Vanneste et al., 2009), but in human cells its depletion leads to highly enhanced sensitivity to kinesin-5 inhibitors (Tanenbaum et al., 2009; Vanneste et al., 2009), thus indicating that the two motors act redundantly to promote bipolar spindle assembly.

In some cases, motors that bind overlapping microtubules can exert an inward directed force on the two microtubules. For example, this is the case of the C-terminal motor Ncd in *Drosophila* embryos that counteracts the outward push of kinesin-5 during spindle maintainance (Sharp et al., 1999).

1.4 Mechanisms of centrosome separation

During prophase, the two nearby centrosomes start to increase their amount of pericentriolar material and thus to nucleate more microtubules. Concomitantly, the two centrosomes separate while moving along the nuclear surface until they have reached roughly opposite poles of the nucleus (reviewed in Tanenbaum and Medema, 2010). Microtubules are absolutely necessary for this separation of centrosomes, demonstrating that centrosomes are transported by forces acting on the microtubule aster. We will now discuss these forces, which we have introduced earlier already, but now in the context of prophase centrosome separation (Fig. 1.7).

1.4.1 Kinesin-5

One of the main players in centrosome separation in animal cells is kinesin-5 (Fig. 1.7A) (reviewed in Tanenbaum and Medema, 2010; Ferenz et al., 2010). Kinesin-5 represents an attractive mechanism for centrosome separation since it does not require any external attachment site and its force is intrinsically directed to push centrosomes apart. As we have previously discussed, kinesin-5 acts probably in a similar way during centrosome separation and spindle maintenance. Despite this critical importance, several lines of evidence show that kinesin-5 is not the only player governing centrosome separation.

First, while kinesin-5 is needed in many systems for prophase centrosome separation, including humans, it is dispensable in others, including *C. elegans*, *Drosphila* and *Dyctostelium* (Bishop et al., 2005; Saunders et al., 2007; Tikhonenko et al., 2008; Sharp et al., 1999). For example, dynein can support centrosome separation in the absence of kinesin-5 in human cell lines that have evolved in response to increasing amounts of the kinesin-5 inhibitor S-Trityl-L-cysteine (STLC) (Raaijmakers et al., 2012). In addition, since kinesin-5 pushes away the two centrosomes with opposing forces, their average movement away from each other should be symmetric on a long time-scale. However, arguing against this hypothesis, time-lapse recordings in vertebrate cells have shown that centrosome movements were strongly asymmetric during separation (Waters et al., 1993).

Second, even during spindle maintenance, forces other than kinesin-5 can push or pull centrosomes away from each other (reviewed in Tanenbaum and Medema, 2010). For example, in mammalian cells, the bipolar spindle is maintained even when kinesin-5 function is inhibited. In addition, the depletion of some minus-end directed motors that can act at kinetochores, such as kinesin-14 or dynein, can rescue bipolar spindle formation when kinesin-5 is inhibited. Finally, in *C. elegans*, kinesin-5 acts as a brake during anaphase spindle elongation, while another mechanism drives outward movements of spindle poles (Saunders et al., 2007). Taken together, these pieces of evidence show that other forces exist that can push or pull centrosomes in opposite direction.

1.4.2 Microtubule polymerization forces

One model suggests that centrosome separation could be in part powered by microtubule polymerization forces pushing against the opposing centrosome (Fig. 1.7B) (Cytrynbaum et al., 2003). Interestingly, in this mechanism, the exerted force is always directed so as to move centrosomes away from each other. As discussed above for spindle positioning, microtubule

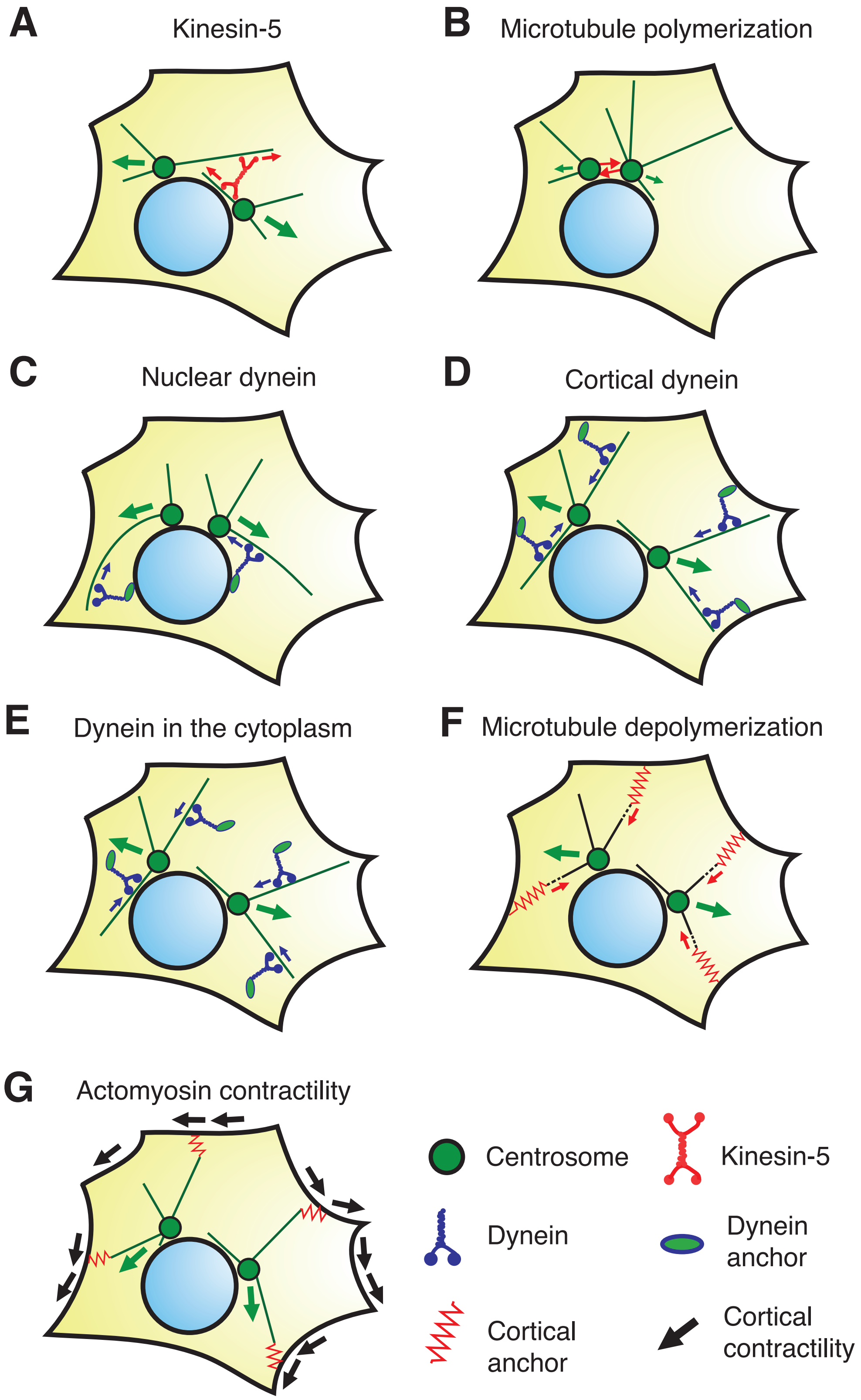
A
Kinesin-5
B
Microtubule polymerization
C
Nuclear dynein
D
Cortical dynein
E
Dynein in the cytoplasm
F
Microtubule depolymerization
G
Actomyosin contractility
Centrosome
Kinesin-5
Dynein
Dynein anchor
Cortical anchor
Cortical contractility

polymerization is unlikely to support sufficient forces when centrosomes are away from each other, since long microtubules buckle easily, but it could be important at the early stages of centrosome separation when centrosomes are close to each other.

1.4.3 Dynein

The minus-end directed motor dynein is an important contributor to centrosome separation (Fig. 1.7C, D, E). The first evidence that dynein was involved in this process was provided by injection into Ptk1 cells of anti-dynein antibodies that blocked dynein motility (Vaisberg et al., 1993). Injections during prophase prevented centrosome separation and led to the formation of monopolar spindles (Vaisberg et al., 1993). Indeed, later studies have shown that dynein is essential for centrosome separation in several species, including *C. elegans* and *Drosophila* (Gönczy et al., 1999; Robinson et al., 1999; Sharp et al., 2000), raising the possibility that this represents an ancestral separation mechanism (reviewed in Dujardin and Vallee, 2002). Despite important progress in recent years, the mechanisms by which dynein governs centrosome separation remain incompletely understood.

One model posits that dynein uniformly distributed on the nuclear envelope could separate centrosomes by exerting pulling forces on microtubules emanating from them Fig. (1.7C) (Gönczy et al., 1999). In line with this view, as mentioned before, dynein anchored on the nuclear envelope contributes to centrosome separation in human cells when kinesin-5 function is partially compromised (Raaijmakers et al., 2012). However, whether this reflects the mechanism by which dynein contributes to centrosome separation in unperturbed conditions is not known. Moreover, nuclear dynein is not essential for centrosome separation in *C. elegans*, as evidenced by the fact that centrosomes move apart in embryos depleted of the dynein anchor ZYG-12 in which dynein does not localize to the nucleus (Malone et al., 2003). Similarly, hypomorphic mutations of the dynein heavy chain can lead to centrosome detachment in *Drosophila* embryos, yet result only in a partial impairment of centrosome separation (Robinson et al., 1999). Overall, the exact contribution of nuclear dynein to centrosome separation remains to be established.

Another model proposes that cortical dynein pulling on microtubules abutting the cortex could

Figure 1.7 *(preceding page)* – **Mechanisms of centrosome separation. A** Kinesin-5 can separate centrosomes by sliding microtubules apart. **B** Polymerization forces can push centrosomes away from each other in the initial phase of separation. Microtubules pushing against the opposing centrosomes are represented in red. **C, D, E** Dynein can act from the cortex, the nuclear envelope or the cytoplasm. **F, G** When microtubule ends are tethered at the cortex, microtubule depolymerization forces and actomyosin contractility can pull the two centrosomes in opposite directions. When relevant, the direction of kinesin-5 and dynein movement is represented by red and blue arrows, respectively, microtubule polymerization by arrowheads, depolymerization by dashed plus-ends and depolymerization forces by red arrows. Cortical anchors can be motors, non-motor anchors or direct interaction with the actomyosin network.

drive centrosomes separation (Fig. 1.7D). Even if this mechanism has not been demonstrated to be involved in centrosome separation in any system, it was initially proposed in *Drosophila* embryos, where dynein is needed for centrosome separation and is indeed, suggestively, enriched at the cortex (Robinson et al., 1999; Sharp et al., 2000). Subsequent mathematical modeling has shown that cortical dynein can drive centrosome separation in this system provided a symmetry-breaking mechanism is incorporated (Cytrynbaum et al., 2005).

Nuclear dynein presents two advantages over cortical dynein in principle (Tanenbaum and Medema, 2010). First, in the case of nuclear dynein, force is generated parallel to the nuclear envelope, while in the case of cortical dynein it is directed away from the nucleus, so that only a small component of this force is directed to drive centrosome separation. Second, since centrosomes are attached to the nuclear envelope, it is easy for them to reach nuclear motors, while only the fraction of microtubules reaching the cortex can interact with cortical dynein. On the other hand, this second point is not an issue if centrosomes are located nearby the cortex, as in most embryos just after fertilization, or if the typical microtubule length is similar to cell size, since in these cases the majority of microtubules can reach cortical dynein. Finally, the centrosome separation mechanism based on nuclear dynein is intrinsic to the microtubule aster-nucleus system and could function independently of where the nucleus is located. Conversely, in the case of cortical dynein, the forces exerted on microtubules depend in principle on the position of the microtubule aster-nucleus complex in the cell and on the shape of the cortex.

Finally, length-dependent forces have been proposed to drive outward centrosome movements during telophase in the first cell cycles of *Xenopus laevis* and zebrafish embryos (Fig. 1.7E) (Wühr et al., 2009). At the beginning of anaphase, centrosomes are located in the center of these unusually large cells and nucleate a spindle that is small compared to cell size. During anaphase-telophase, the two microtubule asters grow and concomitantly move away from each other. Suggestively, during telophase, on each side of the spindle the two sister centrosomes are already separated, oriented perpendicular to the spindle axis and located in the center of the future daughter cell , thus already positioned for the consecutive mitosis. Interestingly, these centrosome movements are dynein-dependent since they can be blocked by injecting dominant-negative dynactin complex fragments. Furthermore, these movements cannot be driven by microtubule-based cortical forces since they occur before the microtubule asters have reached the cortex. Instead, the authors demonstrated that length-dependent pulling forces are acting on the microtubule asters by an experiment reminiscent of the one performed by Hamaguchi and Hiramoto in sand dollar eggs (see section 1.3.3) (Hamaguchi and Hiramoto, 1986). In this case, the authors depolymerized a portion of the microtubule aster by activating the microtubule depolymerizing drug combretastatin 4A through UV light and observed that the aster was moving in the direction of the intact, and thus longer, microtubules. Together, these evidences suggest that length-dependent pulling forces are acting during telophase in those large cells to position centrosomes.

In all these cases, dynein at the cortex, nuclear envelope or cytoplasm, it is not clear how forces are organized to direct the movements of the two centrosomes away from each other. We will discuss the potential nature of this symmetry breaking mechanism in section 1.4.5.

1.4.4 Actomyosin cortex

The actomyosin network plays a role in centrosome separation in some systems (reviewed in Tanenbaum and Medema, 2010). Thus, actin is required for centrosome separation in *Drosophila* embryos, although contractility of the actomyosin network is not required, suggesting that actin is playing a rather structural role (Cao et al., 2010). Compatible with this view, both actin and dynein depletion lead to decreased centrosome separation in that system, which is consistent with actin functioning as a scaffold for cortical dynein anchoring. Furthermore, *Drosophila* embryos with impaired function of the protein kinase Akt lack localization of the microtubule-tip binding protein EB-1 at the cortex and undergo incomplete centrosome separation (Buttrick et al., 2008). Therefore, Akt might be required for stabilizing microtubule tips at the cortex and thus increase cortical dynein binding and force generation, but unfortunately in that work the authors did not test whether indeed Akt depletion lead to reduced microtubule-tip residency time at the cortex or impaired microtubule aster architecture. Regardless, together this data suggest that cortical dynein might be involved in *Drosophila* centrosome separation in an actin-dependent manner.

The contractility of the actomyosin network can also drive centrosome separation (Fig 1.7G). Indeed, actin is needed for separation in the minority of vertebrate Ptk2 cells in which centrosomes separate after nuclear envelope breakdown. However, in this case, actomyosin contractility is required, as evidenced by myosin inhibition through drugs/RNAi or by crosslinking the cell surface, and thus blocking cortical flows, using tetravalent lectins (Rosenblatt et al., 2004). By contrast, actomyosin contractility does not play a role in centrosome separation during prophase even in that system (Rosenblatt et al., 2004). Moreover, as mentioned before, the authors showed that the movements of centrosomes after nuclear envelope breakdown were approximately oriented in the same direction as those of the actomyosin cortical flows. Despite these findings, it is not known how actomyosin contractility-based forces are transmitted to microtubules to move centrosomes. Furthermore, it is unclear how the pattern of actomyosin network cortical flow is organized to ensure that the two centrosomes always move in opposite directions.

1.4.5 Symmetry breaking mechanisms

The forces exerted by kinesin-5 motors and microtubule polymerization are intrinsically organized to drive centrosomes away from each other (reviewed in Ferenz et al., 2010). By contrast, dynein motors require an external symmetry breaking mechanism (Cytrynbaum et al., 2005 and reviewed in Tanenbaum and Medema, 2010). For example, in the case of nuclear dynein, if nuclear motors are homogeneously distributed on the nuclear envelope and microtubules grow in all directions in the same way, the forces exerted on the microtubule

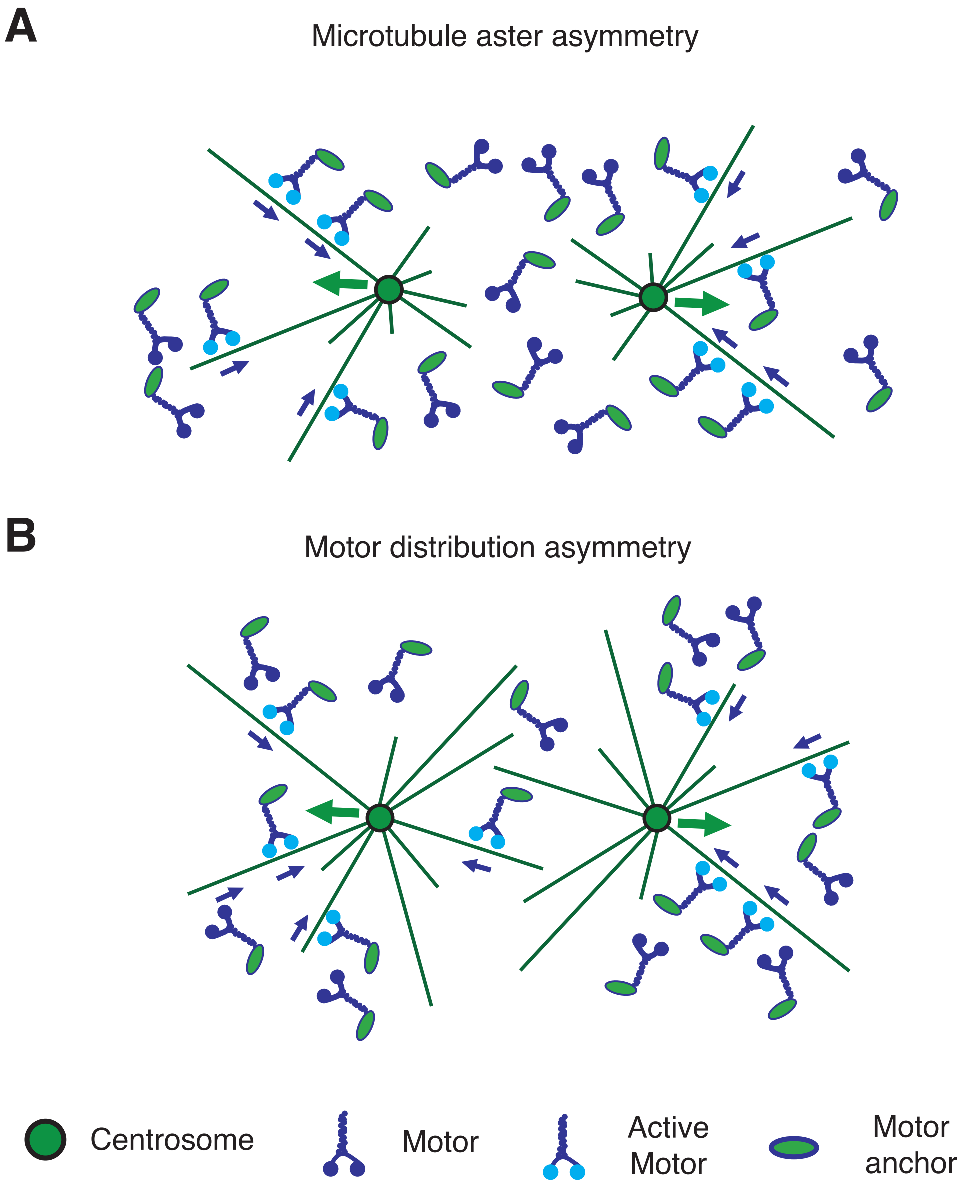
A
Microtubule aster asymmetry
B
Motor distribution asymmetry
Centrosome
Motor
Active Motor
Motor anchor

Figure 1.8 – **Examples of symmetry breaking mechanisms.** Two symmetry breaking mechanisms are compared. **A** Longer or denser microtubules in the outer region lead to stronger length-dependent forces in outward direction. **B** Higher concentration of molecular motors in the outer region lead to stronger length-dependent forces in the outward direction. Actively pulling motors are represented with light blue motor domains.

aster should on average balance each other and thus result in a null net force. The case of cortical forces, based on dynein or actomyosin contractility, is more complex since the direction of forces depends also on the position of centrosomes in the cell and on the shape of the cortex, but similar issues arise. Therefore, in both cases, a mechanism is required to break the isotropic symmetry of forces in order to drive centrosome outward movement (Fig. 1.8).

The asymmetric organization of forces that is needed for the separation process can originate at least from two different sources: an asymmetry in microtubule aster organization or an asymmetric distribution/activation of motors. In the case of aster asymmetry, microtubule dynamics must be somehow imbalanced on the two sides of the aster, so that microtubules are longer or denser in a certain direction (Fig. 1.8 A). If microtubules are longer or denser in a certain direction, more motors will bind and then stronger forces will be exerted in that direction. Microtubule aster asymmetry has been observed in *Drosophila* embryos, but the underlying reason was not clear (Cytrynbaum et al., 2005). Intriguingly, an aster asymmetry is observed also in *Xenopus laevis* and zebrafish embryos (Wühr et al., 2010). In these embryos, the two telophase microtubule asters touch each other, but do not overlap with one another, since microtubule growth is limited in the region between centrosomes, thus leading to an asymmetry of the aster and likely stronger length-dependent forces in the outward direction. Also in this case, it is not known how microtubule growth is prevented at the interface between the two asters. In general, microtubule aster asymmetry can be generated by a regulator of microtubule dynamics. If, for example, this postulated regulator is accumulated at and around centrosomes, it can trigger the catastrophe of microtubules directed from one centrosome toward the other and thus deplete microtubules in the region between them. Similarly, the collisions of microtubules from one centrosome against the other can trigger microtubule catastrophe and result in the depletion of microtubules in the region between centrosomes (Janson et al., 2003). Clearly, this last mechanism would be most efficient when centrosomes are close to each other. Finally, boundaries such as the cell cortex or the nuclear envelope can constrain microtubule growth, trigger catastrophe and therefore shape the microtubule aster.

In a similar way, asymmetric distribution of forces can originate from an inhomogeneous distribution of motor (Fig. 1.8B). If, for example, dynein motors are depleted in the region between centrosomes, less forces are expected in that direction, thus resulting in centrosomes ouward movement. Also in this case, a centrosomal signal that regulates motor activity could be at the root of such a potential bias (Cytrynbaum et al., 2005). If, for example, a motor inhibitor is produced at centrosomes and diffuses away from there, it will form two concentration profiles, centered one on each centrosome. In the region between centrosomes the two profiles overlap and, as a result, this postulated inhibitor is more concentrated. This would lead to more active motors in the outer direction and centrosomes outward movement. Both aster and motor asymmetry models have been studied computationally in the case of *Drosophila* embryos (Cytrynbaum et al., 2005) and demonstrated that they can in principle organize forces anisotropically.

1.5 The one-cell stage *C. elegans* embryo

C. elegans is a 1 mm long nematode that can live and reproduce roughly between 12° and 25° (reviewed in Corsi et al., 2015). Self-fertilizing XX hermaphrodites are the most common sex, but a small percentage (< 0.2%) of X0 males spontaneously arise from non-disjunction of the sexual chromosomes during meiosis, so that different worm strains can be easily bred. Each

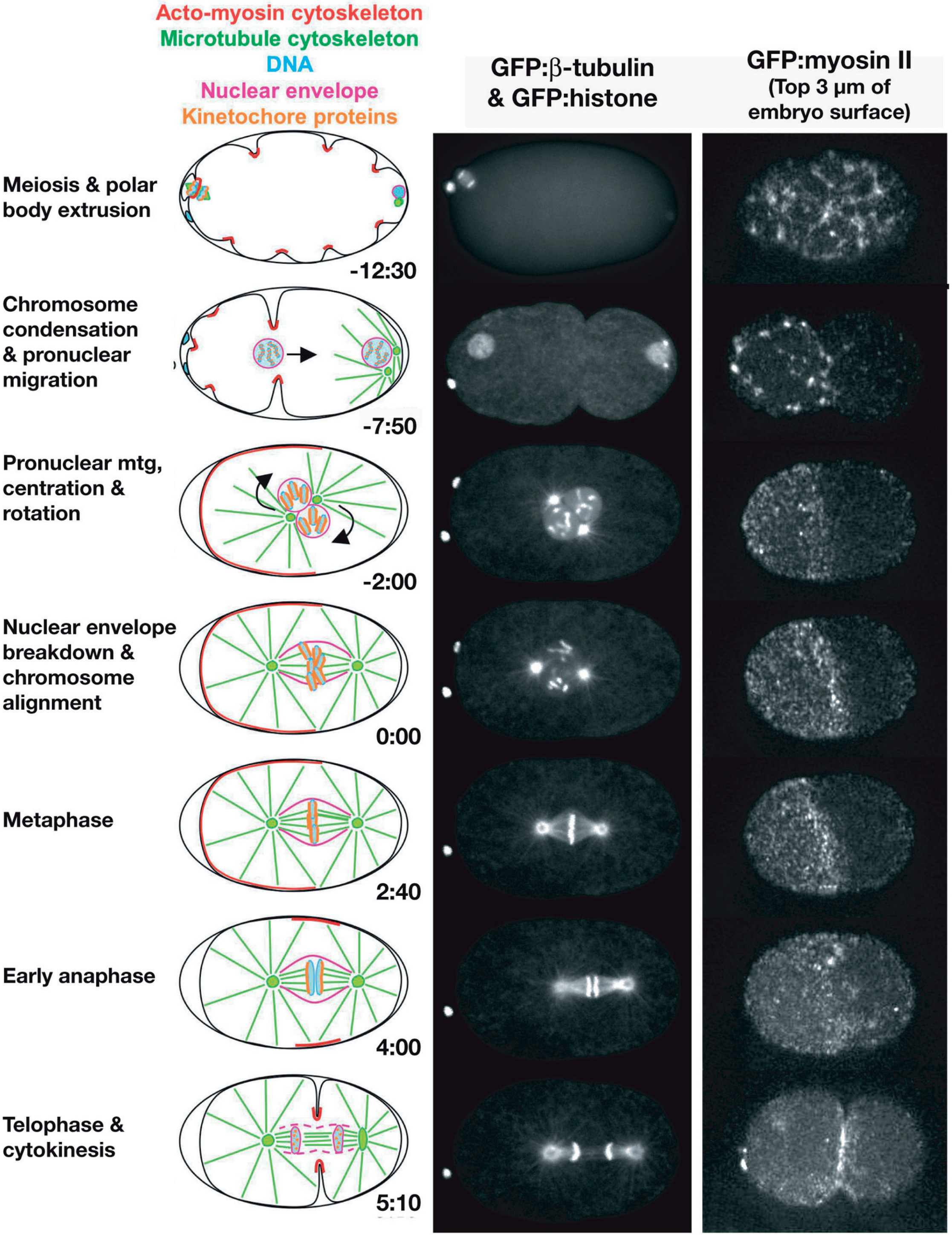
Acto-myosin cytoskeleton
Microtubule cytoskeleton
DNA
Nuclear envelope
Kinetochore proteins
GFP:β-tubulin & GFP:histone
GFP:myosin II (Top 3 μm of embryo surface)
Meiosis & polar body extrusion
-12:30
Chromosome condensation & pronuclear migration
-7:50
Pronuclear mtg, centration & rotation
-2:00
Nuclear envelope breakdown & chromosome alignment
0:00
Metaphase
2:40
Early anaphase
4:00
Telophase & cytokinesis
5:10

hermaphrodite has about 200 progeny that develop into adults within 2.5-6 days, depending on the temperature.

1.5.1 Cell polarization and mitosis

The *C. elegans* one-cell stage zygote is an important system to study the mechanical processes that drive cell division (reviewed in Oegema and Hyman, 2006). In that system, cell division follows a stereotyped sequence of events that occur robustly in the majority of cells. The large cell size allows us to analyze the localization and dynamics of the components of the cytoskeleton with high spatial and temporal resolution. The invariant nature of the first cell cycle facilitates the quantitative analysis of the consequences of molecular perturbations.

One of strongest advantages of *C. elegans* is the ease of protein depletion by RNAi, which can be performed by gonad injection, worm soaking or feeding and leads to efficient depletion in the embryo (reviewed in Ahringer, 2006; Oegema and Hyman, 2006). In addition to RNAi, the development of gene insertion and gene editing techniques has allowed the creation of a large collection of strains expressing fluorescently tagged proteins and mutants, thus helping the study of protein localization and function. Weak checkpoints which let the embryo proceed through the cell cycle even when the mitotic spindle, chromosomes and/or nuclei are strongly affected (Brauchle et al., 2003; Encalada et al., 2005), allow us to study the effects on cell mechanics of the depletion of essential proteins.

We will now discuss the most important mechanical process that occur during the first embryonic cell division, focusing on the events that lead to correct spindle positioning and on the role of molecular motors in this process (Fig. 1.9).

The *C. elegans* one-cell stage embryo is a 50x30x30 μm ellipsoid surrounded by an eggshell. It undergoes the first cell division in about 20 minutes at 25°, from the end of meiosis to cytokinesis (reviewed in Oegema and Hyman, 2006) (Fig. 1.9). During this first cell cycle, the cell polarizes and divides asymmetrically, so that the newly fertilized oocyte P_0 is eventually divided into a larger anterior blastomere AB and a smaller germ-line precursor P_1. A stereotyped sequence of events goes from fertilization to correct asymmetric cell division. Typically, the female DNA is on one end of the embryo and fertilization occurs at other end. After fertilization, two rounds of meiosis, characterized by small meiotic spindles, extrude

Figure 1.9 *(preceding page)* – ***C. elegans* embryo first cell cycle.** Schematics of the main events of the first cell cycle from meiosis to cytokinesis (left panel). Snapshots of DNA and microtubules during the first cell cycle (central panel). Actomyosin cortex during the first cell cycle (right panel): at the time of meiosis, a contractile actomyosin network is uniformly distributed along the embryo cortex. Thereafter, the actomyosin network retracts toward the anterior and forms an anterior cap. During cytokinesis, non-muscle myosin-II (NMY-2) accumulates in the plane defined by the spindle midzone and forms the cleavage furrow. Time is indicated in minutes:seconds. Reprinted with permission from (Oegema and Hyman, 2006).

three copies of the female genome. During that time, the actomyosin cortex exhibits uniform contractions.

At the end of meiosis II, the DNA starts to decondense and the female and male pronuclei start to grow in size (Nigon, 1949). At the same time, the single pair of centrioles, which is donated by the sperm and is kept in the vicinity of the male DNA, starts to accumulate pericentriolar material and nucleate microtubules (O'Connell et al., 2000; Pelletier et al., 2004).

This newly formed centrosome triggers the onset of polarization and, in this way, defines the anterior-posterior (A-P) axis, with the posterior being where centrosomes reside (Goldstein and Hird, 1996; Sadler and Shakes, 2000). The polarization process is triggered by an unknown centrosomal cue that leads to the depletion of the non-muscle myosin-II activator ECT-2 from the vicinity of the centrosome, therefore leading to a reduction of cortical tension in that region (Motegi and Sugimoto, 2006). This reduction of tensile forces generates a movement of the actomyosin network that starts to flow away from the centrosomes toward the anterior side of the embryo (Hird and White, 1993; Goldstein and Hird, 1996; Mayer et al., 2010). This flow produces an overall retraction of the actomyosin network toward the anterior side, so that an anterior contractile cap forms, while the posterior side relaxes (Strome, 1986). The flow of the actomyosin network transports polarity proteins, such as the anterior proteins PAR-6, PAR-3 and PKC-3, toward the anterior side of the embryo, while posterior proteins, such as PAR-2, accumulate at the posterior following the depletion of anterior proteins on that side (Munro et al., 2004). This asymmetric distribution of polarity proteins leads to the establishment of stable embryonic polarity that drives asymmetric distribution of fate determinants and asymmetric cell division (reviewed in Rose and Gönczy, 2014).

At the onset of polarization, the two not yet-separate centrosomes are brought, together with the associated male pronucleus, to the posterior pole of the embryo by an unknown mechanism (Goldstein and Hird, 1996; Bienkowska and Cowan, 2012). Around the time of completion of this process, two distinct centrosomes become visible and start to separate along the surface of the male pronucleus while moving toward its anterior side (Albertson, 1984). Once centrosomes are separated, the male pronucleus starts to move toward the embryo anterior, while the female pronucleus start to move toward the posterior. The two pronuclei meet and associate at roughly ~ 70% of embryo length and thereafter move together toward the cell center. During that process, called centration/rotation, the pronuclei-centrosomes complex is positioned at the cell center and oriented along the AP axis. Then, the nuclear envelope breaks down and the mitotic spindle is assembled.

While at the beginning of metaphase the spindle is in the center of the cell, later during metaphase and in anaphase cortical forces displace the mitotic spindle toward the posterior side of the embryo, while elongating it and provoking massive oscillations of the spindle poles (Albertson, 1984 and reviewed in Rose and Gönczy, 2014). These oscillations are more pronounced in the posterior pole, thus suggesting that stronger forces act on it than on the anterior one. As a result of spindle posterior displacement, the cytokinetic furrow is positioned toward the posterior side of the embryo and the cell divides unequally.

1.5.2 The *C. elegans* centrosome

At the end of meiosis II, centrosomes starts to accumulate pericentriolar material and dramatically increase in size (Hannak et al., 2001). Three components are absolutely needed for the assembly of pericentriolar material: SPD-5, SPD-2 and AIR-1 (reviewed in Oegema and Hyman, 2006). SPD-5 is thought to be the main structural component of the pericentriolar matrix (Hamill et al., 2002). When SPD-5 is depleted, pericentriolar material does not accumulate around centrioles and no microtubule aster is formed (Hamill et al., 2002). Strong defects in pericentriolar material accumulation and microtubule nucleation are also observed upon SPD-2 and AIR-1 depletion (Kemp et al., 2004; Hannak et al., 2001; O'Connell et al., 2000; Pelletier et al., 2004). Quantitative analysis of SPD-5 accumulation at centrosomes suggests that SPD-5 autocatalyses its accumulation at centrosomes (Zwicker et al., 2014). Indeed, SPD-5 is a coiled-coil protein that has been demonstrated to be able to oligomerize *in vitro* (Woodruff et al., 2015).

Centrosomes accumulate several proteins that regulate microtubule nucleation and dynamics. Thus, the microtubule nucleator γ-tubulin is enriched at centrosomes and its depletion reduces microtubule nucleation rate and therefore aster size (Hannak et al., 2002; Strome et al., 2001). Furthermore, centrosomes accumulate the microtubule-dynamics regulators ZYG-9 and its interactor TAC-1. These two proteins are needed for normal aster formation, since their depletion leads to reduced aster size and therefore prevents pronuclear migration and meeting (Bellanger and Gönczy, 2003; Le Bot et al., 2003; Matthews et al., 1998; Srayko et al., 2003). Finally, centrosomes accumulate proteins needed for the assembly of centrioles during S phase (reviewed in Oegema and Hyman, 2006)

1.5.3 The roles of dynein

In the *C. elegans* embryo, dynein is abundantly present in the cytoplasm and enriched both at the cortex and at the nuclear envelope (Gönczy et al., 1999). The depletion of the dynein heavy chain DHC-1 by RNAi completely prevents centrosome separation, pronuclear migration and centration/rotation (Gönczy et al., 1999). As a result, centrosomes do not move from their initial posterior localization and do not form a bipolar spindle during mitosis. On the other hand, the cell cycle progresses, polarity is correctly established, centrosomes are assembled and a microtubule aster is formed (Gönczy et al., 1999). These results suggest that the defects resulting from dynein depletion are due to the lack of dynein-dependent force generation rather than a more complex impairment of overall cell division.

Dynein is anchored at the nuclear envelope by the trans-membrane KASH domain protein ZYG-12 (Malone et al., 2003). Following ZYG-12 depletion, dynein is lost from the nuclear envelope and centrosomes detach from it. However, it is not clear whether ZYG-12 tethers centrosomes at the nuclear envelope only through dynein or if it contributes also independently. Since ZYG-12 can homodimerize *in vitro* with its splicing variant that is enriched at centrosomes (Malone et al., 2003), it could tether centrosomes by homodimerization between the nuclear and centrosomal pools. Indeed, in embryos depleted of the dynein heavy chain, centrosomes are found close to the male pronucleus in 85% of the cases, suggesting that ZYG-12 might also tether centrosomes in a dynein-independent way. Unfortunately, this condition is difficult to interpret with certainty since the microtubule aster is not moving and therefore it could be merely close to the male pronucleus, but not directly bound (Gönczy et al., 1999). Therefore, it remains unclear whether ZYG-12 tethers centrosomes only through dynein or if it contributes independently by homodimerization. Regardless, nuclear dynein is not absolutely needed for centrosome separation, since detached centrosomes are able to separate in ZYG-12 depleted embryos (Malone et al., 2003).

Nuclear dynein is thought to be one of the main drivers of female pronucleus migration (Gönczy et al., 1999 and reviewed in Reinsch and Gönczy, 1998). The migration of the female pronucleus toward the male pronucleus occurs in two phases (Albertson, 1984; O'Connell et al., 2000). First, a slow phase of migration that has been proposed to be driven by cytoplasmic flows. Then, a second fast phase during which the female proucleus quickly reaches the male. The current model of the fast phase posits that dynein at the female nuclear envelope binds to astral microtubules emanating from the centrosomes and pulls on them (O'Connell et al., 2000 and reviewed in Reinsch and Gönczy, 1998). Therefore, the female pronucleus moves by tracking along centrosomal microtubules. Compatible with this model, female pronucleus migration does not occur when dynein or tubulin are depleted (Strome and Wood, 1983; Malone et al., 2003) or when the microtubule aster size is reduced (Bellanger and Gönczy, 2003; Le Bot et al., 2003; Srayko et al., 2003). Finally, the fast phase of pronuclei migration does not occur when centrosome formation is impaired or the centrosomal nucleator γ-tubulin is depleted (Hamill et al., 2002; O'Connell et al., 2000; Hannak et al., 2002).

Cortical dynein plays a fundamental role in spindle positioning and asymmetric cell division (reviewed in Gönczy, 2008; Kotak and Gönczy, 2013). Dynein is anchored at the cortex though the ternary complex comprising G_α/GPR-1/2/LIN-5 and the complete depletion of any of these three components leads to symmetric cell division. Evidence of cortical forces acting during anaphase on the mitotic spindle came from laser micro-dissection experiments in which the ablation of interpolar microtubules lead to fast spindle pole movements toward the cell cortex (Grill et al., 2001). Subsequent reverse genetics and laser micro-dissection studies have shown that depletion of any component of the ternary complex prevents dynein cortical localization, impairs cortical forces and thus blocks spindle elongation, posterior displacement and oscillation, ultimately leading to symmetric cell division (Colombo et al., 2003; Nguyen-Ngoc et al., 2007). Indeed, depletion of any component of the ternary complex impairs cortical forces, as revealed by further laser micro-dissection experiments (Colombo et al., 2003; Nguyen-Ngoc et al., 2007). In addition, invaginations of the plasma membrane that depend on cortical dynein and microtubules have been observed (Redemann et al., 2011), thus further revealing the existence of a pull between microtubules and cortex. Importantly, spindle severing experiments have demonstrated that spindle posterior displacements is driven by an asymmetric force deployment between the two sides of the embryo (Grill et al., 2001, 2003). This force asymmetry depends on polarity proteins, so that cell polarity controls asymmetric cell division through force generation (Grill et al., 2001 and reviewed in Rose and Gönczy, 2014). Computer simulations showed that such an asymmetric force could arise from an enrichment of active motors at the posterior or from an asymmetry in cortical tension due to the enrichment of actomyosin at the anterior, that in turn results from polarization (Kozlowski et al., 2007). Indeed, previously, an elegant study quantified the number of motors actively pulling at each embryo side by measuring the movements toward the cortex of fragments generated by laser-induced centrosome disintegration (Grill et al., 2003). From that analysis the authors concluded that a higher number of motors is pulling at the posterior than at the anterior and estimated the number of active posterior motors at any time to be likely below 50.

Cortical dynein contributes also to the rotation of the centrosome-pronuclei complex toward the AP-axis. Indeed, laser microtubule-severing experiments, depletion of ternary complex components, analysis of centrosome micromovements and computer simulations demonstrated that cortical forces are indeed active at that stage and that they are spatially regulated to precisely control centrosome rotation (Labbé et al., 2004; Tsou et al., 2002; Kimura and Onami, 2007). In particular, comparison of centrosome micromovements at high time-resolution in wild-type, G_α and dynein depleted embryos revealed that dynein-dependent cortical forces are enhanced at the posterior side, but are inhibited in the lateroposterior region (Kimura and Onami, 2007). Such repression is likely due to the GPR-1/2 antagonist LET-99 that accumulates in that lateral portion of the cortex (Tsou et al., 2002). Regardless of the molecular regulation, the observed distribution of forces applies a torque to centrosomes that favors their rotation toward the AP-axis (Kimura and Onami, 2007). In addition, as a result of force repression in the lateroposterior cortex, the total anterior and posterior forces are balanced and the spindle is maintained in the center of the embryo at the beginning of metaphase (Kimura and Onami, 2007). Finally, in line with the presence of cortical forces acting during centration/rotation, depletion of the ternary complex components G_α and GPR-1/2 leads to faster centrosome centration, therefore suggesting that cortical dynein tethers the microtubule aster at the cortex and partially counteracts centration forces (Kimura and Onami, 2007).

The question remains open whether cortical dynein exerts force during centration/rotation and anaphase through its motor activity or by holding the depolymerizing microtubule tip (Kozlowski et al., 2007). A study has attempted to measure cortical dynein motor activity by tracking short microtubules liberated from centrosome in a katanin gain-of-function mutant (Gusnowski and Srayko, 2011). A subset of these short microtubules exhibits fast cortical dynein-dependent movements. These fast movements, indicators of dynein motor activity, depend on LIN-5, but surprisingly not on the other two components of the ternary complex, G_α and GPR-1/2. This result suggests that the subset of cortical dynein that exerts force by motor activity is not the one responsible for spindle positioning, which instead requires both G_α and GPR-1/2.

Finally, dynein anchored in the cytoplasm can exert length-dependent forces that are thought to drive male pronucleus migration and centrosomes centration. Computational simulations have shown that this model is compatible with the observed dynamics of migration and centration (Kimura and Onami, 2005; Kimura and Kimura, 2011b; Shinar et al., 2011). In addition, the number of minus-end directed movements of vesicles correlate with the speed of centration (Kimura and Kimura, 2011b). Accordingly, depletion of cytoplasmic vesicles or of some dynein adapter proteins leads to defects in centration, but does not prevent pronuclear meeting, thus suggesting a more critical role in centration of the dynein cytoplasmic pool (Kimura and Kimura, 2011b). Finally, computational simulations show that cytoplasmic length-dependent forces are required, together with cortical forces, to robustly rotate the centrosomes-pronuclei complex toward the AP axis (Kimura and Onami, 2007).

Together, these studies demonstrated that dynein motors have different and important roles in the *C. elegans* one cell-stage embryo and have implicated dynein in the majority of microtubule-dependent processes. However, it remains unknown which pool of dynein motors drives centrosome separation and how the forces are organized to move centrosomes in opposite directions.

1.6 Aim of this work

The aim of this work is to investigate the mechanisms of centrosome separation, in particular to understand how cells can robustly separate centrosomes when kinesin-5 is absent or non functional. This fundamental biological question has a strong impact on the understanding of cell division and, in particular, of cell mechanics. Furthermore, this question is relevant for medical research since delayed centrosome separation can lead to chromosome segregation defects, thus genome instability and potentially cancer (Silkworth et al., 2012 and reviewed in Tanenbaum and Medema, 2010). Finally, given that kinesin-5 is currently studied as a potential target for cancer treatment, dissecting the mechanisms that separate centrosomes when kinesin-5 is inhibited will shed light on the potential improvements of this approach (reviewed in Rath and Kozielski, 2012).

We decided to focus on the mechanisms of centrosome separation that rely on the minus-end directed motor dynein since it has been implicated in centrosome separation in different systems and its precise mechanism and location of action is still unknown. Therefore, we set out to investigate centrosome separation in the *C. elegans* one-cell stage embryo, which relies entirely on dynein for centrosome separation, thus eliminating the potentially confounding effect of kinesin-5. Furthermore, the advantages of *C. elegans* as a model system that we have mentioned before, such as the robustness of mechanical processes during the first cell cycle and the accessibility to protein depletion techniques, allow one to quantitatively analyze centrosome separation and dissect the underlying mechanisms by comparing wild-type and mutant/RNAi conditions.

In this thesis, we will investigate the mechanisms of centrosome separation by combining microscopy, reverse genetics, image processing and computational modeling. First, we will quantitatively characterize centrosome separation in the wild-type by imaging and tracking centrosomes in 3D at high spatial and temporal resolution (Chapter 3). In a second step, aiming at dissecting the mechanisms driving centrosome separation, we will deplete select proteins and compare centrosome dynamics in these depleted embryos with the wild-type. In particular, we will remove dynein from select subcellular localizations and deplete components of the cytoskeleton. Thanks to this approach, we will draw a qualitative model of centrosome separation that we will further challenge with additional experiments (Chapter 4). Then, we will develop a 3D computational simulation of centrosome dynamics to investigate whether the proposed model is sufficient to explain quantitatively the features of centrosome separation (Chapter 5). Indeed, the computational model will prove to be a faithful and predictive representation of centrosome separation in one-cell stage *C. elegans* embryo. Thus, we will use it to further investigate the drivers of centrosome dynamics *in silico*. In particular, we will investigate the origin of the symmetry breaking mechanisms that organizes forces to move centrosomes away from each other (Chapter 6). Overall, this analysis will shed light on the mechanisms of centrosome separation and will reveal the importance of the interplay between the cytoskeleton and cell geometry. To conclude, we will discuss the solidity of these findings, the potential improvements and future developments of this research, as well as its general relevance for the understanding of cell division mechanics (Chapter 7).

2 Materials and Methods

2.1 Worm strains

Transgenic worms expressing GFP::TAC-1 (Bellanger and Gönczy, 2003), GFP::AIR-1 (gift from Asako Sugimoto) (Toya et al., 2011), YFP::GPR-1 (strain TH242; gift from Henrik Bringmann) (Redemann et al., 2011), Lifeact::mKate2 (strain SWG001; gift from Anne-Cécile Reymond and Stephan Grill) (Naganathan et al., 2014), GFP::NMY-2 (strain JJ1473; gift from Ed Munro) (Nance et al., 2003), *bmk-1(ok391)* (strain RB820; Caenorhabditis Genetics Center) (Bishop et al., 2005) were maintained at 24°C. The temperature sensitive strain *zyg-12(ct350)* (Caenorhabditis Genetic Center) (Malone et al., 2003) was crossed with GFP::TAC-1, maintained at 16°C and shifted to the restrictive temperature (24° C) for 1-4 hr or, when treated with RNAi, for the duration indicated in the following text. Likewise, GFP::TAC-1 was crossed with GFP::NMY-2 and worms homozygous for both transgenes maintained at 24° C. YFP::GPR-1 was crossed with Lifeact::mKate2 and worms homozygous for both transgenes were maintained at 24° C. *bmk-1(ok391)* was crossed with GFP-TAC-1 and maintained at 24° C.

2.2 RNAi bacterial feeding

The RNAi feeding strains were obtained from the ORFeome RNAi library (a gift from M. Vidal) (Rual et al., 2004) or, when not available in that library, from the *Caenorhabditis elegans* RNAi feeding library (Kamath and Ahringer, 2003), except for *goa-1/gpa-16(RNAi)* (Colombo et al., 2003). RNAi was performed by feeding animals as follows: *goa-1/gpa-16(RNAi)* and *goa-1/gpa-16(RNAi) zyg-12 (ct350)* by letting adults lay eggs on *goa-1/gpa-16(RNAi)* feeding plates and imaging the progeny of the F1 animals after 134-163 h at 16°C, and then 1-4 h at 24°C; *nmy-2(RNAi)* and *nmy-2(RNAi) zyg-12(ct350)* for 42-47 h at 16°C, then 1-4 h at 24°C; *lin-5(RNAi)* and *lin-5(RNAi) zyg-12(ct350)* for 42-47 h at 16°C, then 1-4 h at 24°C; *gpr-1/2(RNAi)* for 24-36 at 24°C; *rho-1(RNAi) zyg-12(ct350)* for 62-67 h at 16°C, then 1-4 h at 24°C; partial *rho-1(RNAi) zyg-12(ct350)* for 14-36 h at 24°C; *rga-3/4(RNAi)* and *rga-3/4(RNAi) zyg-12(ct350)* for 42-47 h at 16°C, then 1-4 h at 24°C; partial *rga-3/4(RNAi) zyg-12(ct350)* for 14-36 h at 24°C; *dhc-1(RNAi)* *zyg-12(ct350)* for 42-47 h at 16°C, then 1-4 h at 24°C; partial *dhc-1(RNAi)* for 6-8 h at 24°C; *dyrb-1(RNAi)* for 40-48 h at 16°C, then 2-21 h at 24°C; *nop-1(RNAi)* and *nop-1(RNAi) zyg-12(ct350)* for 42-47 h at 16°, then 1-4 h at 24°C; *zyg-12(RNAi)* for 42-47 h at 24°C; *klp-7(RNAi) zyg-12(ct350)* for 40-48 h at 24°C; *zyg-9(RNAi)* was performed by feeding worms expressing GFP::AIR-1 for 48-56 h at 24°C. The efficiency of protein depletion by RNAi was assessed phenotypically as follows: for GOA-1/GPA-16, GPR-1/2 or LIN-5 by the absence of spindle oscillations and the impairment of spindle elongation/positioning during mitosis (Grill et al., 2001; Nguyen-Ngoc et al., 2007).; for ZYG-12 by the detachment of centrosomes from the male pronucleus and the lack of pronuclear migration/meeting (Malone et al., 2003); for NMY-2 and RHO-1 by lack of cortical contractions and cortical flow (Motegi and Sugimoto, 2006; Shelton et al., 1999); for NOP-1 by lack of pseudo-cleavage furrow (Rose et al., 1995); for RGA-3/4 by the presence of excess cortical ruffling and anterior displacement of the pseudo-cleavage furrow (Schmutz et al., 2007); for ZYG-9 by the lack of pronuclear migration (Kemphues et al., 1986); for KLP-7 by the breakage of the mitotic spindle during anaphase (Grill et al., 2001).

2.3 Indirect immunofluorescence

For indirect immunofluorescence, embryos were fixed in methanol at $-20°$ for 1 h, followed by washes with PBS 0.5% Tween 20 (PBT) and incubation with primary antibodies for 15 h at room temperature. After washes with PBT, embryos were incubated with secondary antibodies for 45 min at room temperature, and slides were then washed with PBT, and stained with 1μg/ml Hoechst 33258 to visualize DNA. Primary antibodies were 1:200 rabbit anti–DHC-1 (Gönczy et al., 1999), 1:500 mouse anti–α-tubulin (DM1a; Sigma-Aldrich). Secondary antibodies were 1:500 Alexa Fluor 488–coupled anti–mouse and 1:500 Alexa Fluor 568–coupled anti–rabbit. Confocal images were acquired on an inverted confocal microscope (LSM 700; Carl Zeiss) equipped with a charge-coupled device camera (black and white; AxioCam MRm; Carl Zeiss) and a 63x, NA 1.40 oil objective; acquired images were then processed in ImageJ (National Institutes of Health), maintaining relative image intensities.

2.4 Imaging

Embryos were dissected in osmotically balanced blastomere culture medium (Shelton and Bowerman, 1996) and imaging was performed at $24 \pm 0.5°C$. Centrosomes were imaged using dual time-lapse DIC and fluorescent microscopy on a Zeiss Axioplan 2 with a 63x 1.40 NA lens and a 6% neutral density filter to attenuate the 120 W Arc Mercury epifluorescent source. The motorized filter wheel, two external shutters, and the 1392x1040 pixels 12-bit Photometrics CoolSNAP ES2 camera were controlled by μManager (www.micro-manager.org). For all images, a hardware binning 2 was used, resulting in a $0.2048\,\mu$m pixel size. For *zyg-12(ct350)* and *lin-5(RNAi)* embryos, a z-stack of 13 planes $1.5\,\mu$m apart was taken every 12 s. For all other conditions, a z-stack of 7 planes $1.5\,\mu$m apart was taken every 6 s. Images were taken with an exposure time of 60-100 ms per plane for DIC and 30-60 ms per plane for the fluorescence channel using the Zeiss Filter Set 10. Imaging of Lifeact::mKate2 YFP::GPR-1 and GFP::NMY-2 GFP::TAC-1 was performed using an inverted Olympus IX 81 microscope equipped with a Yokogawa spinning disk CSU - W1 with a 63x 1.40 NA lens, acquiring images with a 2560x2160 pixels 16-bit PCO Edge sCMOS black and white camera, resulting in 0.1086 pixel size. Transmission light was used to unambiguously identify the embryo stage and eggshell. For Lifeact::mKate2 YFP::GPR-1, a stack of 3 planes $0.25\,\mu\text{m}$ apart was acquired every $3\,s$ for $27\,s$. Lifeact::mKate2 was imaged for 400 ms per plane using a 561 nm solid-state laser at 40% laser power, YFP-GPR-1 for 400 ms per plane using a 488 nm solid-state laser at $40 - 60\%$ laser power. For GFP::NMY-2 GFP::TAC-1, a stack of 20 planes $1\,\mu\text{m}$ apart was acquired every $6\,s$ for $60\,s$ during the centrosome separation phase; every plane was imaged for 200 ms using a 488 nm solid-state laser at $20 - 40\%$ laser power.

2.5 Centrosome and pronuclear tracking

Centrosomes were tracked in 3D using the Imaris Spot Detection feature (Bitplane) from the onset of separation until pronuclear meeting. In embryos where pronuclear meeting does not occur, the centrosomes were tracked until nuclear envelope breakdown. After synchronization with the wild-type time-reference (see below), centrosome separation curves were analyzed from the onset of separation to a time equivalent to that required for pronuclear meeting in the wild-type (t<500 s, referred to as “the equivalent time” in the text). Pronuclei were tracked in 3D using custom software written in MATLAB (MathWorks) based on the homogenous appearance of pronuclei with respect to the rough texture of the cytoplasm-containing yolk granules (Hamahashi et al., 2005). Initially, a standard deviation filter is applied; embryo volume is then segmented by applying a binary threshold, followed by iterated morphological operations and automatic detection of connected components. Connected components with an unrealistic volume for average embryo size are automatically removed. Thereafter, a mask is applied to remove the background, the pronuclear volumes are roughly segmented by applying a binary threshold, followed by iterated morphological operations and automatic detection of connected components. Connected components with an unrealistic volume for average pronuclei size are automatically removed. The male and female pronuclei are then manually selected at their first appearance and automatically tracked thereafter by minimizing the travelled distance between successive frames. Pronuclear positions are refined by fitting the standard deviation images with a custom spherical-symmetric function (piecewise: constant – Hill function with Hill coefficient 6), seeded at every time-point by the position detected at the previous time-point. The variation of pronuclear size between successive frames is constrained. The time of nuclear envelope breakdown and pronuclear meeting are manually annotated. The MATLAB code for tracking pronuclear position and size is available upon request.

2.6 Centrosome separation curves synchronization

We synchronized centrosome separation curves in embryos within each experimental condition by maximizing the overall overlap of centrosome-centrosome distance curves (automatic overall minimization of mean squared deviation). Afterwards, we used the above-mentioned synchronization to calculate the mean male pronuclear size and found it to grow approximately linearly over time.

Thus, we used the average male pronucleus size as a reference to compare the mean separation curves from different experimental conditions. More specifically, for every condition, we performed a two-step synchronization procedure. In such a synchronization, wild-type is used as a reference and time 0 s is defined as the earliest time-point in which two separate centrosomes can be detected in the whole synchronized wild-type dataset. All centrosome separation curves presented here have been synchronized using this procedure, thus allowing comparing the time-scale between different figures. In the first step, we calculated a time-shift by minimizing the mean squared deviation of the male pronucleus size curves of the given condition from the wild-type average centrosome separation curve; in a second step, we performed a second refining synchronization by using the same procedure, but considering the male pronucleus size curves only in the range between 0 and 500 s, corresponding to the timing of centrosome separation (Fig. 2.1A,B).

In order to estimate the error in the synchronization procedure, we calculated the mean squared deviation for different time-shifts and derived the confidence interval as follows. First, we fitted the wild-type average male pronucleus size curve in the range from 0 to 500 s with the regression line $d(t) = mt + q$, where m is the slope of the line and q the offset. Then, we considered the final synchronized average male pronucleus size curve of the given condition in the same range and calculated the normalized squared deviation from the wild-type regression line for different time-shifts δt

$$\chi^2 = \sum_{n=1}^{N} \frac{(d_n - m * (t_n - \delta t) - q)^2}{{\sigma_m}^2 (t_n - \delta t)^2 + {\sigma_q}^2 + {\sigma_{dn}}^2} \tag{2.1}$$

where N is the number of points of the average male pronucleus size curve of the given condition, $[t_n, d_n]$ is a point of the average male pronucleus size curve, σ_{dn} is its standard deviation along the y-axis and σ_m,and σ_q are the errors in the slope and offset of the wild-type regression line, respectively.

The synchronization procedure is considered successful when the average male pronucleus size curve of the given condition is statistically compatible at 95% confidence with the wild-type regression line, i.e. when the P-value associated with the best-fit ${\chi^2}_{\text{min}}$ is above 0.05. In this case, by assuming the errors to be normally distributed, the 68% confidence interval for the estimated time-shift is given by the parameter range in which $\Delta\chi^2 = \chi^2 - {\chi^2}_{\text{min}} < 1$ (Press et al., 2007) (Fig. 2.1C). The time-shift error is calculated as half of this confidence interval.

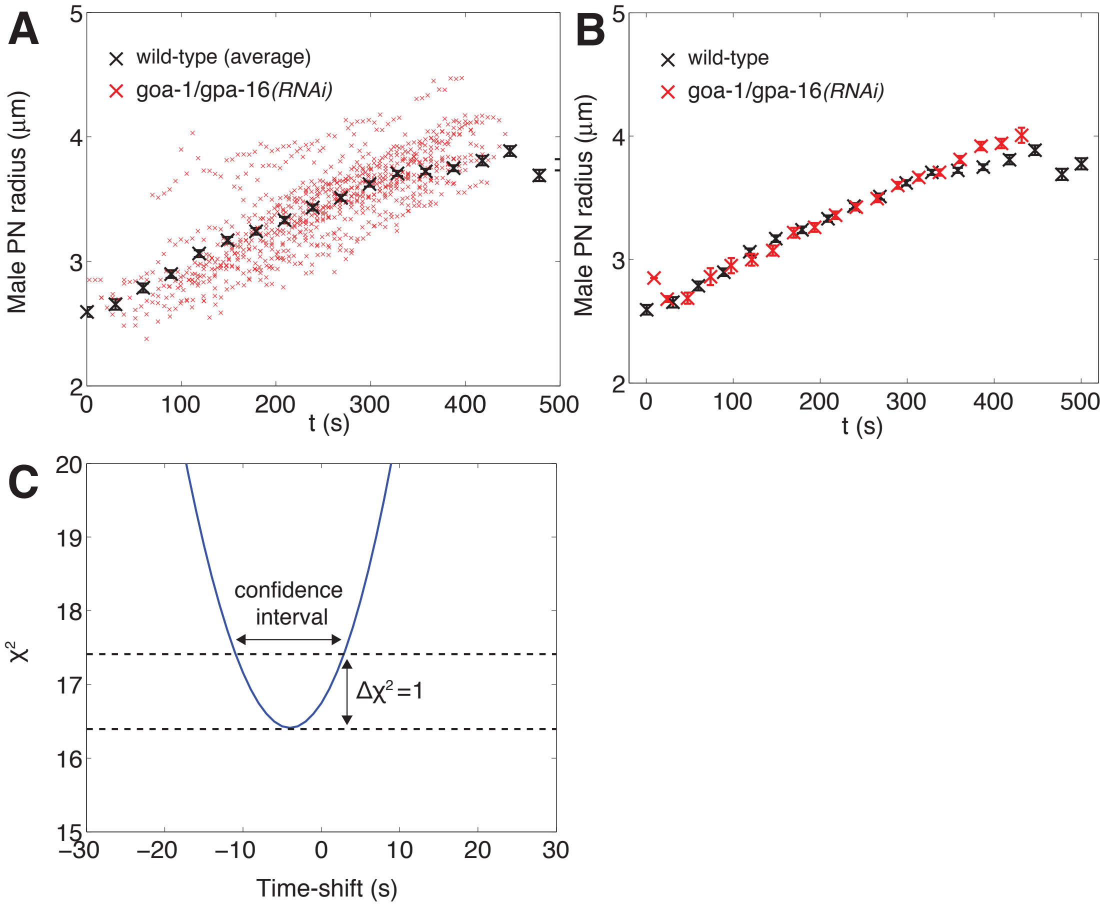

Figure 2.1 – **Example of synchronization procedure for *goa-1/gpa-16(RNAi)* embryos. A** Synchronization of male pronucleus size curves for *goa-1/gpa-16(RNAi)* embryos with average wild-type size curve (indicated with SEM). **B** Result of synchronization procedure. Synchronized average male pronucleus size curves are shown together with SEM. **C** Estimation of the synchronization time error. The P-value of the χ^2 for different time-shifts is shown together with the threshold $\Delta\chi^2 = 1$ (68% confidence) and the resulting confidence interval.

2.7 Centration and pronuclear migration curves synchronization

In the case of centrosome centration, a similar procedure was followed. Centrosome centration does not necessarily occur with the same timing as centrosome separation. Therefore, centrosome centration curves were synchronized by maximizing their overlap. Then, centrosome centration was synchronized with centrosome separation by using male pronucleus size as a time-reference. To this end, the male pronucleus size curves of the given condition, synchronized by using centrosome centration, were further synchronized with the male pronucleus size curves from the same condition, synchronized by using centrosome separation. A similar procedure was followed for pronuclei migration.

2.8 Cortical flow measurements

Cortical flows were measured using Particle Image Velocimetry (PIV) as previously described (Mayer et al., 2010). Image sequences were prepared for PIV as follows: for YFP::GPR-1, the entire stack of 3-planes was z-projected (maximum intensity) and binning 2 was applied to enhance signal intensity; accordingly, binning 2 was applied to the Lifeact::mKate2 single imaged plane; for GFP::NMY-2 two successive planes with the relevant signal were z-projected (maximum intensity) and binning 2 was applied to enhance signal intensity. PIV was performed using the MATLAB based MPIV toolbox (Nobuhito and Kuang-An, 2006) and the Minimum Quadric Differences algorithm. We tested different PIV parameters, which gave comparable results. We segmented the cortical region of the embryo by applying a binary threshold, followed by iterated morphological operations and automatic detection of connected components. Only velocity vectors within the segmented embryo region have been considered. For Lifeact::mKate2 YFP::GPR-1, in order to minimize flow detection errors, we restricted our analysis to velocity vectors whose PIV initial sub-window was entirely within the segmented embryo region. For GFP::NMY-2, we segmented the mid-plane eggshell contour by automatically fitting an ellipse on >20 manually selected points along the eggshell. The AP-axis was defined as the major axis of the fitted ellipse. For the correlation analysis between cortical flows and centrosome separation velocities, the reference flow velocity at each time-point was computed by averaging flow velocity vectors within 70 – 90% of embryo length. Centrosomes were tracked in 3D using the Imaris Spot Detection feature (Bitplane). To select the phase during which centrosomes separate at constant velocity, we considered only frames in which centrosome-centrosome distance was comprised between 3 and 12 μm. For the correlation analysis of the separation movements of the closest and furthest centrosomes, considering that in our experimental conditions the whole embryo height is approximately 20 μm, we conducted this analysis only on those embryos in which the closest centrosome was <8 μm from the imaged cortical plane at the end of the movie. Conversely, the furthest centrosome was retained for correlation analysis only if it was located >12 μm from the imaged cortical section at the end of the movie. The velocity of the separation movements of the centrosomes was computed as in (Waters et al., 1993)

$$v_{\text{closest}} = \frac{(\mathbf{x}_{\text{closest}}(t+1) - \mathbf{x}_{\text{closest}}(t)) \cdot (\mathbf{x}_{\text{closest}}(t) - \mathbf{x}_{\text{furthest}}(t))}{||(\mathbf{x}_{\text{closest}}(t) - \mathbf{x}_{\text{furthest}}(t))||} \tag{2.2}$$

$$v_{\text{furthest}} = \frac{(\mathbf{x}_{\text{furthest}}(t+1) - \mathbf{x}_{\text{furthest}}(t)) \cdot (\mathbf{x}_{\text{furthest}}(t) - \mathbf{x}_{\text{closest}}(t))}{||(\mathbf{x}_{\text{furthest}}(t) - \mathbf{x}_{\text{closest}}(t))||} \tag{2.3}$$

where $\mathbf{x}_{\text{closest}}(t)$ is the position of the indicated centrosome at frame t (Fig. 4.12).

2.9 Calculation of angle between centrosomes

The angle between the two centrosomes and the center of the male pronucleus is calculated

$$\theta = \arccos \frac{(\mathbf{x}_1 - \mathbf{x}_c) \cdot (\mathbf{x}_2 - \mathbf{x}_c)}{||\mathbf{x}_1 - \mathbf{x}_c||||\mathbf{x}_2 - \mathbf{x}_c||} \tag{2.4}$$

where $\mathbf{x}_{1,2}$ are the positions of the two centrosomes and $\mathbf{x}_c$ is that of the center of the male pronucleus.

2.10 Statistical comparison of centrosome separation in different conditions

To quantitatively compare centrosome separation in different conditions, we determined centrosome separation rates and centrosome separation onset time from the centrosome distance curves. First, we fitted the wild-type centrosome distance curve (complete synchronized dataset) with the effective model

$$d(t) = d_0 + \frac{K}{1 + e^{-\alpha(t-t_0)+2}} \tag{2.5}$$

where t is time, $d(t)$ is centrosome distance, d_0 is the initial centrosome separation, α is the separation rate and K is the equilibrium distance. t_0 represents centrosome separation onset time, defined as the intercept on $d = d_0 + K$ of the tangent in the inflection point for which $d = d_0 + \frac{K}{2}$. d_0 is fitted for the wild-type condition and the fitted value is set for all the mutant/RNAi conditions. All fits have been performed by non-linear least square method (NonLinearModel.fit MATLAB function). Parameters from different conditions have been compared using z-test. For comparison of the centrosome separation onset time t_0, the synchronization error σ_{sync} has been considered.

2.11 Centrosomes overshoot

During centrosome separation, centrosomes move from the posterior to the anterior side of the male pronucleus. To detect if some embryos reach this position by passing through opposite poles (180°) and then overshooting, we calculated the cross product $\mathbf{n} = (\mathbf{x}_1 - \mathbf{x}_c) \times (\mathbf{x}_2 - \mathbf{x}_c)$ In an overshoot event, the vector $\mathbf{n}$ inverts abruptly. Therefore, we assigned an overshoot event to an embryo when the angle between the vectors $\mathbf{n}$ in successive frames was larger than a threshold (135°). This enabled us to spot 5 overshoot events out of 42 wild-type embryos. Importantly, the separation behavior in these 5 embryos is compatible with that in the other 37, reaching approximately 226°, which is the symmetric value of 134° with respect to 180° (Fig. 3.4A). Since we could not detect any feature associated with the overshoot events, we pooled overshooting embryos with the non-overshooting ones in the subsequent analysis.

2.12 Computer simulation

Computer simulations were performed using Cytosim (Nedelec and Foethke, 2007). Briefly, overdamped Langevin equations are used to describe the motion of elastic fibers and solids in a viscous fluid in the presence of Brownian motion. All stochastic events (motor binding, catastrophes, nucleation) are generated as first-order random events. The simulation parameters are summarized in Table D.1. The embryo is simulated as a 50x30x30 μm ellipsoid with the cytoplasm having homogenous constant viscosity. The cell cortex is considered to be the embryo boundary that confines microtubules, centrosomes and pronuclei. A soft excluded volume interaction applies to centrosomes, microtubules and pronuclei, preventing these objects from overlapping, except that microtubule-microtubule interactions are not considered.

2.12.1 Microtubules and centrosomes

Centrosomes and microtubules are simulated as described (Kozlowski et al., 2007). In brief, microtubules are flexible fibers that follow a 2-state dynamic instability model. Shrinkage rate is constant, and growth rate is reduced by antagonistic force. If the projected force F is negative, the growth rate is

$$v = v_g e^{\frac{F}{F_s}} \tag{2.6}$$

where F_s is the typical stall force and v_g is the free velocity. Otherwise, if the projected force F is positive, the growth velocity is constant $v = v_g$. The catastrophe rate depends on whether the microtubule tip touches the cortex or is in the cytoplasm, and is also induced by force as described (Foethke et al., 2009). When a microtubule depolymerizes completely, it is deleted from the simulation. Centrosomes are spheres 1 μm in diameter covered by microtubule nucleation sites. Empty nucleation sites can lead to the nucleation of a microtubule with a constant probability and subsequently remains inactive until this microtubule depolymerizes entirely.

2.12.2 Pronuclei

The pronuclei are simulated as spherical objects as described (Foethke et al., 2009). Pronuclei can move, rotate and grow in size at a constant rate. Since the size of the pronuclei is comparable to that of the embryo, cytoplasmic flows produced by their movement are affected by the confinement imposed by the eggshell. As a result, the cytoplasmic drag exerted on the pronuclei is increased with respect to the prediction of Stokes law (Shinar et al., 2011). To solve this issue, we adjusted the pronuclei effective drag according to the estimation of a precedent computational model (see Table D.1; Shinar et al. (2011)). During centrosome separation *in vivo*, the female pronucleus drifts slowly towards the posterior before it accelerates to meet the male pronucleus. The early drift is likely not due to interactions with the microtubule asters, since it is not abolished when centrosomal microtubule nucleation is impaired (for example in *spd-5(RNAi)* (Hamill et al., 2002)). We modeled this drift by adding an effective force directed toward the posterior acting on the female pronucleus.

2.12.3 Dynein motors

Individual minus-directed dynein complexes are simulated as described (Rupp and Nédélec, 2012). In brief, dynein motors have a base fixed on the pronucleus or at the cortex and can bind to microtubule that are within their binding range. A bound dynein motor exerts a force between the base and the attachment point on the microtubule that is Hookean with zero resting length. Motors unbinding rate k_{off} depends on the applied force F as

$$k_{\text{off}} = k_0 e^{\frac{F}{F_0}} \tag{2.7}$$

where k_0 is the unbinding rate when no force is applied and F_0 is the typical unbinding force. Motors force-velocity relationship is

$$F = F_0(1 - \frac{v}{v_{\text{max}}}) \tag{2.8}$$

where F_0 is the stall force and v_{max} is the unloaded velocity. The density of motors on the surface of the pronuclei is constant and inactive motors can bind with a certain rate. Cortical motors are considered to be in excess and homogenously distributed on the cell cortex, such that only active cortical motors are simulated. When a microtubule tip touches the cortex, with a certain capture rate an active cortical dynein motor is created in the simulation and attached to the microtubule. Each microtubule can bind multiple dynein motors simultaneously. When a cortical dynein motor detaches from the microtubule, it is removed from the simulation. The effect of cortical flow is implemented by displacing the anchor points of the cortical motors away from the source of the flow with a speed tangent to the cortex. When the source of the flow is at the posterior pole, the flow linearly increases along the anterior-posterior embryonic axis (AP) to reflect the situation in the embryo (Mayer et al., 2010; Munro et al., 2004). The flow does not have any twist component with respect to the anterior-posterior axis. To simulate the cases in which centrosomes are positioned not at the pole but on the cell cortex along the side of the ellipsoidal embryo, a cortical flow that originates from the projection on the cell cortex of the midpoint between the centrosomes was implemented. The flow decreases linearly with the distance from its origin, where it is maximum, being null when the distance from the flow source is equal to the embryo AP-axis length. Also in this case, the flow does not have any twist component.

2.12.4 Initial condition

At the start of the simulation, the male and female pronuclei are at the presumptive posterior and anterior sides of the embryos, respectively. The centrosomes are located between the male pronucleus and the posterior cortex. The initial centrosome-centrosome distance is 1.2 μm. No microtubules are polymerized and all dynein motors are unbound.

2.12.5 Parameters fit

Two parameter values were derived from a fit to the experimental data: pronuclear motor density and cortical motors attachment rate. The objective of the fit was to simultaneously match centrosome distance curves in wild-type, *zyg-12(ct350)* and *goa-1/gpa-16(RNAi)* conditions. To this end, we minimized the total χ^2 , defined as the sum of integrals of the squared differences (weighted by the inverse of the squared SEM of the experimental average curves) between the average of 10 independent simulations and the experimental average curves.

3 Centrosome separation in one-cell stage *C. elegans* embryos

The *C. elegans* one-cell stage embryo becomes polarized along the anterior-posterior (AP) axis shortly after fertilization (Fig. 3.1 and Movie 1). Initially, the male pronucleus is located on the presumptive posterior side and the female pronucleus on the future anterior side (Fig. 3.1, 57 s). As in other systems, the sperm contributes the sole pair of centrioles to the zygote in *C. elegans*, such that the two centrosomes present at the onset of mitosis are associated with the male pronucleus, positioned near the cell cortex (Fig. 3.1, 57 s). Centrosome separation begins during early prophase and occurs along the surface of the male pronucleus (Fig 3.1, 225 s). Thereafter, the two pronuclei migrate towards each other and meet in the embryo center (Fig. 3.1, 333 s and 369 s).

To decipher the mechanisms governing centrosome separation, we performed high temporal and spatial resolution 3D time-lapse microscopy of one-cell *C. elegans* embryos expressing the centrosomal marker GFP::TAC-1 (otherwise wild-type, hereinafter referred to as "wild-type") (Bellanger and Gönczy, 2003; Le Bot et al., 2003; Srayko et al., 2003). We tracked centrosomes using GFP fluorescence and developed an algorithm to automatically detect the position and size of pronuclei using differential interference contrast (DIC) microscopy (Fig. 3.1, Materials and Methods).

3.1 Measurement of centrosome separation

We decided to calculate the distance between centrosomes in 3D as a measure of centrosome separation (Fig. 3.2). To compare centrosome separation dynamics in different embryos, it is desirable to use a set time reference within the cell cycle. However, the time difference between centrosome separation onset and other cell cycle progression landmarks detectable by DIC imaging (such as the end of meiosis II, pseudo-cleavage furrow ingression, pronuclear meeting, nuclear envelope breakdown) was found to be quite variable even in the wild-type. Therefore, we synchronized centrosome separation curves in embryos in wild-type by maximizing the overall overlap of centrosome-centrosome distance curves by automatic overall minimization of mean squared deviation (Fig. 3.2A). In such a way, different embryos are synchronized by

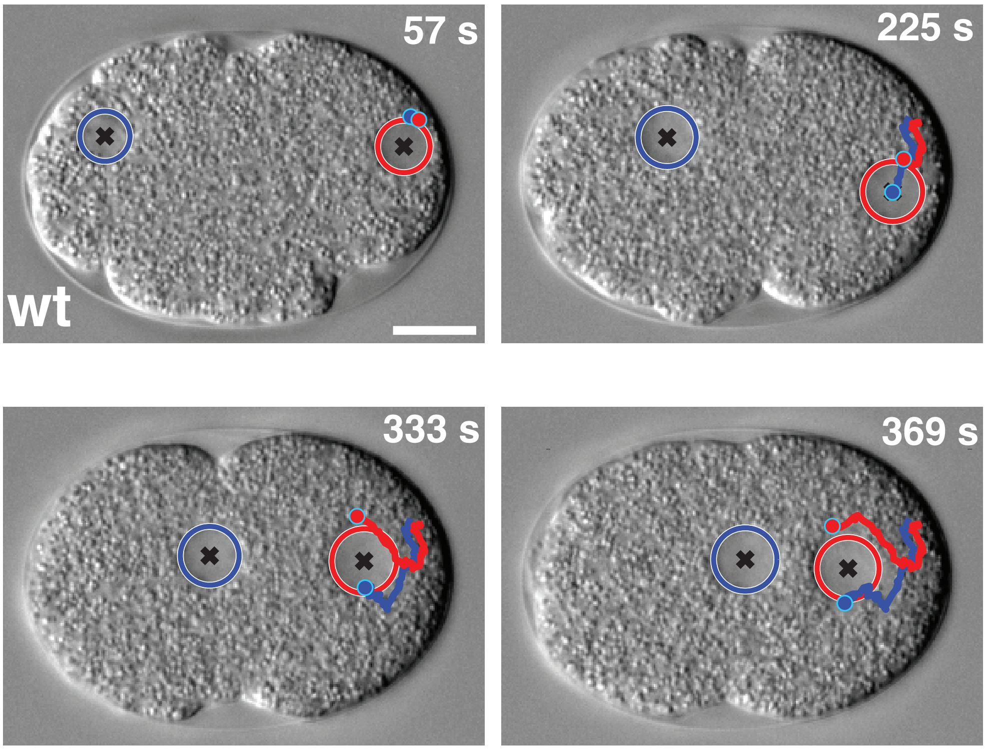

Figure 3.1 – **Centrosome separation in one-cell *C. elegans* embryo.** Centrosome separation monitored with 3D time-lapse DIC and fluorescent microscopy (GFP) in embryos expressing GFP::TAC-1. Here and thereafter, centrosome positions (blue and red dots) are represented with their trajectories (blue and red tracks - z maximum projections). Pronuclei are highlighted (blue disc, female pronucleus; red disc, male pronucleus; black crosses: centers). Here and thereafter, time is indicated in seconds. Wild-type embryos have been synchronized by maximizing the overlap of centrosome-centrosome separation curves, with 0 s defined as the earliest time-point in which two distinct centrosomes could be detected in the whole synchronized wild-type dataset (Material and Methods). Scale bar in this and other figures: 10 μm.

using the timing of centrosome separation (Materials and Methods).

Analysis of the average centrosome-centrosome distance revealed that centrosome separation occurs in three phases (Fig. 3.2B): an initial phase where centrosomes begin moving apart (onset), an intermediate phase with maximal velocity during which most of the separation occurs (separation), and a final equilibrium phase where separation slows down significantly and almost stops (equilibrium). In addition, we measured male pronucleus size by using the above mentioned synchronization and found that on average it grows linearly over time, so that it can be used as a time reference to compare centrosome separation timing between wild-type and mutant/RNAi conditions (Fig. 3.3A, B, see Materials and Methods).

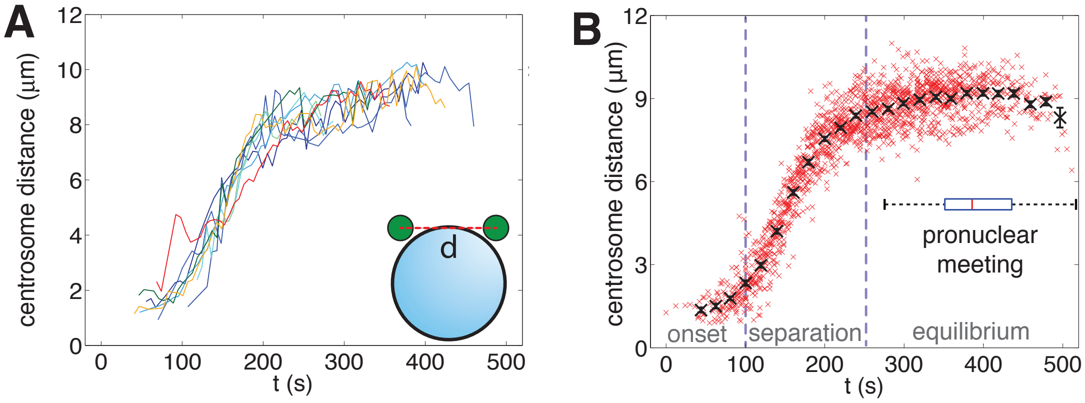

Figure 3.2 – **Quantification of centrosome separation. A** Centrosome-centrosome distance as a function of time for 9 representative embryos. **B** Average centrosome-centrosome distance as a function of time (n= 42 embryos). Separation distances for individual embryos (red crosses) and average with SEM (black crosses) are depicted. The box plot represents the timing of pronuclear meeting (quartiles are represented).

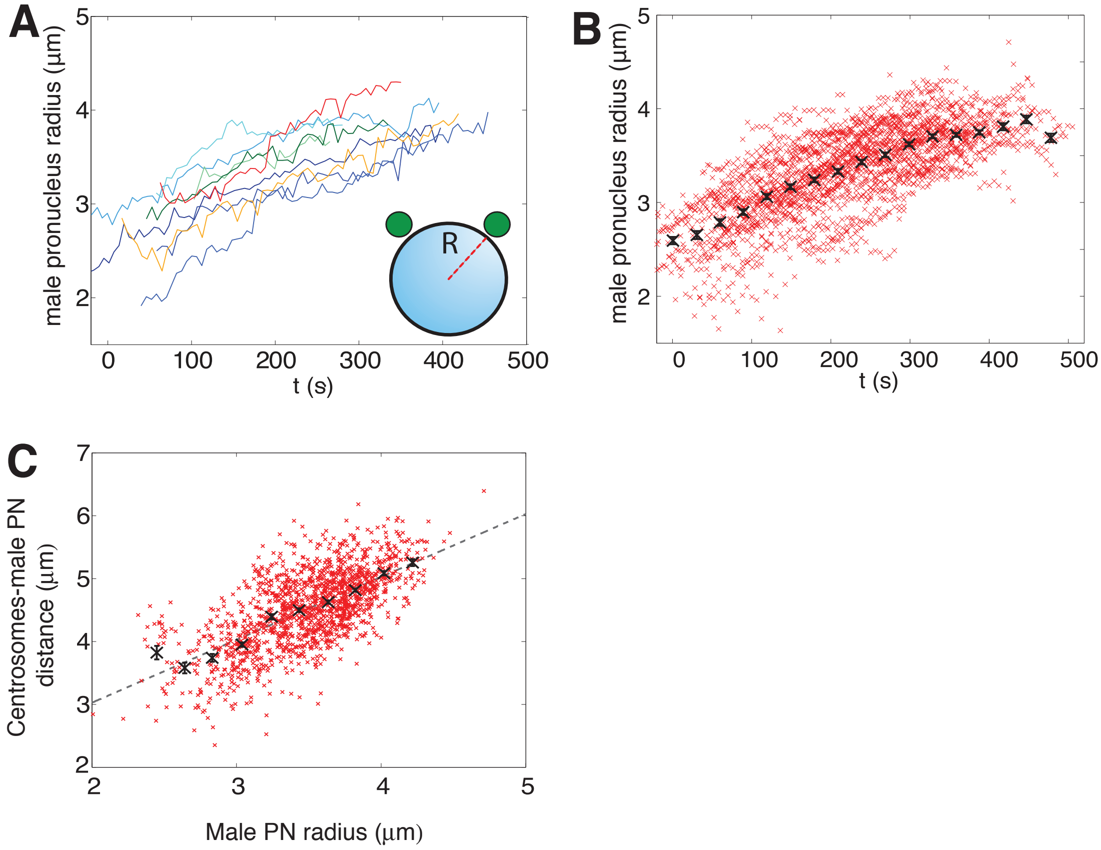

Figure 3.3 – **Quantification of male pronucleus size during centrosome separation. A** Average male pronucleus radius as a function of time for 9 representative embryos. **B** Male pronucleus size as a function of time. Here and thereafter, male pronucleus radii for individual embryos (red crosses) and average with SEM (black crosses) are depicted. **C** Centrosomes-male pronucleus center distance as a function of male pronucleus radius (linear fit with unitary slope: fitted offset $(1.01 \pm 0.03)\,\mu m$.

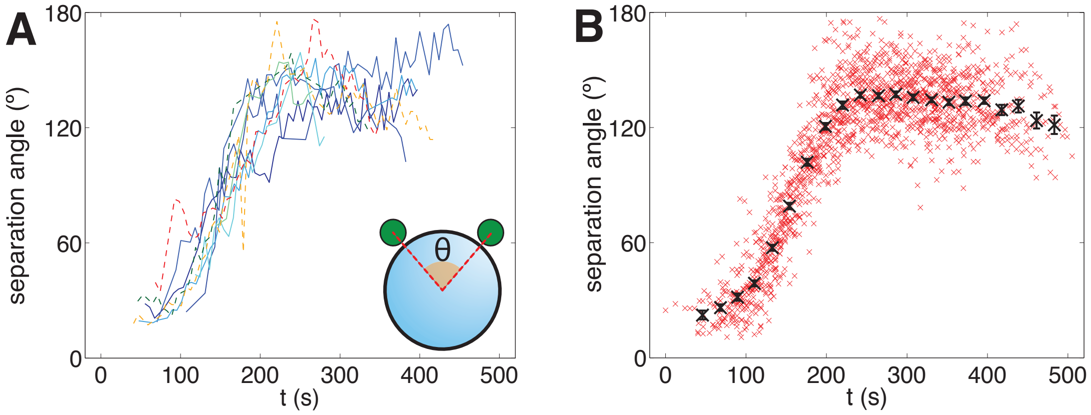

Figure 3.4 – **Quantification of angle between centrosomes during centrosome separation. A** Centrosome-centrosome angle as a function of time for 9 representative embryos (centrosome-centrosome distance for corresponding embryos is represented in 1B). 3 dashed lines indicate overshooting embryos (5 overshooting embryos /42 total, Material and Methods) **B** Average centrosome-centrosome angle as a function of time (n= 42 embryos). Separation angles for individual embryos (red crosses) and average with SEM (black crosses) are depicted.

Since the male pronucleus grows in size over time, it pushes the two bound centrosomes away from its center. Indeed, the distance between centrosomes and the center of the male pronucleus grows linearly as male pronucleus size increases (Fig. 3.3C). In the simple case in which centrosomes-male pronucleus distance increases because of the growth of the male pronucleus, the two metrics should increase with the same rate. To test this hypothesis, we fitted the centrosome-male pronucleus distance curve as a function of male pronucleus size with a straight line and found that the regression line is compatible with that model (line slope $= 1.00 \pm 0.03$). Thus, we repeated the fit with a linear model with unitary slope and calculated the offset of the regression line, obtaining an offset of $(1.01 \pm 0.03)\,\mu$m that is in the order of the average radius of the centrosome at that stage of the cell cycle (Jaensch et al., 2010).

The growth of the male pronucleus could also slightly contribute to push the two centrosomes away from the each other. We reasoned that, in this case, this push should increase the distance between the two centrosomes, but not the angle between them and the center of the pronucleus itself. Indeed, centrosome angle shows the same features as centrosome distance but, interestingly, does not increase in the final equilibrium phase. This result suggests that the residual centrosome distance increase in this last phase (Fig. 3.2B) is due to the growth of the male pronucleus.

3.2 Opposing forces keep centrosomes at an equilibrium angle after separation

Our analysis revealed that centrosomes reach an average angle of about 134°, instead of the theoretical maximal separation angle of 180° (Fig. 3.4, 3.5).

We investigated whether the average angle of ~ 134° could reflect an artifact resulting from a systematic error in determining pronuclear position, which could conceivably lead to a decrease in the recorded angle between the centrosomes (Fig. 3.5A). To investigate whether this may be the case, we considered a situation in which the centrosomes are at opposite poles of a male pronucleus of radius $4\,\mu\text{m}$ (i.e. 180°) and the position of the pronucleus center is affected by a gaussian error with null mean. We computed the distribution of angles and fitted the standard deviation to the experimentally observed distribution, and found that this is not compatible with the observed distribution (Fig. 3.5B - maximum likelihood method). Thus, this analysis suggests that the average angle of 134° is not an artifact of pronucleus position detection.

To understand how centrosomes are kept at an average angle of 134°, we developed a mathematical model based on the diffusion-advection Fokker-Planck equation, in which centrosomes are subjected to advection forces and diffuse under the effect of stochastic forces. The probability density function $p(\theta)$ describes the angle between centrosomes at equilibrium, assuming azimuthal symmetry. This angle obeys the stationary Fokker-Planck equation

$$\frac{D}{R^2 \sin\theta}\frac{\partial}{\partial\theta}\left(\sin\theta\frac{\partial p}{\partial\theta}\right) = \frac{1}{R\sin\theta}\frac{\partial}{\partial\theta}\left(\sin\theta\, v_\theta(\theta)\, p\right) \tag{3.1}$$

where D is the effective diffusivity deriving from stochastic forces and $v_\theta(\theta)$ is the advection term. The normalization condition for the probability density $p(\theta)$ is

$$\int_0^{2\pi} 2\pi\sin\theta\, p(\theta)\, d\theta = 1 \tag{3.2}$$

Thus, the empirical probability density is

$$p_{\text{emp}}(\theta) = \frac{P_{\text{emp}}(\theta)}{2\pi\sin\theta} \tag{3.3}$$

where P_{emp} is the measured distribution of separation angles. The advection derives from the total deterministic force and reads

$$v_\theta(\theta) = \frac{\mathbf{F}(\theta)\cdot\hat{\theta}}{\gamma} \tag{3.4}$$

where $\hat{\theta}$ is the unit vector describing the direction in which the angle θ increases and γ is the viscous drag. The advection term can be written as the derivative of an effective potential $U(\theta)$

$$v_\theta(\theta) = -\nabla U \cdot \hat{\theta} = -\frac{1}{R}\frac{\partial U}{\partial \theta} \tag{3.5}$$

Thus, assuming that the diffusivity D is constant, the equilibrium probability density reads

$$p(\theta) = Ce^{-\frac{U(\theta)}{D}} \tag{3.6}$$

where C is the normalization constant. Therefore, the ratio between the effective potential and the diffusion constant can be calculated from the empirical probability density $p_{\text{emp}}(\theta)$ as

$$\frac{U(\theta)}{D} = -\log(p_{\text{emp}}(\theta)) + \text{const} \tag{3.7}$$

We calculated the effective potential and obtained that it can be well approximated with the elastic potential

$$\frac{U(\theta)}{D} = \frac{k}{2D}(\theta - \theta_0)^2 + \text{const} \tag{3.8}$$

where k is the elastic constant and θ_0 is the equilibrium angle at which force is null (Fig. 3.5C - fit (with 95% confidence intervals): $\frac{k}{D} = 10.6\ (8.9 - 12.2)\,\text{rad}^{-2}$; $\theta_0 = 141\ (139 - 142)°$). Thus, the advection term is linearly proportional to the angle $(\theta - \theta_0)$ as

$$\frac{v_\theta(\theta)R}{D} = -\frac{k}{D}(\theta - \theta_0) \tag{3.9}$$

and pushes centrosomes toward each other when θ is larger than the fitted equilibrium angle $\theta_0 \simeq 141°$. It is worth noting that the distribution average angle 134° is smaller than the equilibrium angle $\theta_0 \simeq 141°$, since the geometry of the sphere favors diffusion toward $\theta = 90°$, thus skewing the probability density and resulting in a shifted average with respect to the equilibrium angle θ_0.

Such analysis reveals that centrosomes are kept at equilibrium by opposing forces that counteract separation forces and balance them at the angle θ_0. We can speculate that the opposing forces might be the same as those that drive centrosome centration and which are directed toward the cell center. Indeed, those forces start to move the centrosomes-pronucleus complex at the same time that the equilibrium phase of centrosome separation occurs (see Appendix A). In the next chapters, we will focus on the mechanisms that drive the central phase of fast centrosome separation and will not consider the forces that later keep centrosomes at the equilibrium angles. We will discuss the potential nature of those forces in Appendix A where we will investigate centrosome centration forces.

Part of the work presented in this Chapter was published in (De Simone et al., 2016).

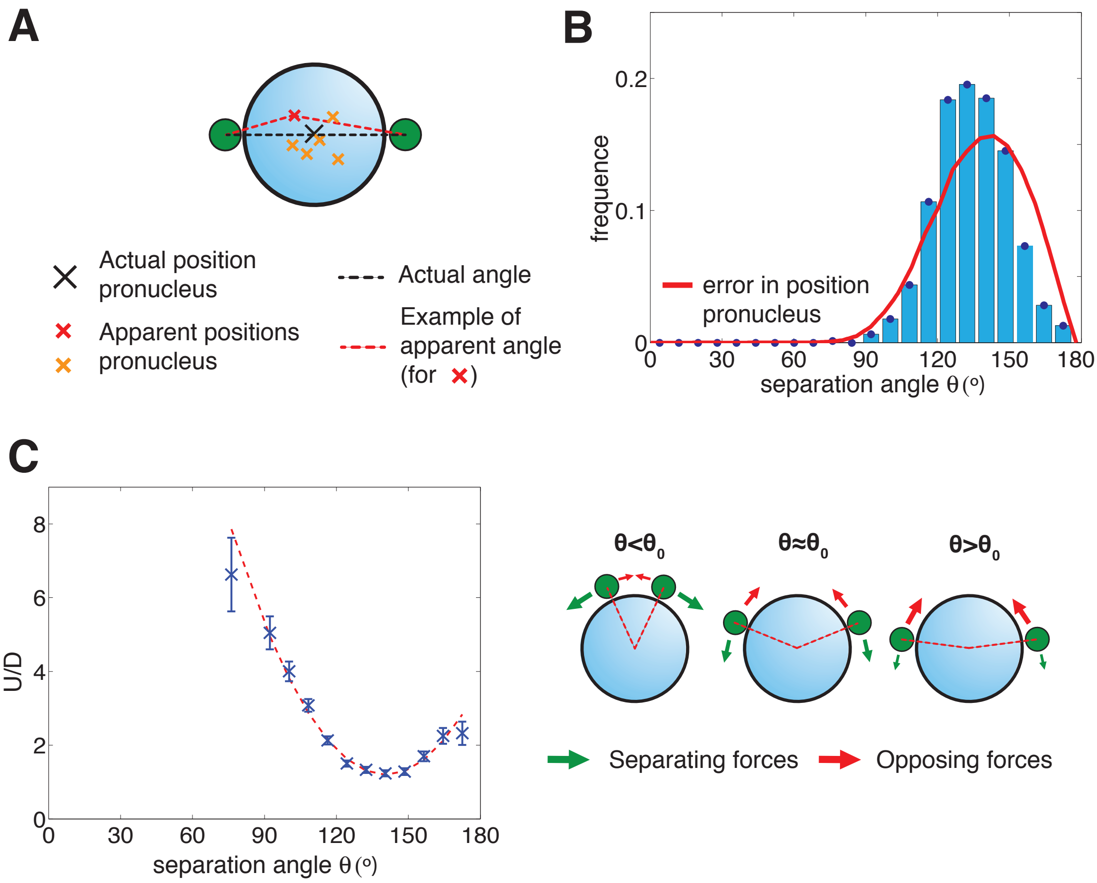

Figure 3.5 – **Centrosome angles at equilibrium and comparison with mathematical models.** **A** Schematic representation of how a potential detection error of male pronucleus center would affect centrosome angle distribution. Shown is a depiction of the mathematical model with centrosomes (green disks) at opposite poles of the male pronucleus (blue disk), so that the angle between the centrosomes with respect to the center of the male pronucleus (black cross) is 180°. The apparent position of the male pronucleus (red cross) is affected by a Gaussian error, thus resulting in the measurement of a lower angle between the centrosomes than the actual angle. **B** Measured centrosome-centrosome angle distribution (histogram) compared with the prediction of the mathematical model (red curve - fitted standard deviation = $1.2\,\mu$m). The distribution is not compatible with the model (Kolmogorov-Smirnov test (KS) $P = 8 \cdot 10^{-10}$), thus indicating that the observed distribution cannot result from a potential systematic detection error of male pronucleus position. **C** The advection potential is calculated from the equilibrium angle distribution. The potential is compatible with the elastic potential $\frac{U}{D} = \frac{k}{2D}(\theta - \theta_0)^2 + \text{const}$ (fit (with 95% confidence intervals): $\frac{k}{D} = 10.6\ (8.9 - 12.2)\,\text{rad}^{-2}$; $\theta_0 = 141\ (139 - 142)°$; $\chi^2 = 9.4$ $P = 0.4$).

4 Mechanisms of centrosome separations

In the previous chapter, we have quantitatively characterized centrosome separation in wild-type and obtained the corresponding centrosome distance reference curve. We have recognized three phases of centrosome separation: an onset phase, a separation phase where most of the separation occurs and a final equilibrium phase, where opposing forces keep centrosomes at a fixed angle. Now, we will investigate the nature of the forces that separate centrosomes prior to the equilibrium phase. In order to decipher the nature of these forces, we will deplete different proteins, in particular dynein, either in the whole embryo or in selected locations. Then, we will calculate the average centrosome separation curve and synchronize it with the reference wild-type by using the male pronucleus size as a time reference (Materials and Methods). Thanks to this approach, we will be able to measure differences in centrosome separation dynamics in different conditions, that will shed light on the underlying mechanisms.

4.1 Kinesin-5 does not contribute to centrosome separation in *C. elegans*

We start the analysis of centrosome separation in mutant/RNAi conditions by testing if the *C. elegans* kinesin-5 homologue BMK-1 partially contributes (Bishop et al., 2005). BMK-1 is expressed in the one-cell embryo, but it has been reported previously to be dispensable for centrosome separation (Bishop et al., 2005). In addition, during anaphase BMK-1 act as a brake of microtubule sliding and therefore limits the speed of spindle elongation (Saunders et al., 2007). Overall, BMK-1 is not necessary for viability and fertility.

To test the role of BMK-1 during prophase centrosome separation, we measured centrosome separation in the *bmk-1(ok391)* deletion mutant (Bishop et al., 2005). We found that, in this mutant, centrosome separation occurs with the same rate as in wild-type (Fig. 4.1), demonstrating that kinesin-5 does not contribute to the pace of centrosome separation in *C. elegans*.

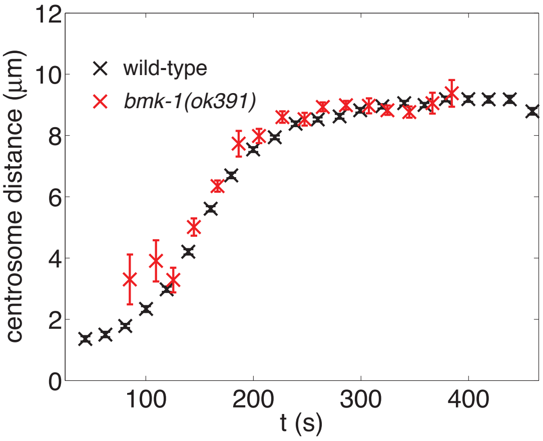

Figure 4.1 – **Centrosome separation in kinesin-5 BMK-1 deletion mutant embryos** Centrosome-centrosome distance as a function of time for representative embryos in wild-type and *bmk-1(ok391)* (with SEM). Average wild-type with SEM: black curve. Number of embryos analyzed: *bmk-1(ok391)* n=10. Here and thereafter, average curves from each experimental condition have been synchronized with wild-type using the average male pronucleus radius as time-reference (Materials and Methods), with time 0 s defined as the earliest time-point in which two separate centrosomes could be detected in the whole synchronized wild-type dataset. Quantification of centrosome separation rates and timing are reported in the Tables C.1, C.2 and C.3. Please note that, even if the average distance in the the first two points of the *bmk-1(ok391)* curve is apparently larger than in the wild-type, this difference is not statistically significant (z-test between *bmk-1(ok391)* average distance and the interpolation of the wild-type distance curve; first and second point: $P = 0.09$ (NS) and $P = 0.17$ (NS), respectively). *bmk-1(ok391)* experiments have been performed together with Ivan Istomin (EPFL "Summer Research Project" Program).

4.2 Nuclear and cortical dynein cooperate to ensure timely centrosome separation

We proceeded by analyzing the contribution of the minus-end directed motor dynein, which is known to be essential for centrosome separation in *C. elegans* (Gönczy et al., 1999) (Fig. 4.2A, B). In this system, dynein is enriched slightly on the nuclear envelope and on the cell cortex in the one-cell embryo (Gönczy et al., 1999). We set out to investigate in a quantitative manner whether dynein in these two locations plays a role in centrosome separation.

We started by removing dynein from the nuclear envelope by depleting the anchor protein ZYG-12 (Malone et al., 2003). We found that the centrosomes detach from the male pronucleus in *zyg-12(ct350)* mutant embryos and separate from one another, as previously reported (Malone et al., 2003). In this condition, centrosome separation occurs at the same rate as in the wild-type, but start with a slight delay of (48 ± 12) s. Strikingly, in addition, our analysis uncovered that centrosomes do not separate normally in such mutant embryos, but instead undergo excess separation along the cortex (Fig. 4.3C, D, 4.4, and Movie 2). Thereafter, centrosomes

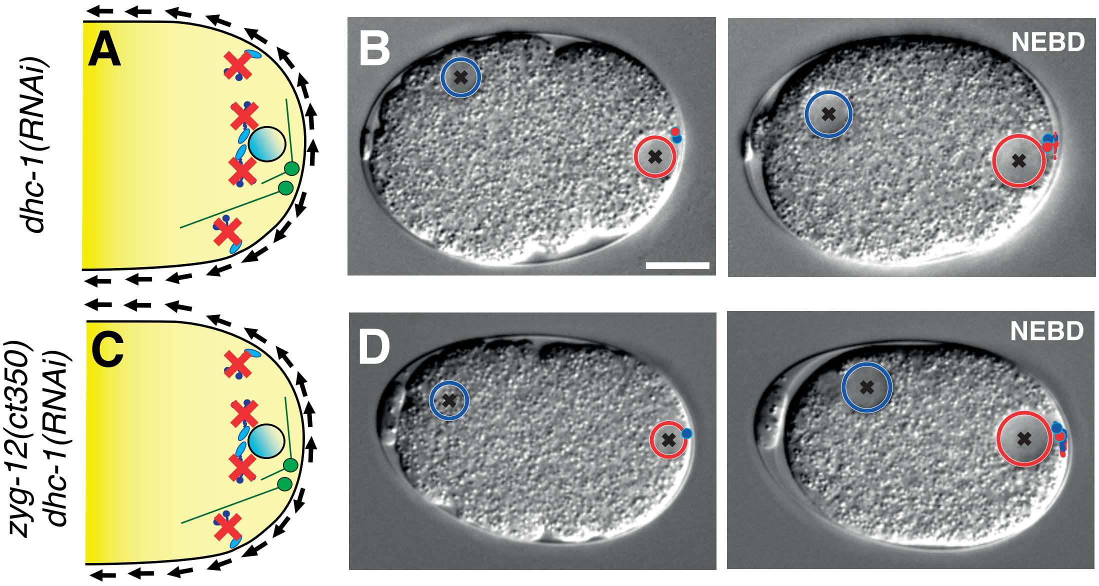

Figure 4.2 – **Centrosome separation upon dynein heavy-chain DHC-1 depletion.** Schematics (A, C) and snapshots (B, D) of centrosome separation in indicated RNAi/mutant conditions (left: onset of separation, right: moment preceding nuclear envelope breakdown; Experimental Procedures). Depleted motors are indicated with red crosses. Number of embryos analyzed: *dhc-1(RNAi)*, $n = 12$; *dhc-1(RNAi) zyg-12(ct350)*, $n = 9$.

approach each other whilst moving towards the cell center, likely reflecting the action of centering forces that are known to act at this later stage (Kimura and Onami, 2005). Overall, these results reveal that, in the absence of nuclear dynein, the path of centrosome separation differs strikingly from that in the wild-type. We conclude that nuclear dynein plays a critical role in limiting the extent of, and in imposing spatial constraints on, centrosome separation.

We set out to decipher the mechanisms governing excess centrosome separation in *zyg-12(ct350)* mutant embryos. To verify that dynein is needed, we depleted the dynein heavy-chain DHC-1 by RNAi in *zyg-12(ct350)* mutant embryos. As anticipated, we found that centrosome separation is abolished in such embryos (Fig. 4.2C, D). Which remaining pool of dynein may drive excess centrosome separation in *zyg-12(ct350)* mutant embryos? We reasoned that cortical dynein is a likely candidate, because excess separation occurs along the cell cortex in *zyg-12(ct350)* mutant embryos. Cortical anchoring of dynein in one-cell *C. elegans* embryos during mitosis depends upon the heterotrimeric G_α proteins GOA-1 and GPA-16, as well as on their interacting partners GPR-1/2 and LIN-5 (reviewed in Kotak and Gönczy, 2013). Therefore, to test the requirement for cortical dynein in the excess centrosome separation occurring upon impaired *zyg-12* function, we analyzed *goa-1/gpa-16(RNAi) zyg-12(ct350)* embryos. Strikingly, we found that excess centrosome movements are prevented and that centrosome separation is essentially abolished in such embryos (Fig. 4.3E, F, 4.4 and Movie 3). We noted also that centrosomes move towards the center thereafter (Fig. 4.3H), again likely reflecting centering forces acting at this later stage. Moreover, we found that the sole depletion of cortical dynein

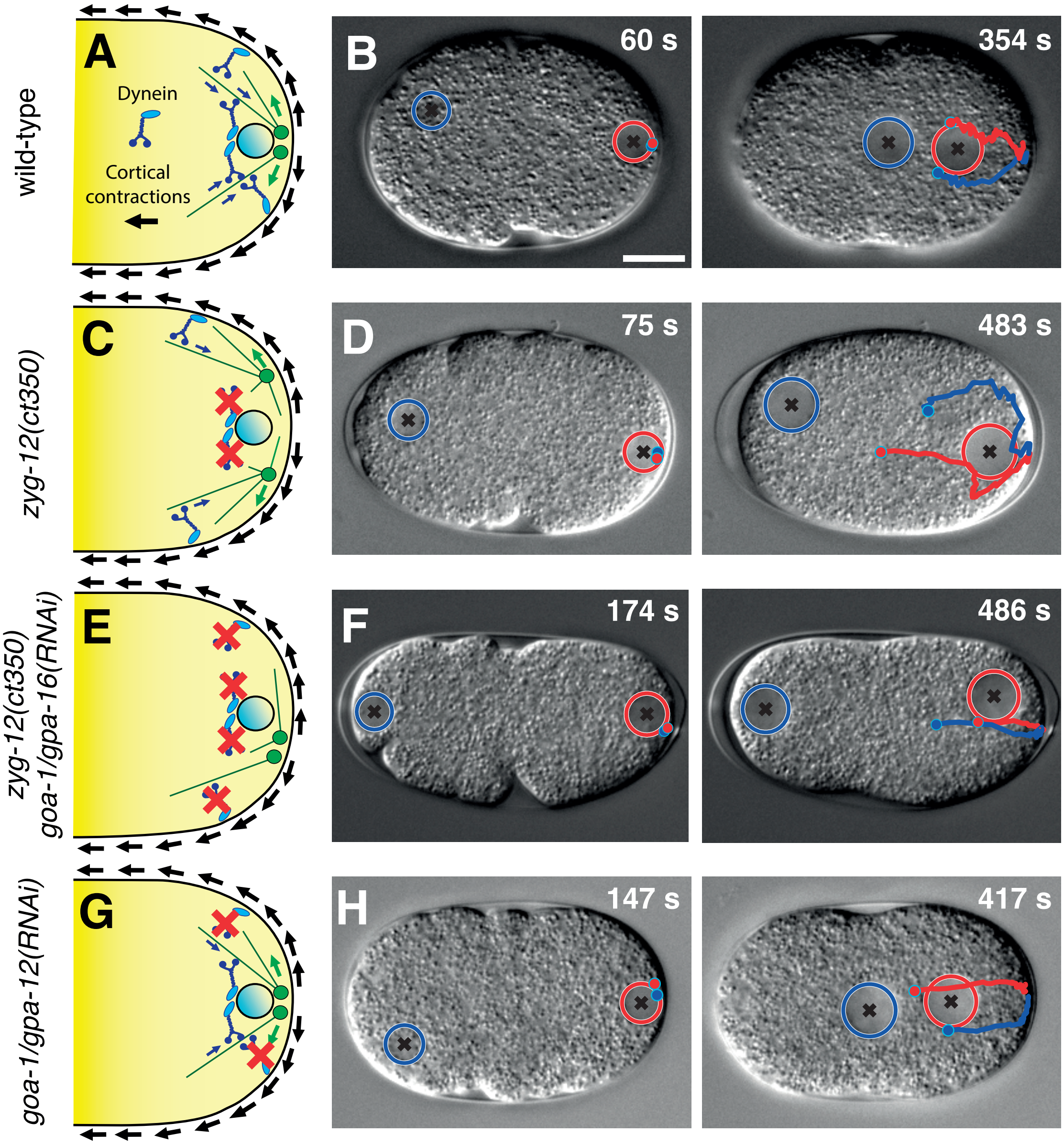
wild-type
A
Dynein
Cortical contractions
B
60 s
354 s
zyg-12(ct350)
C
D
75 s
483 s
zyg-12(ct350)
goa-1/gpa-16(RNAi)
E
F
174 s
486 s
goa-1/gpa-12(RNAi)
G
H
147 s
417 s

Figure 4.3 – **Cortical and nuclear dynein cooperate to separate centrosomes.** Schematics (A, C, E, G) and snapshots (B, D, F, H) of centrosome separation in wild-type and indicated RNAi/mutant conditions (left: onset of separation, right: moment preceding pronuclear meeting or equivalent time; Materials and Methods). Depleted motors are indicated with red crosses.

by *goa-1/gpa-16(RNAi)* slows down centrosome separation, but does not prevent it (Fig. 4.3G, H, 4.4, and Movie 4). This demonstrates that cortical dynein plays a partially redundant role in this process, with nuclear dynein driving the remaining separation. Analogous results were obtained with *lin-5(RNAi)*, *zyg-12(ct350) lin-5(RNAi)* and *gpr-1/2(RNAi)* embryos (Fig. 4.5).

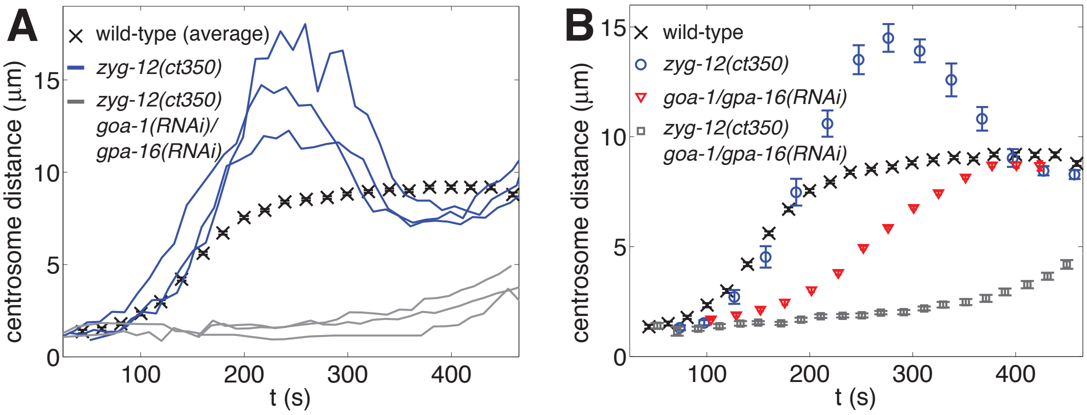

Figure 4.4 – **Quantification of centrosome separation in embryos depleted of cortical and/or nuclear dynein. A** Centrosome-centrosome distance as a function of time for representative embryos in the indicated RNAi/mutant conditions. Average wild-type with SEM: black curve. **B** Average centrosome-centrosome distance with SEM as a function of time in the indicated RNAi/mutant conditions. Number of embryos analyzed: *goa-1/gpa-16(RNAi)*, n=20; *zyg-12(RNAi)*, n=10; *zyg-12(ct350) goa-1/gpa-16(RNAi)*, n=16. Quantification of centrosome separation rates and timing are reported in the Tables C.1, C.2 and C.3.

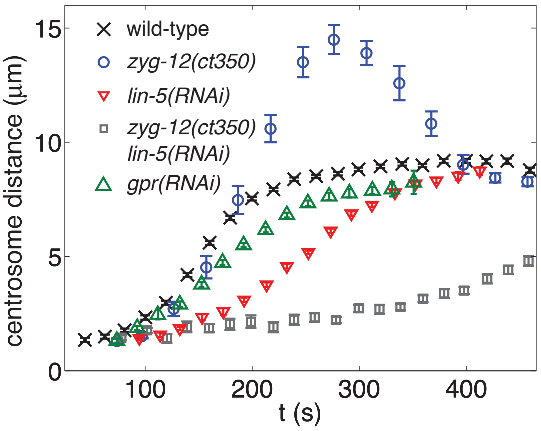

Figure 4.5 – **Centrosome separation in embryos depleted of other components of the ternary complex.** Average centrosome-centrosome distance with SEM as a function of time in the indicated RNAi/mutant conditions. Number of embryos analyzed: *lin-5(RNAi)*, n=12; *zyg-12(RNAi*, n=10; *zyg-12(ct350) lin-5(RNAi)*, n=9, *gpr(RNAi)*, n=10. Quantification of centrosome separation rates and timing are reported in the Tables C.1, C.2 and C.3.

Together, these results lead us to conclude that proper centrosome separation in one-cell *C. elegans* embryos results from the combined contributions of dynein acting at the nuclear envelope and at the cell cortex.

4.3 Actomyosin contractions power cortical dynein-mediated centrosome separation

How does cortical dynein contribute to centrosome separation? One possibility is that motor activity is needed to exert a pull on astral microtubules at the cortex, as during spindle positioning in fungi or during anaphase in *C. elegans* embryos. However, given that the contractile cortical actomyosin network flows towards the anterior at the very same time that centrosome separate (reviewed in Rose and Gönczy, 2014), we reasoned that an attractive alternative is that cortical dynein serves as a coupling device to transmit forces from the actomyosin cortex to centrosomes. Interestingly, the centrosomes themselves trigger the actomyosin flow (Goldstein and Hird, 1996; Bienkowska and Cowan, 2012), such that the pattern of flow is always directed away from them. We set out to test this coupling model by impairing actomyosin contractility through depletion of the non-muscle myosin NMY-2 in *zyg-12(ct350)* mutant embryos. Depleting NMY-2 by *RNAi* does not impair cortical dynein distribution either in the wild-type or in embryos expressing YFP::GPR-1 that were utilized to increase base-line levels of cortical DHC-1 (Fig. 4.6).

Importantly, we found that centrosome separation is essentially abolished in *nmy-2(RNAi) zyg-12(ct350)* mutant embryos (Fig. 4.7E, F, 4.8 and Movie 5). The slightly less penetrant phenotype compared to *goa-1/gpa-16(RNAi) zyg-12(ct350)* (compare Fig. 4.4B and 4.8B past 300 s) could be due to incomplete NMY-2 depletion by RNAi, reflect a minor contribution of cortical dynein motor activity or that of length-dependent forces acting in the cytoplasm. Regardless, like for *goa-1/gpa-16(RNAi)*, we found that the sole depletion of NMY-2 significantly slows down centrosome separation (Fig. 4.7G, H, 4.8B and Movie 6).

In order to further confirm these results, we analyzed centrosome separation in embryos in which cortical contractility was compromised by other means. The small GTPase RhoA, RHO-1 in *C. elegans*, is a central regulator of cellular contractility, which stimulates actin polymerization and myosin activation. Thus, RHO-1 is essential for contractility of the actomyosin network (Motegi and Sugimoto, 2006). Similarly to NMY-2 depletion, we found that centrosome separation is delayed and slowed down in *zyg-12(ct350) rho-1(RNAi)* embryos (Fig. 4.9A).

In the *C. elegans* one-cell embryo, RHO-1 is activated by the redundant action of CYK-4, a component of the centralspindlin complex, and of NOP-1, which lacks known orthologues outside the *Caenorhabditis* genus. Interestingly, during the polarization phase, NOP-1 is the principal activator of RHO-1 and its depletion reduces cortical contractility, in particular pseudocleavage furrow ingression (Tse et al., 2012). Therefore, we depleted NOP-1 to study a condition in which cortical contractility was partially depleted. While centrosome separation is slowed down in *nop-1(RNAi)* embryos, in *zyg-12(ct350) nop-1(RNAi)* embryos centrosome separation onset is delayed, but the pace is not significantly reduced (Fig. 4.9B). It appears that NOP-1 depletion impairs centrosome separation, but in a more complex and less potent way than NMY-2 depletion. This complex impairment might be due to incomplete NOP-1 depletion or to the partially

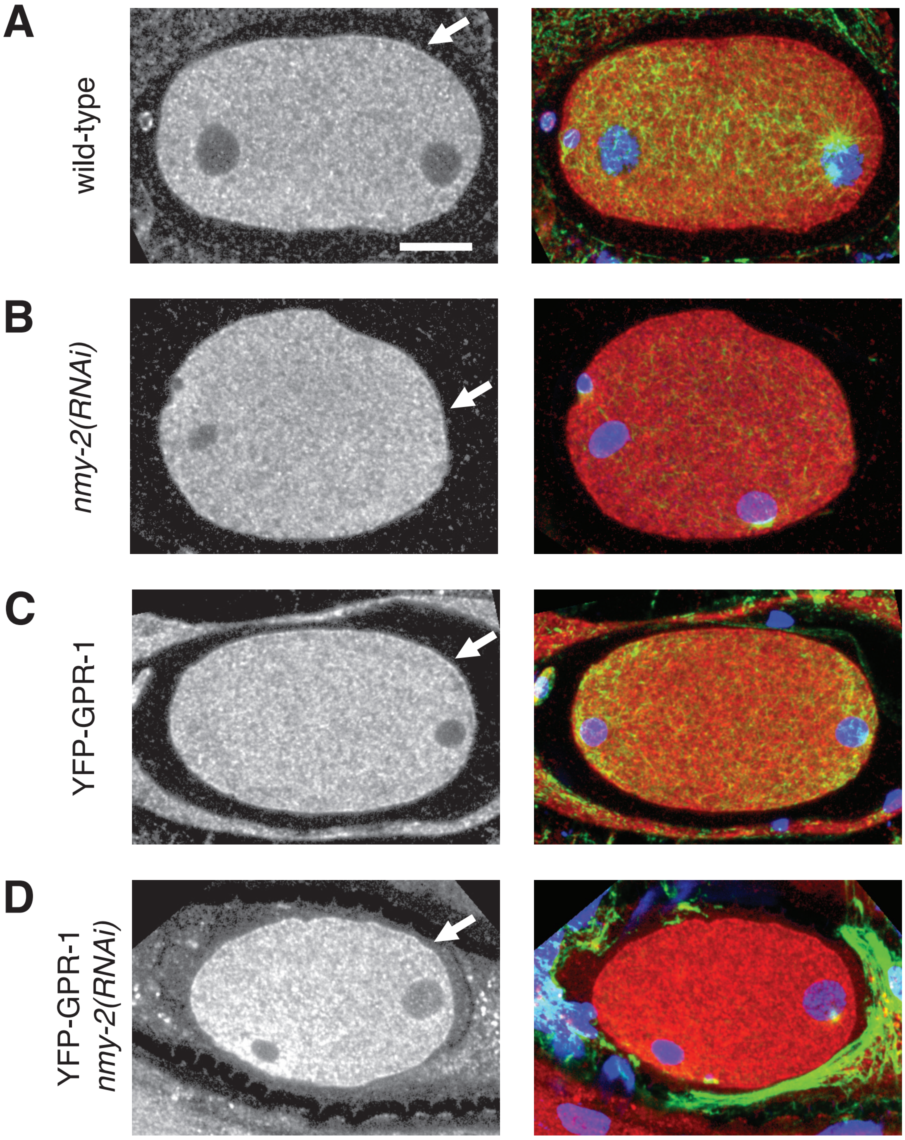

Figure 4.6 – **NMY-2 depletion does not impair cortical dynein localization**
Immunofluorescence analysis of one-cell stage embryos during centrosome separation (A, B: wild-type, C, D: YFP::GPR-1), either untreated (A, C), or subjected to *nmy-2(RNAi)* (B,D) Embryos were stained with antibodies against DHC-1 (gray on the left panels, red in the merges) and α -tubulin (green in the merges). DNA is seen in blue in the merges. Scale bar: 10μm.

redundant activation of RHO-1 by CYK-4. In addition, both in NOP-1 and RHO-1 depleted embryos, residual centrosome separation could be driven by cortical flows that depend on PAR-2, but are independent of RHO-1 (Tse et al., 2012). These hypothesis could be tested by measuring centrosome separation in embryos depleted of CYK-4 or PAR-2 together with NOP-1, for example by performing *cyk-4(RNAi)* or *par-2(RNAi)* in *nop-1(it42)* embryos (Rose et al., 1995).

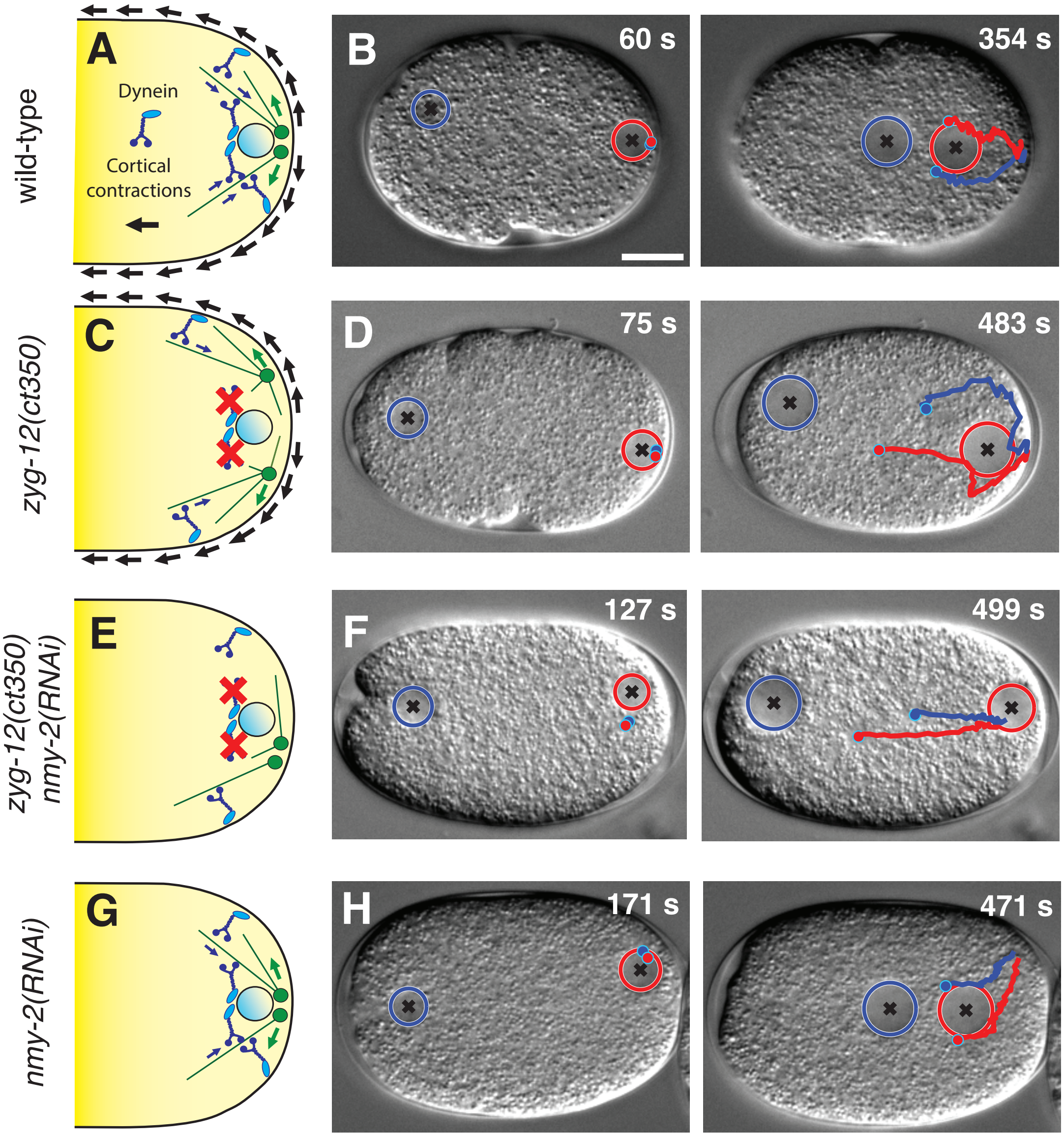
wild-type
A
Dynein
Cortical contractions
B
60 s
354 s
zyg-12(ct350)
C
D
75 s
483 s
zyg-12(ct350) nmy-2(RNAi)
E
F
127 s
499 s
nmy-2(RNAi)
G
H
171 s
471 s

Figure 4.7 – **Actomyosin contractions power centrosome separation through cortical dynein.** Schematics (A, C, E, G) and snapshots (B, D, F, H) of centrosome separation in wild-type and indicated RNAi/mutant conditions (left: onset of separation, right: moment preceding pronuclear meeting or equivalent time; Materials and Methods).

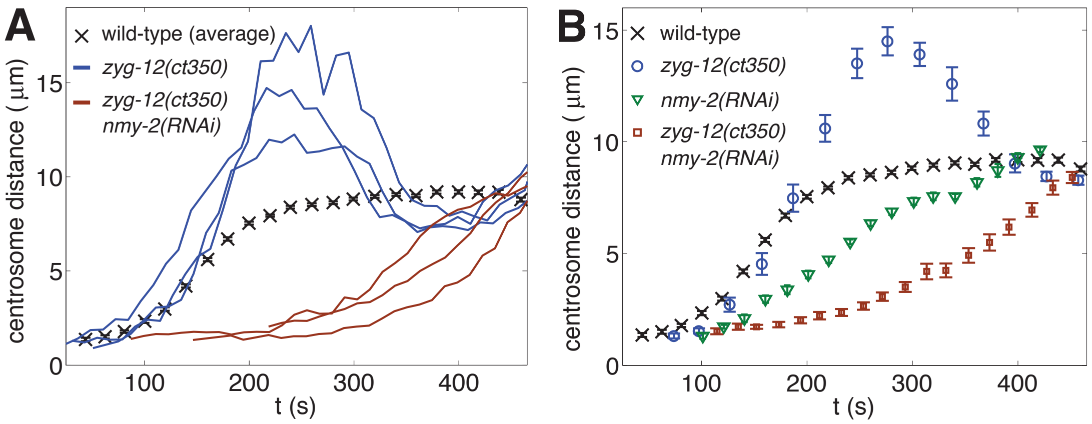

Figure 4.8 – **Quantification of centrosome separation in embryos depleted of actomyosin contractility. A** Centrosome-centrosome distance as a function of time for representative embryos in the indicated RNAi/mutant conditions. Average wild-type with SEM: black curve. **B** Average centrosome-centrosome distance with SEM as a function of time in the indicated RNAi/mutant conditions. Number of embryos analyzed: *nmy-2(RNAi)*, n=10; *zyg-12(RNAi*, n=10; *zyg-12(ct350) nmy-2(RNAi)*, n=19). Quantification of centrosome separation rates and timing are reported in the Tables C.1, C.2 and C.3.

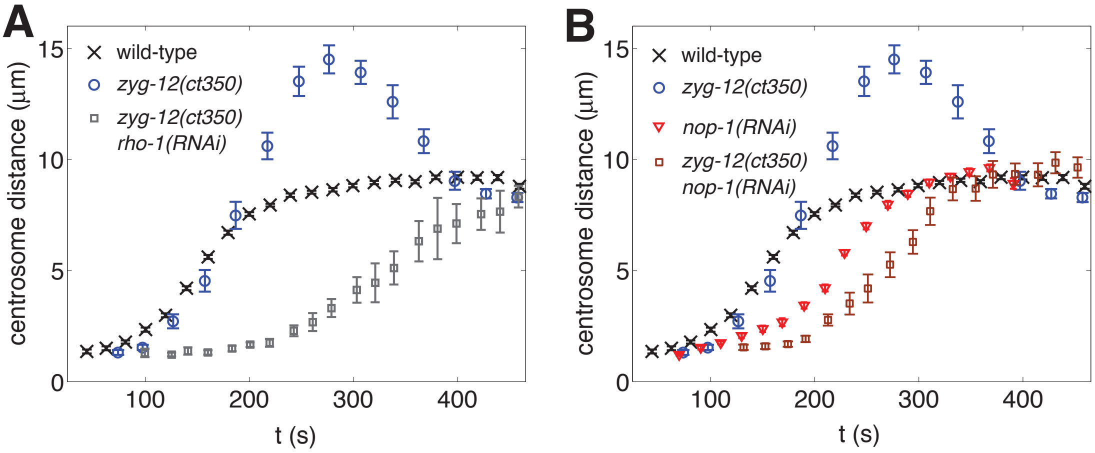

Figure 4.9 – **Centrosome separation in embryos with perturbed actomyosin contractility. A, B** Average centrosome-centrosome distance with SEM as a function of time in the indicated RNAi/mutant conditions. Number of embryos analyzed: *zyg-12(RNAi)*, n=10; *nop-1(RNAi)*, n=12; *zyg-12(ct350) nop-1(RNAi)*, n=11; *zyg-12(ct350) rho-1(RNAi)*, n=9. Quantification of centrosome separation rates and timing are reported in the Tables C.1, C.2 and C.3.

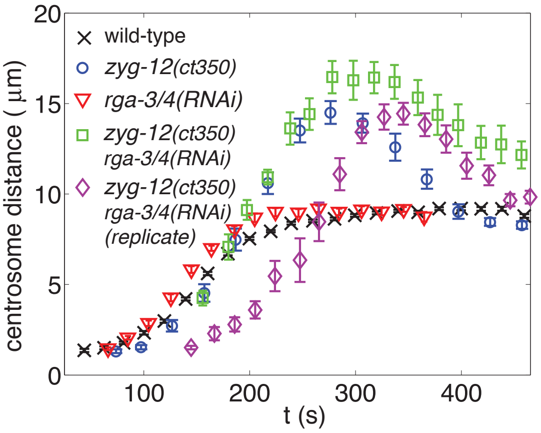

Figure 4.10 – **Centrosome separation in embryos enhanced of actomyosin contractility.** Average centrosome-centrosome distance with SEM as a function of time in the indicated RNAi/mutant conditions. Number of embryos analyzed: *rga-3/4(RNAi)*, n=13; *zyg-12(ct350) rga-3/4(RNAi)*, n=8; *zyg-12(ct350) rga-3/4(RNAi)* (replicate), n=10. Quantification of centrosome separation rates and timing are reported in the Tables C.1, C.2 and C.3.

Since reduced actomyosin contractility results in slower centrosome separation, we tested whether, conversely, enhanced contractility results in faster separation. To this end, we analyzed embryos in which the RHO-1 antagonists RGA-3/4 was depleted (Schonegg et al., 2007; Schmutz et al., 2007; Mayer et al., 2010) (Fig. 4.10 and Movie 8). Indeed, a slight (25% enhancement of centrosome separation rate was observed in *rga-3/4(RNAi)* embryos. Intriguingly, on the contrary, when RGA-3/4 is depleted together with nuclear dynein in *rga-3/4(RNAi) zyg-12(ct350)* embryos, centrosome separation rate is not affected. Nevertheless, in *rga-3/4(RNAi)* and *zyg-12(ct350) rga-3/4(RNAi)* embryos, the distance between centrosomes during the equilibrium phase (t > 250 s) is larger than in *zyg-12(ct350)*, potentially revealing the effect of stronger forces acting at that stage. Given the low number of embryos in *zyg-12(ct350) rga-3/4(RNAi)*, we repeated the experiment in the same conditions. Surprisingly, we found that in these additional *zyg-12(ct350) rga-3/4(RNAi)* embryos, centrosome separation onset is strongly delayed. This inconsistency between the two *zyg-12(ct350) rga-3/4(RNAi)* replicates will require further experiments to investigate the source of this difference. Taken together, RGA-3/4 depletion experiments indicate that higher actomyosin contractility does not simply result in increased centrosome separation rate. We will further analyze the effects of enhanced actomyosin contractility on centrosome separation in section 4.4.3, where we will quantify the dependency of centrosome separation velocity on that of cortical flows.

Overall, these results lead us to conclude that contractility of the actomyosin network is critical for centrosome separation and that even a partial reduction of actomyosin contractility can impact on the rate and timing of centrosome dynamics.

4.4 Dynein couples actomyosin cortical flow with centrosome separation

The observation that cortical dynein powers centrosome separation and that actomyosin contractility is necessary for this function lead us to propose a model in which centrosomes trigger the flow of the actomyosin network that moves away from them, thus imparting antero-directed forces to cortical dynein motors. These motors, when attached to astral microtubules, transmit the flow forces to centrosomes and power their separation. In this section, we will challenge this model by testing two of its key predictions.

4.4.1 Cortical dynein complexes flow together with the actomyosin network

If anteriorly-directed cortical actomyosin flows provide separation forces and if dynein serves as a coupling device to transmit these forces, then cortical dynein should exhibit similar flows to the cortical actomyosin network itself. To test this prediction of the coupling model, we used Particle Image Velocimetry to determine in the same embryos cortical flows of the actomyosin network using Lifeact::mKate2 and of dynein complexes using YFP::GPR-1 (Fig. 4.11A and Movie 9) (Mayer et al., 2010). As shown in Fig. 4.11B, these experiments revealed that, at each time point, the local flow of Lifeact::mKate2 strongly correlates with that of YFP::GPR-1. Likewise, the direction of the local flow vectors is extremely similar between the two fusion proteins (Fig. 4.11C). These findings are fully compatible with the notion that cortical dynein complexes are transported by actomyosin cortical flows.

4.4.2 Centrosome separation movements correlate locally with actomyosin cortical flows

We reasoned that if cortical dynein indeed serves as a coupling device to transmit forces generated by anteriorly-directed cortical actomyosin flows, then in the absence of nuclear dynein, the velocities of centrosome separation should correlate overall with those of cortical actomyosin flows. To test this prediction, we measured the velocities of centrosome separation and of cortical flows simultaneously using GFP::TAC-1 and GFP::NMY-2 in embryos depleted of nuclear dynein via *zyg-12(RNAi)* (Fig. 4.12A). We found that, at each time interval, centrosome separation velocities exhibit a mild, but significant, correlation with cortical flow velocities (Fig. 4.12B; $\rho = 0.17$; P = 0.03). Furthermore, we found a stronger correlation when average centrosome separation velocities and cortical flows are considered over the entire imaging period in each embryo (Fig. 4.12E; $\rho = 0.47$; P = 0.02).

We set out to further uncover the root of this correlation. We reasoned that since cortical flows are imaged at the surface of the ellipsoidal embryo which is closest to the lens, if the overall correlation results from the specific action of actomyosin cortical flows on centrosomes through cortical dynein and microtubules, then a stronger correlation with cortical flows should be observed for the centrosome that is the closest to the imaged cortical plane.

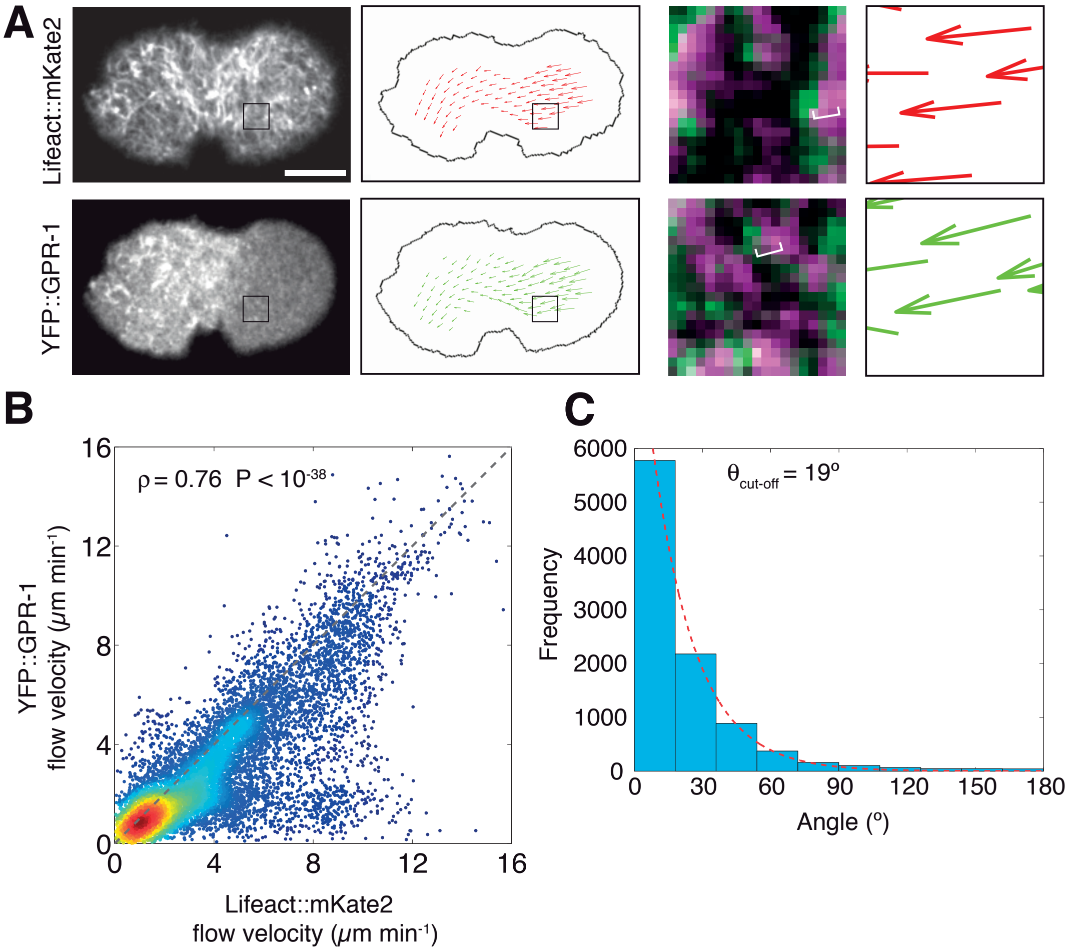

Figure 4.11 – **Correlated flows of cortical actomyosin network and cortical dynein anchors.** **A** Imaging and measurement of cortical flows of the actomyosin network (top, Lifeact::mKate2) and of cortical dynein anchors (bottom, YFP::GPR-1) during centrosome separation in the same embryo. A snapshot of cortical distribution is shown (left panel) together with the measured flow velocity field (right panel). Insets: two successive frames are superimposed (magenta and green, respectively), with brackets exemplifying protein enrichments that changed position between the two time frames. **B, C** Correlation of instantaneous local flows of Lifeact::mKate2 and YFP::GPR-1. **B** YFP::GPR-1 flow velocity is represented as a function of Lifeact::mKate2 flow velocity in the same position. Flow velocities are highly correlated (n = 10 embryos, 10 time-frames per embryo, Pearson correlation coefficient $\rho = 0.76$, P-value $< 10^{-38}$). **C** Distribution of angles between Lifeact::mKate2 and YFP::GPR-1 flow directions in the same data set. The angle distribution is peaked in $\theta = 0°$ and decays exponentially (cut-off angle 19°). The probability that two independent velocity fields result in the observed angle distribution is P-value $< 10^{-38}$. In this comparative analysis, we have excluded the flow vectors whose initial PIV window is partially outside the segmented embryo region, as represented in **A**, to minimize discrepancies in the flow fields due to detection errors (Material and Methods). However, identical conclusions can be reached when all the velocity vectors within the segmented embryo region are considered (correlation flow velocities $\rho = 0.61$, P-value $< 10^{-38}$; cut-off angle 25°).

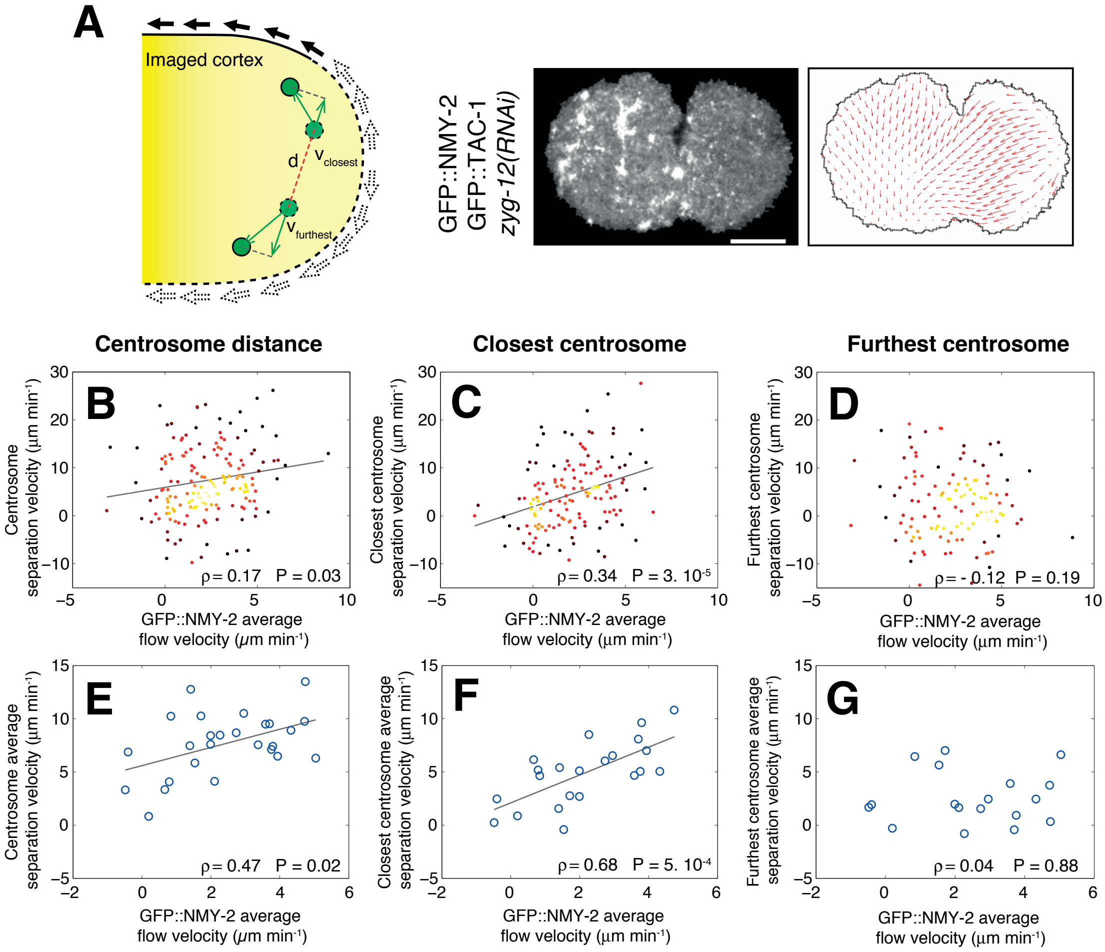

Figure 4.12 – **Actomyosin cortex flows correlate with separation movements of the closest centrosome. A** Schematic describing how the contribution of the movement of each centrosome to separation velocity was computed (left panel, see also Materials and Methods). Imaging and PIV-derived measurement of GFP::NMY-2 cortical flows (two right-most panels). **B, C, D** AP-directed velocities of the actomyosin cortical flow correlate with centrosome separation velocity measured at the same time (B, n = 28 embryos here and thereafter; Pearson correlation coefficient, $\rho = 0.17$, P = 0.03; one outlier data-point with cortical flow 11.6 μm min^{-1} and centrosome separation velocity 4.4 μm min^{-1} is not shown). Cortical flows correlates with the velocity of the separation movements of the closest centrosome measured at the same time (C, $n = 22, \rho = 0.34$, P = $3 \cdot 10^{-5}$), but not with those of the furthest centrosome (D, $n = 18$, $\rho = -0.12$, P = 0.19 (NS)). **E, F, G** Average posterior AP-directed cortical flows correlate well with average centrosome separation velocity (E, $n = 28$, $\rho = 0.47$, $P = 0.02$), even better with average separation movements of the closest centrosome (F, $n = 22$, $\rho = 0.68$, P = $5 \cdot 10^{-4}$), but not with the average separation movements of the furthest centrosome (G, $n = 18$, $\rho = 0.04$, $P = 0.88$ (NS)).

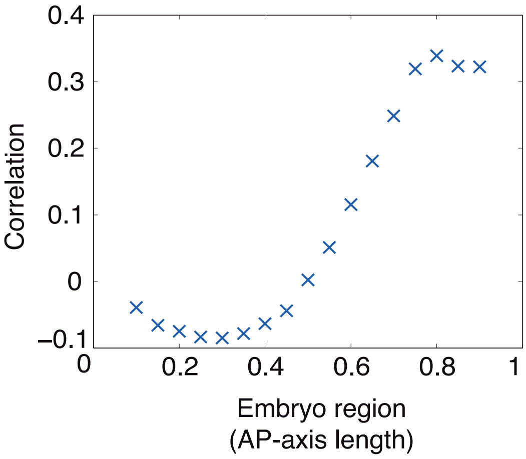

Figure 4.13 – **Separation movements of the closest centrosome correlate with flow of the closest region of the actomyosin cortex.** Correlation between separation movements of the closest centrosome to the imaged cortical plane and different regions along embryo length. The embryo regions are centered as indicated and span 20% of embryo length each.

To test this prediction, we measured separately the contributions of the two centrosomes to the separation process (Materials and Methods). Strikingly, this analysis revealed that at each time interval, local cortical flows are highly correlated with the movements of the closest centrosome (Fig. 4.12C; $\rho = 0.34$; $P = 3 \cdot 10^{-5}$), but not with those of the furthest one (Fig. 4.12D; $\rho = -0.12$; $P = 0.19$ (NS)). Furthermore, this differential correlation is even more pronounced when considering the averaged cortical flows and average centrosome movements in each embryo (Fig. 4.12F, G; closest; $\rho = 0.68$; $P = 5 \cdot 10^{-4}$; furthest: $\rho = 0.04$; $P = 0.88$ (NS)).

Moreover, we tested whether the slope and offset of this linear relationship is compatible with the model in which cortical flows power centrosome separation. Ideally, centrosome separation velocity should be similar or smaller than that of cortical flows (slope smaller or equal to 1) and be null in the absence of cortical flows (offset equal to zero). We found that the slope of the regression line is indeed compatible with such a model (Fig. 4.12C, regression line slope 95% confidence interval = $(0.7-1.8)$), even if this estimate is imprecise due to substantial variability of centrosome separation velocities between embryos and time-points. Moreover, the offset of the regression line predicts a small residual centrosome movement in the absence of cortical flows in the region considered for the correlation analysis (i.e. $70-90$% embryo length; regression line offset 95% confidence interval = $(0.3-3.5)\,\mu\text{m min}^{-1}$). We reasoned that such residual centrosome movement might reflect the impact of cortical flows situated in a more anterior region. Considering a larger region (i.e. $60-90$% embryo length) worsens the correlation between centrosome movement and cortical flow velocities, as expected (Fig. 5H), while remaining significant ($\rho = 0.30$;$P = 3 \cdot 10^{-4}$. Importantly, however, under these conditions the slope is compatible with unit (regression line slope 95% confidence interval = $(0.5-1.7)$) and the offset with zero (regression line offset 95% confidence interval = $(-1.0-3.3)\,\mu\text{m min}^{-1}$). We conclude that more distant flows provide a minor contribution to centrosome movements and are responsible for the slight offset noted when analyzing solely the region between 70 – 90% embryo length.

Another expectation of the coupling model is that the correlation between the cortical flows and the movements of the closest centrosome should be maximal in the vicinity of the centrosome as compared to elsewhere along the cortex, and we found this to be the case indeed (Fig. 4.13). Overall, this analysis demonstrates that the correlation between cortical flows and centrosome separation results from a local interaction between the actomyosin cortical flows and the nearby centrosome.

Taken together, these findings lead us to conclude that cortical dynein acts as a coupling device to transmit forces produced by anteriorly-directed actomyosin-dependent flows, thus ensuring robust centrosome separation.

4.4.3 Centrosome separation upon perturbation of cortical flow velocity

In the previous section, we have demonstrated that centrosome separation velocity correlates with the intensity of cortical flows. To reach this conclusion, we used the intrinsic variability of cortical flows in wild-type to compare the behavior correspondent to different cortical flow velocities (Fig. 4.12B, C, D). In order to extend the explored range of cortical flows and further challenge the validity of our model, we set out to, in turn, use RNAi to reduce or enhance actomyosin contractility (Fig. 4.14).

In order to reduce cortical contractility, we partially depleted RHO-1 by RNAi. Conversely, we increased cortical flows by depleting the RHO-1 antagonists RGA-3/4 (Schonegg et al., 2007; Schmutz et al., 2007; Mayer et al., 2010). As expected, we observed that average cortical flow intensity was reduced in *rho-1(RNAi)* embryos and increased in *rga-3/4(RNAi)* (Fig. 4.14A). Then, we measured the velocity of the separation movements of the closest centrosome (Fig. 4.14B). In *rho-1(RNAi)* embryos, the average movement velocity is decreased with respect to the wild-type, in agreement with the model in which separation velocity is proportional to the speed of cortical flows. Instead, centrosome separation velocity is not increased upon enhancement of cortical flows through *rga-3/4(RNAi)*, similarly to what was reported earlier in section 4.3. This data further indicates that a simple model in which centrosome separation velocity is proportional to cortical flows is not sufficient to explain centrosome separation for high flow velocities. To understand whether this non-linearity is in contradiction with our model of centrosome separation, in the next Chapter 5 (section 5.4) we will use a computational model that will allow to study centrosome separation in different conditions and also to address how separation velocity depends on cortical flow speed.

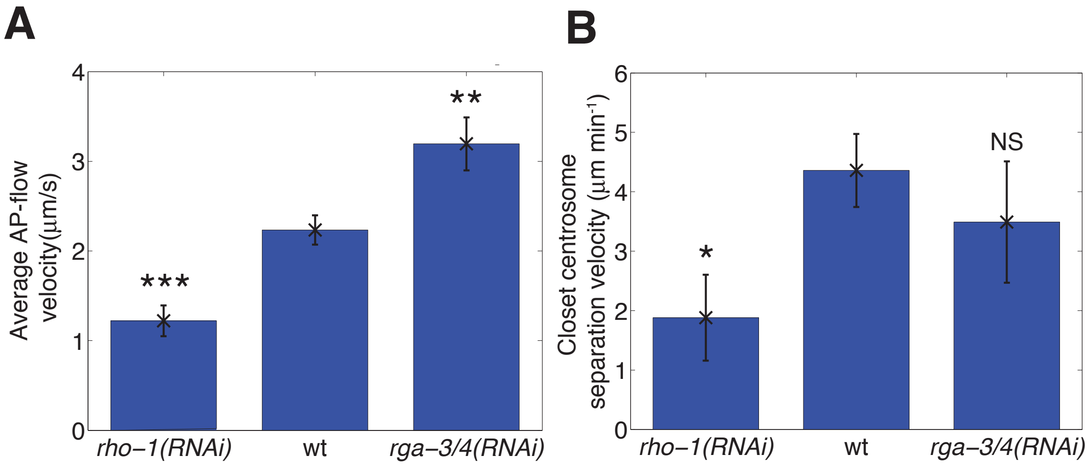

Figure 4.14 – **Separation movements of the closest centrosome upon perturbation of cortical flows. A** AP-directed average velocity (with SEM) of the actomyosin cortical flow measured in partial *rho-1(RNAi)* and *rga-3/4(RNAi)* embryos (t-test, *rho-1(RNAi)* P-value = $1 \cdot 10^{-4}$; *rga-3/4(RNAi)*: P-value = 0.003). **B** Average velocity (with SEM) of separation movements of the closest centrosome in partial *rho-1(RNAi)* and *rga-3/4(RNAi)* embryos (t-test, partial *rho-1(RNAi)*, n = 11 embryos, P = 0.01 ; *rga-3/4(RNAi)*: n = 10 embryos, P = 0.46 (NS)). The significance of the P-value is shown (t-test) (***: $P < 0.001$, **: $P < 0.01$, *: $P < 0.05$, NS (not significant): $P > 0.05$).

4.5 Working model

Overall, the results presented in this Chapter lead us to propose the following model of centrosome separation. At the end of meiosis II, centrosomes are located close to the cortex. The actomyosin network is homogeneously distributed and uniformly contractile. Centrosomes impart a symmetry-breaking cue that triggers a flow of the actomyosin network away from them and that will define embryo polarity. Indeed, this flow transports polarity proteins, such as PAR-3, PAR-6 and PKC-3, toward the embryo side opposite to the one where centrosomes are located. As a result, the side where centrosomes are located will become the posterior and the opposite side the anterior of the developing embryo. Importantly, cortical dynein, attached to the plasma membrane by the ternary complex comprising G_α, GPR-1/2 and LIN-5, is transported by the flow away from centrosomes. While flowing, cortical dynein can bind to microtubules, and thus transmit forces produced by the cortical flow and drive centrosome separation. At the same time, dynein is also attached to the nuclear envelope by the anchoring protein ZYG-12. Nuclear dynein pulls on microtubules and, in this way, holds centrosomes at the nuclear envelope and also contributes to power their separation.

In the next Chapter 5, we will develop a computational simulation of centrosome dynamics to address whether the model that we have presented here can explain quantitatively the features of centrosome separation that we have observed experimentally. Furthermore, this

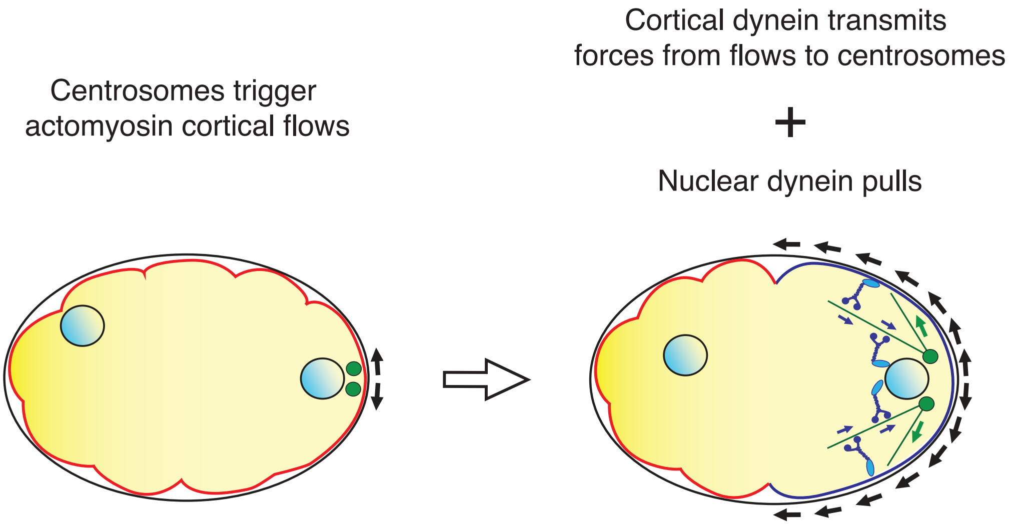
Centrosomes trigger actomyosin cortical flows
Cortical dynein transmits forces from flows to centrosomes
+
Nuclear dynein pulls

Figure 4.15 – **Working model of centrosome separation in the *C. elegans* one-cell stage embryo** At the end of meiosis II, centrosomes are located close to the cortex and the actomyosin network is homogeneous and contractile. Centrosomes trigger a flow of the actomyosin network that moves away from them and that will lead to cell polarization. The forces produced by this flow are transmitted to microtubules by cortical dynein and power centrosome separation. Meanwhile, nuclear dynein maintains centrosomes close to the nucleus and contributes to centrosome separation by pulling on microtubules.

computational model will be a powerful tool to predict centrosome behavior in additional experimental conditions and investigate the nature of the symmetry breaking mechanism that organizes forces to separate centrosomes.

4.6 Considerations on dynein motility

Our working model posits that dynein at the cortex and at the nuclear envelope together separate centrosomes. However, we have shown that centrosomes separate at an average speed in the order of $0.1\,\mu\text{m}\,\text{s}^{-1}$, which is an order of magnitude slower than the typical free velocity of dynein which is $1-2\,\mu\text{m}\,\text{s}^{-1}$ (reviewed in Howard, 2001). The computational model that we will present in the next Chapter 5 will allow us to address quantitatively whether this slower centrosome separation is compatible with dynein activity. Nevertheless, we can already get some insights regarding the cause of the slower centrosome separation from the following simple considerations on dynein motility.

Dynein motors exert forces on microtubules with a linear force-velocity relationship

$$F(v) = F_0\left(1 - \frac{v}{v_{\max}}\right) \qquad v > 0 \tag{4.1}$$

where F_0 is the stall force and $v_{\max}$ is the free velocity. When a dynein motor is bound to a cargo, it has to overcome the viscous drag exerted by the surrounding cytoplasm. If we approximate the cargo with a sphere of radius R, the viscous drag is

$$F = 6\pi\eta R v \tag{4.2}$$

where η is the viscosity in the cytoplasm. As a result, the motor will move with a speed

$$v = \frac{v_{\max}}{1+r} \tag{4.3}$$

and the applied force will be

$$F = F_0\left(1 - \frac{1}{1+r}\right) \tag{4.4}$$

where r is the dimensionless ratio

$$r = \frac{6\pi\mu R v_{\max}}{F_0} \tag{4.5}$$

Cytoplasm viscosity is several order of magnitudes higher than that of water ($\gamma \simeq 1\,\mathrm{Pa\,s}$ in the *C. elegans* embryo (Daniels et al., 2006)), so that, even for a small cargo, the drag force is high and the ratio r large. Indeed, assuming dynein free velocity to be $1.5\,\mu\mathrm{m\,s^{-1}}$ and stall force $2.5\,\mathrm{pN}$ (see Table D.1), already for a $1\,\mu\mathrm{m}$-sized cargo, such as a yolk granule, the ratio r reaches the value of 10. For $r \gg 1$, dynein motors exert the stall force F_0 and travel with the velocity

$$v \simeq \frac{v_{\max}}{r} = \frac{F_0}{6\pi\gamma R} \ll v_{\max} \tag{4.6}$$

Thus, the velocity of dynein motors is strongly reduced by the drag exerted on their cargo. When a single dynein motor binds to a microtubule, the force exerted on the centrosome is negligible, given the high drag of the microtubule aster. Therefore, in the case of nuclear dynein, centrosome movements are the result of the cooperative power exerted by a large number of motors. In fact, in such a high drag condition, dynein motors share the applied load and the total exerted force is the sum of the stall forces of each motor (Klumpp and Lipowsky, 2005). For example, in theory about 20 dynein motors are simultaneously needed to move a yolk granule of $1\,\mu\mathrm{m}$ diameter at the speed of $1\,\mu\mathrm{m\,s^{-1}}$. Thus, centrosome velocity depends on the net force acting on them and on the drag of the microtubule aster, while it is not related to dynein free velocity. Finally, in the case of cortical dynein, separation is powered by cortical flows and not by dynein motor activity in our model. Therefore, the velocity of the cortical flow is the upper limit of flow-driven centrosome separation velocity. Indeed, the maximum speed of cortical flows is in the order of magnitude of $0.1\,\mu\mathrm{m\,s^{-1}}$, thus similar to that of centrosome separation movements. In conclusion, our model is compatible with the observation that centrosome separation is an order of magnitude slower than free dynein velocity.

Part of the work presented in this Chapter was published in (De Simone et al., 2016).

5 Computational model of centrosome separation

In the previous chapter, we have proposed a model in which centrosome separation is driven by the combined action of dynein at the nuclear envelope and at the cortex, where the latter works as a force transmission device from the cortical actomyosin network to centrosomes. Even if we have reached a qualitative understanding of this model, some questions remain unanswered. Is the action of dynein on the nuclear envelope and as a cortical coupling device sufficient to drive centrosome separation? Can this mechanism explain quantitatively the observed centrosome separation dynamics? Are other mechanisms needed to trigger or sustain centrosome separation? What is the nature of the symmetry breaking mechanisms that ensure a persistent imbalance of forces produced by dynein motors to favor centrosome movement away from each other? Are additional symmetry breaking mechanisms needed to sustain centrosome separation? How is centrosome separation dependent on different factors such as motor concentration, cortical flow velocity and microtubule aster size?

To address these and related questions, we developed a computational model of centrosome separation in one-cell *C. elegans* embryos using the cytoskeleton simulation engine Cytosim (Nedelec and Foethke, 2007) (Fig. 5.1). We focused on the period prior to reaching equilibrium, thus not including the opposing and centering forces.

5.1 Description of the computational model

In the computational model, overdamped Langevin equations are used to describe the movements of microtubules and pronuclei in a viscous fluid in the presence of Brownian motion. Centrosomes are represented as two solid spheres that nucleate microtubules, which undergo dynamic instability with rates that depend on the applied force. Microtubules can interact with dynein motors located at the nuclear envelope and at the cell cortex.

A given density of dynein motors is evenly distributed on the pronuclear surfaces at a fixed position and nuclear motor numbers increases while the pronuclei grow, so that motor density is kept constant. To reduce computational time, only active cortical motors are simulated: when a microtubule reaches the cortex, motor binding occurs with a certain effective attachment rate that depends on the total cortical density of motors. If binding occurs, a cortical motor is created in the simulation and attached to the microtubule. When one motor detaches from the bound microtubule, it is deleted from the simulation. As in (Kozlowski et al., 2007), we assumed that the total number of cortical motors is in excess with respect to the fraction that is actively bound to microtubules, so that the cortical density of motors and thus their effective attachment rate are constant.

Both nuclear and cortical dynein motors move along bound microtubules and exert forces with a linear force-velocity relationship. Moreover, cortical motors flow towards the anterior, reflecting the effect of anteriorly-directed actomyosin contractions, with a velocity tangential to the cell cortex that increases linearly from the anterior to the posterior, as measured in (Mayer et al., 2010). All simulation parameters are set using measured values when possible or varied within a reasonable range (Table D.1).

5.2 Predictions of the computational model

In order to select the density of dynein motors at the nucleus and the effective attachment rate of the cortical motors, we performed a simultaneous fit by using the wild-type, *goa-1/gpa-16(RNAi)* and *zyg-12(ct350)* separation curves. Remarkably, by fitting these two parameters, we could obtain very good qualitative and quantitative agreement between the simulations and the experimental data. Thus, centrosomes separate with a pace comparable with that of wild-type in the presence of cortical and nuclear motors (Fig. 5.1A,B and Movie 10), undergo excess separation along the cortex in the absence of nuclear motors (Fig. 5.1 C,D and Movie 11) and separate in a delayed fashion in the absence of cortical motors (Fig. 5.1E,F and Movie 12).

We then addressed whether the parameter values thus selected could predict centrosome behavior in *zyg-12(ct350) goa-1/gpa-16(RNAi)*, *zyg-12(ct350) nmy-2(RNAi)* and *nmy-2(RNAi)* embryos, which were not used for the fitting. Importantly, we found that simulations of all these conditions indeed quantitatively predicted the observed behavior (Fig. 5.2). First, no separation occurs when nuclear motors are depleted together with cortical motors (Fig. 5.2A,B and Movie 13). Nuclear dynein is able to separate centrosomes in the absence of cortical flows, but, as expected, at a slower pace than in the wild-type (Fig. 5.2C,D and Movie 14). Finally and most importantly, the computational model shows that the forces exerted by cortical dynein are not able to drive centrosome separation on their own in the absence of cortical flows of the actomyosin network (Fig. 5.2E,F and Movie 15). Remarkably, in addition, we found that all the described features of centrosome separation in the computational model are robust to changes in motor densities at the nucleus and at the cortex (Fig. 5.3).

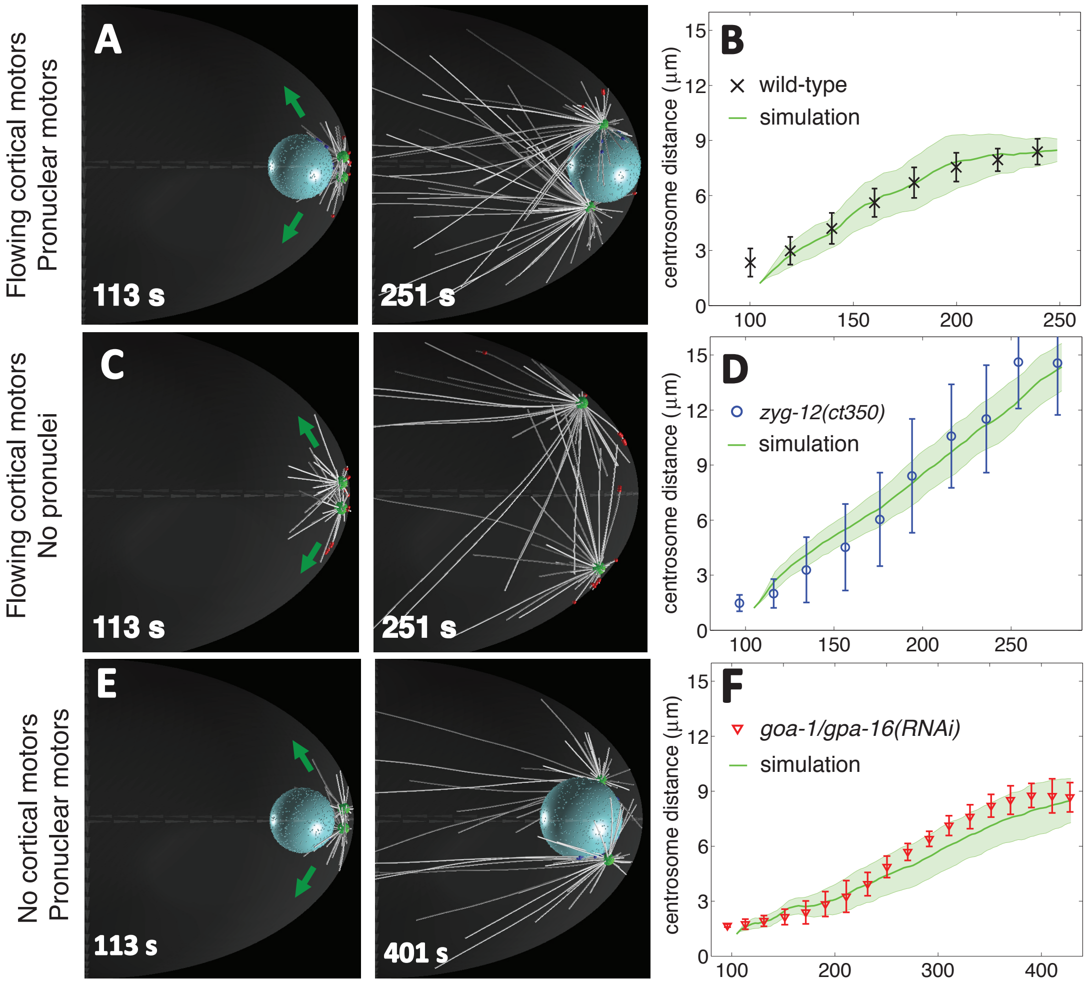

Figure 5.1 – **Computer simulation and fitting of centrosome separation. A, C, E** Snapshots from computer simulation of centrosome separation. Here and thereafter, nuclear dynein (blue dots), cortical dynein (red dots), pronuclei (blue spheres), centrosomes (green dots), microtubules (white lines) and cortex (light grey ellipse in transparence) are depicted. For visual clarity, inactive motors are not shown and only 1/4 microtubules are shown. Here and thereafter, the start of simulations corresponds to time = 104 s of the synchronized experimental dataset, which is roughly the start of the centrosome separation phase (see Fig. 3.2B). **B, D, F** Quantification of centrosome separation in computer simulations compared with experimental data from indicated RNAi/mutant conditions with SD. Green curves: average simulated centrosome-centrosome distance with SD (shaded error-bars, n=10) using the parameters given in Table D.1.

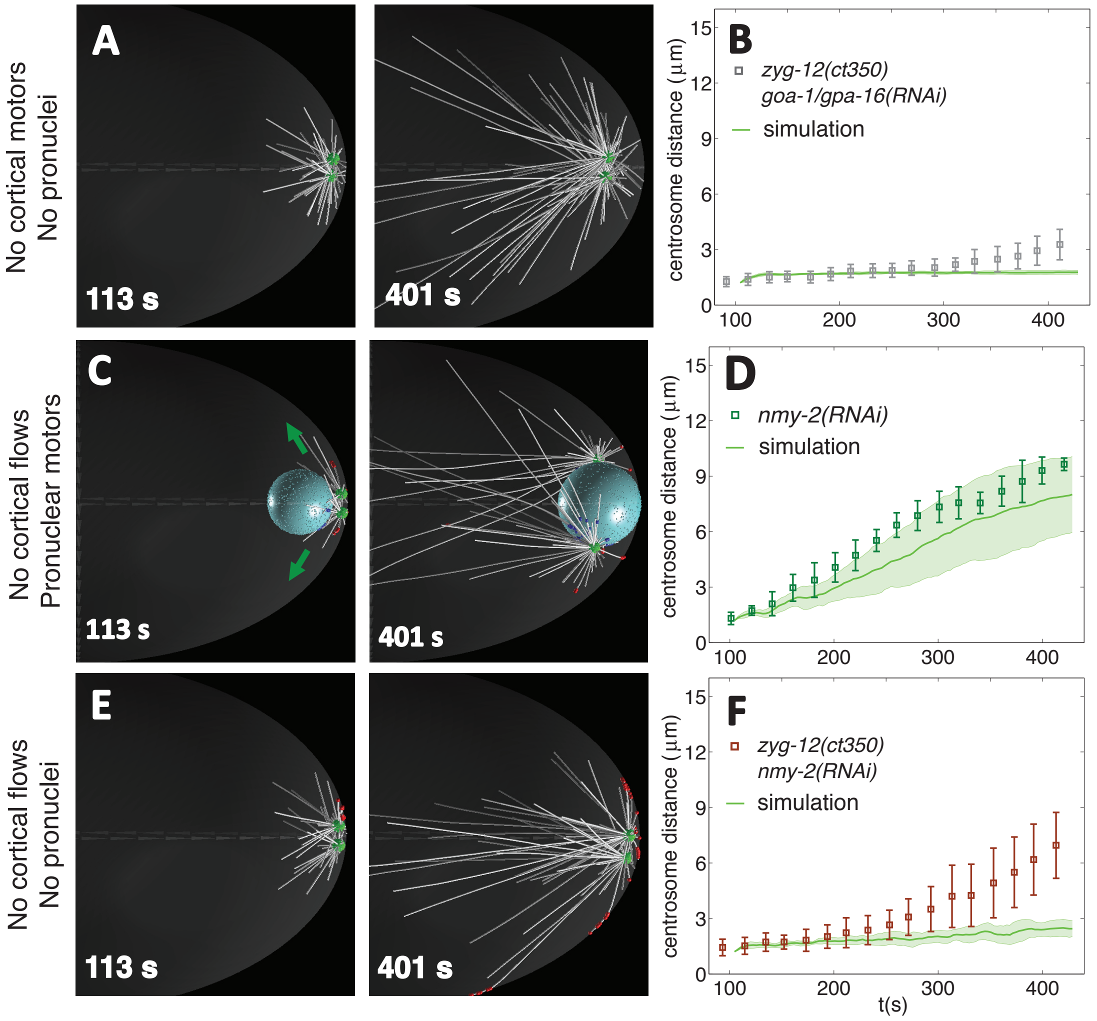

Figure 5.2 – **Computer simulation and validation of centrosome separation. A, C, E** Snapshots from computer simulation of centrosome separation. **B, D, F** Quantification of centrosome separation in computer simulations compared with experimental data from indicated RNAi/mutant conditions with SD. Green curves: average simulated centrosome-centrosome distance with SD (shaded error-bars, n=10) using the parameters given in Table D.1. Note that while centrosomes show residual separation velocity in *zyg-12(ct350) nmy-2(RNAi)* (see Fig. 4.8C,D), the computational model predicts that, in the absence of nuclear dynein and cortical flow, centrosome separation is completely impaired (panel F). See main text for a discussion of this point.

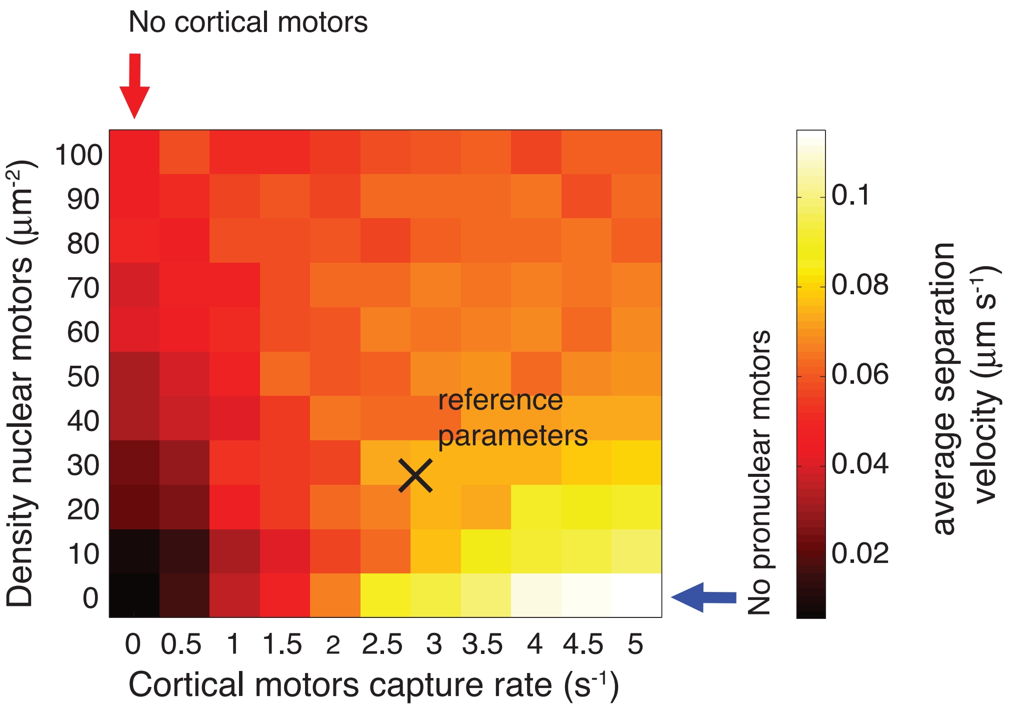

Figure 5.3 – **Computer simulations parameter sensitivity analysis**
Average centrosome separation velocity compared for different values of cortical motors attachment rate (x-axis) and motor density at the nuclear envelope (y-axis). The cortical motor attachment rate is an effective parameter that summarizes motor binding rate, binding range and density at the cortex. Each value is the mean of 10 independent simulations and the first 100 s of each simulation are considered. The black cross indicates the parameter values used in the reference simulations (Fig. 5.1A, B). The red and blue arrows indicate, respectively, cortical motor depletion (correspondent to *goa-1/gpa-16(RNAi)*) and pronuclear motor depletion (correspondent to *zyg-12(ct350)*).

As a further validation test, we addressed whether the computational model could predict the consequences of another condition that was not considered before. We thus chose to study centrosome separation upon reduction of the microtubule aster. To this end, we imaged embryos depleted of the XMAP215 family protein ZYG-9, which have smaller microtubule asters (Bellanger and Gönczy, 2003; Srayko et al., 2003; Le Bot et al., 2003) and found that centrosomes separate slower in *zyg-9(RNAi)* embryos (Fig. 5.4B and Movie 7).

Depletion of XMAP215 reduces microtubule aster size by reducing the rate of microtubule growth (Srayko et al., 2005) and potentially by enhancing microtubule catastrophe rate (Tournebize et al., 2000), but no measurement of the latter has been made in *C. elegans*. Therefore, we set microtubule growth rate to the reduced value measured in *zyg-9(RNAi)* embryos and microtubule catastrophe rate to a value from 2 to 5-fold larger then the one measured in the wild-type (Kozlowski et al., 2007). Strikingly, we found that, when growth rate is reduced and microtubule catastrophe rate is increased with respect to the wild-type, centrosome separation is predicted to be slower than in the wild-type, similarly to what observed in

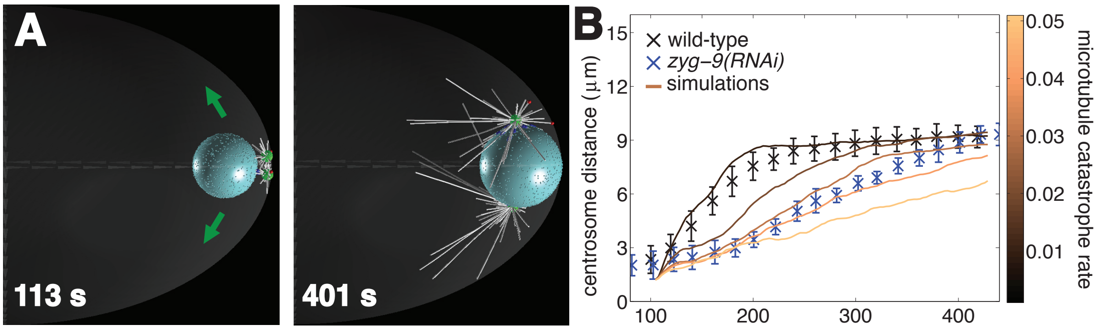

Smaller MT aster

Figure 5.4 – **Centrosome separation upon reduction of microtubule aster size** Centrosome separation upon reduction of microtubule aster size assessed by computer simulations (A) and experimentally in *zyg-9(RNAi)* embryos (B). In the simulations, microtubule aster size is reduced by decreasing microtubule growth rate to $v = 0.17\,\mu\mathrm{m\,s^{-1}}$ and by varying microtubule catastrophe rate as indicated. **A** Snapshots from computer simulation of centrosome separation upon reduction of aster size. Microtubule catastrophe rate is set to $0.03\,\mathrm{s^{-1}}$ (see B). **B** Quantifications of simulated centrosome separation upon reduction of aster size (color bar indicates cytoplasmic catastrophe rate for free microtubules - cortical and stalled catastrophe rates are varied accordingly - Table D.1). Each curve is the average of 10 independent simulations with the same parameters. The results of the simulations are compared with centrosome separation in *zyg-9(RNAi)* embryos (blue curve, n=10, SEM is indicated). Wild-type: black curve with SEM. Since the centrosomal GFP-TAC-1 signal is depleted in *zyg-9(RNAi)*, we tracked centrosome separation using GFP-AIR-1 for this condition.

zyg-9(RNAi) embryos (Fig. 5.4A, B).

Overall, we conclude that the computational model is a faithful and predictive representation of centrosome separation in one-cell stage *C. elegans* embryos, demonstrating that dynein acting as a motor on the nuclear envelope and as a cortical coupling device on the cortex is sufficient to explain centrosome separation.

5.3 The role of dynein motility in centrosome separation

Our analysis revealed that cortical dynein works as an anchor that transmits forces from cortical flows to separate centrosome. Nevertheless, it remains unclear whether binding of dynein to microtubules is sufficient to promote centrosome separation, or whether motor activity (i.e. motility) is needed in addition. Thus, we set out to use the computational model to address this question. First, as shown in Figure 5.5A, B, we found that rendering dynein non-motile prevents nuclear dynein-based centrosome separation, as anticipated. By contrast, we found that rendering dynein non-motile does not prevent cortical flow-based centrosome separation, although the process occurs at a slower pace than when dynein is motile (Fig. 5.5C, D). Such a partial impairment might reflect the fact that, normally, cortical dynein

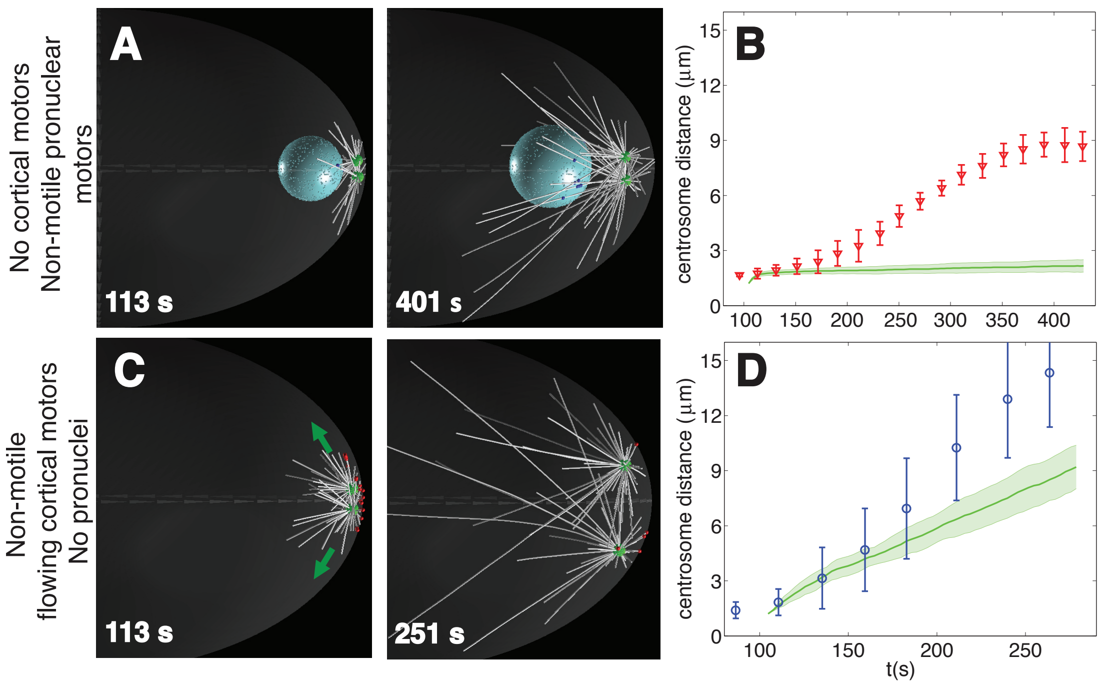

Figure 5.5 – **Computer simulations of centrosome dynamics upon impairment of nuclear and cortical dynein motility.** Centrosome dynamics is simulated in conditions in which either cortical or nuclear dynein are present, but their free velocity is null. **A, C** Snapshots from computer simulation of centrosome separation in indicated conditions. **B, D** Quantification of centrosome separation in computer simulations compared with experimental data from indicated RNAi/mutant conditions with SD. Green curves: average simulated centrosome-centrosome distance with SD (shaded error-bars, n = 10) using the optimal set of parameters (see Table D.1).

motility favors the capture of microtubules by pulling them toward the cortex. Together, the computational simulations suggest that dynein functions in centrosome separation both as a motor protein from the nuclear envelope and as a cross-linker from the cortex to transmit forces deployed by flows, a role that is facilitated by motor activity.

5.4 Impact of cortical flow velocity on centrosome separation

In the previous chapter, we have analyzed centrosome separation upon RNAi-mediated reduction or enhancement of cortical flow velocity and have observed that, while slower cortical flow correlates with a reduction of separation speed, surprisingly, faster cortical flows do not increase centrosome separation velocity. This result suggests that centrosome separation velocity is not simply linearly dependent on cortical flow velocity in the whole range of flow intensities, as initially supposed, but that it potentially saturates at a maximum separation velocity for fast flows. To verify whether this experimental observation is compatible with our quantitative model, we have simulated centrosome dynamics upon variation of cortical

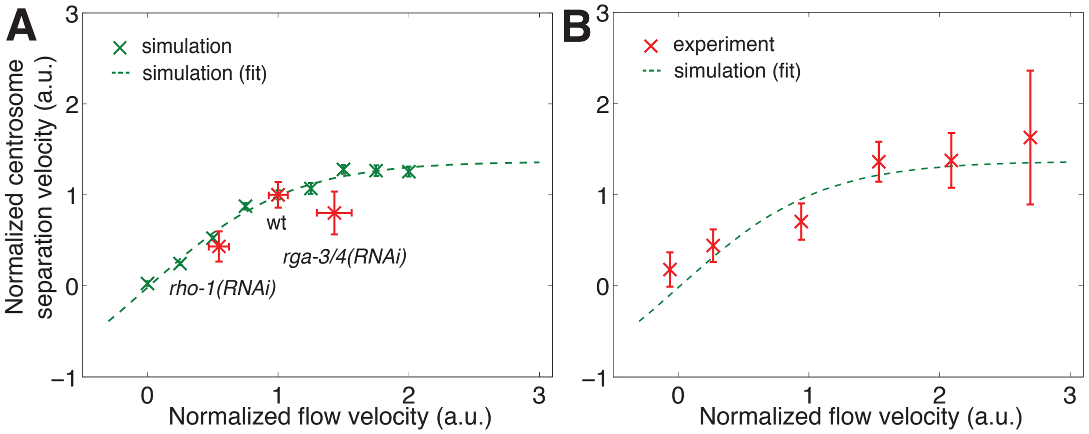

Figure 5.6 – **Centrosome separation upon variation of cortical flow speed.** **A** Simulated average centrosome separation speed for different flow velocities (in green, represented with SEM, average of 10 independent simulations) and fit with custom logistic function (see text, fit results with error (68% confidence bounds): $v_{\max} = 1.8 \pm 0.2$ and $r = 1.9 \pm 0.3$). The variation in centrosome separation velocity with respect to the wild-type in the indicated RNAi condition (closest centrosome, see 4.4.2) is compatible with the predictions of the computational model (z-test: *rho-1(RNAi)* P = 0.24 (NS); *rga-3/4(RNAi)* P = 0.10 (NS)). **B** Average centrosome separation speed as a function of average cortical flow speed for the whole dataset including *zyg-12(RNAi)*, *zyg-12(ct350) rga-3/4(RNAi)* and *zyg-12(ct350) rho-1(RNAi)*. The measured centrosome separation velocity curve is compatible with the predictions of the computational model (χ^2 test: P = 0.56 (NS)).

flows (Fig. 5.6A crosses). Strikingly, we found that the resulting centrosome separation velocity linearly increases for low and intermediate flow velocities, but saturates at a maximum speed for high flow velocities (> 150% of wild-type flow velocity). To test whether such predicted saturation can explain the experimentally measured separation velocity for fast flows, we extrapolated from simulation results the predicted separation velocity curve as a function of cortical flow velocity by fitting with the custom logistic function (Fig. 5.6A dashed line)

$$v_{\text{sep}}(v_{\text{flow}}) = \frac{v_{\max}}{(1 + e^{-r\,v_{\text{flow}}})} - \frac{v_{\max}}{2} \tag{5.1}$$

where $v_{\max}$ is the saturation velocity and r controls the slope of the linear region.

Strikingly, while the measured separation velocity in *rga-3/4(RNAi)* embryos is significantly different from the predictions of a linear model (z-test between average separation velocity in *rga-3/4(RNAi)* and linear approximation of Eq. (5.1) for slow flow $v \ll r^{-1}$: $P = 2 \cdot 10^{-5}$), it is compatible with the saturation curve predicted by the computational model (z-test: $P = 0.10$ (NS), Fig. 5.6A). As another means to test whether the experimentally measured velocity of separation scales with that of the flow as predicted by the computational model, we pooled together the measurements from *zyg-12(RNAi)*,*zyg-12(ct350) rho-1(RNAi)*, *zyg-12(ct350) rga-3/4(RNAi)* embryos and calculated the average centrosome separation velocity curve as a function of flow velocity. Importantly, the average centrosome separation curve shows saturation for high cortical flow velocities and is statistically compatible with the simulated behavior (χ^2-test: $P = 0.56$ (NS), Fig. 5.6B).

Overall, this analysis reveals that the saturation of centrosome separation that we measured in *rga-3/4(RNAi)* embryos is fully compatible with the model in which cortical flow powers centrosome separation by using cortical dynein as a force transmission device. Why does separation velocity saturate for fast cortical flows? A possibility is that, when flows are too fast, cortical motors detach quickly from their bound microtubules and thus are not able to exert a substantial total force (i.e. impulse). We will discuss a similar mechanism in Appendix B to explain the increase of cortical forces acting during centration/rotation in embryos with partially impaired actomyosin network. In the future, further simulations are required to verify that indeed cortical motor detachment limits the velocity of centrosome separation for fast flows. In addition, it will be necessary to consider in the computational model the variation of cortical tension resulting from RHO-1 or RGA-3/4 depletion by correspondingly modulating the stiffness of cortical motor attachment at the cortex ("cortical rigidity" in Table D.1). Finally, it will be useful to develop a minimal mathematical model of the total force generated by cortical flows on microtubules. Such an analytical model will complement our computational model by indicating how centrosome separation velocity depends on other quantities such as characteristic motor detachment force, cortical tension and microtubule catastrophe rate.

5.5 Partial dynein depletion

In the previous sections, we have shown that our computational model can be used to investigate how centrosome separation depends on microtubule aster size and on cortical flow velocity. A similar analysis can be performed to investigate the dependency of centrosome separation on all the features of the cytoskeleton that we have considered in our computational model (summarized in Table D.1). As an additional example, we have performed a preliminary analysis of how centrosome separation depends on dynein motor concentration. To perform this analysis, we simulated centrosome dynamics upon simultaneous reduction of cortical and nuclear dynein. As anticipated, centrosome separation progressively slows down for increasing levels of dynein depletion (Fig. 5.7A).

We tested experimentally this prediction by studying centrosome separation in conditions in which dynein function is partially depleted. Thus, we measured centrosome separation in embryos partially depleted of DHC-1 by RNAi (Fig. 5.7B). Unfortunately, in this condition centrosome separation curves are very heterogeneous and difficult to temporally align, potentially because of variable efficiency of DHC-1 depletion (data not shown). As a result, average centrosome separation in partial *dhc-1(RNAi)* is difficult to synchronize with wild-type and, therefore, it is not possible to compare the timing of onset of centrosome separation in the two conditions. In addition, in contrast with the prediction of our model, we observed that centrosome separation occurs at higher velocity in embryos partially depleted of dynein than in the wild-type. However, we cannot exclude that this faster rate is an artifact resulting from

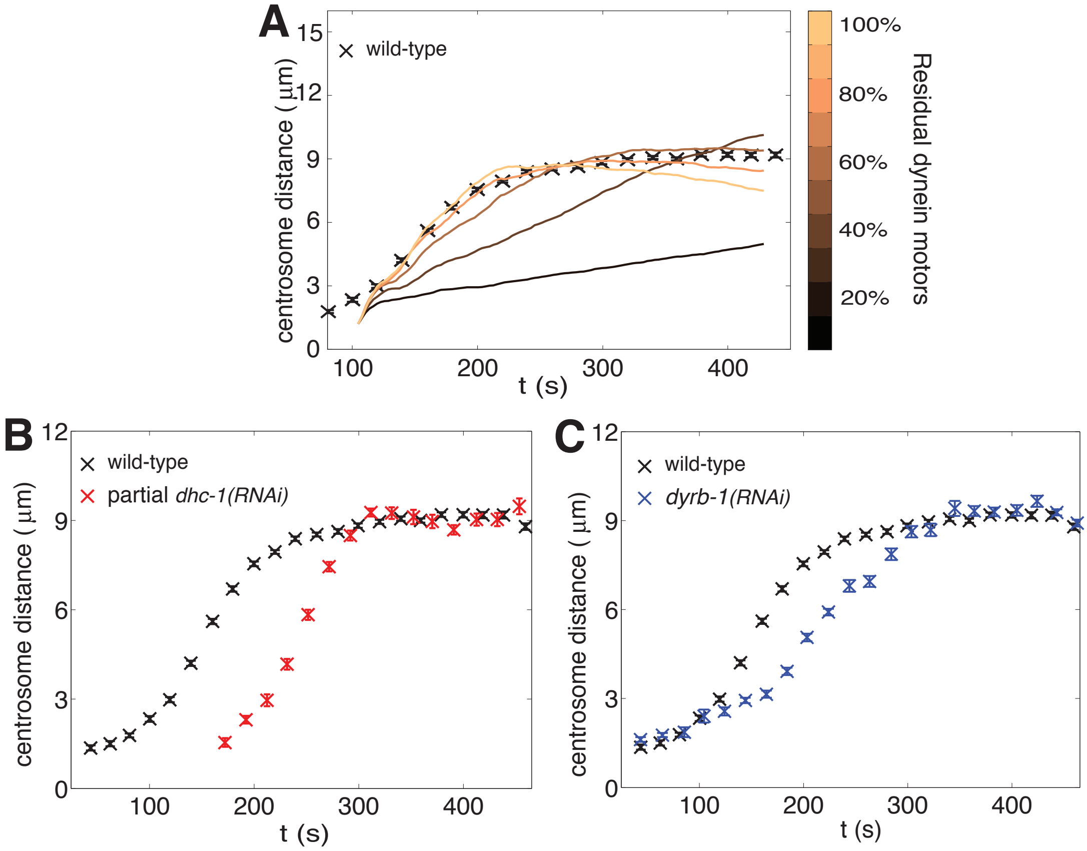

Figure 5.7 – **Centrosome separation upon partial dynein depletion**
A Simulation of centrosome separation upon joint partial depletion of dynein pools at the nuclear envelope and the cortex. Each curve is the average of n=10 simulations. **B** Centrosome separation upon partial *dhc-1(RNAi)* (6-8 hours) indicated with SEM (8 embryos analyzed). **C** Centrosome separation upon *dyrb-1(RNAi)* indicated with SEM (11 embryos analyzed).

the unreliable synchronization of partial *dhc-1(RNAi)* centrosome separation curves. However, assuming that centrosome separation indeed occurs faster in partial *dhc-1(RNAi)* embryos, a potential explanation of the discrepancy with respect to the prediction of our simulations is that cortical and nuclear anchors likely have different affinities for dynein. Thus, depleting the total dynein concentration could affect in different ways cortical and nuclear dynein, in contrast to our simulations that assumed that these two pools were depleted similarly. For example, we can imagine a situation in which the nuclear dynein pool is more sensitive to reductions of total dynein concentration than the cortical one. As a result, less force would hold centrosomes at the nuclear envelope and, therefore, cortical dynein might be able to separate them at a faster rate than when they are tightly bound to the nucleus.

As a complementary approach to generally slightly impair dynein function, we depleted the dynein light chain DYRB-1. DYRB-1 is an adapter protein that enhances dynein binding to cargos, such as vesicles, and to the LIN-5/GPR-1/2/G_α cortical complex. Thus, DYRB-1 depletion affects cortical dynein-dependent forces acting on astral microtubules and minus-end directed movements of cytoplasmic vesicles (O'Rourke et al., 2007; Couwenbergs et al., 2007; Kimura and Kimura, 2011b). Therefore, we depleted DYRB-1 by RNAi with the aim of partially reducing dynein function. In this condition, centrosome separation occurs at a slightly slower pace than in wild-type (~ 30%) (Fig. 5.7C), compatibly with the predictions of the computational model. However, the experimental centrosome separation curve differs in shape from the curve predicted by simulations (compare Fig. 5.7A and C). Such a difference could be due to a different impairment of cortical and nuclear dynein binding to their anchors upon DYRB-1 depletion, as discussed above for partial *dhc-1(RNAi)*. We conclude that partial dynein impairment through DYRB-1 depletion slows down centrosome separation, but that further experiments and simulations are required to understand to what extent each pool of dynein is impaired and how centrosome separation is consequently affected.

Part of the work presented in this Chapter was published in (De Simone et al., 2016).

6 Symmetry breaking mechanisms

We have demonstrated by using our computational model that cortical dynein powered by cortical flows, together with nuclear dynein, are able to drive centrosome separation without the need of any additional components. However, the nature of the symmetry breaking system that produces the force anisotropy that continuously drives centrosome outward movement during the separation process is still not clear. Since no additional mechanism is needed to organize forces anisotropically in our computational model, the breaking of symmetry of forces must somehow originate from interactions between microtubules, centrosomes, pronuclei and the cell cortex.

As we have discussed in the Introduction (section 1.4.5), the asymmetric organization of forces can originate from at least two different sources: an asymmetry in microtubule aster organization or an asymmetry in the distribution/activation of motors. In the case of aster asymmetry, microtubules are longer or denser in a certain direction and thus more motors can bind and exert forces in that direction. If, for example, microtubules are shorter in the region between centrosomes, then less force will be exerted toward that region and the force balance will favor outward centrosome movement. Similarly, in the case of motor asymmetry, motor distribution or activation is not homogeneous and therefore different forces are deployed in different directions. Analogously to the case of microtubule aster asymmetry, if for example dynein motors are depleted in the region between centrosomes, less forces are expected in that direction, thus resulting again in centrosomes moving away from each other.

In this chapter, we will investigate, by using our computational model, the nature of such symmetry breaking mechanisms in the case of the one-cell stage *C. elegans* embryo. We will consider separately the cases of cortical and nuclear dynein.

6.1 Nuclear dynein

The computational model has revealed that motors at the nuclear envelope can keep centrosomes on the surface of the nucleus and contribute to their separation. In this model, identical

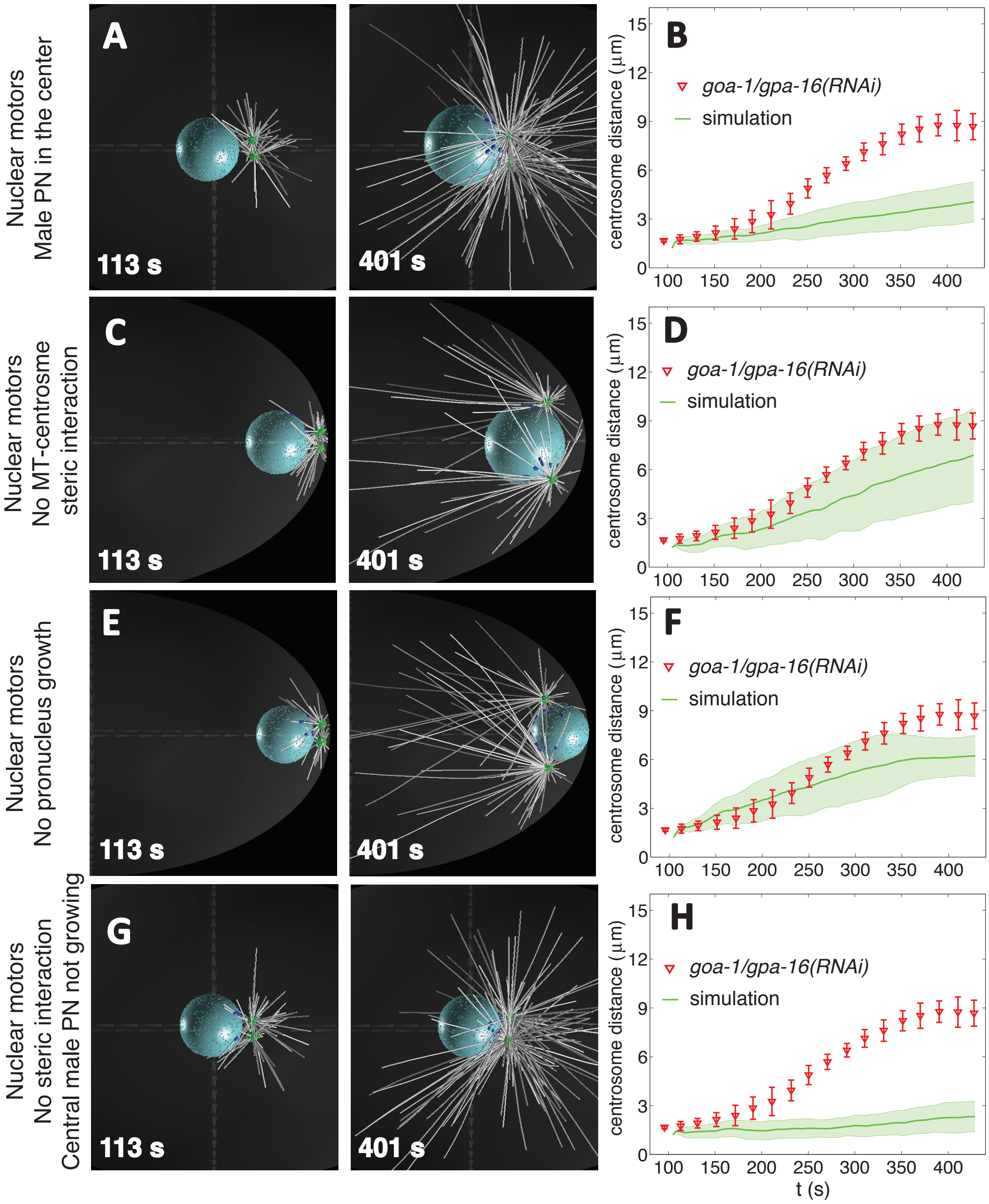
Nuclear motors
Male PN in the center
A
113 s
401 s
B
goa-1/gpa-16(RNAi)
simulation
centrosome distance (μm)
0
3
6
9
12
15
100
150
200
250
300
350
400
Nuclear motors
No MT-centrosome steric interaction
C
113 s
401 s
D
goa-1/gpa-16(RNAi)
simulation
Nuclear motors
No pronucleus growth
E
113 s
401 s
F
goa-1/gpa-16(RNAi)
simulation
Nuclear motors
No steric interaction
Central male PN not growing
G
113 s
401 s
H
goa-1/gpa-16(RNAi)
simulation
t (s)

dynein motors are distributed homogeneously on the surface of the pronuclei, reflecting the fact that dynein and the dynein anchor ZYG-12 appear to be enriched homogeneously at the nuclear envelope in the *C. elegans* embryo (Gönczy et al., 1999; Malone et al., 2003). Therefore, in our simulations the distribution/activation of dynein motors is symmetric and cannot organize forces asymmetrically.

Instead, the position of the centrosomes between the male pronucleus and the cell cortex on the posterior side of the embryo imposes a strong asymmetry in the organization of the microtubule aster. Indeed, because of this position, microtubules in the region between the two centrosomes encounter the posterior cell cortex and undergo catastrophes more often than those that are directed outward. Since longer microtubules grow in the outward direction, more nuclear dynein motors can exert forces on them (see for example 5.1C right panel). Thus, this asymmetry results in higher forces toward the outward direction. To test whether indeed the localization of centrosomes between the male pronucleus and the cortex is important for the force distribution asymmetry that leads to centrosome separation, we have simulated centrosome dynamics in an alternative situation where the male pronucleus, together with the attached centrosomes, is positioned in the center of the cell. Strikingly, we found that centrosome separation is strongly delayed in such a situation (Fig. 6.1A, B and Movie 17). Despite this strong slowing down, centrosome separation is not completely blocked, revealing the presence of additional symmetry breaking mechanisms.

A second potential contribution to aster asymmetry comes from the interaction between microtubules and the opposing centrosome. In this mechanism, microtubules originating from one centrosome and directed toward the opposing one will eventually collide with it and start pushing. Even if this force cannot separate centrosomes on its own, as demonstrated experimentally and theoretically by the joint depletion of nuclear and cortical dynein, it can trigger catastrophe of the colliding microtubules. As a result, microtubules will be depleted in the region between centrosomes, therefore leading to a slight aster asymmetry. To simulate

Figure 6.1 *(preceding page)* – **Computational analysis of symmetry breaking mechanisms: nuclear dynein.** Computer simulation of nuclear dynein-based centrosome separation in the absence of three potential symmetry breaking mechanism: position of the centrosomes between the male pronucleus and the posterior cortex, steric interaction between microtubules and centrosomes and anisotropic push imparted by the growth of the male pronucleus. **A, B** Centrosomes and male pronucleus are positioned in the cell center and not at the posterior pole. **C,D** No steric interaction between microtubules and opposing centrosomes. **E, F** The pronucleus does not grow in size. **G, H** Centrosomes and male pronucleus are positioned in the cell center, centrosomes do not interact sterically with microtubules and the pronucleus does not grow in size. **A, C, E, G** Snapshots from computer simulations of centrosome separation. **B, D, F, H** Quantifications of centrosome separation (with SD) in computer simulations is compared with experimental data from embryos depleted of cortical dynein by *goa-1/gpa-16(RNAi)*. Green curves: average simulated centrosome-centrosome distance with SD (shaded error-bars, n=10).

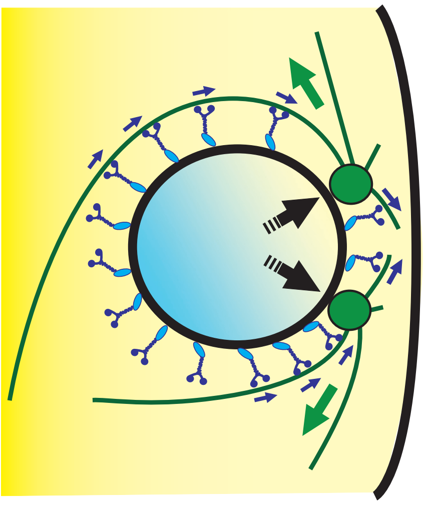

Figure 6.2 – **Schematics of symmetry breaking mechanism for nuclear dynein-based centrosome separation.** Microtubules growing between centrosomes are shorter than the ones oriented in the outward direction since they collide against the cortex and the opposing centrosome and thus undergo catastrophe. Therefore, the microtubule aster is asymmetric and nuclear dynein exerts stronger forces in the outward direction. In addition, the male pronucleus grows and thus pushes centrosomes apart (black dashed arrows).

the impact of this interaction on centrosome separation, we removed the steric interaction between microtubules and centrosomes in our simulation. In this case, centrosome separation is slightly reduced on average, but, more importantly, it becomes less robust, so that in a fraction of the cases (n = 3/10 simulations) it is strongly impaired, resulting in a large standard deviation of the average centrosome separation curve (Fig. 6.1C, D and Movie 18). Thus, the steric interaction between centrosomes and microtubules is not absolutely necessary for nuclear dynein-mediated centrosome separation, but it is important to guarantee its robustness. This may possibly indicate that steric interaction between microtubules and centrosomes contributes to the initial imbalance of forces that trigger centrosomes separation and that, once centrosomes are slightly apart, other symmetry breaking mechanisms can continue to separate them independently of this steric interaction. To test this hypothesis, further simulations in which centrosomes are initially slightly separated, but do not interact sterically with microtubules, are required.

An additional anisotropic contribution to the forces acting on centrosomes in the presence of nuclear dynein is imparted by the growth of the male pronucleus. Since centrosomes are attached to the nuclear envelope, the male pronucleus, while growing in size, pushes them apart. Such force depends on nuclear dynein binding to hold centrosomes at the pronucleus, but is powered by pronucleus growth and is intrinsically directed to move centrosomes away from each other. To test the impact of pronucleus growth on centrosome separation, we simulated centrosome dynamics in a situation where the male pronucleus has a constant size. In this case, centrosome separation is slightly slowed down with respect to the case in which the pronuclues grows (Fig. 6.1E, F and Movie 19).

Finally, we set out to test whether these three contributions, i.e. the position of the centrosome-pronuclei complex, the steric interaction between microtubules and centrosomes and the anisotropic push imparted by the growing male pronucleus, are together sufficient to explain the force asymmetry that leads to centrosome separation powered by nuclear dynein. To this end, we simulated centrosome dynamics in a condition where non steric-centrosomes are positioned in the center of the cell in the vicinity of a male pronucleus that does not increase in size. In this case, centrosome separation is almost completely impaired (Fig. 6.1G, H and Movie 20).

Overall, this analysis demonstrates that centrosome position and microtubule-centrosome steric interaction organize asymmetrically the microtubule aster, so that length-dependent nuclear dynein forces are imbalanced toward the outward direction (Fig. 6.2). In addition to these two mechanisms that break the symmetry of forces exerted by nuclear dynein, in the third mechanism nuclear dynein does not generate the separating force, but it is necessary to anchor centrosomes at the nuclear envelope so that they can receive the push imparted by the growth of the male pronucleus, which is intrinsically directed in the outward direction (Fig. 6.2 black arrows).

6.2 Cortical dynein

Cortical dynein can exert forces by pulling on the microtubules plus-end. In our simulation, cortical motors are distributed homogeneously, therefore cortical dynein forces are isotropic, balance each other and thus are not able to drive centrosome separation in the absence of nuclear dynein. Indeed, simulations demonstrate that cortical dynein does not separate centrosomes unless a a cortical flow is introduced (see Fig. 5.2F). Interestingly, even if the microtubule aster is slightly asymmetric because of catastrophes induced by the push of microtubules against the opposing centrosome, as mentioned above this asymmetry alone is not sufficient to imbalance the force produced by cortical dynein motor activity to drive centrosome separation (Fig. 5.2F).

Instead, the symmetry breaking mechanism imparted by cortical dynein has a different root. As mentioned earlier, cortical dynein transmits to the bound microtubules forces that are produced by the actomyosin cortical flow and that are intrinsically directed to move centrosomes away from each other. Indeed, centrosomes trigger the actomyosin flow which, as a result, is always directed away from them (Goldstein and Hird, 1996; Bienkowska and Cowan, 2012). This cortical flow transports cortical dynein motors that, while flowing, pull microtubules bound to them in the outward direction. Therefore, the forces produced by the cortical flow are intrinsically directed to move centrosomes in opposite directions. Thus, this remarkable mechanism guarantees robust centrosome separation independently of their position along the cell cortex.

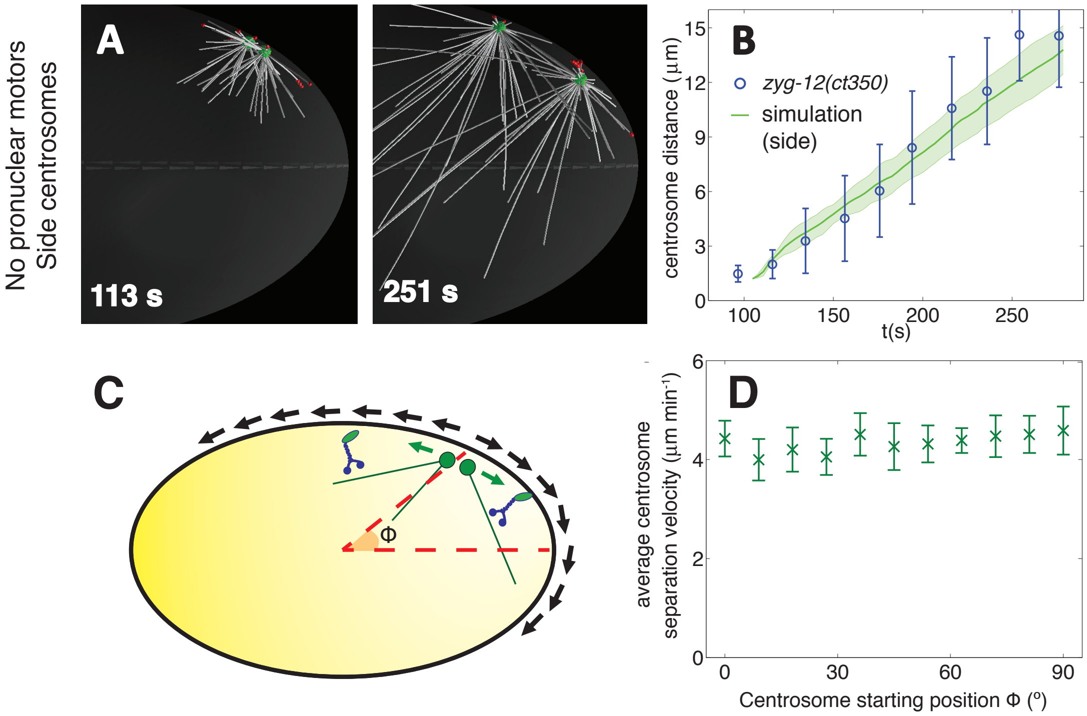

Figure 6.3 – **Computational analysis of symmetry breaking mechanisms: cortical dynein**
A, B Computer simulation of cortical dynein-based centrosome separation when centrosomes are at a lateral position along the cell cortex. **A** Snapshots from computer simulation of centrosome separation. **B** Quantification of cortical dynein-based centrosome separation when centrosomes are at a lateral position along the cell cortex. Simulation results are depicted with SD (shaded error-bars, n=10) and compared with experimental data for *zyg-12(ct350)* (with SD). The simulation parameters are given in Table D.1. **C, D** Computer simulation of cortical dynein-based centrosome separation for centrosomes located in different positions along the cell cortex characterized by the angle ϕ measured from the AP-axis (illustrated in C). In D, the average simulated centrosome separation velocity is compared for different starting positions along the cell cortex (each value is the mean of 10 independent simulations with SD, shaded error-bars).

To test whether cortical dynein can indeed separate centrosomes even when they are at a different cortical position than the posterior pole, we simulated centrosome dynamics in this condition. In this case, we implemented the flow pattern so that it moves away from the centrosomes midpoint (Materials and Methods), as it has been previously documented experimentally (Goldstein and Hird, 1996). Strikingly, this analysis revealed that cortical dynein powered by cortical flows can indeed separate centrosomes independently of their position along the cell cortex (Fig. 6.3A, B and Movie 21), and this with the same pace as in the wild-type (Fig. 6.3B, D). We conclude that this mechanism does not require any additional components to ensure symmetry-breaking and, thus, robust centrosome separation.

In conclusion, this computational analysis has revealed that the main contributors that organize the forces acting on centrosomes asymmetrically are the asymmetric shape of the microtubule aster, resulting from the position of centrosomes between the male pronucleus and the cortex, and the pattern of the actomyosin flow . Such microtubule aster asymmetry results in stronger forces exerted by nuclear dynein in the outward direction and thus centrosome separation (Fig. 6.2). Instead, cortical dynein separates centrosomes by harnessing the forces produces by the flows of the actomyosin network, which are intrinsically directed in the outward direction (Fig. 6.3C).

6.3 Centrosomes and the control of cortical flow pattern

In the previous section, we have shown that cortical dynein-mediated forces can separate centrosomes thanks to the pattern of actomyosin flows and that this separation does not require any direct interaction between centrosomes. Nevertheless, one centrosome could contribute to determine the forces acting on the other by influencing how the pattern of the actomyosin flow is organized. Indeed, if centrosomes continuously control the origin of the flows even after they have started separating, for example imposing the origin at the midpoint between them, then the flow pattern continuously depend on their positions. In this case, the position of one centrosome affects the forces acting on the other by influencing the position of the origin, and therefore the spatial organization, of the flows. By contrast, if the origin of the flow is imposed by centrosomes before their separation and thereafter the flow proceeds independently of where they are positioned, then each centrosome moves independently and is not affected by the position of the other.

In embryos in which two centrosomes are present, as is the case in wild-type or in *zyg-12(ct350)*, the centrosomes behave in a similar way in these two scenarios, since they move on average symmetrically away from each other; therefore, their midpoint along the cortex remains stationary at the starting point of separation. As a result, in both cases, the flow origin is stable at the embryo posterior (compare 6.3D (first scenario) and 5.1D (second scenario)).

Interestingly, centrosome movements should differ strikingly in these two scenarios if there is a single centrosome instead of two, as for example in mutants defective in a centriole assembly gene such as or *zyg-1* or *sas-5* (O'Connell et al., 1998; Delattre et al., 2004). The computational model predicts that, if the flow origin is continuously positioned in the vicinity of the single centrosome, as a result the forces exerted by the flow balance each other in every direction. Thus, the single centrosome will move stochastically close to the posterior, but will not be transported away along the cortex (Fig. 6.4 A, B and Movie 22). By contrast, in the second scenario, the cortical flow proceeds independently of centrosome position after the initial trigger. Therefore, if the single centrosome moves stochastically away from the posterior pole in a certain direction, then it will be transported away by the flow in that direction, similarly to the case in which two centrosomes are present (Fig. 6.4C, D and Movie 23).

Therefore, by studying centrosome dynamics in embryos with a single centrosome, we should

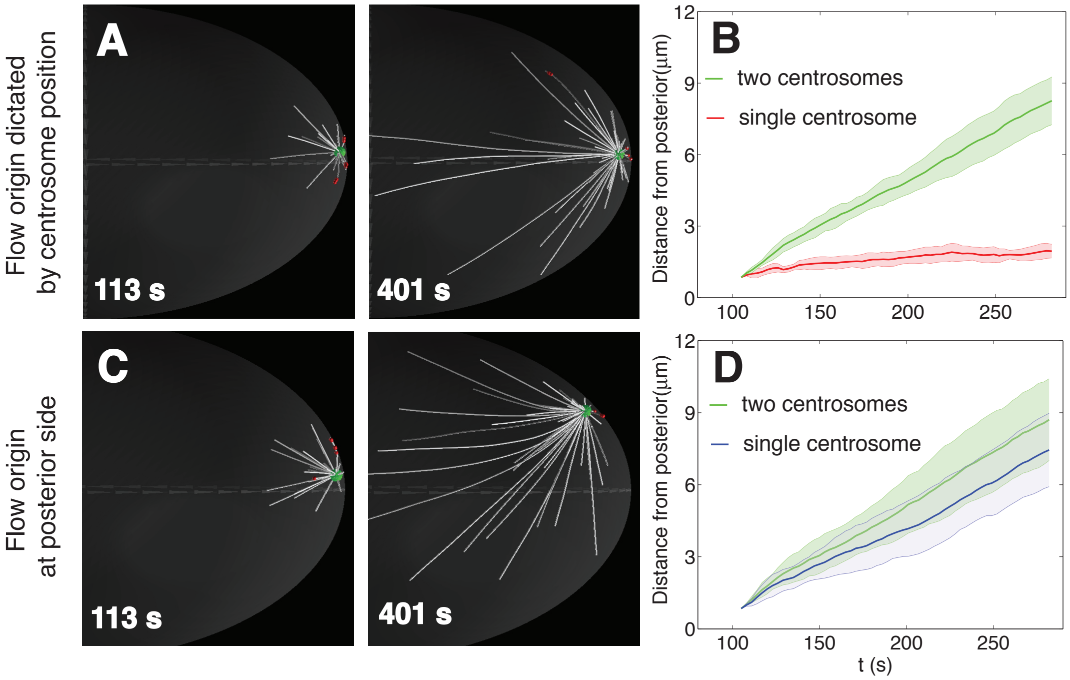

Figure 6.4 – **Computer simulation of the dynamics of a single centrosome. A, B** Computer simulation of cortical dynein-based centrosome movements when the flow origin follows centrosome position. **C, D** Computer simulation of cortical dynein-based centrosome movements of a single centrosome when the flow origin is fixed at the posterior side of the embryo. **A, C** Snapshots from computer simulation of single centrosome dynamics. **B, D** Comparison of total traveled distance for the cases with one or two centrosomes. Simulation results are depicted with SD (shaded error-bars, n=10). The simulation parameters are given in Table D.1.

be able to obtain interesting insights on the mechanism by which centrosomes organize the pattern of actomyosin cortical flow that, in turn, drives centrosome separation through cortical dynein. We have already conducted a preliminary analysis in this direction by studying *sas-5(t2079) zyg-12(ct350)* embryos that harbor a single centrosome (data not shown). In these embryos, the single centrosome was not moving along the cortex, but was staying at the posterior pole until centrosome centration. Unfortunately, in these embryos, actomyosin flow was also impaired, so that it was possible that the lack of centrosome movement along the cortex was due to the impairment of cortical flows. The impairment of actomyosin contractility could be due to a potential reduction of the centrosomal signal that triggers the actomyosin flow, deriving from the presence of a single centrosome, instead of two. Additional simulations are required to test the effect of impaired actomyosin contractility on the movements of a single centrosome. On the experimental side, the dynamics of a single centrosome should be investigated in embryos in which the actomyosin flow is not reduced. For example, actomyosin contractility could be rescued to wild-type levels in *sas-5(t2079)* embryos by depleting the contractility inhibitor RGA-3/4 (Schonegg et al., 2007; Schmutz et al., 2007). Alternatively, we could enhance centrosome size, for example by depleting SZY-20 (Song et al., 2008), aiming at increasing the levels of the centrosomal cue that triggers the actomyosin flow. In addition, we could analyze centrosome movements in conditions in which two centrosomes are presented, but cannot disengage, as in embryos depleted of the separase homologue SEP-1 (Cabral et al., 2013).

6.4 KLP-7: a potential external symmetry breaking mechanism

We have demonstrated computationally that aster geometry and flow organization are sufficient to organize forces to drive centrosome separation and that an additional external symmetry breaking mechanism is not necessary. However, it is possible that additional symmetry breaking mechanisms are present in the embryo to ensure robust centrosome separation. For example, molecular regulation of aster organization, dynein distribution or activation could contribute to imbalance the forces applied on each centrosomes and favor their separation.

The depolymerizing kinesin KLP-7 is an attractive example of this possibility. KLP-7 is the unique *C. elegans* member of the Kinesin-13/MCAK family that promotes microtubule depolymerization in other systems (reviewed in Ems-McClung and Walczak, 2010). During mitosis, kinesin-13 has multiple roles, including promoting amphitelic kinetochore-microtubule attachments, but it also have an established, yet not fully understood, role in the assembly of the bipolar spindle (reviewed in Ems-McClung and Walczak, 2010). For example, MCAK depletion in *Xenopus egg* extracts strongly increases monopolar spindles (Zhang et al., 2007). In mammalian cells, whereas MCAK RNAi does not prevent bipolar spindle formation, the depletion of Kif2a and Kif2b, two other members of the kinesin-13 family, leads to the formation of monopolar spindles (Manning et al., 2007). In the early *C. elegans* embryo, KLP-7 is enriched at kinetochores and centrosomes and limits the number of nucleated microtubules, probably by triggering catastrophe of microtubule tips before they grow out of the centrosome (Oegema et al., 2001; Srayko et al., 2005).

Given the above considerations, KLP-7 could promote centrosome separation by regulating microtubule aster asymmetry: when a microtubule originating from a centrosome approaches the opposing centrosome, the KLP-7 pool could favour microtubule catastrophe, thus leading to depletion of microtubules in the intra-centrosomal region. Such an asymmetry would then result in more length-dependent forces in the outer direction and thus centrosome separation.

To test this hypothesis, we have measured centrosome dynamics in *zyg-12(ct350) klp-7(RNAi)* embryos. In this case, centrosome separation is slightly slower than for the sole nuclear dynein depletion by *zyg-12(ct350)* and reaches a smaller maximum separation (Fig. 6.5). Unfortunately, KLP-7 depletion also results in a reduction of microtubule growth rate, potentially due to depletion of free tubulin, consumed by the excess number of microtubules (Srayko et al., 2005). Thus, we cannot distinguish whether slower centrosome separation is due to the lack of a KLP-7-mediated symmetry breaking mechanism or to slower microtubule growth, which can potentially result in a smaller aster size.

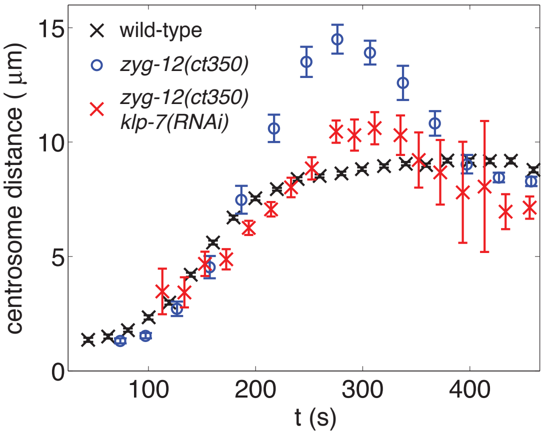

Figure 6.5 – **Centrosome separation upon depletion of the depolymerizing kinesin KLP-7** Average centrosome-centrosome distance with SEM as a function of time in the indicated RNAi/mutant conditions. Number of embryos analyzed: *zyg-12(ct350) klp-7(RNAi)*, n=7. Quantification of centrosome separation rates and timing are reported in the Tables C.1, C.2 and C.3.*zyg-12(ct350) klp-7(RNAi)* experiments have been performed together with Matthias Größner and Marc Salm ("La Science appelle les Jeunes" Program).

7 Discussion

Centrosome separation must be regulated in time and space to ensure faithful chromosome segregation (Silkworth et al., 2012). In particular, centrosomes must be completely separated during prophase to avoid error-prone chromosome segregation in mammalian cells (Silkworth et al., 2012). Previous work established that dynein is essential for, or contributes to, centrosome separation in a broad range of organisms, including *C. elegans*, *D. melanogaster* and *H. sapiens* (reviewed in Tanenbaum and Medema, 2010). However, where in the cell and through which mechanisms dynein is required for this process in a physiological context was unclear from prior work. In this thesis, by selectively removing dynein from the nucleus or from the cortex, we teased apart the distinct functions of these two pools of dynein in promoting centrosome separation. By combining these experimental interrogations with computer simulations, we developed a model that explains how these two pools of dynein together separate centrosomes in the developing *C. elegans* embryo.

7.1 Overview of results

As a first step, we have developed a method to quantitatively measure centrosome separation. In this method, we imaged prophase one-cell stage embryos expressing the centrosomal marker GFP-TAC-1 in 3D at high spatial and temporal resolution. Then, we tracked centrosomes and pronuclei using automated image processing. We calculated centrosome distance as a measure of centrosome separation and synchronized different embryos by maximizing the overlap of their centrosome distance curves. We find that average centrosome separation shows three phases: an initial onset phase when centrosome separation starts, an intermediate phase when most of the separation occurs and a final equilibrium phase when centrosome separation stops.

Interestingly, in the final equilibrium phase, separation does not stop because centrosomes have reached their maximum distance at opposite poles of the male pronucleus. Instead, centrosomes stop at an average angle of ~ 134°. To understand how this equilibrium angle is maintained, we have calculated the net forces acting on centrosomes by using a diffusion-advection mathematical model. This comparison suggests that two pools of forces balance each other and maintain centrosomes at the equilibrium angle: one that separates centrosomes and another that opposes centrosome separation.

After having analyzed the equilibrium phase, we investigated the drivers of centrosome separation in the intermediate phase when most of separation occurs. To dissect the underlying mechanisms, we have removed dynein from the nucleus and/or from the cortex and measured the pace and path of centrosome separation in the different cases. These experiments demonstrate that nuclear and cortical dynein cooperate to separate centrosomes. In particular, when nuclear dynein is depleted, centrosomes detach from the male pronucleus and undergo excess separation along the cortex, driven by cortical dynein. When cortical dynein is depleted together with nuclear dynein, centrosome separation is completely impaired.

Concomitant with centrosome separation, the actomyosin cortex flows from the posterior pole of the embryo where centrosomes are located toward the anterior side, a process that will lead to cell polarization. Since centrosomes separate while moving along the cortex when nuclear dynein is depleted, we tested whether this actomyosin anterograde flow is involved in centrosome movement. Strikingly, in the absence of actomyosin contractility, we found that centrosomes do not undergo cortical dynein-driven excess separation along the cortex. These experiments lead us to propose that cortical dynein acts by transmitting to centrosomes forces produced by the flow of the actomyosin network. We challenged this model by testing two of its key predictions. First, we demonstrated that cortical dynein complexes flow toward the anterior together with the actomyosin flow. Second, we demonstrated that centrosome separation velocity correlates with cortical flow velocity. More specifically, we showed that flows in the most posterior part of the cortex interact locally with the centrosome located closest to it, thus driving its separation movements.

After having delineated these aspects of centrosome separation, we set out to develop a computational model of centrosome dynamics to assess whether it can explain quantitatively the features of centrosome separation we have observed. The computational model has two parameters that are unknown, the density of motors at the nuclear envelope and at the cortex, which were fitted by using the data of centrosome separation in wild-type and upon nuclear or cortical dynein depletion. Remarkably, the computational model could predict the observed separation behavior qualitatively and quantitatively for all the considered experimental conditions, including those not used in the fitting procedure.

The computational model demonstrated that nuclear and cortical dynein together with cortical flows are sufficient to quantitatively explain the observed centrosome separation dynamics. Therefore, the symmetry breaking mechanism that organizes the forces acting on centrosome to move them in opposite directions must result from the interaction between centrosomes, microtubules, pronuclei and cortex. We investigated the source of this symmetry breaking mechanism by using the computational model. We could demonstrate that, in the case of nuclear dynein, since centrosomes are positioned between the male pronucleus and the cortex, microtubule asters grows asymmetrically and have shorter microtubules in the region between centrosomes. As a result, stronger forces are exerted in the outward direction. Regarding the case of cortical dynein, the pattern of the actomyosin flow is always directed away from centrosomes and therefore intrinsically favors their movements in the outward direction.

In conclusion, our work has demonstrated that centrosome separation is driven by nuclear dynein together with cortical dynein, with the latter harnessing forces produced by the actomyosin cortical flows. These two mechanisms rely on cell geometry and on cortical flow pattern to move centrosomes in opposite directions. We developed a 3D computational model that recapitulates quantitatively the features of centrosome separation, which has predictive power and that can be used to further investigate centrosome dynamics in the one-cell stage *C. elegans* embryo.

7.2 Cortical dynein as a novel coupling device

Dynein anchored at the cell cortex exerts pulling forces on astral microtubules in several systems, including during spindle positioning in fungi, worms and human cells (reviewed in Kotak and Gönczy, 2013). Moreover, cortical dynein was proposed to be involved in centrosome separation in *Drosophila* based on the presence of the motor protein at the cell cortex, although whether this is indeed the site from which the motor is acting has not been tested in that system (Sharp et al., 2000; Cytrynbaum et al., 2003). By contrast, our work provides unequivocal experimental evidence that cortical dynein is critical for centrosome separation.

This conclusion notwithstanding, our work has also revealed that cortical dynein is not sufficient for centrosome separation without cortical flow. Indeed, cortical dynein-driven centrosome separation is completely impaired when actomyosin contractility is prevented. Accordingly, computational modeling predicts that the forces produced by cortical dynein in the inward and outward direct on average balance each other and thus cannot drive centrosome separation. Instead, the flow of cortical motors imparted by actomyosin is sufficient to drive centrosome separation.

Actomyosin contractility and cortical flows have been implicated in centrosome separation in vertebrate cells (Rosenblatt et al., 2004). However, this pertains to centrosome movements only in cells in which separation occurs after nuclear envelope breakdown; even in that subset of cells, it was unclear also how flows were directed to drive outward centrosome movements. Furthermore, how forces developed in the actomyosin network could be transmitted to centrosomes was not known. Here, we show that when actomyosin contractility is compromised in *C. elegans*, cortical dynein-based centrosome separation is severely impaired. In principle, such impairment could be due to a reduction either in the cortical flows or in the rigidity of the actomyosin network, which could lead to the cortex not being able to sustain strong forces. Embryos depleted of NMY-2 and RHO-1 do not allow one to distinguish between these possibilities, as both flows and rigidity are compromised in these cases (Munro et al., 2004; Mayer et al., 2010; Redemann et al., 2011). By contrast, analysis of centrosome movements in *zyg-12(RNAi)* expressing GFP::TAC-1 and GFP::NMY-2 shows that separation movements are proportional to the velocity of the neighboring cortical flows, even when actomyosin contractility is not altered. Alternatively, in principle, the impairment of centrosome separation upon depletion of NMY-2 or RHO-1 could reflect the reduction of cytoplasmic streaming that in the wild-type situation might exert forces on centrosomes through viscous drag. Cortical dynein could facilitate this process by pulling microtubules toward the cortex, where cytoplasmic flows are the fastest and thus exert maximal viscous drag force. However, we view this possibility as unlikely because centrosomes do not move in the direction of cytoplasmic streaming when cortical and nuclear dynein are jointly depleted.

Computational simulations show also that cortical dynein, together with cortical flows, can separate centrosomes even when dynein motility is impaired. However, separation occurs at a slower pace with respect to the case in which dynein is motile, thus indicating that dynein motor activity contributes slightly to centrosome separation, likely by pulling the microtubule aster toward the cortex and thus enhancing motor binding.

In conclusion, our work reveals a novel organizing principle in which cortical dynein acts as a force transmission device that harnesses polarized flows of the actomyosin network. Importantly, since the cortical flow is initiated by the centrosomes themselves, this mechanism functions irrespective of where centrosomes are located along the cell cortex, thus guaranteeing mechanism robustness. We propose that this novel mechanism is broadly utilized to promote correct bipolar spindle assembly and thus ensure genome stability, including in tissue settings where cell volume is constrained by a compact geometry, with centrosomes being in close proximity to the actomyosin cortex.

7.3 On the role of nuclear dynein

Dynein at the nuclear envelope plays an important role in several processes in one-cell stage *C. elegans* embryos. Thus, dynein tethered on the female pronucleus is thought to power its migration towards the male pronucleus by virtue of pulling along astral microtubules emanating from the centrosomes (Gönczy et al., 1999). In addition, nuclear dynein helps to maintain the association between centrosomes and pronuclei and is thus fundamental for the positioning of the genetic material (Gönczy et al., 1999; Robinson et al., 1999; Malone et al., 2003). Our work reveals that, prior to that, dynein tethered on the male pronucleus plays a partially redundant role in centrosome separation, since this process can take place in the absence of cortical dynein, but at a slower pace than in the wild-type, while it is completely prevented when both nuclear and cortical dynein are depleted. Since in other systems slower centrosome separation leads to defects in chromosome attachment and error-prone chromosome segregation (Silkworth et al., 2012), we surmise that nuclear dynein is important for maintaining genome integrity. Importantly in addition, our analysis reveals that nuclear dynein, while maintaining centrosomes in the vicinity of the nucleus (Gönczy et al., 1999; Robinson et al., 1999; Malone et al., 2003), prevents an aberrant path of cortical-dynein driven centrosome separation. Therefore, nuclear dynein is pivotal for proper temporal and spatial regulation of centrosome separation.

Furthermore, our analysis shows that the position of centrosomes between the male pronucleus and the cortex is essential to organize nuclear dynein forces to move centrosomes in opposite directions. Thus, cell geometry, in this instance the position of centrosomes and pronuclei, together with cell shape, organizes the microtubule asters and therefore determines the balance of forces exerted by nuclear dynein on them. Interestingly, nuclear dynein was shown to be able to drive centrosome separation in mammalian cells derived by directed evolution following kinesin-5 impairment (Raaijmakers et al., 2012). We propose that, also in that case, the position of the nucleus might be important to ensure centrosome outward movement. Similarly, in *Drosophila* embryos centrosomes are positioned between the cortex and the nucleus like in the one-cell *C. elegans* embryo and dynein holds centrosomes at the nuclear envelope (Robinson et al., 1999). Also in this case, dynein at the nucleus, together with this specific geometry, could contribute to move centrosomes away from each other. Furthermore, it is possible that in mammalian cells, *Drosophila* embryos or *C. elegans*, a regulator of microtubule dynamics contributes to shape the microtubule aster and break the symmetry between outward and inward centrosome movements. For example, depolymerizing motors of the kinesin-13 family, when enriched at centrosomes, could depolymerize microtubules directed from one centrosome toward the other and thus lead to aster asymmetry and centrosome outward movement. We have performed an initial attempt to test this hypothesis in the case of cortical dynein-based centrosome separation by analyzing *klp-7(RNAi) zyg-12(ct350)* embryos. Indeed, centrosome separation is partially impaired in these embryos, but this result is difficult to interpret since KLP-7 depletion results also in slower microtubule growth and thus likely affects microtubule aster size. Further experiments are required to measure the asymmetry of the microtubule aster, for example by imaging GFP::TBB-1 embryos, and test whether such postulated asymmetry is partially dependent on KLP-7.

7.4 Dynein in the cytoplasm: possible root of opposing forces

Dynein in the cytoplasm can exert length-dependent forces on microtubules while transporting cargos along them or while being anchored on a stable substrate in the cytoplasm (reviewed in Reinsch and Gönczy, 1998). Such dynein-mediated length-dependent forces have been implicated in the centration of centrosomes that occurs after their separation in one-cell *C. elegans* embryos (Kimura and Onami, 2005; Kimura and Kimura, 2011b). In that case, dynein in the cytoplasm exerts higher forces on the long microtubules directed toward the cell center than on the short ones directed toward the periphery, thus leading to centrosome centration. By contrast, our data indicates that dynein in the cytoplasm does not drive the process of centrosome separation that occurs earlier, before pronuclear meeting, in *C. elegans* embryos, since separation is entirely abolished when both nuclear dynein and cortical dynein are depleted.

Although not important during the separation phase, dynein-mediated length-dependent forces could oppose centrosome separation during the equilibrium phase. Indeed, mathematical modeling suggests that, at the equilibrium angle of 141°, an opposing force balances centrosome separation forces. Given that dynein-mediated length-dependent forces operate during the centration phase that immediately follows separation, it is tempting to speculate that they also oppose separation forces during the equilibrium phase.

7.5 Microtubule polymerization forces

Microtubules can exert pushing forces on barriers while polymerizing (reviewed in Dogterom et al., 2005). Even if this mechanism has been demonstrated to exert significant force and to position the mitotic spindle in fission yeast (Tran et al., 2001), microtubule polymerization is unlikely to exert sufficient force for centrosome separation in the large *C. elegans* embryo, since the maximum force that a microtubule can exert decreases quadratically with its length (Dogterom and Yurke, 1997). Indeed, centrosomes do not separate at all when dynein is depleted (Gönczy et al., 1999), even when they are detached from the nuclear envelope, as demonstrated in *dhc-1(RNAi) zyg-12(ct350)* embryos (this work). Similarly, when dynein is depleted from the cortex and from the nucleus, centrosomes are immobile until the start of centrosome centration. Accordingly, computational modeling predicts that polymerization forces are not sufficient to significantly push centrosomes apart in the absence of dynein. Taken together, these findings demonstrate that microtubule polymerization is not the major driving force of centrosome separation in *C. elegans*. Nevertheless, microtubule polymerization could contribute slightly to move centrosomes apart at the initial steps of separation, when centrosomes are close to each other.

Furthermore, microtubule polymerization can contribute to generate an asymmetry in the microtubule aster by triggering catastrophe of microtubules colliding against the opposing centrosome (Janson et al., 2003). This symmetry breaking mechanism could direct the forces exerted by motors in the outward direction. For example, this mechanism could contribute to organize nuclear dynein forces to separate centrosome. Unfortunately, we could no test this hypothesis experimentally, since conditions that affect microtubule stability also affect the microtubule aster more globally, such that the result of the experiment would be difficult to interpret. However, we could use our computational model to analyze a condition in which centrosomes do not interact with microtubule plus-ends and thus do not trigger their catastrophe. In these simulations, centrosome separation appeared more variable than in normal conditions, with strong delay in 30% of the cases, and wild-type-like behavior in the other cases. This result suggests that microtubule polymerization, even if not sufficient to power centrosome separation, contributes to organize nuclear dynein forces asymmetrically and that this symmetry breaking mechanism is important for the robustness of centrosome separation. Potentially, a similar mechanism could contribute to generate the microtubule aster asymmetry that has been observed in *Drosophila* embryos (Cytrynbaum et al., 2005).

7.6 Kinesin-5: a silent spectator?

Kinesin-5 drives prophase centrosome separation in several systems (reviewed in Ferenz et al., 2010). In addition, during the spindle maintenance phase, kinesin-5 pushes the two spindles poles apart, thus preventing them from collapsing onto each other. Despite the key importance of kinesin-5 in these two processes in many cases, this motor is partially dispensable in several systems (reviewed in Tanenbaum and Medema, 2010). In addition, BMK-1, the only kinesin-5 motor in *C. elegans*, is completely dispensable for viability (Bishop et al., 2005; Saunders et al., 2007). It was previously reported that BMK-1 is enriched at the microtubule aster in the early embryo and that it slows down spindle elongation by acting as a brake (Bishop et al., 2005; Saunders et al., 2007). Here, we have demonstrated that BMK-1 depletion does not affect the rate and timing of centrosome separation. Therefore, BMK-1 does not contribute positively to centrosome separation in the *C. elegans* one-cell stage embryo and also does not act as a brake in this process as it does during spindle elongation. We speculate that this might be due to the fact that, in the early stages of centrosome separation, kinesin-5 cannot act since not enough opposing microtubules are aligned in an anti-parallel fashion. In later stages, when centrosomes are further away, a larger portion of the two microtubule asters is aligned, potentially also due to motors that promote anti-parallel microtubule bundling as observed in fission yeast (Fu et al., 2009), and thus a larger number of kinesin-5 motors could bind and act as a brake.

7.7 Limitations, improvements and further developments

7.7.1 Centrosome separation: further experiments

On the experimental side, our work has demonstrated by using reverse genetics and correlation analysis that cortical flows transmitted by cortical dynein, together with nuclear dynein, drive centrosome separation. Further experiments could be envisaged to strengthen our model and potentially give new insights. For example, it would be desirable to analyze centrosome separation in conditions in which cortical flows are impaired without affecting microtubule aster or actomyosin contractility. Unfortunately, to our knowledge no such condition has ever been reported. Genes involved in the trigger of cortical flow, such as *spd-5*, are also needed for proper microtubule aster formation, so that when these genes are inhibited it is difficult to distinguish effects due to the lack of cortical flows from those due to impairment of the microtubule aster (Hamill et al., 2002). Similarly, cortical flows are driven by actomyosin contractility (Mayer et al., 2010) and it is not possible to block the former without affecting the latter. An alternative strategy would be to partially reduce actomyosin contractility in the anterior of the embryo to generate a gradient of contractility that increases from the anterior to the posterior and thus potentially lead to posterior-directed cortical flow. Such a flow would pull centrosomes toward each other and thus prevent their separation. Localized inactivation of contractility could be achieved, for example, by using an infrared laser to heat-inactivate myosin in the anterior-cortex in extant *nmy-2(ne3409)* termosensitive mutant embryos (Liu et al., 2010).

A different method to test the coupling model would be to image microtubule plus-ends at the cortex and test whether they move together with the actomyosin network. This experiment can be performed by imaging embryos expressing a microtubule plus-end marker, for example GFP-EB-1, together with an actin marker, for example mKate-2::Lifeact, and measuring their movements by Particle Image Velocimetry in wild-type and cortical dynein-depleted embryos. This experiment could potentially reveal that plus-end tips and actin move together and that this coupling is abolished in the absence of cortical dynein. Unfortunately, a negative result would be difficult to interpret. For example, in the extreme case in which posterior cortical flows are heterogeneous in space and microtubules are rigid, the microtubule aster would move as a rigid-body proportionally to the sum of all forces acting on it, but the force exerted on a single microtubule by the near cortical region would not produce a direct and proportional movement of its tip. Thus, in this case, microtubule aster movements at a certain time would correlate with the average cortical flow at the same time, but each microtubule tip would not move together with its surrounding cortex.

Regarding dynein function, as mentioned before, computational simulations indicate that centrosomes can separate even when cortical dynein motility is impaired. In the future, it will be interesting to test this hypothesis by separating the function of binding and motor of dynein. For example, one could inhibit dynein motor activity without affecting its binding using ATPase inhibitors of the ciliobrevin family (Firestone et al., 2012). However, in our hands, permeablized *C. elegans* embryos treated with ciliobrevin A and D show only mild defects in early dynein-dependent processes, such as centrosome separation and pronuclear meeting, followed sometimes by cell cycle arrest at metaphase (data not shown). Therefore, the results of these preliminary experiments are difficult to interpret. An alternative would be to identify a *dhc-1* mutant allele in which a mutation in one of the six AAA ATPase domains leads to impaired dynein motility, while dynein binding properties are not affected, which would greatly contribute to further dissect the mechanisms by which dynein functions in *C. elegans*. We have started some preliminary attempts to identify such a mutant by testing the dominant-negative termosensitive *dhc-1(ct42)* and the recessive termosensitive *dhc-1(or352)* mutant strains, that are both mutated in a AAA ATPase motor domain, while their MT-binding domain is putatively unperturbed (Mains et al., 1990; Hamill et al., 2002; Schmidt et al., 2005). As previously reported (Hamill et al., 2002; Schmidt et al., 2005; Nguyen-Ngoc et al., 2007), both mutants show defects in some dynein-dependent processes, for example in centrosome rotation and in chromosome segregation, but most dynein-dependent processes, such as pronuclear migration and centration, still occur, thus suggesting that dynein motor activity is only partially compromised (data not shown). Therefore, these mutants are not well suited for studying centrosome separation in conditions in which dynein motility, and not binding, are affected.

Computational modeling of centrosome separation indicated that the position of centrosomes between the cortex and the male pronucleus, as well as the flow pattern, are the sources of the symmetry breaking mechanisms that organize forces anisotropically. These clear predictions need to be tested experimentally. In particular, the computational model predicts that, in the absence of cortical motors, nuclear dynein cannot separate centrosomes efficiently if the male pronucleus is located elsewhere than in the vicinity of the cortex. This prediction could be tested experimentally by analyzing conditions in which the male pronucleus is away from the cortex, such as in *pam-1* mutants (Lyczak et al., 2006) or potentially as a result of embryo centrifugation. If the predictions of the model would not be confirmed, we would conclude that an additional symmetry breaking mechanism, independent of cell geometry, is present, thus paving the way for further investigations. For example, centrosomal KLP-7 or an equivalent microtubule depolymerizing protein could work as an additional backup symmetry breaking mechanism. In a similar way, the analysis of the dynamics of a single centrosome or of a pair of centrosomes located in different positions in the embryo than usual, either at the cortex or away from it, will give insights on cortical dynein-driven centrosome separation and, more generally, on the interplay between centrosomes, actomyosin contractility and cell polarization.

7.7.2 Limitations and improvements of the computational model

Computational simulations demonstrate that the model proposed here is sufficient to explain the observed quantitative dynamics of centrosome separation. In addition, the qualitative predictions of the computational model are robust to changes in its parameters. Nevertheless, a more realistic description of cell mechanics would allow us to make more precise predictions and therefore identify discrepancies between our model and the experimental observations. These potential discrepancies could also provide insights on other mechanisms that have been neglected so far and thus lead to new discoveries.

Among the improvements that would lead to a more realistic description of cell mechanics, the most important is the precise quantification of model parameters such as the number of microtubules, the number of motors at the cortex and on the nuclear envelope, as well as the dynamic properties of dynein. Regarding dynein abundance, single-molecule imaging of endogenous dynein heavy-chain tagged with GFP could greatly help in estimating the number of motors in these two location. A method to image single-molecule dynamics at the cortex in *C. elegans* has recently been published (Robin et al., 2014). In principle, this method does not allow quantification of the number of motors since it requires their depletion by RNAi to perform single-molecule detection, but it is possible that the density of dynein motors at the cortex during prophase is low enough to distinguish single-molecules, thus allowing their quantification. Even if this is not the case and the number of motors cannot be quantified, this technique might provide insights regarding the dynamics of motors at the cortex. This analysis could allow, for example, to estimate the attachment and detachment rate of cortical dynein motors (Redemann et al., 2011). In addition, it would be useful to experimentally verify whether cortical dynein can work cooperatively and thus multiple motors can bind simultaneously on a single microtubule tip, as is assumed in our model. For example, cortical dynein cooperativity could be revealed by monitoring at high time-resolution the intensities of cortical GFP::DHC-1 puncta in correspondence to a microtubule-tip, revealed for example by using EB-1 tagged with a red fluorescent protein. Indeed, if multiple motors can bind to a single microtubule tip, the intensity of each punctum should vary in a step-wise manner, reflecting motor binding or unbinding events. Interestingly, cortical dynein binding and unbinding rates could then be calculated from the frequency of these binding and unbinding events, respectively.

Our current computational model does not allow us to estimate the total force acting on the microtubule aster since a reliable estimate of its viscous drag is still lacking. Even if the viscosity of the cytoplasm in *C. elegans* embryos has been estimated (Daniels et al., 2006), the complex and dynamic shape of the microtubule aster has not allowed so far to calculate its viscous drag from hydrodynamics equations. In addition, since microtubules are elastic, a simulation that includes cytoplasm hydrodynamics is computationally cumbersome, since hydrodynamic equations introduce a coupling between every mechanical element in the model and therefore the computational time scales with the square of the number of simulated elements. In our work, we have avoided this issue by approximating the drag coefficient of the microtubule aster with the sum of the local drag of each microtubule. This approximation neglects non-linear effects introduced by hydrodynamics and probably overestimates the drag acting on the microtubule aster. A significant step forward has been achieved in recent work that developed a new computational framework to simulate cytoskeleton mechanics, together with cytoplasm hydrodynamics by using parallel computing (Nazockdast et al., 2015). This work has shown that a precise hydrodynamic description is important to correctly calculate the viscous drag acting on the microtubule aster and, in particular, that the local drag approximation that we have used in our study indeed overestimates the total drag by an order of magnitude. We think that this does not represent a major issue in the context of centrosome separation, since the number of dynein motors in the embryo is unknown anyway, and an overestimated drag can be balanced by a corresponding increase in motor densities. On the other hand, a precise estimate of the drag of the microtubule aster is important when the reciprocal movements of the microtubule aster and pronuclei are studied, for example for the analysis of pronuclear migration. Similarly, a correct estimation of the dependency of the drag coefficient on microtubule aster size is fundamental to study the mechanics of the growing microtubule aster.

In addition to more precise modeling, in the future it will be important to determine the microtubule aster viscous drag experimentally. Along these lines, we have already estimated the drag coefficient of the microtubule aster by analyzing the fast phase of pronuclear migration in embryos depleted of cortical dynein (see section A.3). This estimate can be improved by enlarging the dataset and comparing the result with similar cortical forces depletion conditions. Furthermore, we plan to measure how the drag coefficient of the microtubule aster scales with microtubule number. To this end, we will estimate centrosome nucleation rate by imaging GFP::EB-1 (Srayko et al., 2005) and simultaneously determine microtubule aster drag coefficient by analyzing pronuclear migration. In addition, we will increase the range of centrosomal microtubule numbers by partially depleting the microtubule nucleator γ-tubulin. Thanks to these measurements, we will be able to determine experimentally how the aster drag scales with microtubule number and potentially compare these results with the predictions of the model presented recently in (Nazockdast et al., 2015).

In addition to these estimates, a more realistic computational simulation requires a more comprehensive modeling of the forces acting in the embryos. For example, as a quantitative improvement of our model, we could consider spatial asymmetries in the density of cortical motors and actomyosin contractility. For example, the computational model could include the anterior increase of cortical dynein motors and contractility that results from cortical flows and polarization.

Furthermore, the model could be extended to study the equilibrium phase of centrosome separation. For example, our current model does not consider motors anchored in the cytoplasm that exert length-dependent forces and that likely drive centrosome centration. By including these motors, we will be able to test whether these forces can oppose centrosome separation during the equilibrium phase.

Similarly, the computational model can be extended to study the mechanical processes that occur at the onset of centrosome separation. In the current model, at the beginning of the simulations, centrosomes start to nucleate microtubules and to separate at constant speed. This is in contrast with the experimental observation that centrosome separation accelerates during the "onset" phase. Therefore, some components are missing to describe in detail these early moments of centrosome separation. For example, *in vivo* cortical flow velocity is not constant, as in our computational model, but increases with time, reaches a peak and then slows down (Blanchoud et al., 2015). Along the same lines, a significant advance will be provided by physical modeling of the contractile dynamics of the actomyosin network, for example represented as an active fluid (Naganathan et al., 2014). A computational model that includes the mechanics of the microtubule aster together with the dynamics of the actomyosin cortex would allow us to explore their interplay during the initial phases of cell polarization. For example, such a model could allow one to investigate movements of centrosomes towards the embryo posterior pole that occurs when centrosomes are initially located at a side position along the cortex. Are these components sufficient to transport centrosomes toward the posterior? Does the model suggest that additional regulation is required and, if so, what would be its function? What is the role of the newly nucleated microtubule aster in this process? Are cortical dynein motors contributing? How is the timing and robustness of centrosome separation affected by this posterior-directed transport?

7.7.3 Centrosome separation beyond dynein

The methods that we have developed in this work can be used to study the role of other motors besides dynein in centrosome separation. For example, we have already investigated here centrosome separation in embryos depleted of the kinesin-5 BMK-1 and of the kinesin-13

KLP-7. In the future, the same methods can be applied to study the role of each *C. elegans* kinesin, or more generally of microtubule-associated proteins, in centrosome separation. Our computational model can be extended in a straightforward manner to include additional proteins and thus to obtain a more comprehensive model of centrosome separation, capable of higher predictive power.

7.7.4 Beyond centrosome separation

The methods presented in this thesis can also be utilized to study centrosome dynamics in a broader context, for example during pronuclear migration and centration/rotation. We have started this path by studying quantitatively centrosome centration and female pronuclear migration in embryos depleted of dynein motors and/or actomyosin contractility. This preliminary analysis can be extended to additional conditions that will, for example, shed light on the dependency of centrosome centration on microtubule aster size, motor localization and embryo polarity. On the computational side, the inclusion of length dependent forces, spatial distribution of cortical motors and potential other factors that will emerge from further experimental investigations will lead to a comprehensive model of centrosome dynamics from the onset of centrosome separation, through centration/rotation and until nuclear envelope breakdown. This model will allow us to investigate centrosome and pronuclei dynamics in a unique quantitative framework, potentially guiding the discovery of new critical components.

7.8 Concluding remarks

In this thesis, we have investigated the mechanisms of centrosome separation in *C. elegans* one-cell embryos. Experiments, data analysis and computational simulations lead us to a model in which cortical and nuclear dynein cooperate to separate centrosomes. Furthermore, we have revealed a new mechanism in which cortical dynein acts by transmitting the forces generated by polarized cortical flows. In addition, computational modeling revealed that cell geometry and the pattern of cortical flows are sufficient to direct centrosome movements away from each other.

The mechanisms that we have here demonstrated are important for ensuring timely centrosome separation. However, they are not strictly necessary for spindle assembly since other mechanisms can act later to separate centrosomes, as demonstrated by the fact that at anaphase centrosomes are distant from each other in all conditions that we have considered here, apart from complete dynein heavy-chain depletion. In addition, almost all the components that we have implicated in centrosome separation are essential for other processes, so that their impairment would lead to embryonic lethality. We think that such redundancies do not decrease the importance of the mechanisms proposed here. Indeed, discoveries since the dawn of molecular biology have shown that organisms are not machines in which each component has an essential and unique function, as would be the case for an *a priori* designed artifact derived from human engineering. On the contrary, evolution proceeds by blindly copying and adapting existing mechanisms. As a result, genes often have multiple functions and multiple genes are able to redundantly perform the same task, yet with different efficiency. Despite their relative ease of discovery with genetic or genomic approaches, essential genes are rarities. We believe that many important and widespread mechanisms that are relevant for efficient cellular processes and that are involved in disease are not essential and must be revealed by carefully analyzing small perturbations of cell functions. To give an example, the acentrosomal spindle assembly pathway can assemble a functional mitotic spindle in the absence of centrosomes, but at the cost of spindle positioning defects (Basto et al., 2006; Hinchcliffe et al., 2001; Khodjakov and Rieder, 2001).

Finally, in this work we have not only discovered mechanisms used by cells to control their internal mechanics, but also contributed to shed light on the underlying physical constraints and organizing principles. For example, cell geometry shapes the microtubule aster and therefore affects the direction of forces acting on it; polymerization forces are not sufficient to push centrosomes away from each other in large cells, but may deplete microtubules between them; homogeneously distributed cortical motors cannot separate centrosomes without an external symmetry breaking mechanism, such as that imparted by cortical flow; the male pronucleus pushes centrosomes apart while growing in size. The mechanisms of centrosome separation that act in *C. elegans* are probably conserved in other systems, but, even more importantly, each system is affected by analogous physical constraints. The relative importance of each of these constraints depends on the actual physical properties of each cell, but every cell must have adapted to cope with them. In some cases a cell would have evolved to use these constraints to perform a function, for example using cell geometry to separate centrosomes. In another case, a cell would produce proteins to break these limits, for example using kinesin-5 motors to push centrosomes away from each other, independently of cell geometry.

The classical tools of biology have greatly contributed to identify the actors that are at play in a wealth of important processes. We believe that quantitative biology will support and guide developments along the same path, but that it will also contribute to the understanding of the underlying physical background to which organisms had to adapt. These constraints are general; the answers that Nature has provided are often similar, sometimes different, in some instances necessary, at times surprisingly baroque. These solutions have blossomed in the Tree of Life and testify to the creative power and beauty of self-organization.

A Mechanisms of centration

The correct positioning of centrosomes and chromosomes is fundamental for faithful cell division and genome integrity. In the *C. elegans* one-cell stage embryo, the two pronuclei together with the associated microtubule asters meet and move to the cell center at the time of chromosome condensation (Fig. A.1) (Albertson, 1984). This process starts during the equilibrium phase of centrosome separation, when the male pronucleus-microtubule asters complex is positioned at the posterior side of the embryo and begins to slowly migrate toward the cell center (Fig. A.1A). In the meantime, the female pronucleus, positioned on the anterior side, starts to move toward the male until the two pronuclei meet (Fig. A.1B). Thereafter, the two joint pronuclei are driven by the microtubule asters toward the center (Fig. A.1C, D). We will here refer to the whole process of centrosome movement from the posterior pole of the embryo to the cell center, before and after pronuclear meeting, as centrosome centration.

A.1 Centrosome centration

The centration process has been compared in wild-type and mutant/RNAi conditions (Goulding et al., 2007; Kimura and Onami, 2007). These analyses revealed that two mechanisms, one that is dynein-dependent and one that is dynein and actomyosin network-dependent, are involved. However, these studies could not precisely compare centration dynamics in the different conditions due to the lack of a reliable time-reference. The experimental and image processing methods that we have developed to analyze centrosome separation can be used to study the mechanics of centrosome centration and pronuclear migration using a reliable time-reference, i.e. male pronucleus size.

We started this investigation by analyzing centrosome centration in the wild-type. To this end, we measured centrosome position along the AP-axis from the start of centrosome separation until the end of centrosome centration. Thereafter, we synchronized the resulting curves by maximizing their overlap (Fig. A.2A).

As previously reported (Kimura and Onami, 2005), the centrosome centration curve shows a

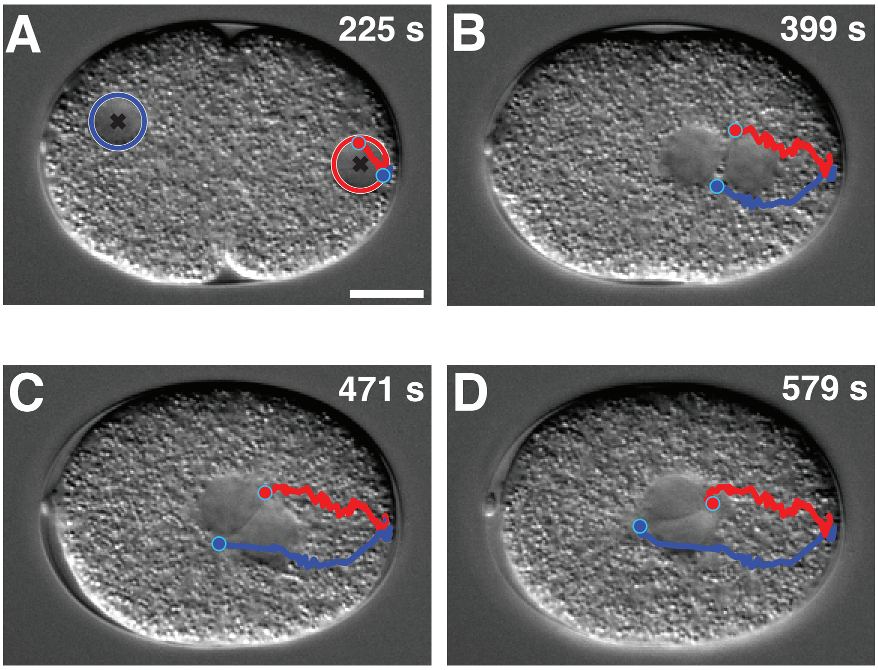

Figure A.1 – **Pronuclear migration and centrosome/pronuclear centration.** Pronuclear migration and centrosome/pronuclear centration monitored with 3D time-lapse DIC and fluorescent microscopy (GFP) in embryos expressing GFP::TAC-1. Centrosome positions (blue and red dots) are represented with their trajectories (blue and red tracks - z maximum projections). Before pronuclear meeting, pronuclei are highlighted (blue disc, female pronucleus; red disc, male pronucleus; black crosses: centers). After pronuclear meeting, pronuclei are not tracked. **A** Start of pronuclear migration. **B** Pronuclear meeting. **D, E** Pronuclear centration and rotation. Centrosome centration is the whole movement of centrosomes from the posterior pole of the embryo to the cell center before and after pronuclear meeting (A,B,C,D).

sigmoidal shape characterized by an acceleration and followed by a deceleration that occurs when centrosomes are in the vicinity of the cell center (Fig. A.2B).

Length-dependent forces produced by dynein anchored in the cytoplasm are thought to drive centrosome centration (Reinsch and Gönczy, 1998; Gönczy et al., 1999; Kimura and Onami, 2005; Kimura and Kimura, 2011b). In this model, motors in the cytoplasm bind to and exert forces on microtubules, so that more force is exerted on longer microtubules. The two microtubule asters located at the posterior side have longer microtubules growing toward the anterior side, thus higher forces are exerted toward the anterior and the whole centrosomes-pronuclei complex is brought toward the cell center. While centrosomes move away from the posterior, the length imbalance between the anterior and posterior-directed sides of the microtubule aster progressively decreases, until the microtubule asters reach the cell center where the forces in the two direction equilibrate each other and the movement stops.

While this model can explain the deceleration phase of centrosome centration, it is unclear why centrosomes accelerate during the first phase. Computer simulations suggested that this acceleration might be due to microtubule growth that results in increasingly stronger length-dependent forces (Kimura and Onami, 2005). However, in that computational model, the authors had considered a velocity of microtubule growth that is 7 times smaller than what was later measured in *C. elegans* one-cell stage embryos (Srayko et al. (2005), see measurements at 24°). Given that the measured growth velocity is $v_g \sim 0.7\ \mu\text{m}$ and since the embryo length is $\sim 50\ \mu\text{m}$, we calculate that it takes about 70 s for the microtubule aster to grow enough to span the whole embryo, while the acceleration process takes about 400 s. Thus, it is unlikely that microtubule growth is causing acceleration of centrosomes.

Alternatively, centrosome centration could accelerate because the microtubule aster is nucleating an increasing number of microtubules, compatible with the fact that centrosomes accumulate increasing amounts of microtubule nucleators, such as γ-tubulin, during that time (Hannak et al., 2002). This alternative mechanism of centration acceleration also raises some theoretical issues. For example, both length-dependent forces and the viscous drag acting on the microtubule aster increase with the number of nucleated microtubules, and the acceleration of centrosomes depends on the exact form of these dependencies. After pronuclear meeting, centration velocity depends on the drag of the complex comprising the male and female pronuclei and the two microtubule asters; to a first approximation, if we neglect the effect that the cytoplasmic flow produced by the movement of the pronuclei has on the microtubule asters and vice versa, the viscous drag coefficient of the pronuclei-microtubule asters complex $\gamma_{\text{PN}-\text{MA}}$ is the sum of the drag coefficients of the pronuclei γ_{PN} and those of the microtubule asters γ_{MA}

$$\gamma_{\text{PN}-\text{MA}} = 2\gamma_{\text{PN}} + 2\gamma_{\text{MA}} \tag{A.1}$$

Thus, the AP-centration velocity v is

$$v = \frac{F}{2\gamma_{\text{PN}} + 2\gamma_{\text{MA}}} \tag{A.2}$$

where F is the net applied force and the equation for overdamped dynamics was used. We will now discuss different scenarios depending on the relative magnitude of the drag coefficients.

If the drag coefficient of the pronuclei is small compared to the drag coefficient of the microtubule asters $\gamma_{\text{PN}} \ll \gamma_{\text{MA}}$, the centration velocity is

$$v = \frac{F}{2\gamma_{\text{MA}}} \tag{A.3}$$

When the number of microtubules N increases, if the pool of motors is not rate limiting, the applied force will increase proportionally. At the same time, the drag coefficient of the microtubule aster will also increase. When the aster is sparse, the drag coefficients of each microtubule will simply add to each other, so that the final drag will be proportional to the number of microtubules N. Therefore, in this case, centration velocity is independent of the

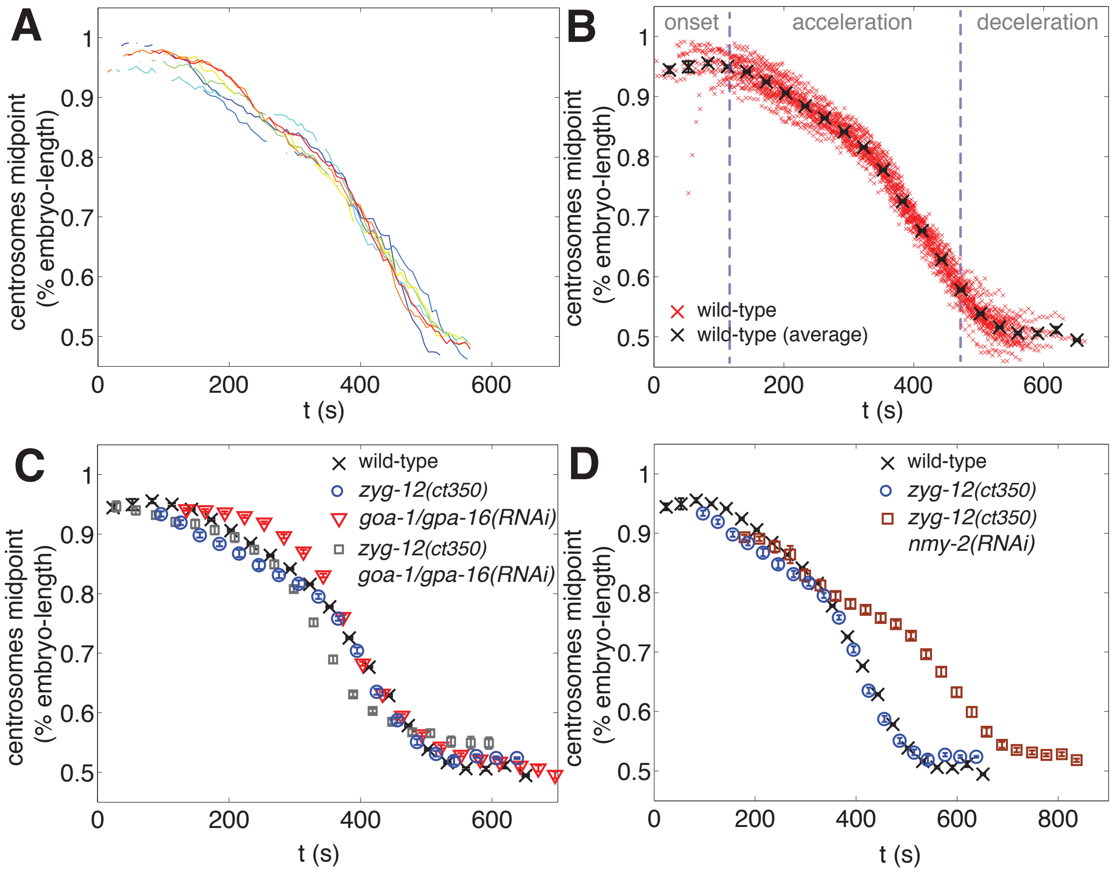

Figure A.2 – **Quantification of centrosomes centration.** **A** Centrosomes position along the embryo AP-axis as a function of time for representative wild-type embryos. Here and in the next panels, centrosomes position is calculated as the midpoint between the two centrosomes. **B** Average wild-type centrosomes position along the AP-axis with SEM (n = 40 embryos analyzed). **C, D** Average centrosomes position along the AP-axis with SEM as a function of time in the indicated RNAi/mutant conditions. Number of embryos analyzed: *goa-1/gpa-16(RNAi)*, n=13; *zyg-12(RNAi*, n=10; *zyg-12(ct350) goa-1/gpa-16(RNAi)*, n=11; *zyg-12(ct350) nmy-2(RNAi)*, n=10.

number of microtubules

$$v = \frac{F}{2\gamma_{\mathrm{MA}}} = \frac{fN}{2\gamma_0 N} = \mathrm{const} \tag{A.4}$$

where γ_0 and f are respectively the drag coefficient of, and the force applied on, a single microtubule. By contrast, when the microtubule aster is dense, it behaves hydrodynamically similarly to a solid body: the cytoplasm moves around it and the drag coefficient reaches a maximum value $\gamma_{\max}$, independent of the number of microtubules. In this condition, centrosome velocity scales linearly with microtubule number

$$v = \frac{F}{\gamma_{\mathrm{MA}}} = \frac{fN}{\gamma_{\max}} \sim N \tag{A.5}$$

In the intermediate case, the drag coefficient of the microtubule aster increases non-linearly with the number of microtubules, so that the final velocity is somehow increasing with microtubule number. Finally, in the case in which the pronuclei drag coefficient is not negligible, the drag coefficient of the pronuclei - microtubule asters complex is non-directly proportional to microtubule number. In conclusion, if the microtubule aster is dense enough or if the drag on the pronuclei is not negligible, the drag of the microtubule aster-pronuclei complex is non-directly proportional to microtubule number and therefore centrosome acceleration can be explained by increasing microtubule nucleation.

Since we do not know the relative drag of pronuclei and microtubule asters, we attempted to estimate the effect of the drag of the pronuclei on centrosome centration by comparing wild-type with *zyg-12(ct350)* embryos, in which the microtubule asters are detached from the pronuclei. We calculated the projection of the positions of centrosomes onto the AP-axis, synchronized centration curves from different embryos by maximizing their overlap and calculated the average centration curve. Then, we synchronized the average centration curve with wild-type by using the average male pronucleus size prior to pronuclei meeting as a time-reference (Materials & Methods). Strikingly, in this condition, AP-centrosome centration occurs at a velocity comparable with that of the wild-type (Fig. A.2C). This result can be interpreted in two ways. First, the drag coefficient of the pronuclei could be negligible with respect to the drag coefficient of the microtubule aster, so that centration velocity is independent of whether the pronuclei are bound to the microtubule asters or not. Second, since in *zyg-12(ct350)* embryos microtubule growth is less limited by collisions with the pronuclei, as a result the microtubule aster could experience different length-dependent forces and drag, which could somehow balance with the lack of drag on the pronuclei and coincidentally result in the same centration velocity as in the wild-type. At the moment, we cannot distinguish between these two scenarios, but will further discuss this problem in section A.3 after we will have gained further insights on the drag coefficient of the microtubule asters.

A third mechanism that could explain centrosome acceleration is the progressive removal of a putative tethering force that would initially hold microtubules at the posterior side and that would be released afterwards. A natural candidate to exert this tether is cortical dynein, which indeed has been demonstrated to negatively regulate centrosome centration (Kimura and Onami, 2007). In agreement with this observation, we observed faster centrosome migration in *goa-1/gpa-16(RNAi)* embryos (Fig. A.2C). Similarly, slightly faster centrosome centration is also obtained when cortical dynein is depleted together with nuclear dynein in *zyg-12(ct350) goa-1/gpa-16(RNAi)* embryos. Nevertheless, in both conditions, centration acceleration still occurs and thus a potential progressive removal of cortical dynein from the posterior cannot be the sole cause of such acceleration.

Interestingly, as previously reported (Goulding et al., 2007), centrosome centration is partially slowed down in *nmy-2(RNAi)* embryos in which actomyosin contractility is impaired. Our analysis reveals that, in *nmy-2(RNAi) zyg-12(ct350)* embryos, centrosome centration is not only slower, but also proceeds at a roughly constant speed before reaching the cell center. We can speculate that a potential trigger of centrosome acceleration might be the transport of the actomyosin network and associated proteins away from the embryos posterior side. In this intriguing model, centrosomes are kept at the posterior by actomyosin contractility or by a protein associated with the actomyosin network, so that the tethering force is progressively removed when the whole actomyosin network is transported toward the anterior. In the absence of actomyosin flow, the tethering force is not removed, so that the acceleration of centrosome centration does not occur and centrosome move at a slow velocity toward the cell center.

Finally, centrosome centration could accelerate because motors in the cytoplasm progressively bind to microtubules, so that the number of bound motors increases over time. In this model, a certain concentration T of motors is present in the cytoplasm and they bind with a binding rate k_+. At the same time, unbinding occurs with a rate k_-. Thus, the mass action kinetics reads

$$\frac{dB}{dt} = k_+ U - k_- B \tag{A.6}$$

where U and B are the unbound and bound motor fraction, respectively. The number of bound motors as a function of time is

$$B(t) = \frac{k_+ T}{k_+ + k_-}\left(1 - \left(1 - B_0 \frac{k_+ + k_-}{k_+ T}\right) e^{-t(k_+ + k_-)}\right) \tag{A.7}$$

where B_0 is the number of bound motors at time $t = 0$. Therefore, bound motors reach the equilibrium constant concentration

$$B_{\text{st}} = \frac{k_+ T}{k_+ + k_-} \tag{A.8}$$

in the time-scale τ

$$\tau = \frac{1}{k_+ + k_-} \tag{A.9}$$

Thus, the time required for reaching the equilibrium number of bound motors is set by the largest of the binding and unbinding rates. Since dynein in the cytoplasm typically unbinds with a rate in the order of $1\,\text{s}^{-1}$ (Reck-Peterson et al., 2012), this time-scale is necessarily below 1 s. Therefore, it is not possible that centration acceleration is due to the progressive binding of motors from a constant cytoplasmic pool, since the time needed to reach the equilibrium number of bound motors is below 1 s and centration occurs on the time-scale of hundreds of seconds. By contrast, centrosome acceleration could be driven by the progressive production of motors which would quickly bind to microtubules. Such a potential effect could be measured, for example, by monitoring over time the amount of endogenous dynein motors. Alternatively, the total motor amount could be constant, but an increasing number of them could be activated over time. Such an effect could be measured, for example, by monitoring whether the number of vesicle minus-end directed movements per microtubule unit-length increases while centrosome centration progresses. Along these lines, an increase in total vesicle minus-end directed movements during centration acceleration has been previously observed, but in that case it was not investigated whether this increase was caused by a corresponding increase in active motors or in number/length of microtubules (Kimura and Kimura, 2011b). To distinguish these two possibilities, one could measure the number and length of microtubules during centration, for example by imaging GFP::TBA-1 embryos, and calculate whether the potentially measured increase in total microtubule length can account for the observed increase in vesicle minus-end directed movements on its own or if a simultaneous increase in total number of motors must be postulated.

A.2 Migration of the female pronucleus

When the male pronucleus moves toward the cell center, the female pronucleus starts to move toward the embryo posterior. In a first phase, this migration proceeds slowly and independently of centrosomal microtubules (Hannak et al., 2002; Oegema and Hyman, 2006). In a second phase, the female pronucleus accelerates toward the male pronucleus until the two pronuclei meet. This fast movement is likely to be dependent on the pull of dynein motors present on the surface of the female pronucleus on the opposing centrosomal microtubules (Gönczy et al., 1999; Hamill et al., 2002; Hannak et al., 2002; Malone et al., 2003).

To investigate the mechanisms that drive the slow phase of female migration, we measured the movements of the female pronucleus from the start of migration to pronuclear meeting. Our measurement confirmed the existence of the two phases of female migration (Fig. A.3A,B). As expected, cortical dynein depletion in *goa-1/gpa-16(RNAi)* embryos does not affect the migration of the female pronucleus (Fig.A.3C).

Surprisingly, in *zyg-12(ct350)* embryos, both fast and slow phases of female migration are completely impaired (Fig. A.3C). While this result was expected for the fast phase, likely dependent on nuclear dynein, it is surprising for the slow phase of migration. Since the slow phase of female migration is not dependent on the microtubule aster (Hannak et al., 2002; Oegema and Hyman, 2006), this analysis suggests that the initial slow migration of the female pronucleus might be driven by the pull of female nuclear dynein on non-centrosomal microtubules.

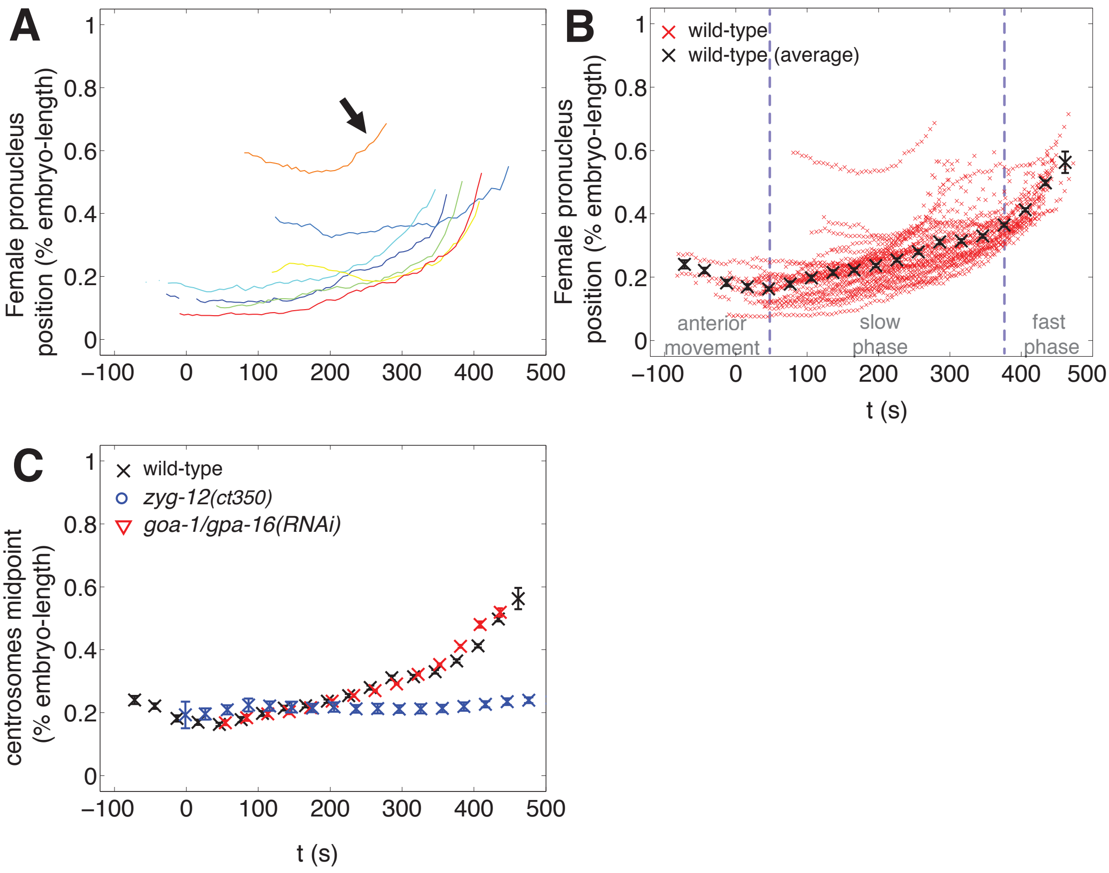

Figure A.3 – **Female pronucleus migration.** **A** Female pronucleus position along the embryo AP-axis as a function of time for representative wild-type embryos (n = 40 embryos analyzed). Black arrow indicates an embryo that was difficult to synchronize precisely since the female was initially located in the posterior side of the embryo. **B** Average wild-type female pronucleus position along the AP-axis with SEM. **C** Average female pronucleus position along the AP-axis with SEM as a function of time in the indicated RNAi/mutant conditions. Number of embryos analyzed: *goa-1/gpa-16(RNAi)*, n=13; *zyg-12(RNAi)*, n=10.

A.3 Estimation of the microtubule asters drag coefficient

The analysis of the fast phase of female pronucleus migration can give insights on the drag coefficient of the male pronucleus-microtubule asters complex (Fig. A.4A). If the phase of fast migration is driven by a force exerted between the two pronuclei, their speeds of migration along the AP-axis v_M and v_F will be

$$v_F = \frac{F_F}{\gamma_F} \qquad v_M = \frac{F_M + F_{\text{cort}} + F_{\text{cent}}}{\gamma_{\text{M-MA}}} \tag{A.10}$$

where we have again used the equation for the overdamped regime and velocities are taken positive in the direction of the posterior side. F_M and F_F are the forces exerted by the female pronucleus on the male and viceversa. F_{cort} is the net cortical force acting on the microtubule asters and F_{cent} is the net centering force. γ_F is the drag of the female pronucleus and $\gamma_{\text{M-MA}}$ is that of the male pronucleus-microtubule asters complex.

From the third principle of mechanics, the force that the female pronucleus exerts on the male is associated with a force, equal in magnitude and opposite in direction, that the male pronucleus exerts on the female, so that $F_M = -F_F$. As a result, in this model, the velocities of the two pronuclei are related

$$v_F = -\left(\frac{\gamma_{\text{M-MA}}}{\gamma_F}\right) v_M + \frac{F_{\text{cort}} + F_{\text{cent}}}{\gamma_F} \tag{A.11}$$

From this equation, if cortical and centering net forces are small compared to the force between pronuclei or if they are independent of pronuclei velocities, then the velocity of the female pronucleus is linearly proportional to that of the male. Intriguingly, in this case the ratio between the drag coefficient of the microtubule aster-male pronucleus complex and that of the female can be calculated as the angular coefficient of this linear relationship. Unfortunately, cortical forces tether microtubules at the cortex and likely react with an elastic opposing force to forces applied on the microtubule aster. Therefore, cortical forces are probably dependent on the force applied on the male pronucleus and thus on its velocity. As a result, the relationship between pronuclei velocities could be difficult to interpret since cortical forces could add a term that depends on the velocity of the male pronucleus and whose specifics are unknown. Thus, we decided to remove this potentially confounding factor by depleting cortical forces.

Therefore, we analyzed the fast phase of female pronucleus migration along the AP-axis in *goa-1/gpa-16(RNAi)* embryos. Strikingly, in this condition, the velocity of the male pronucleus is directly proportional to that of the female pronucleus and the offset of the linear relationship is null (Fig. A.4B). This indicates that, in the absence of cortical dynein, the fast phase of female pronucleus migration is driven by reciprocal forces exerted between the two pronuclei and that, in this phase, the net centering force F_{cent} is small compared to the force between the two pronuclei. By contrast, during the slow migration phase, the velocities of the male and female pronuclei are not correlated, thus demonstrating that the pull exerted between them is small compared to the other forces acting on them (Fig. A.4C). Finally, as anticipated, in wild-type embryos the velocities of the male and of the female pronuclei are strikingly less correlated than in *goa-1/gpa-16(RNAi)* embryos (Pearson correlation coefficient, wild-type: $\rho = 0.30$; *goa-1/gpa-16(RNAi)*: $\rho = 0.68$) and the regression line has a significant offset ($(10 \pm 1)\,\mu\mathrm{m\,min}^{-1}$) (Fig. A.4D). We conclude that, in the wild-type, cortical forces are not negligible and thus likely introduce an unpredictable bias in the slope of the regression line. Instead, *goa-1/gpa-16(RNAi)* embryos are best-suited to compare the velocities of the male and female pronucleus in order to calculate the drag of the male pronucleus-microtubule asters complex.

To this end, we calculated the angular coefficient of the linear relationship between the velocities of the male and female pronucleus in *goa-1/gpa-16(RNAi)* embryos, obtaining $m = (-1.7 \pm 0.2)$. Thus, the drag coefficient on the male pronucleus-microtubule asters is roughly 70% higher than that of the female pronucleus. If we assume that the drag of the microtubule asters and that of the male pronucleus are independent from each other (i.e. that the male pronucleus and the microtubule asters do not interact hydrodynamically), we obtain

$$\gamma_{\mathrm{M-MA}} = \gamma_{\mathrm{M}} + 2\gamma_{\mathrm{MA}} \tag{A.12}$$

where γ_{MA} is the drag coefficient of the microtubule aster and γ_{M} is that of the male pronucleus. Since the male and female pronuclei have roughly the same size, we can assume that they have the same drag coefficient. In this case, we calculate that the drag coefficient of each microtubule aster is approximately 35% of the drag coefficient of the pronuclei.

We can now discuss the centration behavior in *zyg-12(ct350)* embryos on a more solid ground. Indeed, the drag coefficient of the male pronucleus is not negligible compared with the drag coefficient of the microtubule asters, so that this cannot be the explanation for the similar rate of centration measured in *zyg-12(ct350)* and in wild-type embryos. Instead, we conclude that the higher length-dependent force applied on the detached centrosomes, the lack of interaction with the female pronucleus and the increased viscous drag of the microtubule aster balance each other and result in the unaltered centration velocity compared with the wild-type.

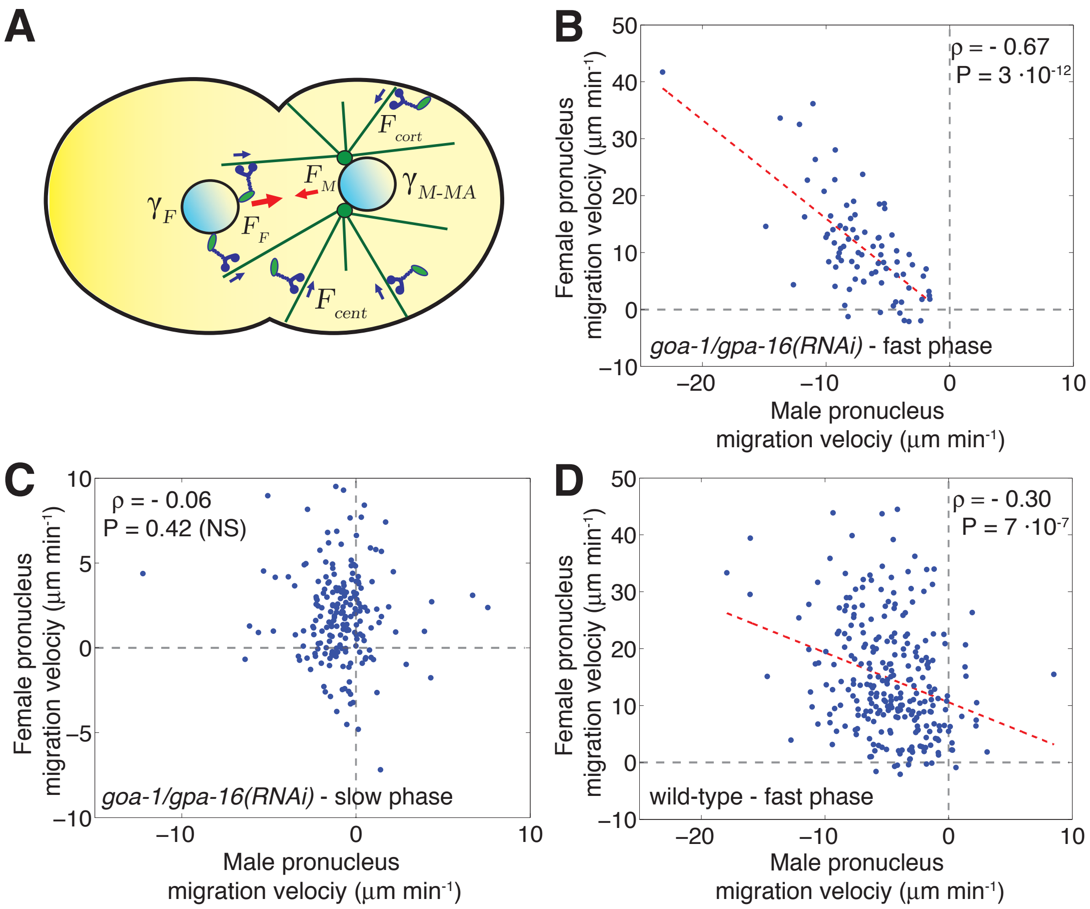

Figure A.4 – **Estimation of the drag coefficient of the male pronucleus-microtubule aster complex**. **A** Schematics of forces acting during pronuclear migration. Nuclear, cortical and cytoplasmic dynein motors are depicted. Red arrows represent the velocities of the male and female pronuclei. **B, C** AP female pronucleus migration velocity as a function of male pronucleus migration velocity during the fast and slow migration phases in *goa-1/gpa-16(RNAi)* embryo. **B** Fast phase: a 50 s time-window of female migration has been considered. Pearson correlation coefficient $\rho = -0.68$, $P = 3 \cdot 10^{-12}$ (Pearson correlation coefficient removing the outlier in (-2.3,4.2): $\rho = -0.60$, $P = 3 \cdot 10^{-9}$). Linear fit: angular coefficient = (-1.7 ± 0.2), offset = (-2 ± 3) μm min^{-1}. Henceforth, errors are indicated as 68% confidence bounds. **C** Slow phase: a time-window between 200 s and 100 s before pronuclear meeting has been considered. Pearson correlation coefficient $\rho = -0.06$, $P = 0.42$ (NS). **D** AP female pronucleus migration velocity as a function of male pronucleus migration velocity during the fast migration phase in wild-type embryos. A 50 s time-window of female migration has been considered. Pearson correlation coefficient $\rho = -0.30$, $P = 7 \cdot 10^{-7}$ Linear fit: angular coefficient = (-0.9 ± 0.2), offset = (11 ± 1) μm min^{-1}.

B Modeling the effect of clathrin heavy chain on force generation

At the time we were investigating the mechanisms of centrosome separation by reverse genetics (Chapter 4), a project was ongoing in the lab aimed at dissecting the role of the clathrin heavy chain CHC-1 in *C. elegans* embryos. The attention to clathrin was initially sparked by an RNAi-based functional genomic screen (Gönczy et al., 2000) that revealed that depletion of the clathrin heavy chain CHC-1 resulted in several phenotypes in one-cell embryos and, in particular, in excess centrosome movements during centration/rotation. Initial experiments performed in the lab revealed that excess cortical forces are responsible for excess centrosome movements. Thereafter, Zoltan Spiró demonstrated that clathrin heavy chain depletion perturbs the structure of the actomyosin network and results in partially reduced cortical tension with respect to wild-type. Strikingly, Zoltan Spiró demonstrated that similar excess movements are observed if cortical tension is partially but not completely compromised, independently of clathrin. How can a partial reduction of cortical tension lead to excess cortical forces? Since at the same time I was investigating the forces acting on centrosomes and was planning to develop a computational model of centrosome separation, I joined the project to contribute to shed light on this question from a theoretical perspective. We have developed a minimal model of centrosome rotation that builds on an idea initially proposed in (Kozlowski et al., 2007) and that described the essential features of the interplay between cortical forces and centrosomes. We summarize here our main experimental and theoretical findings.

This work was published in (Spiró et al., 2014), where more experimental details can be found. The experiments were performed by Zoltan Spiró, Kalyani Thyagarajan, Katayoun Afshar and Sylvain Träger. Figures, tables and extracts have been reported here with permission by The Company of Biologists Ltd.

Clathrin heavy chain depletion leads to several defects visible by DIC in one-cell stage embryos (Gönczy et al., 2000). As in other systems, clathrin plays a role in receptor-mediated endocytosis in *C. elegans* and is thus required for proper yolk intake in the oocyte (Fig. B.1A,B, insets) (Grant and Hirsh, 1999). In addition, *chc-1(RNAi)* one-cell embryos exhibit stereotyped microtubule aster positioning defects. In particular, during centration/rotation, instead of the smooth movement of centrosomes and associated pronuclei towards the anterior that

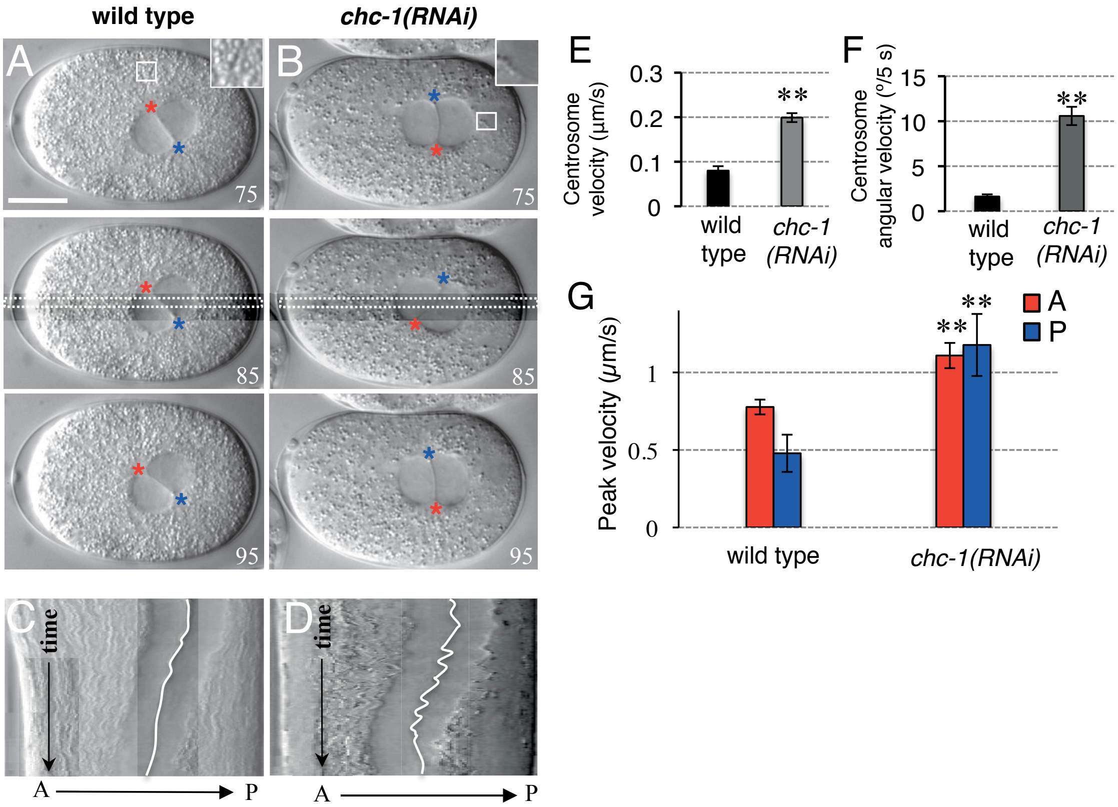

Figure B.1 – **Clathrin negatively regulates net pulling forces acting on centrosomes during centration/rotation. A, B** Centrosome position in wild-type and *chc-1(RNAi)* embryos monitored by time-lapse DIC microscopy. Centrosomes are asterisks (anterior: red; posterior:blue). Insets illustrate the depletion of yolk granules in *chc-1(RNAi)* embryos. Time is indicated in seconds, with $t = 0$ corresponding to pronuclear meeting; scale bar represents 10 μm. **C, D** Kymographs of the areas marked by dashed white rectangles in A and B. The white line delineates the position of the nuclear envelopes of the joined pronuclei. Here, the embryos were imaged with a frame rate of 0.5 s to acquire a kymograph with high resolution. We used the first 150 s from pronuclear meeting onwards to compose the kymographs. **E, F** Average centrosome movements (E) and average angular displacement (F) in wild-type and *chc-1(RNAi)* embryos. n=10 embryos from three experiments in every case. Here and in all figures, error bars represent the SEM and the statistical significance was calculated using unpaired Student's t-test; (**) $P < 0.01$. **G** Average peak velocities of centrosomes following laser severing of microtubules during centration rotation. Posterior cuts (red) and anterior cuts (blue) were performed to evaluate forces acting in both directions. Experiments performed by Zoltan Spiró and Kalyani Thyagarajan.

are characteristic of the wild-type, excess back and forth movements are observed in *chc-1(RNAi)* embryos (Fig. B.1A,B). More specifically, on a short time-scale the absolute velocity of centrosomes as well as their absolute angular displacement during centration/rotation is significantly higher in *chc-1(RNAi)* embryos than in the wild type (Fig. B.1C,D).

A set of experiments performed by collaborators in the lab, in particular Zoltan Spiró and Kalyani Thyagarajan, demonstrated that CHC-1 depletion leads to enhancement of cortical pulling forces during centration/rotation and mitosis. In these experiments, they severed astral microtubules emanating from the anterior or the posterior centrosome. The extent of anteriorly directed net pulling forces was inferred from the velocity of anteriorly directed movements following posterior severing, and that of posteriorly directed net pulling forces from the velocity of posteriorly directed movements following anterior severing (Grill et al., 2001). These experiments revealed that net pulling forces are substantially higher both on the anterior and posterior centrosomes in *chc-1(RNAi)* embryos, compared with the wild type (Fig. B.1E).

Surprisingly, the cortical enrichment of force generators is not increased in *chc-1(RNAi)* embryos (data not shown). Instead, Zoltan Spiró showed that CHC-1 depletion affects the actomyosin network, as demonstrated in other systems (Calabia-Linares et al., 2011; Humphries et al., 2012). In particular, CHC-1 depletion alters the organization of the cortical actomyosin network and leads to diminished cortical tension. To reach this conclusion, Zoltan Spiró performed cortical laser ablation experiments during centration/rotation (COLA; Mayer et al. (2010)). In this assay, cortical tension is deduced from measuring the outward velocities of actin (GFP-MOE) foci following a laser cut along the longitudinal axis of the embryo (Fig. B.2A). These experiments demonstrated that cortical tension is significantly increased during centration/rotation in *chc-1(RNAi)* embryos compared with wild-type (Fig. B.2B,C,D). Importantly, normal cortical pulling forces were partially rescued by treating *chc-1(RNAi)* embryos with the actin polymerizing drug Jasplakinolide (Spiró et al., 2014).

Furthermore, Zoltan Spiró demonstrated that partial inhibition of actomyosin contractility in wild-type embryos, performed by drug treatment or by using the *nmy-2(ne3409)* termosensitive mutant (Liu et al., 2010), results in excess forces (Spiró et al., 2014). Interestingly, further actomyosin contractility inhibition reduces again forces to wild-type levels (Spiró et al., 2014). Thus, high forces are observed only for result for partial inhibition of cortical tension.

How can partial impairment of the actomyosin network result in higher net pulling forces on the microtubule aster? It has been proposed that, during anaphase, depolymerizing microtubules bound to cortical force generators exert a pulling force proportional to the rigidity of the cell cortex, which is related to its tension (Kozlowski et al., 2007). We considered an analogous mechanism during prophase, which is illustrated in Fig. B.3 and summarized hereafter. When a microtubule bound to a cortical force generator depolymerizes, the cortex is stretched and responds with a force that depends on its rigidity and on the stretch. Assuming that the cortex elastic response is linear, the force F applied on the microtubule reads

$$F = kx \tag{B.1}$$

where k is cortical rigidity and x is the stretch.

Moreover, the rate k_{off} at which motors detach from microtubules depends exponentially on

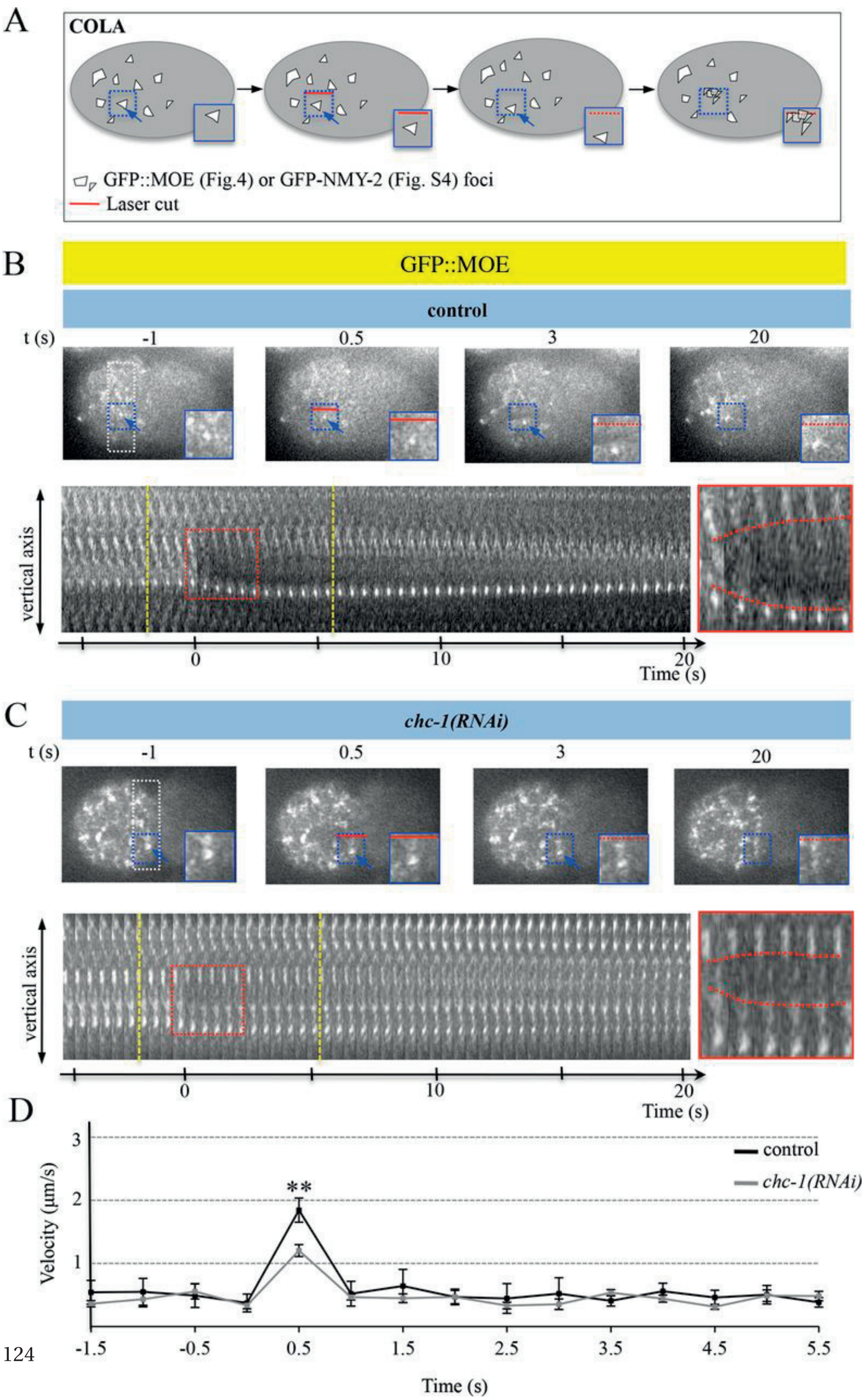
A
COLA
GFP::MOE (Fig.4) or GFP-NMY-2 (Fig. S4) foci
Laser cut
B
GFP::MOE
control
t (s)
-1
0.5
3
20
vertical axis
0
10
20
Time (s)
C
chc-1(RNAi)
t (s)
-1
0.5
3
20
vertical axis
0
10
20
Time (s)
D
Velocity (μm/s)
3
2
1
**
control
chc-1(RNAi)
-1.5
-0.5
0.5
1.5
2.5
3.5
4.5
5.5
Time (s)

the applied force F, as stated by Kramer's theory (Howard (2001)

$$k_{\mathrm{off}} = k_0 e^{\frac{F}{F_0}} \tag{B.2}$$

where k_0 is the detachment rate when no force is applied and F_0 the typical detachment force. Thus, a weaker cortex will produce a less intense force, but for a longer time. In addition, if the stretch overcomes a threshold maximum elongation, detachment follows immediately. This maximum elongation can be set, for example, by the maximum extent the cortex can stretch before giving rise to membrane invagination (Redemann et al., 2010) or by the length of the microtubule itself.

The model predicts maximum total force (i.e. impulse) to be generated for an intermediate value of cortical rigidity, i.e. when motor detachment occurs at a stretch comparable with maximum elongation. Instead, when cortical rigidity is high, an intense force will be exerted for a small time, leading to a reduced impulse. For a small cortical rigidity, a weaker force is applied until the stretch reaches maximum elongation, resulting in reduced impulse as well. Quantitatively, this result can be understood as follows. The typical detachment force is reached when the microtubule has shrunk by a length equal to the detachment stretch $\Delta x_{\mathrm{det}} = \frac{F_0}{k}$. When cortical rigidity is high, i.e. $k > \frac{F_0}{\Delta x_{\mathrm{max}}}$ where Δx_{max} is the maximum elongation, the motor detaches on average at a stretch Δx_{det}, thus before having reached the maximum elongation. In this case, the total impulse J produced by microtubule depolymerization is

$$J = \int_0^{\Delta t_{\mathrm{det}}} F dt = \frac{1}{2}\frac{k}{v_s}\Delta x_{\mathrm{det}}{}^2 = \frac{1}{2}\frac{F_0{}^2}{k v_s} \tag{B.3}$$

and therefore decreases with cortical rigidity. Conversely, when rigidity is low, i.e. when

---

Figure B.2 *(preceding page)* – **Clathrin contributes to cortical tension in *C. elegans* embryos. A** Principle of cortical ablation experiments. Following a longitudinal laser cut in the acto-myosin cell cortex (red line), the movement of GFP::MOE foci (white structures) is monitored. Blue arrows point to one specific focus, whose motion (blue dashed rectangle) is magnified in the insets; the red line marks the position of the cut. The resulting outward velocity is an indirect measure of cortical tension (Mayer et al., 2010). **B, C** Cortical ablation in wild-type and *chc-1(RNAi)* embryos expressing GFP::MOE. Four images from a movie monitoring the cell cortex using spinning disk microscopy are shown, with t=0 corresponding to the time of cut. Blue arrows mark a specific GFP::MOE focus; the red line indicates the cut. The cortex is monitored until the complete recovery of GFP::MOE; the inset in the last frame shows the sealed cortex with the tracked focus coalesced. Below are the kymographs constructed from the area marked by the white rectangle, with the area contoured with the red dashed box magnified on the right to better appreciate the outwards motion (dashed red lines within the box indicate the front of the outward movement). **D** Quantification of initial outward velocities from 1.5 s before to 5.5 s after the cut (indicated with dashed yellow lines on the kymographs); n=9 embryos each from three experiments were analyzed. Experiments performed by Zoltan Spiró.

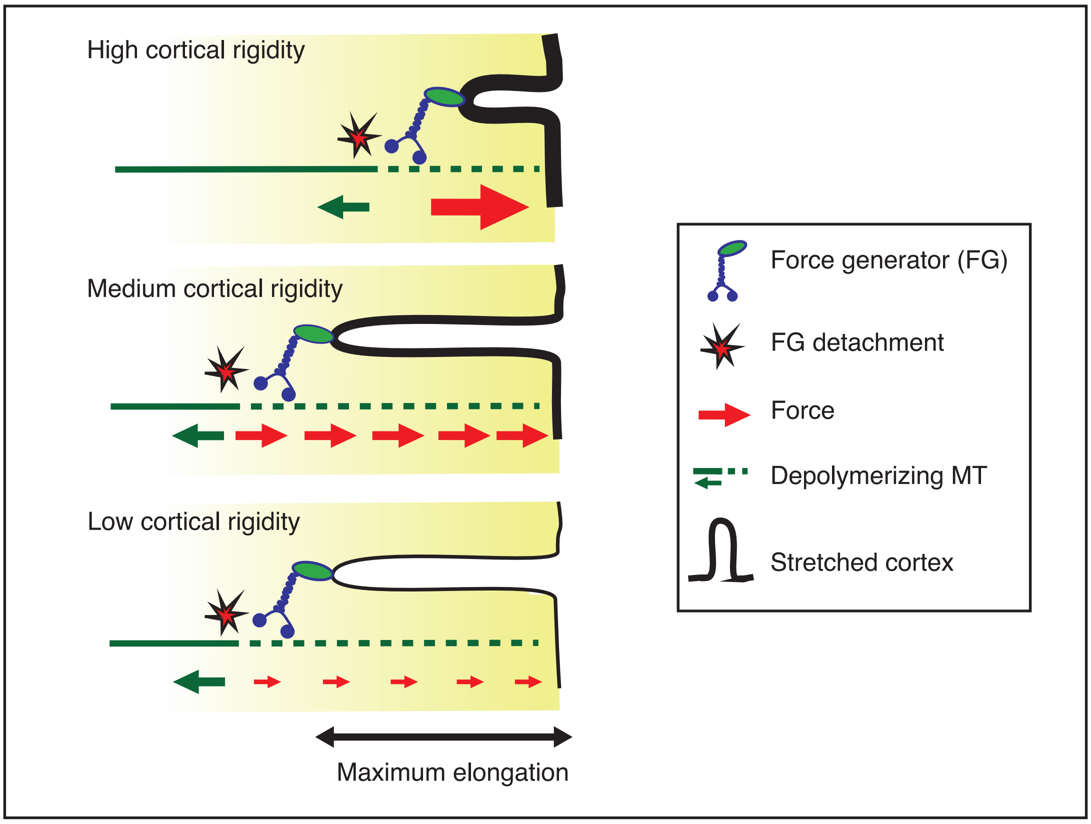
High cortical rigidity
Medium cortical rigidity
Low cortical rigidity
Maximum elongation
Force generator (FG)
FG detachment
Force
Depolymerizing MT
Stretched cortex

Figure B.3 – **Model of cortical force generation** The depolymerizing microtubule bound to a cortical force generator stretches the cortex and thus experiences a pulling reaction force. For high cortical rigidity, a strong elastic force is applied, but the force generator detaches rapidly. For medium cortical rigidity, the stretch reaches the maximum elongation before the force generator detaches, resulting in high total forces (i.e. work). For low cortical rigidity, the stretch also reaches the maximum elongation, but the cortex is too loose to apply a large force.

$k < \frac{F_0}{\Delta x_{\max}}$, the detachment stretch Δx_{det} is larger than the maximum elongation $\Delta x_{\max}$. In this cases, the stretch reaches maximum elongation, therefore causing motor detachment and limiting the total impulse

$$J = \frac{1}{2}\frac{k}{v_s}\Delta x_{\max}{}^2 \tag{B.4}$$

Thus, when cortical rigidity is low, the total impulse produced by microtubule depolymerization increases with rigidity itself. We conclude that the total impulse as a function of cortical rigidity increases for low rigidity, reaches a maximum for the intermediate rigidity $k \sim \frac{F_0}{\Delta x_{\max}}$ and then decreases for high rigidity. This model could thus explain why highest forces are found for intermediate cortical rigidity.

To investigate this mechanism in the context of the *C. elegans* embryo during centration/rotation, we developed a minimal computational model of centrosome rotation driven by cortical force generators (Fig. B.4; see following section for details). This minimal model was developed before our more realistic 3D computational model of centrosome separation based on Cytosim and aimed at describing how centrosome rotational depends on cortical tension by including only the essential components of cytoskeletal dynamics. Therefore, for simplicity, the computational model was developed in 2D, but its qualitative predictions can be extended to the three dimensional case. In this model, a rotating disk representing the two pronuclei is fixed in the center of an ellipsoidal embryo and two microtubule asters emanate from two centrosomes at opposite poles of the disk. Microtubules are dynamic, they undergo growth and shrinkage and can bind to a force generator when abutting the cortex. A pulling force is generated when the microtubule depolymerizes. Parameters for the simulation were set to measured values whenever possible or varied across a reasonable range (Table B.1). Most unknown parameters are similar to the ones that we have chosen later for the 3D computational model of centrosome separation (Table D.1). Notably, some differences in parameters, for example in microtubule number and microtubule growth rate, reflect the later stage of the cell cycle. Strikingly, simulations demonstrate that this model predicts maximum oscillation amplitudes for medium values of cortical rigidity (Fig. B.4D), as evidenced also by plotting the standard deviation of rotational velocity as a function of cortical rigidity (Fig. B.4F). Therefore, the model predicts that excess rotation movements should occur at medium cortical rigidity values, mirroring the phenotypic observations in embryos depleted of CHC-1.

B.1 Computational model details

In the minimal 2D computational model of centrosome oscillatory movements during centration/rotation, the dynamics is overdamped (i.e. inertial effects are neglected) and the cytoplasm is considered at constant viscosity. The hydrodynamics of the cytoplasm is not directly simulated, but the rotational drag coefficient of the pronuclei-microtubule aster is adjusted to consider the effect of confinement of cytoplasm in the eggshell (see section B.1.1; Shinar et al. (2011)). All stochastic events (force generator binding, microtubule catastrophes, microtubule nucleation) occur with a constant probability. The embryo was simulated as a 2D ellipse with a $50\,\mu$m long axis and a $30\,\mu$m short axis. The complex comprising the pronuclei, the centrosomes and the microtubule asters is modeled as a rigid body (Kimura and Onami, 2005). The two pronuclei are modeled as a unique rotating disk positioned in the center of the embryo. The parameters used are listed in Table B.1 and indicated in italics in the text below. Simulations were programmed in MATLAB.

B.1.1 Rotational dynamics

According to rigid body theory (reviewed in Symon, 1971), the rotational speed $\bar{\omega}$ is proportional to the total torque

$$\bar{T} = \sum_{n=1}^{N} \bar{r}_i \times \bar{F}_i = \gamma_{\mathrm{rot}}\bar{\omega} \tag{B.5}$$

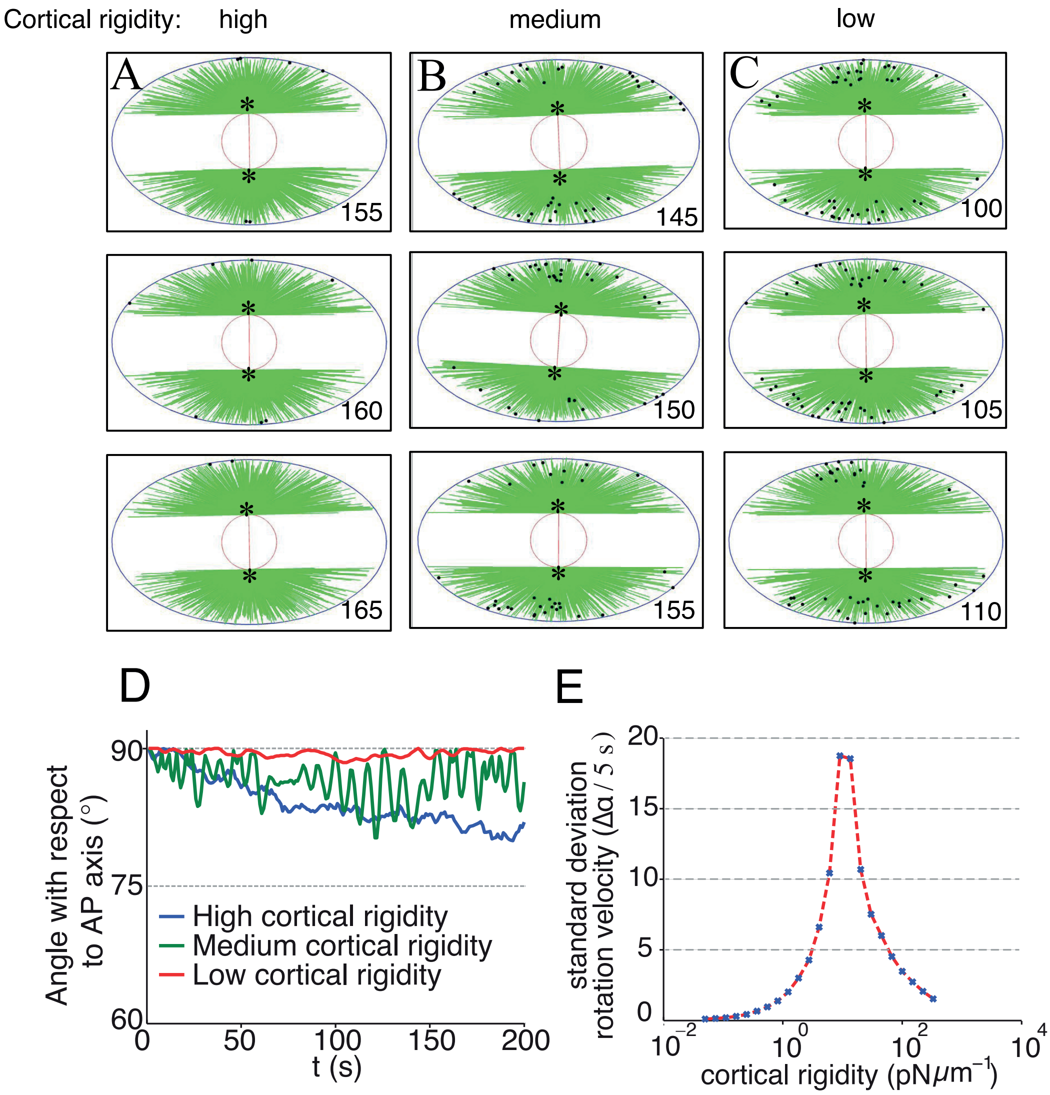

Figure B.4 – **2D computational model of stochastic centrosome movements driven by cortical force generators.A, B, C** Representative frames of simulated movements are shown for high, medium and low cortical rigidity. **D** Representative simulations of stochastic centrosome movements with high (blue), medium (green) or low (red) cortical rigidity (100, 10 and $1\,\mathrm{pN}\,\mu\mathrm{m}^{-1}$, respectively). The centrosome axis is perpendicular to the AP axis. **E** Standard deviation of the angular velocity of the simulated pronuclear oscillations as a function of cortical rigidity. The angular velocity is calculated over time steps of 5 s. n=30 simulations for each cortical rigidity value.

where γ_{rot} is the rotational drag coefficient of the pronuclei-microtubule aster complex resulting from friction with the viscous cytoplasm. Since the size of the pronuclei-microtubule aster complex is comparable to that of the embryo, cytoplasmic flows produced by its movement are affected by the confinement imposed by the eggshell. As a result, the cytoplasmic drag exerted on the pronuclei-microtubule aster complex is increased with respect to the prediction of Stokes law. The impact of confinement on the drag of pronuclei-microtubule aster complex was estimated precedently by using a computational model (Shinar et al., 2011). In that work, a torque comprised between $10-50\,\mathrm{pN}\,\mu\mathrm{m}$ has been estimated for a 90° rotation that occurs approximately in 35 min. From these values and from the Eq. (B.5), it follows that the effective rotational drag can be estimated to be in the order of $5\cdot10^4\,\mathrm{pN\,s}$. It is worth mentioning that this precedent work neglected the hydrodynamic effects due to the drag of the microtubule aster and therefore might result in an underestimation of the total drag (Nazockdast et al., 2015).

B.1.2 Microtubule aster

In our model, the microtubule asters grow from two centrosomes positioned at the two poles of the associated pronuclei. Microtubule nucleation sites are evenly distributed at fixed angles within the two hemicircles around the centrosomes. In the initial configuration, the centrosomes axis is oriented toward the lateral cortex. In (Kozlowski et al., 2007) each centrosome can nucleate up to 300 microtubule fibers and each of them can represent the association of several microtubules. In our model, we have considered 1500 independent microtubules and have thus distributed 1500 nucleation site on each centrosome. Modifying the number of microtubules does not change results qualitatively (microtubule number varied from 1500 to 4500; data not shown). The initial microtubule configuration was set by an initial 100 s phase of microtubule growth and shrinkage during which no forces are applied.

B.1.3 Microtubule dynamics

The dynamic instability of microtubules was modeled as described (Nédélec, 2002; Kimura and Onami, 2005). Microtubules undergo growth and shrinkage dynamics with a catastrophe probability that depends on the applied force. Microtubules pushing against the cortex grow at a slower rate according to the growth-force relationship (Janson et al., 2003). An elastic confinement force limits microtubule growth and restricts them inside the embryo. For simplicity, microtubules shorter than 1 μm are removed from the simulation. In that case, a nucleation site is liberated on the centrosome.

B.1.4 Cortical force generators

Cortical force generators produce force as described (Kozlowski et al., 2007). When a microtubule hits the cortex, it can bind to a force generator with a certain capture rate, which incorporates the density of force generators at the cortex and their binding rate to microtubules. A new cortical force generator is created and fixed to the microtubule tip. During microtubule shrinkage, the association with a given force generator stretches the cortex, thus producing an elastic pulling force. This force is proportional to the distance between the MT tip and the cortex, taken in the prolongation of the microtubule line, as well as to cortical rigidity (note that this cortical rigidity is proportional to cortical tension and reflects the same physical feature of the cortex). The rate k_{off} at which motors detach from microtubules depends exponentially on the applied force F, as stated by Kramer's theory (Howard, 2001)

$$k_{\mathrm{off}} = k_0 e^{\frac{F}{F_0}} \tag{B.6}$$

where k_0 is the detachment rate when no force is applied and F_0 is the typical detachment force. A detached force generator is removed from the simulation.

B.1.5 Asymmetric distribution of force generators

In our model, we have included an asymmetry in the density of cortical force generators to reflect the asymmetry in GPR-1/2 distribution during prophase, being more enriched on the anterior side. This asymmetry has been implemented by a 50% increase in the cortical force generator attachment rate in the anterior with respect to the posterior pole. Moreover, we have implemented a 50% repression in the lateral cortex with respect to the posterior pole to reflect the LET-99 band (Tsou et al., 2002; Kimura and Onami, 2007). These points were implemented by linearly increasing the attachment rate from $0.5\,\mathrm{s}^{-1}$ at the lateral cortex to $1\,\mathrm{s}^{-1}$ at the posterior pole, and $1.5\,\mathrm{s}^{-1}$ on the anterior half. A modification of this asymmetry profile would not change the results from a qualitative point of view.

Simulation Parameter	Value used	References \Notes
Embryo size	50x30x30 μm	
Radius associated pronuclei	5 μm	Kimura and Onami (2005)
Effective rotational drag	$5 \cdot 10^4$ pN s	Estimated from (Shinar et al., 2011)
Time step	0.01 s	
Microtubules		
Rigidity	10 pN μm^2	(Kimura and Onami, 2005)
Nucleation rate	$0.05\,\text{s}^{-1}$	(Kozlowski et al., 2007)
Growth rate	$0.51\,\mu\text{m}\,\text{s}^{-1}$	(Srayko et al., 2005)
Shrinkage rate	$0.84\,\mu\text{m}\,\text{s}^{-1}$	(Kozlowski et al., 2007)
Growth sensitivity to force	1.67 pN	(Dogterom and Yurke, 1997)
Catastrophe rate in cytoplasm	$0.01\,\text{s}^{-1}$	(Kozlowski et al., 2007)
Catastrophe rate at cortex	$5\,\text{s}^{-1}$	
Centrosomes		
MT nucleation sites	1500	(Kozlowski et al., 2007)
Cortical force generators		
Capture rate anterior cortex	$1.5\ s^{-1}$	[1] Varied 1-5 (Kimura and Onami, 2007)
Capture rate posterior cortex	$1\ s^{-1}$	
Capture rate lateroposterior cortex	$0.5\ s^{-1}$	
Unbinding rate unloaded	$k_0 = 0.003\,\text{s}^{-1}$	(Kozlowski et al., 2007)
Unbinding force	10 pN	Varied 3-25 [2] (Kozlowski et al., 2007)
Maximum elongation	5 μm	Varied 1-20 Maximum MT length: 20 μm Average invagination length: 5 μm (Redemann et al., 2010)
Cortical rigidity	200 pN μm^{-1}	Varied 0.1-300 (Kozlowski et al., 2007)

Table B.1 – **Parameters of 2D simulation of cortical tension-dependent centrosome rotation** Simulation parameters used in the simulations are indicated with references. Parameters measured or calculated in the *C. elegans* embryo are italicized.

[1] See main text. The cortical motors capture rate effectively summarizes motor binding rate, binding range and density at the cortex. [2] While motor unbinding force was set equal to dynein stall force in the 3D model of centrosome separation, here cortical force generator unbinding force was set to 10 pN to reflect potentially higher forces deployed by microtubule depolymerization (Grishchuk et al., 2005; Kozlowski et al., 2007). Nevertheless, the qualitative predictions of the model did not change by varying the unbinding force from in the range $3-25$ pN.

C Centrosome separation parameters fit

Condition	α [s^{-1}]	t_0 [s]	K [μm]	σ_{sync} [s]
wild-type [1]	0.0299 ± 0.0009	84 ± 3	8.1 ± 0.1	-
zyg-12(ct350)	0.027 ± 0.004	132 ± 7	17 ± 3	9
bmk-1(ok391)	0.026 ± 0.002	62 ± 7	8.2 ± 0.1	8
goa-1/gpa-16(RNAi)	0.0188 ± 0.0005	150 ± 2	8.4 ± 0.1	6
zyg-12(RNAi) goa-1/gpa-16(RNAi)	0.0054 ± 0.0003	[2]	[2]	8
lin-5(RNAi)	0.0185 ± 0.0005	135 ± 2	8.23 ± 0.09	7
zyg-12(RNAi) lin-5(RNAi)	0.0048 ± 0.0003	[2]	[2]	8
gpr-1/2(RNAi)	0.0221 ± 0.0009	83 ± 3	7.6 ± 0.1	[3]
nmy-2(RNAi)	0.0163 ± 0.0007	112 ± 4	8.6 ± 0.2	8
zyg12(ct350) nmy-2(RNAi)	0.0092 ± 0.0009	[2]	[2]	8
zyg12(ct350) rho-1(RNAi)	0.018 ± 0.004	214 ± 14	8 ± 1	14
nop-1(RNAi)	0.0267 ± 0.0010	145 ± 2	8.72 ± 0.10	[3]
zyg12(ct350) nop-1(RNAi)	0.025 ± 0.003	189 ± 8	9.0 ± 0.3	9
rga-3/4(RNAi)	0.038 ± 0.002	82 ± 3	8.25 ± 0.07	28
zyg-12(ct350) rga-3/4(RNAi)	0.035 ± 0.005	135 ± 9	15.2 ± 0.4	10
zyg-12(ct350) rga-3/4(RNAi) (rep)	0.032 ± 0.004	190 ± 7	13.9 ± 0.6	8
partial *dhc-1(RNAi)*	0.041 ± 0.002	192 ± 2	8.43 ± 0.09	[3]
dyrb-1(RNAi)	0.0198 ± 0.0006	104 ± 3	8.78 ± 0.09	[3]
zyg-12(ct350) klp-7(RNAi)	0.017 ± 0.003	61 ± 17	9.9 ± 0.6	9

Table C.1 – **Fitted parameters of centrosome separation.** Each centrosome separation curve has been fitted with a custom logistic function (Materials and Methods). Each parameter is shown with standard error. α is the centrosome separation rate, t_0 is the centrosome separation onset and K is the equilibrium final distance. σ_{sync} is the error in the curve synchronization procedure.

[1] The initial separation d_0 in all the mutant/RNAi conditions is set to the value fitted for the wild-type $d_0 = (0.8 \pm 0.1)\,\mu$m. *(continues on next page)*

[2] In this condition, centrosome separation onset time and equilibrium distance could not be estimated since the relative centrosome separation curve is not sigmoidal and does not reach an equilibrium plateau.
[3] The P-value of the χ^2 for the best synchronization is below the threshold 0.05, therefore the two average radii curves are significantly different and the synchronization cannot be considered reliable.

Condition	wild-type	*zyg-12(ct350)*
zyg-12(ct350)	0.46 (NS)	-
bmk-1(ok391)	0.09 (NS)	-
goa-1/gpa-16(RNAi)	$< 10^{-38}$ (***)	-
zyg-12(RNAi) goa-1/gpa-16(RNAi)	$< 10^{-38}$(***)	$5 \cdot 10^{-7}$ (***)
lin-5(RNAi)	$< 10^{-38}$ (***)	-
zyg-12(RNAi) lin-5(RNAi)	$< 10^{-38}$(***)	$6 \cdot 10^{-10}$ (***)
gpr-1/2(RNAi)	$2 \cdot 10^{-9}$(***)	-
nmy-2(RNAi)	$< 10^{-38}$ (***)	-
zyg12(ct350) nmy-2(RNAi)	$< 10^{-38}$ (***)	$7 \cdot 10^{-7}$ (***)
zyg12(ct350) rho-1(RNAi)	$4 \cdot 10^{-3}$ (**)	0.04 (*)
nop-1(RNAi)	0.02 (*)	-
zyg12(ct350) nop-1(RNAi)	0.06 (NS)	0.68 (NS)
rga-3/4(RNAi)	$3 \cdot 10^{-5}$ (***)	-
zyg-12(ct350) rga-3/4(RNAi)	0.31 (NS)	0.44 (NS)
zyg-12(ct350) rga-3/4(RNAi) (rep)	0.57 (NS)	0.71 (NS)
partial *dhc-1(RNAi)*	$6 \cdot 10^{-8}$ (***)	-
dyrb-1(RNAi)	$< 10^{-38}$ (***)	-
zyg-12(ct350) klp-7(RNAi)	$9 \cdot 10^{-5}$ (***)	0.01 (*)

Table C.2 – **Comparison of centrosome separation rate α between mutant/RNAi and reference conditions.** The P-value resulting from the comparison of centrosome separation rates α in the indicated conditions is shown (z-test). * : $P < 0.05$, **: $P < 0.01$, ***: $P < 0.001$, NS: not significant difference.

Condition	wild-type	*zyg-12(ct350)*
zyg-12(ct350)	$5 \cdot 10^{-5}$ (***)	-
bmk-1(ok391)	0.05 (NS)	-
goa-1/gpa-16(RNAi)	$< 10^{-38}$ (***)	-
zyg-12(RNAi) goa-1/gpa-16(RNAi)	-	-
lin-5(RNAi)	$2 \cdot 10^{-10}$ (***)	-
zyg-12(RNAi) lin-5(RNAi)	-	-
gpr-1/2(RNAi)	[1]	-
nmy-2(RNAi)	$3 \cdot 10^{-3}$ (**)	-
zyg12(ct350) nmy-2(RNAi)	$3 \cdot 10^{-6}$ (***)	10^{-3} (**)
zyg12(ct350) rho-1(RNAi)	10^{-10} (***)	10^{-4} (***)
nop-1(RNAi)	[1]	-
zyg12(ct350) nop-1(RNAi)	$< 10^{-38}$ (***)	$5 \cdot 10^{-4}$ (***)
rga-3/4(RNAi)	0.94 (NS)	-
zyg-12(ct350) rga-3/4(RNAi)	$2 \cdot 10^{-4}$ (***)	0.68 (NS)
zyg-12(ct350) rga-3/4(RNAi) (rep)	$< 10^{-38}$ (***)	$3 \cdot 10^{-5}$ (***)
partial *dhc-1(RNAi)*	[1]	-
dyrb-1(RNAi)	[1]	-
zyg-12(ct350) klp-7(RNAi)	0.23 (NS)	$2 \cdot 10^{-3}$ (**)

Table C.3 – **Comparison of centrosome separation starting time t_0 between mutant/RNAi and reference conditions.** The P-value resulting from the comparison of centrosome separation rates α in the indicated conditions is shown (z-test). * : P < 0.05, **: P < 0.01, ***: P <0.001, NS: not significant difference.

[1] The onset time of centrosome separation was not comparable in this cases, since synchronization was not reliable.

D Computational model parameters

Simulation Parameter	Value used	References \Notes
Embryo size	50x30x30 μm	
Viscosity	1 Pa s	(Daniels et al., 2006)
Time step	0.01 s	
MT segmentation	1 μm	
Motor anchoring points on pronucleus	1000	[1]
Microtubules		
Rigidity	20 pN μm^2	(Kimura and Onami (2005) Kozlowski et al. (2007) Dogterom and Yurke (1997))
Nucleation rate	$0.05\,\mathrm{s}^{-1}$	(Kozlowski et al., 2007)
Growth rate	$v_g = 0.74\,\mu\mathrm{m\,s}^{-1}$	0.17 in *zyg-9(RNAi)* (Srayko et al., 2005)
Shrinkage rate	$0.84\,\mu\mathrm{m\,s}^{-1}$	(Kozlowski et al., 2007)
Growth sensitivity to force	$f_g = 1.67$ pN	(Dogterom and Yurke, 1997)
Catastrophe rate in cytoplasm	$0.01\,\mathrm{s}^{-1}$	(Kozlowski et al., 2007) Varied 0.01-0.05 in *zyg-9(RNAi)*
Catastrophe rate in cytoplasm (stalled)	$0.05\,\mathrm{s}^{-1}$	(Kozlowski et al., 2007) Varied 0.05-0.25 in *zyg-9(RNAi)*
Catastrophe rate at cortex	$1\,\mathrm{s}^{-1}$	(Kozlowski et al., 2007) Varied 1-5 in *zyg-9(RNAi)*
Centrosomes		
Radius	0.5 μm	

MT nucleation sites	500	Varied 100-2000 (Kozlowski et al., 2007)
Pronuclei		
Initial radius	$R_0 = 3\ \mu\mathrm{m}$	This study
Radius growth rate	$R' = 0.0029\ \mu\mathrm{m}\,\mathrm{s}^{-1}$	This study. $R = R_0 + \mathrm{time}R'$
Effective drag coefficient	$X = 94\,\mathrm{kg}\,\mu\mathrm{m}\,\mathrm{s}^{-1}$	Drag force = XR velocity (Shinar et al., 2011)
Distance center male - posterior	$4\ \mu\mathrm{m}$	Male pronucleus is at the posterior pole
Distance center female - anterior	$8\ \mu\mathrm{m}$	This study
Female drift toward posterior	$0.016\ \mu\mathrm{m}\,\mathrm{s}^{-1}$	This study (for $t < 240$ s)
Dynein Motors (minus-end directed)		
Unbinding force	$f_u = 2.5$ pN	(Rupp and Nédélec, 2012)
Unloaded velocity	$v_0 = 1.5\ \mu\mathrm{m}\,\mathrm{s}^{-1}$	Measurements 1-2 (Kimura and Onami, 2005; Reck-Peterson et al., 2012; Howard, 2001; Athale et al., 2014)
Stall force	$f_s = 2.5$ pN	Measurements 1-7 (Reck-Peterson et al., 2012; Howard, 2001; Athale et al., 2014; Goshima et al., 2005)
Pronuclear dynein motors		
Surface density	$29\,\mu\mathrm{m}^{-2}$	Fitted [2]. Varied 9-90
Binding range	$0.05\,\mu\mathrm{m}$	[3]
Binding rate	$20\,\mathrm{s}^{-1}$	
Unbinding rate	$k_u = 1\,\mathrm{s}^{-1}$	[4]
Cortical dynein motors		
Capture rate	$2.8\ s^{-1}$	Fitted [3,5]. Varied 1-5
Unbinding rate	$k'_u = 0.003\,\mathrm{s}^{-1}$	Varied 0.003-1 [4] [45]
Cortical flow speed	$0.16\ \mu\mathrm{m}\,\mathrm{s}^{-1}$	0 (anterior) to 0.16 (posterior) (Munro et al., 2004; Mayer et al., 2010)

Table D.1 – **Parameters of 3D simulation of centrosome separation** Simulation parameters used in the simulations are indicated with references. Parameters measured or calculated in the *C. elegans* embryo are italicized.

[1] In the wild-type, from 3250 to 5620 motors are distributed over 1000 points on the surface of each pronucleus (each point can harbor multiple motors).

[2] See Materials and Methods.

[3] Dynein complex length is possibly larger than 0.04 μm (Reck-Peterson et al., 2012).

---

[4] Pronuclear motors unbinding rate is deduced from measurements of dynein processivity 1-2 μm (Reck-Peterson et al., 2012) and dynein velocity 1.5 $\mu\mathrm{m\,s^{-1}}$ (Reck-Peterson et al., 2012; Howard, 2001; Athale et al., 2014; Goshima et al., 2005). Decreasing this value does not change the qualitative predictions of the model. Unbinding rate of cortical motors attached to the MT tip has been set according to (Reck-Peterson et al., 2012; Howard, 2001; Athale et al., 2014; Goshima et al., 2005). If cortical unbinding rate is increased up to $1\,\mathrm{s^{-1}}$, as for pronuclear motors, cortical forces are strongly reduced, but can be restored by adjusting other parameters, such as cortical motors unbinding force, capture rate, microtubule aster effective drag or the number of motors acting simultaneously on a microtubule.

[5] See Materials and Methods. The cortical motors capture rate effectively summarizes motor binding rate, binding range and density at the cortex.

E Movies legends

Movie 1	Centrosome separation in wild–type embryos. Here and thereafter (Movie 1 - Movie 8), one-cell stage embryos expressing GFP::TAC-1 are imaged using 3D time-lapse DIC and fluorescent microscopy (GFP). Time is indicated in seconds, with 0 s defined as the earliest time-point in which two separate centrosomes could be detected in the whole synchronized wild-type dataset; scale bars represent 10 μm. An image stack was captured every 6-12 seconds and the z-projection of centrosome position merged with the DIC image (Materials and Methods).
Movie 2	Centrosome separation in *zyg-12(ct350)* embryos.
Movie 3	Centrosome separation in *zyg-12(ct350) goa-1/gpa-16(RNAi)* embryos.
Movie 4	Centrosome separation in *goa-1/gpa-16(RNAi)* embryos.
Movie 5	Centrosome separation in *zyg-12(ct350) nmy-2(RNAi)* embryos. In this movie it can be seen that *zyg-12(ct350) nmy-2(RNAi)* embryos exhibit lack of contractility, an absence of cortical flows and of pseudo-clevage furrow ingression.
Movie 6	Centrosome separation in *nmy-2(RNAi)* embryos.
Movie 7	Centrosome separation in *zyg-9(RNAi)* embryos. In this case centrosomes are marked by GFP::AIR-1 and not by GFP ::TAC-1. The size of the female pronucleus is underestimated since it is partially out of focus.
Movie 8	Centrosome separation in *rga-3/4(RNAi)* embryos.
Movie 9	Simultaneous flow of Lifeact:mKate2 (signal represented by grayscale image; measured velocity represented by red arrows) and YFP::GPR-1 (signal not shown; measured velocity represented by green arrows). Time is indicated in seconds; scale bar 10 μm.
Movie 10	Simulation of centrosome separation in wild-type. Here and thereafter (Movie 9 - Movie 22), nuclear dynein (blue dots), cortical dynein (red dots), pronuclei (blue spheres), centrosomes (green dots), microtubules (white lines) and cortex (light grey ellipse in

transparence) are depicted. For visual clarity, inactive motors are hidden and only 1/4 microtubule is shown. See text, as well as Materials and Methods for additional information.

Movie 11 Simulation of centrosome separation in *zyg-12(ct350)*.

Movie 12 Simulation of centrosome separation in *goa-1/gpa-16(RNAi)*.

Movie 13 Simulation of centrosome separation in *zyg-12(ct350) goa-1/gpa-16(RNAi)* .

Movie 14 Simulation of centrosome separation in *nmy-2(RNAi)*.

Movie 15 Simulation of centrosome separation in *zyg-12(ct350) nmy-2(RNAi)*.

Movie 16 Simulation of centrosome separation in *zyg-9(RNAi)*.

Movie 17 Simulation of nuclear dynein-based centrosome separation in *goa-1/gpa-16(RNAi)* embryos when centrosomes and male pronucleus are positioned in the cell center.

Movie 18 Simulation of nuclear dynein-based centrosome separation in *goa-1/gpa-16(RNAi)* embryos when there is no steric interaction between microtubules and centrosomes.

Movie 19 Simulation of nuclear dynein-based centrosome separation in *goa-1/gpa-16(RNAi)* embryos when the male pronucleus does not grow in size.

Movie 20 Simulation of nuclear dynein-based centrosome separation in *goa-1/gpa-16(RNAi)* embryos when there the centrosomes and male pronucleus are positioned in the cell center, centrosomes do not interact sterically with microtubules and the pronucleus does not grow in size.

Movie 21 Simulation of cortical dynein-based centrosome separation in *zyg-12(ct350)* when centrosomes are initially at a side position along the cortex.

Movie 22 Simulation of cortical dynein-based centrosome movement when the flow origin follows centrosome position.

Movie 23 Simulation of cortical dynein-based centrosome movement when the flow origin is fixed at the posterior pole of the embryo.

Acknowledgements

These four years in Lausanne have been among the most intense, rich and meaningful of my life. I feel to have lived, learned and received a lot. I am thankful to many people for that.

First of all, I would like to thank my advisor, Pierre, to whom I am extremely grateful for having taken me on board and guided through this fascinating project. It is difficult to synthesize years of support and dedication in a few words, but, in particular, I would like to thank him for his patience and for having always been incredibly motivating. After every meeting, I came out of his office full of new energy and ideas. This spirit has sustained me through all these years. In addition, I would like to thank him for all the time he devoted to teach me biology, to help me to grow as a scientist and to find my way. Finally, I would like to thank him for his dedication in teaching me how to communicate science in talks, manuscripts and actions.

I am thankful to Felix, my co-supervisor, for having helped me during my Ph.D. and for having hosted me in his Lab. I am particularly grateful to François Nédélec for having introduced me to Cytosim and greatly supported during these years. In particular, I would like to thank him for having been a reference point in physical biology and having always generously replied to my numerous questions. I am also grateful to him, Stephan Grill, Viesturs Simanis, Daniel Constam and Gisou van der Goot for their feedback on my thesis and to have sacrificed time to be part of my Candidacy Committee and/or Thesis Jury. I would like to express my gratitude to Antonio Celani for his continuing support, guidance and for feedback on this thesis.

During these years at EPFL, I felt at home. For sure, I felt at home in the Gönczy Lab. I would like to thank all the past and present members of the lab for the great moments that we shared, in the lab and outside: Simon, for having unofficially been my mentor and having introduced me to MATLAB; Alex, Christian, Fernando, Lukas and Sachin for having guided me in the wet lab and for their patience in teaching me biology; Zoltan, for the great collaboration on the clathrin project, for teaching me PCR and for the amazing fun time; Aitana, for useful discussions and for help with the pronuclei tracking algorithm; Coralie and Isabelle, because without them I am lost in five minutes, swollen by contamination; Georgios and Melina, for the nice atmosphere that they create in our lab corner; and finally Debora, Jian, Kalyani, Katy, Merixtell, Nicola, Paul, Radek, Sylvain, Veronika, Virginie, Zhou and the Naef Lab for the deep discussions and fun. I would like to express my gratitude to the BiOP team for their support and training, especially Thierry, Olivier and José. I am also thankful to Nicole, for her patience in dealing with my trips, and Tatiana, for her passion and friendly help.

A day in EPFL is incomplete without an amazing lunch-time. Thus, thank you to: the CP Committee, Christian, Mauro e Livio, for our (not so) deeply intellectual conversations; Anna, for the storm of books, movies, stories and wit; Bea, Claudia, Ilaria, Julia, Ingrid and Rosy, for the nice moments we shared and for help in dealing with the challenges of life; Daniele, Fabrizia, Marco, Marco, Samuele and most of friends mentioned above for the big laughs during the Italian Lunches.

Furthermore, I would like to thank all friends with whom I shared rewarding emotions on stage: the Pourquoi-Pas?, for the great adventure of Stile Libero and for having been a reference point; les Polyssons, for welcoming me and dealing with my Italian accent; the Impro-Pas, for having been great pals in learning improvisation theatre and having trusted my leadership during this last summer; the Polyglot, for the challenge and fun of acting in different languages. I would like to thank in particular Luca Bartesaghi, for Stile Libero, for having introduced me to improvisation and lead us with impressive patience; Mirko Bacchini, for having supported me during my time with Les Polyssons.

During these years, I have met great friends that I hope I will keep for life. It would be pretty long to name everybody, but I would like to thank in particular: Christian, for being great and because time together is so much fun; Ilaria, for all the adventures we shared and for her constant help; her and the Moscorojans, for having been a second home; Elettra, for her energy, sincerity and trust; Andrea, for the fascinating conversations and good beers; him and the chess friends, because it feels so good to wake up on Sunday morning and go to play chess at Starbucks; Lukas, Fernando, Simon and Luca, for the board games nights; Andrea, Tanja, all the friends mentioned above and many others, for the evenings and parties together. I would also like to thank Davide, Enrico, Fabrizio, Alberto e Marco, gli Amici Miei. During my education path, I had the luck to meet great mentors, who eventually became friends: thanks to Felicita, for pointing out that I was meant to be a scientist; Mauro, for introducing me to physics and keeping donating me food for the brain; Anna, for teaching me to seek beauty and meaning; Mariella, for teaching me the power of poetry and how to be on stage.

Infine, i miei ringraziamenti più profondi vanno alla mia famiglia, la quale è stata un ambiente felice in cui crescere e che mi ha amato, aiutato e motivato in tutti questi anni. Vorrei ringraziare mamma e papà per essere dei modelli, per essermi sempre stati vicini e per credere in me. Inoltre, vorrei ringraziarli per avermi insegnato la curiosità e dato la libertà di esplorare e approfondire le mie passioni. Vorrei ringraziare Andrea, per aver condiviso con me l'infazia e l'adolescenza, perché è bello ritrovarsi adulti insieme e per avermi insegnato il valore dell'essere diversi. Vorrei ringraziare i nonni, con cui ho avuto la gioia di trascorrere così tanto tempo, per il loro affetto e per le loro affascinanti personalità. E ancora grazie a Marino, Cinzia, Valter, Claudia, Manuel e Silvia per essere una famiglia meravigliosa.

Finally, I would like to thank Erika, for her love, support, inspiration, creative energy, wonder and for connecting the dots of this scattered life.

Bibliography

Afshar, K., Willard, F. S., Colombo, K., Johnston, C. A., McCudden, C. R., Siderovski, D. P., and Gönczy, P. (2004). RIC-8 is required for GPR-1/2-dependent Galpha function during asymmetric division of *C. elegans* embryos. *Cell*, 119(2):219–30.

Afshar, K., Willard, F. S., Colombo, K., Siderovski, D. P., and Gönczy, P. (2005). Cortical localization of the Galpha protein GPA-16 requires RIC-8 function during *C. elegans* asymmetric cell division. *Development*, 132(20):4449–59.

Ahringer, J. (2006). Reverse genetics. In *WormBook : the online review of C. elegans biology*. WormBook.

Aist, J., Liang, H., and Berns, M. (1993). Astral and spindle forces in PtK2 cells during anaphase B: a laser microbeam study. *J. Cell Sci.*, 104(4):1207–1216.

Aist, J. R., Bayles, C. J., Tao, W., and Berns, M. W. (1991). Direct experimental evidence for the existence, structural basis and function of astral forces during anaphase B in vivo. *Journal of cell science*, 100(1981):279–88.

Aist, J. R. and Berns, M. W. (1981). Mechanics of chromosome separation during mitosis in Fusarium (*Fungi imperfecti*): new evidence from ultrastructural and laser microbeam experiments. *The Journal of cell biology*, 91(2 Pt 1):446–58.

Akhmanova, A. and Steinmetz, M. O. (2008). Tracking the ends: a dynamic protein network controls the fate of microtubule tips. *Nature reviews. Molecular cell biology*, 9(4):309–22.

Alberts, B., Johnson, A., Lewis, J., Morgan, D., Raff, M., Roberts, K., and Walter, P. (2014). Molecular biology of the cell. *Garland Science*.

Albertson, D. G. (1984). Formation of the first cleavage spindle in nematode embryos. *Developmental biology*, 101(1):61–72.

Asbury, C. L., Gestaut, D. R., Powers, A. F., Franck, A. D., and Davis, T. N. (2006). The Dam1 kinetochore complex harnesses microtubule dynamics to produce force and movement. *Proceedings of the National Academy of Sciences of the United States of America*, 103(26):9873–8.

Athale, C. a., Dinarina, A., Nedelec, F., and Karsenti, E. (2014). Collective behavior of minus-ended motors in mitotic microtubule asters gliding toward DNA. *Physical biology*, 11(1):016008.

Basto, R., Lau, J., Vinogradova, T., Gardiol, A., Woods, C. G., Khodjakov, A., and Raff, J. W. (2006). Flies without Centrioles. *Cell*, 125(7):1375–1386.

Beaudouin, J., Gerlich, D., Daigle, N., Eils, R., and Ellenberg, J. (2002). Nuclear envelope breakdown proceeds by microtubule-induced tearing of the lamina. *Cell*, 108(1):83–96.

Bellanger and Gönczy (2003). TAC-1 and ZYG-9 form a complex that promotes microtubule assembly in *C. elegans* embryos. *Current Biology*, 13(17):1488–1498.

Bienkowska, D. and Cowan, C. R. (2012). Centrosomes can initiate a polarity axis from any position within one-cell *C. elegans* embryos. *Current biology*, 22(7):583–9.

Bishop, J. D., Han, Z., and Schumacher, J. M. (2005). The *Caenorhabditis elegans* Aurora B kinase AIR-2 phosphorylates and is required for the localization of a BimC kinesin to meiotic and mitotic spindles. *Molecular biology of the cell*, 16(2):742–56.

Blanchoud, S., Busso, C., Naef, F., and Gönczy, P. (2015). Quantitative analysis and modeling probe polarity establishment in *C. elegans* embryos. *Biophysical journal*, 108(4):799–809.

Boettcher, B. and Barral, Y. (2013). The cell biology of open and closed mitosis. *Nucleus*, 4(3):160–5.

Bornens, M. (2012). The centrosome in cells and organisms. *Science*, 335(6067):422–6.

Bornens, M. and Gönczy, P. (2014). Centrosomes back in the limelight. *Philosophical transactions of the Royal Society of London. Series B, Biological sciences*, 369(1650):20130452–.

Brangwynne, C. P. (2006). Microtubules can bear enhanced compressive loads in living cells because of lateral reinforcement. *The Journal of Cell Biology*, 173(5):733–741.

Brauchle, M., Baumer, K., and Gönczy, P. (2003). Differential activation of the DNA replication checkpoint contributes to asynchrony of cell division in *C. elegans* embryos. *Current biology*, 13(10):819–27.

Buttrick, G. J., Beaumont, L. M. A., Leitch, J., Yau, C., Hughes, J. R., and Wakefield, J. G. (2008). Akt regulates centrosome migration and spindle orientation in the early *Drosophila* melanogaster embryo. *The Journal of cell biology*, 180(3):537–48.

Cabral, G., Sanegre Sans, S., Cowan, C. R. R., Dammermann, A., Sans, S. S., Cowan, C. R. R., and Dammermann, A. (2013). Multiple Mechanisms Contribute to Centriole Separation in *C. elegans*. *Current Biology*, 23(14):1380–1387.

Calabia-Linares, C., Robles-Valero, J., de la Fuente, H., Perez-Martinez, M., Martín-Cofreces, N., Alfonso-Pérez, M., Gutierrez-Vázquez, C., Mittelbrunn, M., Ibiza, S., Urbano-Olmos, F. R., Aguado-Ballano, C., Sánchez-Sorzano, C. O., Sanchez-Madrid, F., and Veiga, E. (2011). Endosomal clathrin drives actin accumulation at the immunological synapse. *Journal of cell science*, 124(Pt 5):820–30.

Cao, J., Crest, J., Fasulo, B., and Sullivan, W. (2010). Cortical Actin Dynamics Facilitate Early-Stage Centrosome Separation. *Current Biology*, 20(8):770–776.

Colombo, K., Grill, S. W., Kimple, R. J., Willard, F. S., Siderovski, D. P., and Gönczy, P. (2003). Translation of polarity cues into asymmetric spindle positioning in *Caenorhabditis elegans* embryos. *Science*, 300(5627):1957–1961.

Corsi, A. K., Wightman, B., and Chalfie, M. (2015). A Transparent window into biology: A primer on *Caenorhabditis elegans*. *WormBook : the online review of C. elegans biology*, pages 1–31.

Coue, M., Lombillo, V. A., and McIntosh, J. R. (1991). Microtubule depolymerization promotes particle and chromosome movement in vitro. *The Journal of cell biology*, 112(6):1165–75.

Couwenbergs, C., Labbé, J. C., Goulding, M., Marty, T., Bowerman, B., and Gotta, M. (2007). Heterotrimeric G protein signaling functions with dynein to promote spindle positioning in *C. elegans*. *Journal of Cell Biology*, 179(1):15–22.

Cytrynbaum, E. N., Scholey, J. M., and Mogilner, A. (2003). A force balance model of early spindle pole separation in *Drosophila* embryos. *Biophysical journal*, 84(2 Pt 1):757–69.

Cytrynbaum, E. N., Sommi, P., Brust-Mascher, I., Scholey, J. M., and Mogilner, A. (2005). Early Spindle Assembly in Drosophila Embryos: Role of Force Balance Involving Cytoskeletal Dynamics and Nuclear Mechanics. *Molecular biology of the cell*, 16(10):4967–4981.

Daniels, B. R., Masi, B. C., and Wirtz, D. (2006). Probing single-cell micromechanics in vivo: the microrheology of *C. elegans* developing embryos. *Biophysical journal*, 90(12):4712–4719.

De Simone, A., Nédélec, F., and Gönczy, P. (2016). Dynein transmits polarized actomyosin cortical flows to promote centrosome separation. *Cell Reports*, doi: 10.1016/j.celrep.2016.01.077.

Delattre, M., Leidel, S., Wani, K., Baumer, K., Bamat, J., Schnabel, H., Feichtinger, R., Schnabel, R., and Gönczy, P. (2004). Centriolar SAS-5 is required for centrosome duplication in *C. elegans*. *Nature Cell Biology*, 6(7):656–664.

Desai, A. and Mitchison, T. J. (1997). Microtubule polymerization dynamics. *Annual review of cell and developmental biology*, 13:83–117.

Dogterom, M. (1997). Measurement of the Force-Velocity Relation for Growing Microtubules. *Science*, 278(5339):856–860.

Dogterom, M., Kerssemakers, J. W., Romet-Lemonne, G., and Janson, M. E. (2005). Force generation by dynamic microtubules. *Current Opinion in Cell Biology*, 17(1):67–74.

Dogterom, M. and Leibler, S. (1993). Physical Aspects of the Growth and Regulation of Microtubule Structures. *Physical Review Letters*, 70(9):1347–1350.

Dogterom, M. and Yurke, B. (1997). Measurement of the force-velocity relation for growing microtubules. *Science*, 278(5339):856–860.

Dogterom, M. and Yurke, B. (1998). Microtubule Dynamics and the Positioning of Microtubule Organizing Centers. *Physical Review Letters*, 81(2):485–488.

Dominguez, R. and Holmes, K. C. (2011). Actin structure and function. *Annual review of biophysics*, 40:169–86.

Drummond, D. R. and Cross, R. A. (2000). Dynamics of interphase microtubules in Schizosaccharomyces pombe. *Current Biology*, 10(13):766–775.

Dujardin, D. L. and Vallee, R. B. (2002). Dynein at the cortex. *Current Opinion in Cell Biology*, 14(1):44–49.

Dumont, J. and Desai, A. (2012). Acentrosomal spindle assembly and chromosome segregation during oocyte meiosis. *Trends in cell biology*, 22(5):241–9.

Ems-McClung, S. C. and Walczak, C. E. (2010). Kinesin-13s in mitosis: Key players in the spatial and temporal organization of spindle microtubules. *Seminars in Cell and Developmental Biology*, 21(3):276–282.

Encalada, S. E., Willis, J., Lyczak, R., and Bowerman, B. (2005). A spindle checkpoint functions during mitosis in the early *Caenorhabditis elegans* embryo. *Molecular biology of the cell*, 16(3):1056–70.

Ferenz, N. P., Gable, A., and Wadsworth, P. (2010). Mitotic functions of kinesin-5.

Firestone, A. J., Weinger, J. S., Maldonado, M., Barlan, K., Langston, L. D., O'Donnell, M., Gelfand, V. I., Kapoor, T. M., and Chen, J. K. (2012). Small-molecule inhibitors of the AAA+ ATPase motor cytoplasmic dynein. *Nature*, 484(7392):125–9.

Foethke, D., Makushok, T., Brunner, D., and Nédélec, F. (2009). Force- and length-dependent catastrophe activities explain interphase microtubule organization in fission yeast. *Mol. Sys. Biol.*, 5(241):1–6.

Fu, C., Ward, J. J., Loiodice, I., Velve-Casquillas, G., Nedelec, F. J., and Tran, P. T. (2009). Phospho-regulated interaction between kinesin-6 Klp9p and microtubule bundler Ase1p promotes spindle elongation. *Developmental cell*, 17(2):257–67.

Fygenson, D. K., Marko, J. F., and Libchaber, A. (1997). Mechanics of Microtubule-Based Membrane Extension. *Physical Review Letters*, 79(22):4497–4500.

Goldstein, B. and Hird, S. N. (1996). Specification of the anteroposterior axis in *Caenorhabditis elegans*. *Development*, 122(5):1467–1474.

Gönczy, P. (2008). Mechanisms of asymmetric cell division: flies and worms pave the way. *Nature Reviews Molecular Cell Biology*, 9(5):355–366.

Gönczy, P., Echeverri, C., Oegema, K., Coulson, A., Jones, S. J., Copley, R. R., Duperon, J., Oegema, J., Brehm, M., Cassin, E., Hannak, E., Kirkham, M., Pichler, S., Flohrs, K., Goessen, A., Leidel, S., Alleaume, A. M., Martin, C., Ozlü, N., Bork, P., and Hyman, A. A. (2000). Functional genomic analysis of cell division in *C. elegans* using RNAi of genes on chromosome III. *Nature*, 408(6810):331–6.

Gönczy, P., Pichler, S., Kirkham, M., and Hyman, A. A. (1999). Cytoplasmic dynein is required for distinct aspects of MTOC positioning, including centrosome separation, in the one cell stage *Caenorhabditis elegans* embryo. *Journal of Cell Biology*, 147(1):135–150.

Goshima, G., Nédélec, F., and Vale, R. D. (2005). Mechanisms for focusing mitotic spindle poles by minus end-directed motor proteins. *The Journal of cell biology*, 171(2):229–40.

Gotta, M., Ahringer, J., M, G., JA, A., Gotta, M., and Ahringer, J. (2001). Distinct roles for Galpha and Gbetagamma in regulating spindle position and orientation in *Caenorhabditis elegans* embryos. *Nature cell biology*, 3(3):297–300.

Gotta, M., Dong, Y., Peterson, Y. K., Lanier, S. M., and Ahringer, J. (2003). Asymmetrically distributed *C. elegans* homologs of AGS3/PINS control spindle position in the early embryo. *Current biology*, 13(12):1029–37.

Goulding, M. B., Canman, J. C., Senning, E. N., Marcus, A. H., and Bowerman, B. (2007). Control of nuclear centration in the *C. elegans* zygote by receptor-independent G signaling and myosin II. *The Journal of Cell Biology*, 178(7):1177–1191.

Grant, B. and Hirsh, D. (1999). Receptor-mediated endocytosis in the *Caenorhabditis elegans* oocyte. *Molecular biology of the cell*, 10(12):4311–26.

Gregan, J., Polakova, S., Zhang, L., Tolić-Nørrelykke, I. M., and Cimini, D. (2011). Merotelic kinetochore attachment: causes and effects. *Trends in Cell Biology*, 21(6):374–381.

Grill, S. W., Gönczy, P., Stelzer, E. H., and Hyman, a. a. (2001). Polarity controls forces governing asymmetric spindle positioning in the *Caenorhabditis elegans* embryo. *Nature*, 409(February):630–633.

Grill, S. W., Howard, J., Schäffer, E., Stelzer, E. H. K., and Hyman, A. A. (2003). The Distribution of Active Force Generators Controls Mitotic Spindle Position. *Science*, 301(5632):518–521.

Grishchuk, E. L., Molodtsov, M. I., Ataullakhanov, F. I., and McIntosh, J. R. (2005). Force production by disassembling microtubules. *Nature*, 438(7066):384–388.

Gusnowski, E. M. and Srayko, M. (2011). Visualization of dynein-dependent microtubule gliding at the cell cortex: implications for spindle positioning. *The Journal of cell biology*, 194(3):377–86.

Guyer; Micheal F. (1900). *Spermatogenesis of normal and of hybrid pigeons : a dissertation.* PhD thesis, The University of Chicago.

Hamaguchi, M. S. and Hiramoto, Y. (1986). Analysis of the Role of Astral Rays in Pronuclear Migration in Sand Dollar Eggs by the Colcemid-UV Method. *Devel. Growth and Differ.*, 28(2):143–156.

Hamahashi, S., Onami, S., and Kitano, H. (2005). Detection of nuclei in 4D Nomarski DIC microscope images of early Caenorabditis elegans embryos using local image entropy and object tracking. *BMC bioinformatics*, 6:125.

Hamill, D. R., Severson, A. F., Carter, J. C., and Bowerman, B. (2002). Centrosome maturation and mitotic spindle assembly in *C. elegans* require SPD-5, a protein with multiple coiled-coil domains. *Developmental Cell*, 3(5):673–684.

Hannak, E., Kirkham, M., Hyman, A. A., and Oegema, K. (2001). Aurora-A kinase is required for centrosome maturation in *Caenorhabditis elegans*. *The Journal of cell biology*, 155(7):1109–16.

Hannak, E., Oegema, K., Kirkham, M., Gönczy, P., Habermann, B., and Hyman, A. a. (2002). The kinetically dominant assembly pathway for centrosomal asters in *Caenorhabditis elegans* is γ-tubulin dependent. *Journal of Cell Biology*, 157(4):591–602.

Heald, R., Tournebize, R., Blank, T., Sandaltzopoulos, R., Becker, P., Hyman, A., and Karsenti, E. (1996). Self-organization of microtubules into bipolar spindles around artificial chromosomes in *Xenopus* egg extracts. *Nature*, 382(6590):420–5.

Hinchcliffe, E. H., Miller, F. J., Cham, M., Khodjakov, A., and Sluder, G. (2001). Requirement of a centrosomal activity for cell cycle progression through G1 into S phase. *Science*, 291(5508):1547–50.

Hird, S. N. and White, J. G. (1993). Cortical and cytoplasmic flow polarity in early embryonic cells of *Caenorhabditis elegans*. *The Journal of cell biology*, 121(6):1343–55.

Hirokawa, N., Noda, Y., Tanaka, Y., and Niwa, S. (2009). Kinesin superfamily motor proteins and intracellular transport. *Nature reviews. Molecular cell biology*, 10(10):682–96.

Holy, T. E., Dogterom, M., Yurke, B., and Leibler, S. (1997). Assembly and positioning of microtubule asters in microfabricated chambers. *Proceedings of the National Academy of Sciences of the United States of America*, 94(12):6228–31.

Howard, J. (2001). *Mechanical of motor proteins and the cytoskeleton.* Sinauer Associates, Publishers.

Howard, J. and Hyman, A. A. (2007). Microtubule polymerases and depolymerases. *Current opinion in cell biology*, 19(1):31–5.

Howard, J. and Hyman, A. A. (2009). Growth, fluctuation and switching at microtubule plus ends. *Nature reviews. Molecular cell biology*, 10(8):569–74.

Humphries, A. C., Dodding, M. P., Barry, D. J., Collinson, L. M., Durkin, C. H., and Way, M. (2012). Clathrin potentiates vaccinia-induced actin polymerization to facilitate viral spread. *Cell host & microbe*, 12(3):346–59.

Hyman, A. A. (1989). Centrosome movement in the early divisions of *Caenorhabditis elegans*: a cortical site determining centrosome position. *The Journal of cell biology*, 109(3):1185–93.

Hyman, A. A. and White, J. G. (1987). Determination of cell division axes in the early embryogenesis of *Caenorhabditis elegans*. *The Journal of cell biology*, 105(5):2123–35.

Inoue, S. and Salmon, E. D. (1995). Force Generation by Microtubule Assembly/Disassembly in Mitosis and Related Movements. *Molecular Biology of the Cell*, 6(12):1619–1640.

Jaensch, S., Decker, M., Hyman, A. A., and Myers, E. W. (2010). Automated tracking and analysis of centrosomes in early *Caenorhabditis elegans* embryos. *Bioinformatics*, 26(12):i13–i20.

Janson, M. E., De Dood, M. E., and Dogterom, M. (2003). Dynamic instability of microtubules is regulated by force. *Journal of Cell Biology*, 161(6):1029–1034.

Joglekar, A. P., Bloom, K. S., and Salmon, E. D. (2010). Mechanisms of force generation by end-on kinetochore-microtubule attachments. *Current opinion in cell biology*, 22(1):57–67.

Johnston, C. A., Hirono, K., Prehoda, K. E., and Doe, C. Q. (2009). Identification of an Aurora-A/PinsLINKER/Dlg spindle orientation pathway using induced cell polarity in S2 cells. *Cell*, 138(6):1150–63.

Kalab, P. and Heald, R. (2008). The RanGTP gradient - a GPS for the mitotic spindle. *Journal of Cell Science*, 121(10):1577–1586.

Kamath, R. S. and Ahringer, J. (2003). Genome-wide *RNAi* screening in *Caenorhabditis elegans*. *Methods*, 30(4):313 – 321. {RNA} interference.

Kardon, J. R. and Vale, R. D. (2009). Regulators of the cytoplasmic dynein motor. *Nature Reviews Molecular Cell Biology*, 10(12):854–865.

Kemp, C. A., Kopish, K. R., Zipperlen, P., Ahringer, J., and O'Connell, K. F. (2004). Centrosome maturation and duplication in *C. elegans* require the coiled-coil protein *spd-2*. *Developmental cell*, 6(4):511–23.

Kemphues, K. J., Wolf, N., Wood, W. B., and Hirsh, D. (1986). Two loci required for cytoplasmic organization in early embryos of *Caenorhabditis elegans*. *Developmental biology*, 113(2):449–60.

Khodjakov, a., Cole, R. W., Oakley, B. R., and Rieder, C. L. (2000). Centrosome-independent mitotic spindle formation in vertebrates. *Current biology*, 10:59–67.

Khodjakov, A. and Rieder, C. L. (2001). Centrosomes enhance the fidelity of cytokinesis in vertebrates and are required for cell cycle progression. *The Journal of cell biology*, 153(1):237–42.

Kimura, A. and Onami, S. (2005). Computer simulations and image processing reveal length-dependent pulling force as the primary mechanism for *C. elegans* male pronuclear migration. *Developmental Cell*, 8(5):765–775.

Kimura, A. and Onami, S. (2007). Local cortical pulling-force repression switches centrosomal centration and posterior displacement in *C. elegans*. *The Journal of cell biology*, 179(7):1347–54.

Kimura, K. and Kimura, A. (2011a). A novel mechanism of microtubule length-dependent force to pull centrosomes toward the cell center. *BioArchitecture*, 1(2):74–79.

Kimura, K. and Kimura, A. (2011b). Intracellular organelles mediate cytoplasmic pulling force for centrosome centration in the *Caenorhabditis elegans* early embryo. *Proceedings of the National Academy of Sciences*, 108(1):137–142.

Kinoshita, K., Noetzel, T. L., Arnal, I., Drechsel, D. N., and Hyman, A. A. (2006). Global and local control of microtubule destabilization promoted by a catastrophe kinesin MCAK/XKCM1. *Journal of muscle research and cell motility*, 27(2):107–14.

Kiyomitsu, T. and Cheeseman, I. M. (2012). Chromosome- and spindle-pole-derived signals generate an intrinsic code for spindle position and orientation. *Nature cell biology*, 14(3):311–7.

Klumpp, S. and Lipowsky, R. (2005). Cooperative cargo transport by several molecular motors. *Proc. Natl. Acad. Sci. USA*, 102(48):17284–9.

Koshland, D. E., Mitchison, T. J., and Kirschner, M. W. (1988). Polewards chromosome movement driven by microtubule depolymerization in vitro. *Nature*, 331(6156):499–504.

Kotak, S., Busso, C., and Gönczy, P. (2012). Cortical dynein is critical for proper spindle positioning in human cells. *The Journal of cell biology*, 199(1):97–110.

Kotak, S. and Gönczy, P. (2013). Mechanisms of spindle positioning: cortical force generators in the limelight. *Current opinion in cell biology*, 25(6):741–8.

Kozlowski, C., Srayko, M., and Nedelec, F. (2007). Cortical Microtubule Contacts Position the Spindle in *C. elegans* Embryos. *Cell*, 129(3):499–510.

Labbé, J.-C., McCarthy, E. K., and Goldstein, B. (2004). The forces that position a mitotic spindle asymmetrically are tethered until after the time of spindle assembly. *The Journal of cell biology*, 167(2):245–56.

Le Bot, N., Tsai, M. C., Andrews, R. K., and Ahringer, J. (2003). TAC-1, a regulator of microtubule length in the *C. elegans* embryo. *Current Biology*, 13:1499–1505.

Liu, J., Maduzia, L. L., Shirayama, M., and Mello, C. C. (2010). NMY-2 maintains cellular asymmetry and cell boundaries, and promotes a SRC-dependent asymmetric cell division. *Developmental biology*, 339(2):366–73.

Lorson, M. A., Horvitz, H. R., and van den Heuvel, S. (2000). LIN-5 is a novel component of the spindle apparatus required for chromosome segregation and cleavage plane specification in *Caenorhabditis elegans*. *The Journal of cell biology*, 148(1):73–86.

Lowery, L. A. and Van Vactor, D. (2009). The trip of the tip: understanding the growth cone machinery. *Nature reviews. Molecular cell biology*, 10(5):332–43.

Lutz, D. A., Hamaguchi, Y., and Inoué, S. (1988). Micromanipulation studies of the asymmetric positioning of the maturation spindle in *Chaetopterus sp.* oocytes: I. Anchorage of the spindle to the cortex and migration of a displaced spindle. *Cell motility and the cytoskeleton*, 11(2):83–96.

Lyczak, R., Zweier, L., Group, T., Murrow, M. A., Snyder, C., Kulovitz, L., Beatty, A., Smith, K., and Bowerman, B. (2006). The puromycin-sensitive aminopeptidase PAM-1 is required for meiotic exit and anteroposterior polarity in the one-cell *Caenorhabditis elegans* embryo. *Development*, 133(21):4281–92.

Magidson, V., O'Connell, C. B., Lončarek, J., Paul, R., Mogilner, A., and Khodjakov, A. (2011). The spatial arrangement of chromosomes during prometaphase facilitates spindle assembly. *Cell*, 146(4):555–67.

Mains, P. E., Sulston, I. A., and Wood, W. B. (1990). Dominant maternal-effect mutations causing embryonic lethality in *Caenorhabditis elegans*. *Genetics*, 125(2):351–69.

Malone, C. J., Misner, L., Le Bot, N., Tsai, M. C., Campbell, J. M., Ahringer, J., and White, J. G. (2003). The *C. elegans* Hook Protein, ZYG-12, Mediates the Essential Attachment between the Centrosome and Nucleus. *Cell*, 115(7):825–836.

Manning, A. L., Ganem, N. J., Bakhoum, S. F., Wagenbach, M., Wordeman, L., and Compton, D. A. (2007). The kinesin-13 proteins Kif2a, Kif2b, and Kif2c/MCAK have distinct roles during mitosis in human cells. *Molecular biology of the cell*, 18(8):2970–9.

Matthews, L. R., Carter, P., Thierry-Mieg, D., and Kemphues, K. (1998). ZYG-9, a *Caenorhabditis elegans* protein required for microtubule organization and function, is a component of meiotic and mitotic spindle poles. *Journal of Cell Biology*, 141:1159–1168.

Mayer, M., Depken, M., Bois, J. S., Jülicher, F., and Grill, S. W. (2010). Anisotropies in cortical tension reveal the physical basis of polarizing cortical flows. *Nature*, 467(7315):617–621.

Meunier, S. and Vernos, I. (2015). Acentrosomal Microtubule Assembly in Mitosis: The Where, When, and How. *Trends in cell biology*.

Millecamps, S. and Julien, J.-P. (2013). Axonal transport deficits and neurodegenerative diseases. *Nature reviews. Neuroscience*, 14(3):161–76.

Minc, N., Burgess, D., and Chang, F. (2011). Influence of cell geometry on division-plane positioning. *Cell*, 144(3):414–26.

Molodtsov, M. I., Grishchuk, E. L., Efremov, A. K., McIntosh, J. R., and Ataullakhanov, F. I. (2005). Force production by depolymerizing microtubules: a theoretical study. *Proceedings of the National Academy of Sciences of the United States of America*, 102(12):4353–8.

Moore, J. K. and Cooper, J. A. (2010). Coordinating mitosis with cell polarity: Molecular motors at the cell cortex. *Seminars in cell & developmental biology*, 21(3):283–9.

Motegi, F. and Sugimoto, A. (2006). Sequential functioning of the ECT-2 RhoGEF, RHO-1 and CDC-42 establishes cell polarity in *Caenorhabditis elegans* embryos. *Nature cell biology*, 8:978–985.

Munro, E., Nance, J., and Priess, J. R. (2004). Cortical flows powered by asymmetrical contraction transport PAR proteins to establish and maintain anterior-posterior polarity in the early *C. elegans* embryo. *Developmental Cell*, 7(3):413–424.

Naganathan, S. R., Fürthauer, S., Nishikawa, M., Jülicher, F., and Grill, S. W. (2014). Active torque generation by the actomyosin cell cortex drives left-right symmetry breaking. *eLife*, 3:e04165.

Nance, J., Munro, E. M., and Priess, J. R. (2003). *C. elegans* PAR-3 and PAR-6 are required for apicobasal asymmetries associated with cell adhesion and gastrulation. *Development*, 130:5339–5350.

Nazockdast, E., Rahimian, A., Needleman, D., and Shelley, M. (2015). Cytoplasmic flows as signatures for the mechanics of mitotic positioning. *Bulletin of the American Physical Society*, Volume 60,.

Nédélec, F. (2002). Computer simulations reveal motor properties generating stable antiparallel microtubule interactions. *Journal of Cell Biology*, 158(6):1005–1015.

Nedelec, F. and Foethke, D. (2007). Collective Langevin dynamics of flexible cytoskeletal fibers. *New Journal of Physics*, 9(241).

Nguyen-Ngoc, T., Afshar, K., and Gönczy, P. (2007). Coupling of cortical dynein and G alpha proteins mediates spindle positioning in *Caenorhabditis elegans*. *Nature cell biology*, 9(11):1294–302.

Nigg, E. A. and Raff, J. W. (2009). Centrioles, centrosomes, and cilia in health and disease. *Cell*, 139(4):663–78.

Nigon, V. (1949). Les modalites de la reproduction et le determinisme du sexe chez quelques nematodes libres. *Annales de Sciences Naturelles - Zool. Biol. Anim.*, 11:1–132.

Nobuhito, M. and Kuang-An, C. (2006). PIV toolbox in MATLAB (http://www.oceanwave.jp/softwares/mpiv).

Oakley, B. R., Paolillo, V., and Zheng, Y. (2015). γ-Tubulin complexes in microtubule nucleation and beyond. *Molecular biology of the cell*, 26(17):2957–62.

O'Connell, K. F., Leys, C. M., and White, J. G. (1998). A genetic screen for temperature-sensitive cell-division mutants of *Caenorhabditis elegans*. *Genetics*, 149(3):1303–21.

O'Connell, K. F., Maxwell, K. N., and White, J. G. (2000). The *spd-2* gene is required for polarization of the anteroposterior axis and formation of the sperm asters in the *Caenorhabditis elegans* zygote. *Developmental biology*, 222(1):55–70.

Oegema, K., Desai, A., Rybina, S., Kirkham, M., and Hyman, A. A. (2001). Functional Analysis of Kinetochore Assembly in *Caenorhabditis elegans*. *The Journal of Cell Biology*, 153(6):1209–1226.

Oegema, K. and Hyman, A. A. (2006). Cell division. *WormBook : the online review of C. elegans biology*, pages 1–40.

O'Rourke, S. M., Dorfman, M. D., Carter, J. C., and Bowerman, B. (2007). Dynein modifiers in *C. elegans*: light chains suppress conditional heavy chain mutants. *PLoS genetics*, 3(8):e128.

Pelletier, L., Ozlü, N., Hannak, E., Cowan, C., Habermann, B., Ruer, M., Müller-Reichert, T., and Hyman, A. A. (2004). The *Caenorhabditis elegans* centrosomal protein *spd-2* is required for both pericentriolar material recruitment and centriole duplication. *Current biology*, 14(10):863–73.

Phillips, R., Kondev, J., Theriot, J., and Garcia, H. (2012). *Physical Biology of the Cell, Second Edition*. Garland Science.

Powers, A. F., Franck, A. D., Gestaut, D. R., Cooper, J., Gracyzk, B., Wei, R. R., Wordeman, L., Davis, T. N., and Asbury, C. L. (2009). The Ndc80 kinetochore complex forms load-bearing attachments to dynamic microtubule tips via biased diffusion. *Cell*, 136(5):865–75.

Press, W. H., Flannery, B. P., Teukolsky, S. A., and Vetterling, W. T. (2007). *Numerical Recipes: The Art of Scientific Computing*. Cambridge University Press, New York.

Raaijmakers, J. a., van Heesbeen, R. G. H. P., Meaders, J. L., Geers, E. F., Fernandez-Garcia, B., Medema, R. H., and Tanenbaum, M. E. (2012). Nuclear envelope-associated dynein drives prophase centrosome separation and enables Eg5-independent bipolar spindle formation. *The EMBO Journal*, 31(21):4179–90.

Rago, F. and Cheeseman, I. M. (2013). Review series: The functions and consequences of force at kinetochores. *The Journal of cell biology*, 200(5):557–65.

Rath, O. and Kozielski, F. (2012). Kinesins and cancer. *Nature reviews. Cancer*, 12(8):527–39.

Reck-Peterson, S., Vale, R., and Gennerich, A. (2012). Motile Properties of Cytoplasmic Dynein. In *Handbook of Dynein*, pages 145–172. Pan Stanford Publishing.

Redemann, S., Pecreaux, J., Goehring, N. W., Khairy, K., Stelzer, E. H. K., Hyman, A. a., and Howard, J. (2010). Membrane invaginations reveal cortical sites that pull on mitotic spindles in one-cell *C. elegans* embryos. *PLoS ONE*, 5(8):e12301.

Redemann, S., Schloissnig, S., Ernst, S., Pozniakowsky, A., Ayloo, S., Hyman, A. A., and Bringmann, H. (2011). Codon adaptation-based control of protein expression in *C. elegans*. *Nature methods*, 8:250–252.

Reinsch, S. and Gönczy, P. (1998). Mechanisms of nuclear positioning. *J. Cell Sci.*, 111(16):2283–2295.

Reinsch, S. and Karsenti, E. (1997). Movement of nuclei along microtubules in *Xenopus* egg extracts. *Current biology*, 7:211–214.

Roberts, A. J., Kon, T., Knight, P. J., Sutoh, K., and Burgess, S. A. (2013). Functions and mechanics of dynein motor proteins. *Nature reviews. Molecular cell biology*, 14(11):713–26.

Robin, F. B., McFadden, W. M., Yao, B., and Munro, E. M. (2014). Single-molecule analysis of cell surface dynamics in *Caenorhabditis elegans* embryos. *Nature methods*, 11(6):677–82.

Robinson, J. T., Wojcik, E. J., Sanders, M. A., McGrail, M., and Hays, T. S. (1999). Cytoplasmic dynein is required for the nuclear attachment and migration of centrosomes during mitosis in *Drosophila*. *The Journal of cell biology*, 146(3):597–608.

Rose, L. and Gönczy, P. (2014). Polarity establishment, asymmetric division and segregation of fate determinants in early *C. elegans* embryos. *WormBook : the online review of C. elegans biology*, pages 1–43.

Rose, L. S., Lamb, M. L., Hird, S. N., and Kemphues, K. J. (1995). Pseudocleavage is dispensable for polarity and development in *C. elegans* embryos. *Developmental biology*, 168(2):479–89.

Rosenblatt, J. (2005). Spindle assembly: asters part their separate ways. *Nature cell biology*, 7(3):219–22.

Rosenblatt, J., Cramer, L. P., Baum, B., and McGee, K. M. (2004). Myosin II-dependent cortical movement is required for centrosome separation and positioning during mitotic spindle assembly. *Cell*, 117(3):361–372.

Rual, J.-F., Ceron, J., Koreth, J., Hao, T., Nicot, A.-S., Hirozane-Kishikawa, T., Vandenhaute, J., Orkin, S. H., Hill, D. E., van den Heuvel, S., and Vidal, M. (2004). Toward improving *Caenorhabditis elegans* phenome mapping with an ORFeome-based RNAi library. *Genome research*, 14(10B):2162–8.

Rupp, B. and Nédélec, F. (2012). Patterns of molecular motors that guide and sort filaments. *Lab on a chip*, 12(22):4903–10.

Sadler, P. and Shakes, D. (2000). Anucleate *Caenorhabditis elegans* sperm can crawl, fertilize oocytes and direct anterior-posterior polarization of the 1-cell embryo. *Development*, 127(2):355–366.

Salbreux, G., Charras, G., and Paluch, E. (2012). Actin cortex mechanics and cellular morphogenesis. *Trends in cell biology*, 22(10):536–45.

Salina, D., Bodoor, K., Eckley, D. M., Schroer, T. A., Rattner, J. B., and Burke, B. (2002). Cytoplasmic dynein as a facilitator of nuclear envelope breakdown. *Cell*, 108:97–107.

Saunders, A. M., Powers, J., Strome, S., and Saxton, W. M. (2007). Kinesin-5 acts as a brake in anaphase spindle elongation.

Schmidt, D. J., Rose, D. J., Saxton, W. M., and Strome, S. (2005). Functional analysis of cytoplasmic dynein heavy chain in *Caenorhabditis elegans* with fast-acting temperature-sensitive mutations. *Molecular biology of the cell*, 16(3):1200–12.

Schmutz, C., Stevens, J., and Spang, A. (2007). Functions of the novel RhoGAP proteins RGA-3 and RGA-4 in the germ line and in the early embryo of *C. elegans*. *Development*, 134(19):3495–3505.

Scholey, J. M. (2009). Kinesin-5 in *Drosophila* embryo mitosis: sliding filament or spindle matrix mechanism? *Cell motility and the cytoskeleton*, 66(8):500–8.

Schonegg, S., Constantinescu, A. T., Hoege, C., and Hyman, A. A. (2007). The Rho GTPase-activating proteins RGA-3 and RGA-4 are required to set the initial size of PAR domains in *Caenorhabditis elegans* one-cell embryos. *Proceedings of the National Academy of Sciences of the United States of America*, 104(38):14976–81.

Segbert, C., Barkus, R., Powers, J., Strome, S., Saxton, W. M., and Bossinger, O. (2003). KLP-18, a Klp2 kinesin, is required for assembly of acentrosomal meiotic spindles in *Caenorhabditis elegans*. *Molecular biology of the cell*, 14(11):4458–69.

Sharp, D. J., Brown, H. M., Kwon, M., Rogers, G. C., Holland, G., and Scholey, J. M. (2000). Functional Coordination of Three Mitotic Motors in *Drosophila* Embryos. *Molecular Biology of the Cell*, 11(1):241–253.

Sharp, D. J., Yu, K. R., Sisson, J. C., Sullivan, W., and Scholey, J. M. (1999). Antagonistic microtubule-sliding motors position mitotic centrosomes in *Drosophila* early embryos. *Nature cell biology*, 1(1):51–4.

Shelton, C. A. and Bowerman, B. (1996). Time-dependent responses to *glp-1*-mediated inductions in early *C. elegans* embryos. *Development*, 122:2043–2050.

Shelton, C. A., Carter, J. C., Ellis, G. C., and Bowerman, B. (1999). The nonmuscle myosin regulatory light chain gene *mlc-4* is required for cytokinesis, anterior-posterior polarity, and body morphology during *Caenorhabditis elegans* embryogenesis. *The Journal of cell biology*, 146(2):439–51.

Shinar, T., Mana, M., Piano, F., and Shelley, M. J. (2011). A model of cytoplasmically driven microtubule-based motion in the single-celled *Caenorhabditis elegans* embryo. *Proceedings of the National Academy of Sciences of the United States of America*, 108(26):10508–10513.

Siegrist, S. E. and Doe, C. Q. (2005). Microtubule-induced Pins/Galphai cortical polarity in *Drosophila* neuroblasts. *Cell*, 123(7):1323–35.

Silkworth, W. T., Nardi, I. K., Paul, R., Mogilner, A., and Cimini, D. (2012). Timing of centrosome separation is important for accurate chromosome segregation. *Molecular biology of the cell*, 23(3):401–11.

Sit, S.-T. and Manser, E. (2011). Rho GTPases and their role in organizing the actin cytoskeleton. *Journal of cell science*, 124(Pt 5):679–83.

Song, M. H., Aravind, L., Müller-Reichert, T., and O'Connell, K. F. (2008). The conserved protein SZY-20 opposes the Plk4-related kinase ZYG-1 to limit centrosome size. *Developmental cell*, 15(6):901–12.

Spiró, Z., Thyagarajan, K., De Simone, A., Träger, S., Afshar, K., and Gönczy, P. (2014). Clathrin regulates centrosome positioning by promoting acto-myosin cortical tension in *C. elegans* embryos. *Development*, 141(13):2712–23.

Splinter, D., Tanenbaum, M. E., Lindqvist, A., Jaarsma, D., Flotho, A., Yu, K. L., Grigoriev, I., Engelsma, D., Haasdijk, E. D., Keijzer, N., Demmers, J., Fornerod, M., Melchior, F., Hoogenraad, C. C., Medema, R. H., and Akhmanova, A. (2010). Bicaudal D2, dynein, and kinesin-1 associate with nuclear pore complexes and regulate centrosome and nuclear positioning during mitotic entry. *PLoS Biology*, 8.

Srayko, M., Kaya, A., Stamford, J., and Hyman, A. a. (2005). Identification and characterization of factors required for microtubule growth and nucleation in the early *C. elegans* embryo. *Developmental Cell*, 9(2):223–236.

Srayko, M., Quintin, S., Schwager, A., and Hyman, A. a. (2003). *Caenorhabditis elegans* TAC-1 and ZYG-9 form a complex that is essential for long astral and spindle microtubules. *Current Biology*, 13(17):1506–1511.

Srinivasan, D. G., Fisk, R. M., Xu, H., and van den Heuvel, S. (2003). A complex of LIN-5 and GPR proteins regulates G protein signaling and spindle function in C elegans. *Genes & development*, 17(10):1225–39.

Strome, S. (1986). Fluorescence visualization of the distribution of microfilaments in gonads and early embryos of the nematode *Caenorhabditis elegans*. *The Journal of cell biology*, 103(6 Pt 1):2241–52.

Strome, S., Powers, J., Dunn, M., Reese, K., Malone, C. J., White, J., Seydoux, G., and Saxton, W. (2001). Spindle dynamics and the role of gamma-tubulin in early *Caenorhabditis elegans* embryos. *Molecular biology of the cell*, 12(6):1751–64.

Strome, S. and Wood, W. B. (1983). Generation of asymmetry and segregation of germ-line granules in early *C. elegans* embryos. *Cell*, 35(1):15–25.

Symon, K. R. (1971). *Mechanics*.

Szathmáry, E. and Smith, J. M. (1995). The major evolutionary transitions. *Nature*, 374(6519):227–32.

Tanenbaum, M. E., Macůrek, L., Janssen, A., Geers, E. F., Alvarez-Fernández, M., and Medema, R. H. (2009). Kif15 cooperates with eg5 to promote bipolar spindle assembly. *Current biology*, 19(20):1703–11.

Tanenbaum, M. E. and Medema, R. H. (2010). Mechanisms of Centrosome Separation and Bipolar Spindle Assembly. *Developmental Cell*, 19(6):797–806.

Thyagarajan, K., Afshar, K., and Gönczy, P. (2011). Polarity mediates asymmetric trafficking of the Gbeta heterotrimeric G-protein subunit GPB-1 in *C. elegans* embryos. *Development*, 138(13):2773–82.

Tikhonenko, I., Nag, D. K., Martin, N., and Koonce, M. P. (2008). Kinesin-5 is not essential for mitotic spindle elongation in dictyostelium. *Cell Motility and the Cytoskeleton*, 65:853–862.

Tillement, V., Remy, M.-H., Raynaud-Messina, B., Mazzolini, L., Haren, L., and Merdes, A. (2009). Spindle assembly defects leading to the formation of a monopolar mitotic apparatus. *Biology of the cell / under the auspices of the European Cell Biology Organization*, 101(1):1–11.

Tournebize, R., Popov, A., Kinoshita, K., Ashford, A. J., Rybina, S., Pozniakovsky, A., Mayer, T. U., Walczak, C. E., Karsenti, E., and Hyman, A. A. (2000). Control of microtubule dynamics by the antagonistic activities of XMAP215 and XKCM1 in *Xenopus* egg extracts. *Nature cell biology*, 2:13–19.

Toya, M., Terasawa, M., Nagata, K., Iida, Y., and Sugimoto, A. (2011). A kinase-independent role for Aurora A in the assembly of mitotic spindle microtubules in *Caenorhabditis elegans* embryos. *Nature cell biology*, 13(6):708–14.

Tran, P. T., Marsh, L., Doye, V., Inoué, S., and Chang, F. (2001). A mechanism for nuclear positioning in fission yeast based on microtubule pushing. *The Journal of cell biology*, 153(2):397–411.

Tse, Y. C., Werner, M., Longhini, K. M., Labbe, J.-C., Goldstein, B., and Glotzer, M. (2012). RhoA activation during polarization and cytokinesis of the early *Caenorhabditis elegans* embryo is differentially dependent on NOP-1 and CYK-4. *Molecular Biology of the Cell*, 23(20):4020–4031.

Tsou, M.-F. B., Hayashi, A., DeBella, L. R., McGrath, G., and Rose, L. S. (2002). LET-99 determines spindle position and is asymmetrically enriched in response to PAR polarity cues in *C. elegans* embryos. *Development*, 129(19):4469–81.

Vaisberg, E. A., Koonce, M. P., and McIntosh, J. R. (1993). Cytoplasmic dynein plays a role in mammalian mitotic spindle formation. *The Journal of cell biology*, 123(4):849–58.

Vallee, R. B., McKenney, R. J., and Ori-McKenney, K. M. (2012). Multiple modes of cytoplasmic dynein regulation. *Nature cell biology*, 14(3):224–30.

van der Vaart, B., Akhmanova, A., and Straube, A. (2009). Regulation of microtubule dynamic instability. *Biochemical Society transactions*, 37(Pt 5):1007–13.

Vanneste, D., Takagi, M., Imamoto, N., and Vernos, I. (2009). The role of Hklp2 in the stabilization and maintenance of spindle bipolarity. *Current biology*, 19(20):1712–7.

Verhey, K. J. and Hammond, J. W. (2009). Traffic control: regulation of kinesin motors. *Nature reviews. Molecular cell biology*, 10(11):765–77.

Vicente-Manzanares, M., Ma, X., Adelstein, R. S., and Horwitz, A. R. (2009). Non-muscle myosin II takes centre stage in cell adhesion and migration. *Nature reviews. Molecular cell biology*, 10(11):778–90.

Vogel, S. K., Pavin, N., Maghelli, N., Jülicher, F., and Tolić-Nørrelykke, I. M. (2009). Self-organization of dynein motors generates meiotic nuclear oscillations. *PLoS Biology*, 7:0918–0928.

Walczak, C. E., Cai, S., and Khodjakov, A. (2010). Mechanisms of chromosome behaviour during mitosis. *Nature reviews. Molecular cell biology*, 11(2):91–102.

Walczak, C. E. and Heald, R. (2008). Mechanisms of mitotic spindle assembly and function. *International review of cytology*, 265:111–58.

Waters, J. C., Cole, R. W., and Rieder, C. L. (1993). The force-producing mechanism for centrosome separation during spindle formation in vertebrates is intrinsic to each aster. *Journal of Cell Biology*, 122(2):361–372.

Weinberg, R. (2013). *The Biology of Cancer, Second Edition*. Garland Science.

Westermann, S., Wang, H.-W., Avila-Sakar, A., Drubin, D. G., Nogales, E., and Barnes, G. (2006). The Dam1 kinetochore ring complex moves processively on depolymerizing microtubule ends. *Nature*, 440(7083):565–9.

Wignall, S. M. and Villeneuve, A. M. (2009). Lateral microtubule bundles promote chromosome alignment during acentrosomal oocyte meiosis. *Nature cell biology*, 11(7):839–44.

Woodard, G. E., Huang, N.-N., Cho, H., Miki, T., Tall, G. G., and Kehrl, J. H. (2010). Ric-8A and Gi alpha recruit LGN, NuMA, and dynein to the cell cortex to help orient the mitotic spindle. *Molecular and cellular biology*, 30(14):3519–30.

Woodruff, J. B., Wueseke, O., Viscardi, V., Mahamid, J., Ochoa, S. D., Bunkenborg, J., Widlund, P. O., Pozniakovsky, A., Zanin, E., Bahmanyar, S., Zinke, A., Hong, S. H., Decker, M., Baumeister, W., Andersen, J. S., Oegema, K., and Hyman, A. A. (2015). Regulated assembly of a supramolecular centrosome scaffold in vitro. *Science*, 348(6236):808–812.

Wühr, M., Dumont, S., Groen, A. C., Needleman, D. J., and Mitchison, T. J. (2009). How does a millimeter-sized cell find its center? *Cell cycle (Georgetown, Tex.)*, 8(8):1115–21.

Wühr, M., Tan, E. S., Parker, S. K., Detrich, H. W., and Mitchison, T. J. (2010). A Model for Cleavage Plane Determination in Early Amphibian and Fish Embryos. *Current Biology*, 20(22):2040–2045.

Yamamoto, A., West, R. R., McIntosh, J. R., and Hiraoka, Y. (1999). A cytoplasmic dynein heavy chain is required for oscillatory nuclear movement of meiotic prophase and efficient meiotic recombination in fission yeast. *The Journal of cell biology*, 145(6):1233–49.

Zhang, X., Lan, W., Ems-McClung, S. C., Stukenberg, P. T., and Walczak, C. E. (2007). Aurora B phosphorylates multiple sites on mitotic centromere-associated kinesin to spatially and temporally regulate its function. *Molecular biology of the cell*, 18(9):3264–76.

Zhu, C., Zhao, J., Bibikova, M., Leverson, J. D., Bossy-Wetzel, E., Fan, J.-B., Abraham, R. T., and Jiang, W. (2005). Functional analysis of human microtubule-based motor proteins, the kinesins and dyneins, in mitosis/cytokinesis using RNA interference. *Molecular biology of the cell*, 16(7):3187–99.

Zwicker, D., Decker, M., Jaensch, S., Hyman, A. a., and Jülicher, F. (2014). Centrosomes are autocatalytic droplets of pericentriolar material organized by centrioles. *Proceedings of the National Academy of Sciences of the United States of America*, 111(26):E2636–45.

Alessandro De Simone

Personal Information

Avenue de la poste 24
1020 Renens (VD) - CH
tel: +41 (0)76 732 43 44
ale.dsmn@gmail.com
Date of birth: 12/11/1987
Nationality: Italian
B Permit

Highlights

- ✓ **M.Sc. in Physics of Complex Systems**
- ✓ **Ph.D. in Molecular Biology**
- ✓ **Quantitative and Computational Biology**
- ✓ **Cell and Developmental Biology**
- ✓ **Passionate communicator**

Education

Ph.D. in Molecular Biology (Federal Institute of Technology Lausanne - EPFL)
2011 - expected March 2016

Master degree in Physics of Complex Systems (University of Turin)
2009 - 2011
Final Mark: 110/110 Magna Cum Laude
Average exams mark: 30/30 with 6 Honors on 12 exams.

Bachelor degree in Physics (University of Turin)
2006 - 2009
Final Mark: 110/110 Cum Laude
Average exams mark: 30/30 with 11 Honors on 27 exams.

Research activities

Research and teaching assistant Gönczy Lab - ISREC (EPFL), Lausanne
September 2011 - ongoing

I have studied the mechanics of centrosome separation by developing an interdisciplinary approach that combines microscopy, reverse genetics, image processing and computational modeling. I have learned molecular biology methods and performed experiments. I have established a collaboration with the Nédélec Lab at EMBL (Heidelberg) and collaborated to three additional projects within EPFL, focusing on data analysis and modeling. In addition to peer-reviewed publications, I have presented my results in international conferences (3 award-winning posters and 2 talks).

Master student Systems Biology Lab - IRCC, Candiolo (Turin)
September 2010 - July 2011

I have worked in an interdisciplinary team to understand the mechanisms of aggregation of prostatic cancer cells. I have analyzed experimental data and developed a theoretical model of chemotactic aggregation.

Summer student SINQ - Paul Scherrer Institut (PSI), Villigen
June-September 2009

I have computationally modeled the SINQ neutron source and studied its optimization. In addition, I have designed a fast neutron irradiation station for the production of medical radioisotopes.

Courses

Modeling cellular processes in space and time - 2014 (Porquerolles, FR)
Microscopy, modeling and biophysical methods - EMBO, 2012 (EMBL)
Complex materials in physics and biology - SIF, 2010 (Varenna, IT)

Talks

Selected speaker - Biophysical Society Meeting 2015 (Baltimore, USA)
Selected speaker - Basel Worm Meeting 2015 (Basel, CH)

Prizes & Awards

First Prizes (Jury and audience) My Thesis in 180s (EPFL) 2015
Best Poster Award SystemsX.ch Conference on Systems Biology 2014
Poster Prize Physics and Biological Systems Conference 2014
Student Poster Prize British Society for Cell Biology Autumn Meeting 2013
Optime Award 2010 Best new graduate 2009 - Turin's Industrial Union

Computer skills

I can proficiently program in C++, Python, Mathematica and MATLAB that I used on a daily basis during my master thesis and Ph.D. studies.

Language skills

Italian: mother tongue **English**: professional fluent
French: conversational fluent

Extra curricular activities

Writer on www.aspassoconsmith.it (2014). I wrote the popular science column **Science After Eight** (in italian).

Popular science seminars (2008-2009). I have given seminars for students and citizens on complexity, scientific programming and cellular automata.

Additional Information

Amateur theatre actor since 1998. I played in several amateur theatre companies in italian and french, participating to more than 15 plays and 6 improvisation shows, often assuming leading roles. Director of the EPFL italophone amateur improvisation group during 2015. Co-founder of the theater group Mimesis in Turin.

Co-founder and President (2009-2010) of the association "P. Borsellino" for the development of the city of Moncalieri (IT). The association participated to the city elections in March 2010 together with the winning coalition, resulting in the election of three city council members from our group.

I worked in a waiter team in London (Skylon) during the summer of 2008.

I love reading, skiing, wind-surfing and cooking.

Research Publications

De Simone A, Nédélec F, and Gönczy P. Dynein transmits polarized actomyosin cortical flows to promote centrosome separation, *Cell Reports*, 2016, http://dx.doi.org/10.1016/j.celrep.2016.01.077

Puliafito A, De Simone A, Seano S, Gagliardi P, di Blasio L, Chianale F, Gamba A, Primo L, and Celani A. Three-dimensional chemotaxis-driven aggregation of tumor cells, *Scientific Reports*, 5:15205, 2015

Spiro Z, Thyagarajan K, De Simone A, Trager S, Afhsar K, and Gönczy P. Clathrin regulates centrosome positioning by promoting acto-myosin cortical tension in *C. elegans* embryos, *Development*, 141(13):2712-23, 2014

d'Eysmond T, De Simone A, and Naef F. Analysis of precision in chemical oscillators: implications for circadian clocks, *Physical biology*, 10(5):056005, 2013

Selected Conference Proceedings

De Simone A and Gönczy P. Cortical Dynein Powered by Polarized Actomyosin Contractions and Pronuclear Dynein Separate Centrosomes, *Biophysical Journal*, 108(2):180a, 2015

Zanini L, De Simone A, Schumann D, Production of Radioisotopes for Medical Applications at the SINQ Spallation Neutron Source using Protons and Fast Neutrons, *Book of Abstracts of the Physics for Health in Europe workshop*, p. 31, CERN Switzerland, 2010

Didactic Publication

Di Tommaso M, De Simone A, Grella M, and Nicola M. *Nuova matematica a colori - Informatica.* De Agostini Scuola, 2013 (in italian)
Online resource: http://keynes.scuole.bo.it/sitididattici/mateacolori/index.htm